Thermal Diffusion
in binary Surfactant Systems
and Microemulsions

Berichterstatter: Prof. Dr. R. Strey
(Gutachter)   PD Dr. S. Wiegand

Tag der mündlichen Prüfung: 28.06.2011

ABSTRACT

In this work the thermal diffusion behavior of micellar systems and microemulsions is studied. These model systems are used to investigate two open questions. The first question focuses on the influence of the micelle formation around the critical micelle concentration (cmc) on the thermal diffusion behavior. In order to answer this, we studied the thermal diffusion behavior of the nonionic surfactant n–Octyl β–D–glucopyranoside ($\mathbf{C_8G_1}$) in water, which shows a fairly high cmc at 0.65 wt% for different concentrations between $w = 0.25$ wt% and $w = 2.0$ wt% in a temperature range from $T = 15$ °C to 60 °C using the classical and infrared thermal diffusion forced Rayleigh scattering ($TDFRS$) setup. The cmc is independently determined by surface tension measurements. In classical TD-FRS experiments, the surfactant solutions show, in the presence of a light-absorbing dye, a pronounced change of the thermal diffusion coefficient, D_T, and the Soret coefficient, S_T, at the cmc. This result agrees with a recent thermal lens study [Santos $et\ al.$, Phys. Rev. E 2008, $\mathbf{77}$, 011403], which showed, also in the presence of dye, a pronounced change of the matter part of the thermal lens signal around the cmc. We found that the change in the thermal diffusion properties becomes less pronounced if the dye is absent or a light source is used which is not absorbed by the dye. At higher concentrations, we observed a temperature-dependent sign inversion of S_T as has also been found for solutions of hard spheres at higher concentrations. We also studied the sugar surfactants n–Heptyl β–D–glucopyranoside ($\mathbf{C_7G_1}$) and n–Octyl β–D–maltopyranoside ($\mathbf{C_8G_2}$), to investigate the influence of the number of head groups and the length of the alkyl chain on the thermal diffusion behavior. In the low concentration regime around the cmc, the abrupt change of S_T was confirmed for $\mathbf{C_7G_1}$ and $\mathbf{C_8G_2}$. Further, the sign change in the high concentration regime was confirmed. The second question is the radial dependence of the Soret coefficient. It is controversially discussed whether the radial dependence of S_T is quadratic

or linear. We shed some light on this discussion by investigating microemulsions which are used as a model system of spherical particles. This thermodynamically stable and nanostructured ternary system of water, oil, and surfactant forms in the one phase (1ϕ) region of the phase diagram oil-in-water (o/w) at the water-rich side or water-in-oil (w/o) microemulsion droplets at the oil-rich side, respectively. Size and shape of these droplets can be tuned by varying temperature or concentration without changing the chemistry of the droplet. We studied the microemulsion H_2O/n-alkane/pentaethylene glycol monodo-decyl ether close to the emulsification failure boundary (efb) to ensure a spherical shape of the microemulsion droplets. Due to the temperature dependence of the efb, not only the size but simultaneously the temperature changes if one considers the microemulsion droplets along the efb. Therefore, the n-alkane was varied in order to make sure that the temperature is the same for all droplets of different sizes. The hydrodynamic radius of the investigated samples varied between 4.72 nm (n-tetradecane) and 15.20 nm (n-octane). Simultaneously also the droplet volume fraction changed from 4.76 vol% (n-tetradecane) to 10.50 vol% (n-octane). For all n-alkane systems, small angle neutron scattering ($SANS$) experiments were performed to verify the spherical structure of the droplets. The analysis of the Soret coefficient of these different microemulsion systems leads to a rather linear size dependence of the droplets on the water-rich side. Preliminary measurements show the same trend for the oil-rich side.

KURZZUSAMMENFASSUNG

In dieser Arbeit haben wir das Thermodiffusionsverhalten von mizellaren Systemen und Mikroemulsionen untersucht. Beide Systeme werden als Modellsysteme genutzt um zwei Fragestellungen zu beantworten. Die erste Fragestellung bezieht sich auf den Einfluss der Mizellenbildung nahe der kritischen Mizellenkonzentration (cmc) auf das Thermodiffusionsverhalten. Dazu untersuchen wir das Thermodiffusionsverhalten des nichtionischen Tensides n–Octyl β–D–glucopyranoside (C_8G_1) in Wasser, welches eine relativ hohe cmc bei 0.65 wt% besitzt, im Konzentrationsbereich zwischen $w = 0.25$ wt% und $w = 2.0$ wt% und im Temperaturbereich von $T = 15\,°C$ bis $60\,°C$ in der klassischen und infraroten *thermal diffusion forced Rayleigh scattering* (*TDFRS*) Anlage. Zudem haben wir unabhängig von den TDFRS Messungen die kritische Mizellenkonzentration durch Oberflächenspannungsmessungen bestimmt. In der klassischen TDFRS Anlage zeigt das Tensidsystem unter Einfluss eines lichtabsorbierenden Farbstoffes eine ausgeprägte Veränderung des Thermodiffusionskoeffizienten, D_T, und des Soret Koeffizienten, S_T, in der Nähe der cmc. Dieses Ergebnis weist in die gleiche Richtung wie eine kürzlich veröffentlichte Arbeit von Santos *et al.* [Phys. Rev. E 2008, **77**, *011403*], in der unter Farbstoffeinfluss ebenfalls eine deutliche Änderung des Messsignals in einem thermischen Linsenexperiment bei der cmc beobachtet wurde. Wir fanden zudem heraus, dass die Änderung des Thermodiffusionskoeffizienten, sowohl ohne Farbstoff als auch wenn die Laserwellenlänge des Schreiblasers nicht durch den Farbstoff absorbiert wird, weniger stark ausgeprägt ist. Bei höheren Konzentrationen konnten wir einen temperaturabhängigen Vorzeichenwechsel des Soret Koeffizienten beobachten. Desweiteren haben wir untersucht, ob strukturelle Änderungen, wie die Zahl der Kopfgruppen oder die Länge der Alkylketten einen Einfluss auf das Thermodiffusionsverhalten haben. Messungen an n–Heptyl β–D–glucopyranoside (C_7G_1) und an n–Octyl β–D–maltopyranoside (C_8G_2) zeigten ebenfalls eine signifikante

Änderung der Thermodiffusionskoeffizienten an der *cmc*. Im höheren Konzentrationsbereich konnten wir nicht nur den S_T-Vorzeichenwechsel bestätigten, sondern durch Skalierung der Konzentration und des Soret Koeffizienten eine Masterkurve erhalten. Die zweite Fragestellung dieser Arbeit betrifft die Bestimmung der radialen Abhängigkeit des Soret Koeffizienten für den bislang experimentell sowohl eine lineare als auch eine quadratische Größenabhängigkeit gefunden wurde. Wir haben diese Fragestellung mithilfe von Mikroemulsionen untersucht, die wir als Modellsystem für sphärische Teilchen benutzt haben. Mikroemulsionen sind thermodynamisch stabile, nanoskopisch strukturierte, ternäre Systeme aus Wasser, Öl und Tensid. Mikroemulsionen formen in den 1ϕ-Regionen des Phasendiagramms auf der wasser- bzw. ölreichen Seite o/w bzw. w/o Tröpfchen. Größe und Form dieser Tröpfchen lassen sich über Temperatur-, Konzentrationsvariationen oder Zusammensetzung der Komponenten einstellen ohne dass sich die Chemie der Mikroemulsionströpfchen ändert. Wir untersuchen H_2O/*n*-Alkan/Pentaethylene glycol monododecyl ether Mikroemulsionen nahe der unteren Entmischungsgrenze des Einphasengebietes auf der wasserreichen Seite, der sogenannten *emulsification failure boundary* (*efb*), an der die Mikroemulsionströpfchen kugelförmig sind. Wenn man die Größe der Tröpfchen ändert indem man sich entlang der *efb* bewegt, verändert sich gleichzeitig auch die Temperatur. Deswegen wurde die Kettenlänge des *n*-Alkanes variiert um Tröpfchen unterschiedlicher Größe bei gleicher Temperatur zu studieren. Die untersuchten Mikroemulsionen decken einen Tröpfchenradius von 4.72 nm (*n*-Tetradecan) bis 15.20 nm (*n*-Octan) ab. Allerdings ändert sich dabei der Volumenbruch der Tröpfchen zwischen 4.76 vol% (*n*-Tetradecan) und 10.50 vol% (*n*-Octan). Für alle untersuchten Mikroemulsionen wurden Form, Größe und Wechselwirkungseffekte der Tröpfchen mit Neutronenstreuung charakterisiert. Die Messungen auf der wasserreichen Seite ergaben eine lineare Abhängigkeit des Soret Koeffizienten vom Radius der Tröpfchen. Erste Messungen auf der ölreichen Seite bestätigen dieses Ergebnis.

CONTENTS

CHAPTER

ONE

INTRODUCTION

The effect of thermodiffusion describes mass separation in a mixture due to a temperature gradient. This effect is also called Ludwig-Soret-Effect denoted after the discoverers Carl Ludwig [1] and Charles Soret [2–4]. Thermodiffusion became not only important for the separation of crude oils [5] and isotopes [6–8] but plays also a role in biological systems or terrestrial cycles [9–11]. Since its discovery, many experimental methods have been developed. In those early days a quantitative determination of the thermal diffusion coefficient was often not possible due to interference with convection. First systematic studies have been performed in a thermal diffusion column [12] for gaseous systems and also for liquid mixtures [13]. Several experimental techniques have been developed, for instance the Soret cell [14, 15], the laser beam deflection technique [16, 17], the thermal lens method [18], the thermal flow field fractionation [19, 20], a fluorescence method [21] or the thermal diffusion forced Rayleigh scattering technique [22–25].

The strength of the concentration gradient caused by a temperature gradient due to thermal diffusion in the steady state is described by the Soret coefficient, S_T:

$$S_T = -\frac{1}{w(1-w)} \cdot \frac{\Delta w}{\Delta T} = \frac{D_T}{D} \tag{1.1}$$

with the resulting difference in concentration, Δw, due to an applied temperature difference, ΔT. Eq.1.1 also introduces the Soret coefficient as the ratio of the mass diffusion coefficient, D, and the thermal diffusion coefficient, D_T.

The first theory, which predicted the thermal diffusion effect for gas mixtures, was the

kinetic gas theory by Chapman and Enskog [26, 27]. All attempts to expand their theory for dense and interacting systems, such as liquids, failed. Although theoretical approaches are able to describe the thermal diffusion behavior of selected systems [28–32], a general description of the Soret effect on a molecular level is still lacking.

Experimentally, many systematic measurements of the thermal diffusion properties of low-molecular weight mixtures, micellar systems of ionic [33–37] and nonionic amphiphiles [38–41], polymers and colloidal suspensions have been performed [21, 42–50] in order to build a reliable database to evaluate theories and simulations. The advantage of low-molecular weight mixtures is that they are accessible by molecular dynamic simulations [51–54]. For polymeric systems power laws as function of the chain length can be derived [31, 32]. The advantage of colloidal model systems is that they can be used as large atomic model systems for which interaction strength and size can be tuned [30, 55–57] and which can be described by analytical theories.

Although there is no full microscopic understanding for the thermal diffusion process, some correlations between certain physical and chemical properties and the Soret or thermal diffusion coefficient can be found. Often, the heavier molecules, the larger molecules, the molecules with the higher symmetry tend to accumulate in the cold region. But there are also exceptions from the rule of thumb which are often related with specific chemical interactions such as hydrogen bonds or changes in the solvent quality [31, 32, 42, 51, 58–62].

In this work we want to use micellar and microemulsions as model systems to shed some light on two open questions. The first question is related to the influence of the micelle formation on the thermal diffusion behavior around the critical micelle concentration, while the second question points to the radial dependence of the Soret coefficient, which should be investigated using microemulsions.

Monomerically dissolved amphiphilic surfactant molecules are regarded as a self-assembling system as they form micelles at a critical micelle concentration (*cmc*). Santos *et al.* [34] recently investigated the thermal diffusion behavior of potassium laurate in water in the vicinity of the *cmc* and found an abrupt change of the matter part of a thermal lens signal at the *cmc*. Unfortunately, an evaluation of S_T was not possible due to the presence of a dye which complicated the analysis. Therefore, it remained unclear to which extend the *cmc* is also visible in the thermal diffusion or Soret coefficient. To clarify these observations, the thermal diffusion behavior of micellar systems with a high *cmc* needs to be investigated without the addition of dye. Among the wide range of

surfactants, we chose a nonionic sugar surfactant with a fairly high *cmc* such as *n*–Octyl *β*–D–glucopyranoside.

For a system consisting of amphiphilic surfactants, unfavored solvent-solute interactions cause the formation of micelles and are thereon the reason for the existence of the *cmc*. Additionally, these interactions and in general changes in the solvent quality induce also a sign change of the Soret coefficient. This sign change behavior is a common observation, which has already been found for many different organic [59, 62, 63], aqueous [48, 64] or charged [33] mixtures. It is one topic of this work to investigate the occurrence of a sign change behavior of the Soret coefficient in sugar surfactant solutions. Beside the concentration dependence also the temperature dependence, which has been described by an empirical equation suggested by Iacopini *et al.* [64], can be studied.

Recent studies have been performed in a thermal diffusion forced Rayleigh scattering (TDFRS) setup. With this experimental method, only small temperature gradients in the order of $20 - 100$ μK are applied, so that for instance microemulsion systems will not undergo a phase transition. Another advantage of the experimental method is that the fringe spacing between the warm and the cold is in the order of only 20 μm, which allows short equilibration times of only a few seconds and avoids convection. In some TDFRS setups, this temperature gradient can only be induced in the presence of dye. Unfortunately, studies with the classical TDFRS setup in the presence of a light absorbing dye showed a pronounced change of the thermal diffusion and the Soret coefficient [38]. But this change is less distinct, if the dye is absent or a light source is used, which is not absorbed by the dye [58].

The radial dependence of the Soret coefficient is an open question. Some experimental studies found a quadratic [65], others a linear [35, 66, 67] relation. While Duhr and Braun [65] observed an unambiguous quadratic radial dependence of S_{T} for carboxyl modified polystyrene (PS) beads in 1 mM TRIS buffer of different radii in the range from 20 nm to 1000 nm using a microscopic fluorescence technique, studies by Putnam and Cahill [67] of carboxyl functionalized PS spheres in a size range from 26 nm to 92 nm in diameter gave some indication that the behavior could also be linear. Additionally, Vigolo *et al.* [35] obtained a linear dependence investigating AOT/isooctane/water microemulsion droplets with a radius between 1.8 nm and 16 nm. Unfortunately, the shape of these microemulsion droplets has not yet systematically been characterized by neutron scattering methods, so that it is not sure that the microemulsion droplets are spherical in the investigated range. Another complication of this system is, that simultaneously with a radial change also the

surface charge density will decrease with increasing radius. This will alter the electrostatic contribution to the thermal diffusion properties, so that the obtained radial dependence is not solely determined by a size change. Recently, Braibanti *et al.* [66] repeated the experiment of Duhr and Braun [65] and studied also the thermal diffusion behavior of highly diluted carboxyl modified PS spheres under the same conditions except that they used a 1:1 mixture of $H_2O + D_2O$ to minimize sedimentation effects which can occur for larger colloids. In the investigated radial range between 11 nm and 253 nm they found a linear radial dependence of S_T. This experimentally observed behavior is in accordance with the theoretical prediction for solid particles. In contrast for soft particles a quadratic radial dependence of S_T is expected [68].

For the investigation of the radial dependence of S_T, the particle size has to be tuned. In the case that the particle density is kept constant, an increase in the particle volume fraction is implied so that particle-particle and particle-solvent interactions have to be considered [29, 69–74]. By keeping the volume fraction constant, the particle density will decrease if the particle size increases. It was shown for colloidal dispersions that in diluted systems particle-particle interactions can be neglected, while in the high concentration regime above approximately 10 vol%, particle-particle interactions dominate the concentration dependence of D_T [42]. An additional requirement for the model system is that the surface properties such as grafting density or charge density of the particles of different sizes should be the same. This prerequisite is difficult to fulfill for colloids, because for each particle size a separate synthesis has to be carried out, which leads in general to different surface properties.

Microemulsions are adaptable model systems, and their microstructure can be varied in size and shape without changing the chemistry of the constituents. They are thermodynamic stable systems of at least three components which are water (polar), oil (nonpolar) and surfactant (amphiphilic). In contrast to colloidal systems, they self-assemble spontaneously and can be regarded as thermodynamically stable but dynamic aggregates. In the isotropic phase, networks of bicontinuous phases are formed in the surfactant-rich region of the phase diagram. Additionally, in the water-rich or oil-rich region, oil-in-water (o/w) or water-in-oil (w/o) droplets are formed, respectively, which can be tuned in size and shape by varying the concentration and temperature. The surface characteristics of a microemulsion droplet do not change. In this work, nonionic microemulsions will be used as a model system for spherical droplets. The droplets surface structure, droplet-droplet interaction effects and their shape can be characterized by small angle neutron scattering

experiments. To our best knowledge the thermal diffusion behavior of microemulsions is rarely investigated [35].

1.1. Motivation and Objectives

This work results from a collaboration between the groups of Prof. R. Strey and PD Dr. T. Sottmann at the Universität zu Köln and Prof. J.K.G. Dhont and PD Dr. S. Wiegand (Forschungszentrum Jülich). The strength of this collaboration is the combination of the experimental expertise in microemulsions and amphiphilic systems in Köln with the thermal diffusion knowledge in Jülich. Amphiphilic systems have been selected, characterized and used as model systems to determine the thermal diffusion behavior of nanostructured fluids. The project was supported by the German Research Society (DFG).

First of all, nonionic sugar surfactants in water are studied below and above the critical micelle concentration (cmc). To our best knowledge, this is the first time, that the Soret coefficient will be systematically investigated in the vicinity of the cmc. Micelles are formed above the cmc. They coexist with single surfactant molecules. By means of surface tension measurements the cmc of three sugar surfactants with a fairly high cmc is determined at different temperatures. The surfactants differ in the number of hydrophilic and hydrophobic units. As the diffusion constant of the micelles is lower than of single molecules, it is expected that the Soret coefficient shows a distinct change at the cmc [34]. Furthermore it is expected, that at even higher surfactant concentrations the Soret coefficient shows a sign change from positive to negative with increasing concentration. The sign change behavior will also be investigated in a temperature dependence. Thermal diffusion experiments will be performed using the infrared thermal diffusion forced Rayleigh scattering (IR-$TDFRS$) setup. This method is optimized for aqueous mixtures [75]. For the determination of the dye influence, also measurements in the classical TDFRS setup [22, 75] are performed.

In the second part we will investigate the thermal diffusion behavior of microemulsions. These ternary mixtures of a polar, a nonpolar and an amphiphilic component [76] form w/o-droplets in an oil-rich 1ϕ region, o/w-droplets in a water-rich 1ϕ region, and networks of bicontinuous phases in the surfactant-rich region of the phase diagram. Within the 1ϕ regimes on the water- or oil-rich side of the phase diagram, these microemulsion droplets can be varied in size and shape by temperature or composition. The respective phase diagrams of H_2O/n-alkane/pentaethylene glycol monododecyl ether ($C_{12}E_5$) mi-

croemulsions are determined. The measurements will focus on the emulsification failure boundary (*efb*) which confines the 1ϕ region to the lower $\underline{2}\phi$ region on the water-rich side. Along this boundary one finds spherical microemulsion droplets, and for a constant surfactant-to-water ratio, their size is tuned by a variation of the weight fraction of the oil component. Small angle neutron scattering (SANS) experiments provide information about the droplet shape, size and interaction effects. SANS measurements are performed to ensure the spherical shape of these investigated droplets. The first microemulsion under investigation, which serves as a model system to determine the radial dependence of the Soret coefficient, is the water/n-octane/$C_{12}E_5$ system. Measurements in the IR-TDFRS are performed along the *efb* to ensure a spherical shape of the microemulsion droplets. Simultaneously with an increasing radius also the temperature had to be raised to ensure measurements close to the *efb* within the 1ϕ region. In order to separate the temperature influence on the Soret coefficient from the radial dependence we will perform systematic measurements by changing the n-alkane from n-octane to n-tetradecane. With this approach the same temperature can be achieved for different droplet sizes, but we have to accept a slight increase in the volume fraction of the droplets with decreasing chain length of the n-alkane. On the contrary we know from other studies [42] that the concentration dependence of the Soret coefficient is below 1 % and can be neglected if the concentration of the investigated aggregates in solution is below 10 vol%.

This work is structured as follows. The reader will be introduced into the field of thermodiffusion by discussing applications, theories and experiments. The used experimental setups are described. For completeness, also those setups are briefly mentioned which are used by the group in Köln, but the main focus will be set on the IR-TDFRS setup and an improved Michelson interferometer. We will introduce in the field of nonionic surfactants, especially the nonionic sugar surfactants. Additionally, a brief summary will be given into microemulsion systems and their phase behavior.

In the experimental part, the thermal diffusion properties of the binary system n–Octyl β–D–glucopyranoside (C_8G_1)/water is investigated in the vicinity of the *cmc* which is determined by surface tension measurements in Köln. The influence of an ionic dye is studied. Higher concentrations are investigated due to the sign change behavior of the Soret coefficient. These findings are confirmed by n–Heptyl β–D–glucopyranoside (C_7G_1)/water and n–Octyl β–D–maltopyranoside (C_8G_2)/water.

The thermal diffusion behavior of further H_2O/n-alkane/$C_{12}E_5$ microemulsions is investigated. The phase boundaries of interest are determined in Köln, while the thermal

diffusion properties of the microemulsion droplets are studied in Jülich. SANS measurements are performed.

At the end of this thesis, the essential results of the experimental chapters will be concluded in a summary and an outlook will be given.

TWO

FUNDAMENTALS

In thermal equilibrium the components of a mixture are homogeneously distributed. If a temperature gradient is applied the components start to diffuse and separate due to the applied thermal grating and one component enriches at the warm side and the other at the cold side. This effect is called thermodiffusion or Ludwig-Soret-Effect named after the discoverers Carl Ludwig (1816-1895) [1] and Charles Soret (1854-1904) [2–4]. Ludwig published his observations in 1856 under the title "Diffusion zwischen ungleich erwärmten Orten gleich zusammengesetzter Lösungen" [*diffusion between unequally thermostated places of equally composed mixtures*]. Since that time, the experimental methods and theoretical concepts have been developed, but there ia still no microscopic description for liquids. In contrast the thermal diffusion process is fully understood.

In the following three sections the basic principles of thermal diffusion, micellar solutions an microemulsions will be introduced.

2.1. General Remarks on Thermodiffusion

This section summarizes recent theoretical and experimental developments and will give examples, where thermodiffusion plays a role in nature or industrial applications. In Sec.2.1.2 the framework of irreversible thermodynamics is introduced in which heat and mass flux are coupled by the so-called Onsager coefficients. The expression for the Soret

coefficient and the diffusion coefficients are derived. Sec.2.1.3 gives an overview of recent theoretical approaches to describe this separation process in a temperature gradient. Some theoretical models are conform with experimental findings, although a general theoretical description for thermodiffusion is still an open question. Although a microscopic model is missing, some rules of thumb are known to predict the direction of the thermal diffusion. These rules relate to the physical and chemical properties of the system (Sec.2.1.4). An effect which cannot be explained by these rules is the sign change of the Soret coefficient with temperature or concentration which was observed for several systems (Sec.2.1.5).

Several experimental setups have been developed to measure the concentration separation in an applied thermal gradient. There are very different methods of applying the temperature gradient and detecting the separation effect. It will be focused on setups which are applicable to liquid systems. Selected setups are compared in Sec.2.1.6 and main advantages or disadvantages will be explained.

The goal of this work is the investigation of the influence of micelle formation around the critical micelle concentration on the thermal diffusion behavior and secondly the radial dependence of the Soret coefficient. Therefore, micellar systems and microemulsions are used as model systems and will be introduced in the end of this chapter.

2.1.1. Practical Applications and Processes in Nature

First important applications is the isotope separation which was developed and described [6, 12, 77, 78] in the early 1940ies. During that time, the enrichment of uranium became an important factor in the Manhattan Engineer District (*Manhattan-project*) [7,8] in 1942 during 2nd world war. The enrichment was necessary as the natural concentration of usable uranium-235 for nuclear fission is approximately 0.7 %. Liquid UF_6 is separated in thermogravitational columns by cooling the inner column and heating the outer walls. As in more detailed explained in Sec.2.1.6, the thermogravitational column uses a combination of thermal diffusion and convection to separate components. The heavier U^{238} tends to enrich at the cold side and U^{235} at the warmer side. Convection transports the U^{238} to the bottom while U^{235} is transported on the top side of the column. Several columns are connected in a line to enhance the separation. In Oak Ridge, Tennessee, 2100 of these columns increased the concentration of U^{235} to 1 %. Thus, this method was simple but energy expansive. Later, this technique was replace by gas centrifuges [79].

The enriched material of 132 lbs ($\approx$ 60 kg) from this plant in Oak Ridge was used for the first nuclear bomb in 1945 [80].

In plants such as water lilies and alders, thermodiffusion ensures the availability of oxygen in the roots and rhizomes. Contrarily to the overground organs of the plant, where stored oxygen is produced and liberated by photosynthetically active plastids into the intercellular system, the roots require an external supply of oxygen to keep the oxygen concentration constant between 1-3 % for normal requirements of mitochondrial respiration. A temperature gradient between the leaves and roots induces the transport of oxygen through the intercellular system of the plant. The release of oxygen from the roots to the surrounding soil along a temperature gradient through the cell membranes is caused by *thermoosmosis*, which is actually thermodiffusion through a membrane [11]. This effect causes a mass flow from the low to the high temperature side and increases linearly with the temperature difference and with the mean temperature [81,82]. Thermoosmosis also works in single-component systems [83].

In oceans, thermal gradients occur due to the heating of the sun. This causes a vertical concentration grating, for instance of dissolved ions. In sea water of high salt content sulfate-depleted brines of extremely high salinity up to 25.7 % and high temperatures up to 56.5 °C at the bottom exist while above the salt concentration is halved [84] and the temperature is reduced to 44.3 °C. This contrast in salt concentration should be balanced by the Fickian diffusion but the thermal gradient causes an additional mass transport and the ions migrate to the brines [9]. This effect is used in *Solar Ponds* to store solar thermal energy. A Solar pond is a pool with salt water of three layers: a low-salinity top layer, a layer with a salt gradient from low salt concentration (low density) at the top to high salt concentration (high density) at the bottom, and a bottom layer of high-salinity. The pond's bottom material absorbs most of the solar thermal energy and heats the high salinity layer. This induces a temperature gradient from the warm (bottom) layer to the cold (top) layer so that the water density decreases with depth. This would imply a heat exchange. However, the salt gradient induces a density gradient which prevents heat transport from the bottom to the top layer. Temperatures of 90 °C can be reached in the bottom layer of a solar pond while at the top layer one measures temperatures of approximately 30 °C. The stored heat can be used for energy production or for heating [85–88].

The thermal flow field fractionation (*ThFFF*) is an established separation method for synthetic polymers and colloids [89] of different sizes of almost three to four orders of

magnitude [90–92] in organic and aqueous solvents. ThFFF offers shorter separation times and a better resolution of mass distribution for high molar weight solutions [93,94], which are difficult to characterize by methods working with a stationary phase, such as size exclusion chromatography [95, 96]. A recent review by Cölfen and Antonietti [97] compares the ThFFF and other FFF methods with size exclusion chromatography.

2.1.2. Theory

There is no complete microscopic theory to explain the thermal diffusion effect. Only a few contributions such as collective effects in colloids or single particle effects of charged colloids have been analyzed on a microscopic level [29,68,71,72,98–103]. In the following, an approach in the framework of irreversible thermodynamics will be drafted.

Two reservoirs are considered of two different temperatures T_1 and T_2 which are energetically insulated from the environment. Both baths are coupled and allow the exchange of particles and heat energy. This exchange parameters are referred to as mass flux, J_1, and heat flux J_Q. The fluxes are taken relative to a center-of-mass system. In the following, the variables characterizing both baths, are denoted by 1 and 2, respectively.

Energy production due to a heat flux. First, the heat flux is considered. The driving force of the heat flux is a temperature gradient ΔT. In the case of small changes, the relaxation of the system from nonequilibrium to an equilibrium state is a linear function and the entropy is increased by spontaneous processes [104]. The difference in entropy due to a temperature gradient is

$$dS = \delta S_2 - \delta S_1 = \frac{\delta Q_2}{T_2} - \frac{\delta Q_1}{T_1} \tag{2.1}$$

with the heat $Q_1 = Q_2 = Q$, the temperatures and entropies of both baths, $T_{1,2}$ and $S_{1,2}$. Thus, the change in entropy is given by

$$dS = \delta Q \left(\frac{1}{T_2} - \frac{1}{T_1} \right) \tag{2.2}$$

and the time derivative of Eq.2.2 is given as the product of heat flow, J_Q, and the gradient of the inverse temperature, $\nabla 1/T$,

$$\frac{dS}{dt} = \frac{dQ}{dT} \left(\frac{1}{T_2} - \frac{1}{T_1} \right) = J_Q \nabla \left(\frac{1}{T} \right) \tag{2.3}$$

with $J_Q = Q/dt$. dS/dt is the entropy production of the heat conduction process.

Energy production due to a mass flux. Also the mass transport can lead to an increase of the entropy. If a local thermal equilibrium is assumed, the Gibbs relation gives the total differential of the entropy [105]:

$$TdS = dU + pdV - \sum_i \mu_i dN_i \tag{2.4}$$

with the internal energy change, $dU = 0$, the work on the system, $pdV = 0$, and the chemical potential and number of particles of the ith component, μ_i and N_i. It remains for the two baths system

$$dS = -\frac{dN_1}{T}(\mu_2 - \mu_1) \tag{2.5}$$

wherein the deficit of particles in system 1 is equal to the gain in system 2: $dN_2 = -dN_1$. The difference in chemical potential is defined as $\nabla\mu = \mu_2 - \mu_1$. The time derivative follows as

$$\frac{dS}{dt} = -J_1 \frac{1}{T}\nabla\mu \tag{2.6}$$

with the mass transport from system 1 to 2, $J_1 = dN_1/dt$, and the thermodynamic force of the mass flux, $X_1 = \nabla\mu$. The entropy production depends on the difference in the chemical potentials. It is assumed, that no chemical reaction nor viscous flow or external forces occur [105]. According to Perronace [106] it follows:

$$\frac{dS}{dt} = J_Q \nabla\left(\frac{1}{T}\right) - J_1 \frac{1}{T}\nabla\mu\,. \tag{2.7}$$

In the following, the equality [102, 105] for the thermodynamic force of the heat flux, X_Q, is used:

$$-\nabla\frac{1}{T} = \frac{1}{T^2}\nabla T = X_Q\,. \tag{2.8}$$

In the linear approximation of irreversible thermodynamics, the flux J_1 is factorized by a composition of thermodynamic forces, X_j, contributing to the entropy production and phenomenological coefficients, L_{1j},

$$J_1 = \sum_{j=1,Q} L_{1j}X_j\,. \tag{2.9}$$

with the expressions for the heat (Eq.2.3) and mass fluxes (Eq.2.6) denoted as Q and 1. Following, the heat flux is L_{QQ} and the Fick's diffusion is L_{11}. Two additional irreversible

fluxes L_{Q1} and L_{1Q} are described as linear functions of the thermodynamic forces X_j. Thus, a temperature gradient can induce a mass transport (L_{Q1}) which is described as the Soret effect [106], and the reverse Dufour [107] effect describes a heat flow due to a concentration gradient (L_{1Q}). According to Onsager relations, L_{ij} is a symmetric matrix which couples both transport processes, the heat and mass. L_{ij} satisfies the conditions $L_{QQ}, L_{11} > 0$ and $L_{QQ}L_{11} - L_{Q1}^2 = 0$ using $L_{1Q} = L_{Q1}$ [104]. It follows

$$J_Q = J_{QQ} - \frac{1}{T^2}\nabla T - L_{Q1}\frac{1}{T}\nabla\mu, \tag{2.10}$$

$$J_1 = J_{1Q} - \frac{1}{T^2}\nabla T - L_{11}\frac{1}{T}\nabla\mu. \tag{2.11}$$

Eqs.2.10 and 2.11 are valid for an isotropic system in which, in equilibrium state, all appearing thermodynamic forces have the same magnitude in all directions. The chemical gradient is replaced using the Gibbs-Duhem-relation [108, 109] under isothermal and isobaric conditions:

$$\nabla\mu = \frac{\mu_{11}\nabla w_1}{w_2} \tag{2.12}$$

with the concentrations $w_{1,2}$ of the concentrations of component 1 and 2, respectively. Following,

$$J_Q = J_{QQ} - \frac{1}{T^2}\nabla T - L_{Q1}\frac{1}{T}\frac{\mu_{11}\nabla w_1}{w_2}, \tag{2.13}$$

$$J_1 = J_{1Q} - \frac{1}{T^2}\nabla T - L_{11}\frac{1}{T}\frac{\mu_{11}\nabla w_1}{w_2}. \tag{2.14}$$

From experimental point of view, the Soret coefficient is a measure of concentration separation due to a temperature gradient in a steady state where the mass flow J_1 is zero. Thus, it depends on the concentrations w_1 and w_2,

$$S_T\Big|_{J=0} = -\frac{1}{w_1 w_2}\frac{|\nabla w|}{|\nabla T|} \tag{2.15}$$

If Eq.2.14 is now transposed to an expression of the gradient ratio

$$\frac{|\nabla w|}{|\nabla T|} = \frac{L_{1Q}}{L_{11}}\frac{w_2}{T^2\mu_{11}}, \tag{2.16}$$

it is inserted in Eq.2.15 and thus yield an expression of S_T as function of the phenomeno-

logical coefficients:

$$S_T = \frac{L_{1Q}}{L_{11}} \frac{1}{T^2 \mu_{11}} \frac{1}{w_1} \tag{2.17}$$

for $J_1 = 0$.

Fick's law relates the mass flux J_1 with a concentration gradient ∇w_1

$$J_1 = -\rho D \nabla w_1 \tag{2.18}$$

with the density, ρ, and the diffusion coefficient, D. In the absence of a temperature gradient, the first part in Eq.2.14 vanishes and the mass flow expressions given by Eq.2.18 and Eq.2.14, lead to:

$$\rho D \nabla w_1 = L_{11} \frac{1}{T} \frac{\mu_{11} \nabla w_1}{w_2} . \tag{2.19}$$

Hence, the diffusion coefficient is a function of the phenomenological coefficient

$$D = L_{11} \frac{1}{T} \frac{\mu_{11}}{w_2 \rho} . \tag{2.20}$$

Finally, the thermal diffusion coefficient is the product of Soret and diffusion coefficient, and using Eqs.2.17 and 2.20, it is obtained

$$D_T = L_{1Q} \frac{1}{T^2} \frac{1}{w_1 w_2 \rho} . \tag{2.21}$$

If $w_2 = 1 - w_1$ is used, Eq.2.15 can be modified to

$$S_T\Big|_{J=0} = -\frac{1}{w_1(1-w_1)} \frac{|\nabla w|}{|\nabla T|} = \frac{D_T}{D} \tag{2.22}$$

Eq.2.22 can be applied in the case that $w \approx w_0$ with the initial concentration in equilibrium, w_0, and the concentration in the steady state in the presence of a temperature gradient, w, as the separation ratio is small compared to the initial concentration.

2.1.3. Theoretical Approaches

Several methods have been used to describe the effect of thermodiffusion, like the Chapman-Enskog theory which describes the thermal diffusion effect in gaseous mixtures [26, 27, 110, 111]. This theory is limited and fails for denser systems like fluids. To a certain extend, the framework of irreversible thermodynamics [112, 113] is used and the

transport coefficients are derived by the Onsager coefficients. Regarding the single-particle and particle-particle interactions in fluids, kinetic theories [100, 114, 115] can be used to express these interactions in terms of potentials. These potentials consider temperature, concentration or charge effects. Molecular dynamic simulations [51, 102, 116–119] allow to study the thermal diffusion properties of a microscopic system. Especially low-molecular weight mixtures have been studied to investigate systematically mass and moment of inertia effects [120]. Force fields are assumed, which define the particle interactions. The method of Monte Carlo simulations [121] is a widely used approach for the investigation of lattice gas dynamics. A potential is introduced to describe the nearest neighbor interactions of a N-particle system. A stochastic formalism is used to calculate the probability of a particle to move in the lattice.

Some of the theoretical approaches yield comparable results to experimental findings under certain restrictions on the investigated model system but a general description of the Soret effect on a molecular level is still lacking. In the following, theoretical approaches will be introduced which describe the radial dependence of the Soret coefficient or predict a sign change of the thermophoretic motion in fluids. As most of the theoretical approaches assume charged particles, this section also sheds some light on charged systems.

Radial dependence of the Soret coefficient. Würger [30, 68] calculated a linear radial dependence of S_T for spherical macromolecules with neglecting particle-particle interactions. This linearity stems from the boundary layer approximation that the particle-solvent forces are short-ranged. Then, D_T becomes independent from the particle radius [122–124]. This approximation is not valid for semidilute systems where D_T depends on the molecular weight [125] or volume fraction [126]. Morozov considered a theoretical approach for single-particle interactions in ionic ferrocolloids. By the assumption of a force balance of electrical and viscous forces he found a linear radial dependence of S_T [101, 103].

A quadratic radial dependence of the Soret coefficient is derived for soft particle interfaces. In this case the sticky boundary condition of short-ranged interaction forces fails [99]. Charged colloids with a thin double layer have been investigated by Ruckenstein [57]. He suggested, that the free energy reduction is responsible for the thermophoretic motion. The thermophoretic motion of colloidal particles is assumed to be driven by an interfacial tension gradient. This gradient is induced by a temperature gradient since the Debye-Hückel screening length depends on the temperature. This approach was recently used

by Piazza and Guarino [37] to express the Soret coefficient as a quadratic function of the Debye-Hückel screening length.

The approach introduced by Ruckenstein turned out to be wrong [127]. Dhont [127] suggested, that it is only the reversible work that determines S_T and not the reduction of free energy. Consequently, Dhont and Briels [29] expressed the Soret coefficient as a linear function of the Debye-Hückel screening length.

Fayolle *et al.* [128, 129] gave an equation for the thermal diffusion coefficient using the Stokes equation with a force term arising from the electric stress in the diffuse double layer of charged colloids. They predict for highly diluted colloids of small valencies, that S_T scales with the squared of the particle radius and depends linearly on the Debye-Hückel screening length.

Sign change behavior. A sign change of the thermophoretic motion originates from changes in the particle-solvent interfaces or from interparticle interaction effects. Thus, theoretical approaches have introduced several contributions to the Soret coefficient which describe these effects. Bringuier and Bourdon [100] expressed the Soret coefficient as a function of the derivative of the total internal energy with temperature. In the case that the internal energy becomes temperature dependent, the contributions to the internal energy determine if the Soret coefficient is increased, decreased or changes the sign. Contributions to the internal energy can be single-particle and particle-particle interaction effects or terms describing charge effects.

Dhont [71, 72] assumed a temperature dependent interaction potential between colloidal spheres to derive the transport coefficients. If the interaction between the colloidal surface and the solvent is known, the thermal diffusion coefficient can be calculated. The temperature dependence of the potential turns out to induce a sign change of the thermal diffusion coefficient with changing temperature or concentration in a certain parameter range.

Reverse non-equilibrium molecular dynamics simulations have been performed by Zhang and Müller-Plathe [116] to derive the thermal diffusion properties of dilute polymer solutions. They have shown that at constant temperature and concentration, a better solvent quality causes a higher affinity for the polymer to the cold region. The Soret coefficient changes sign from negative to positive when the solvent quality becomes bad. A recent theoretical approach by Luettmer-Strathmann *et al.* [31, 32] has indicated a similar trend for polymers in water-ethanol solutions. By changing the solvent composition a sign

change of the Soret coefficient was induced. S_T turned from negative to positive as the water concentration of the solvent was increased.

2.1.4. To the Warm or to the Cold?

There are a few rules of thumb which help to predict which component enriches in the cold or in the warm.

Considering the size or weight distribution, the larger or heavier molecules tend to go to the cold region [130]. Almost all polymers accumulate in the cold. This is not a general feature but depends on specific interactions and the solvent quality. Exceptions are polyvinyl alcohol in water [17] and poly(ethylene oxide) in mixtures of ethanol/water with a high ethanol content [130, 131]. As long as the mixtures consist of almost spherical nonpolar molecules the heavier component enriches in the cold region [132]. But even for the nonpolar n-heptane/benzene mixture this simple rule of thumb fails [133]. Only if the highly branched and more symmetric heptane isomer 2,3,3-trimethylbutane is used instead of n-heptane the heavier component goes to the cold. These results indicate that the more symmetric molecules have a stronger tendency to accumulate in the cold.

Investigating the three structural isomers of the aromatic hydrocarbon dimethylbenzene, it was shown that the para-form moves to the warm region, the meta-form stays between both regions, and the ortho-form moves to the cold region [134].

For polymers and colloids also changes at the interface between the solute particle and the solvent need to be considered. In some cases structural variations of the solvent due to concentration changes of a solvent mixture [47, 130, 131] or temperature effects [61] lead to a sign change in S_T. For charged colloids also the double-layer contributes to the thermal diffusion properties [29] so that due to the complex chemical and electrostatic interactions simple rules of thumb can not be derived.

2.1.5. Sign Inversion of the Soret Coefficient

A sign change of the Soret coefficient is a special case of thermodiffusion which cannot be explained by the rules of thumb in Sec.2.1.4. If a sign change is observed, mainly by a variation in temperature or concentration, the component enriches at the opposite region. This effect has been observed in many gaseous mixtures [135–139] and fluid systems [58, 62, 117, 125, 131, 140]. In the following, only liquids will be discussed.

The assumption by Grew [137] defined three contributions to the thermal diffusion factor ($\alpha_T = S_\mathrm{T} \cdot T$): the difference in mass and in the diameter of the molecules and a contribution which refers to the interaction forces between the molecules. The first and the second contributions are suggested to be independent from a variation of concentration. The third contribution depends on concentration and relates to the collision diameter of the molecules which differs from the mean diameter due to interaction forces [138] and which causes the sign change with concentration. Later, a similar approach by Debuschewitz and Köhler [141] defined three contributions to the Soret coefficient which are the mass, the moment of inertia and a chemical contribution. This chemical contribution will be discussed in the following.

Wittko and Köhler [63] studied mixtures containing protonated and deuterated cyclohexane. At equal mole fractions the Soret coefficient turns from negative to positive values if the difference in molecular mass, ΔM, between solvent and solute increases and a constant slope for $\partial S_\mathrm{T}/\partial \Delta M$ is derived [142]. The same slope was derived for the isotopically substituted cyclohexane [141]. As isotopic substitution is a powerful method to change the mass of a molecule by keeping the chemical properties of the solute and leaving the intermolecular potential almost unaffected.

The investigation of the thermal diffusion properties of the systems di- and tri-glycols in ethanol [143] indicated a sign change behavior of S_T with increasing chain length of the glycols. This is reasonable as ethanol becomes a bad solvent for the long-chained glycols.

Experimental studies [59, 62, 75, 144–148], calculations [31] and simulations [51, 149] of low-molecular water-ethanol mixtures have indicated a sign change of the Soret coefficient from positive to negative with increasing water content. Polyakov and Wiegand [59] investigated mixtures of associated solvents. A sign change was observed at a certain concentration at which the Soret coefficient is independent from temperature for solutes which show pronounced hydrophilic interaction effects with the solvent due to their polarizability [150]. Prigogine [151] claimed that the investigated mixtures are non-ideal solutions. Otherwise, no concentration dependence of S_T should be observed. Some papers indicate, that the sign change of S_T occurs when the hydrogen bond network breaks [62, 152, 153]. Rousseau *et al.* [51, 149] discussed the S_T sign change by means of changes in the particle-particle interactions. Therefore, the strength of solute-solute or solvent-solvent interactions, denoted as *intra-species* interactions, the strength of solute-solvent interactions (*inter-species* interactions) are considered. In the case that the inter-species interaction are larger than the intra-species interactions, a sign change of the thermophoretic mo-

tion is observed. This can be achieved experimentally by variation of the composition, concentration or temperature.

Recently, Vigolo [33] reported a sign change of S_T influenced by charges in micellar SDS solutions by adding sodium hydroxide (NaOH). The highly mobile OH^--ions in a thermal gradient induce a stationary electric field which is responsible for electrophoretic transport phenomena of the SDS micelles. By increasing the ion concentration, the Soret coefficient turns from positive to negative.

A temperature induced sign change of S_T was observed for lysozyme solutions [48,64,154] where S_T goes from negative to positive values with increasing temperature. It was shown that this effect results from thermally induced gradients of the interfacial tension. The sign change temperature is shifted with increasing salt concentration.

Also in colloidal suspension a sign change has been investigated. Ning *et al.* [42] studied the thermal diffusion behavior of octadecyl coated silica particles with a radius of 27 nm in toluene for low and high concentrations. At high dilution, the Soret coefficient is independent from concentration and only differs for different temperatures. Low temperatures cause a negative Soret coefficient which turns to positive values for higher temperatures. Above a concentrations of 10 vol%, colloid-colloid interactions affect the thermal diffusion behavior and S_T decreases with increasing concentration and a sign change occurs. This decreasing behavior has also been observed for polystyrene in toluene [155–157] and was interpreted as an increase of the local viscosity approaching the glass transition [158].

For ferromagnetic colloids, Morozov [103] shows that the sign of S_T is a function of the ratio of double layer thickness and radius, and of the electric potential. It was found that the colloids tend to move to the cold for low electric potentials and an infinitely small double layer thickness. If the double layer thickness increases, and the electric potential reaches a certain strength, the colloids enrich at the warm region.

For a polymer solution of Poly(N-isopropylacrylamide) (PNiPAM) in alcohols a variation of the molecular structure of the solvent can cause a sign change of the Soret coefficient. Kita and Wiegand [140] observed that the Soret coefficient changes from positive to negative with increasing number of carbon atoms of the alcohol. On the other hand, the sign change temperature decreases with increasing carbon atom numbers. For the system PNiPAM-ethanol, a sign change occurs with increasing temperature from positive to negative S_T. The sign change temperature is close to the coil-globule transition temperature of PNiPAM in water at which PNiPAM goes from a swollen hydrated state into a shrunken dehydrated state. Thus, above the phase transition temperature, the former
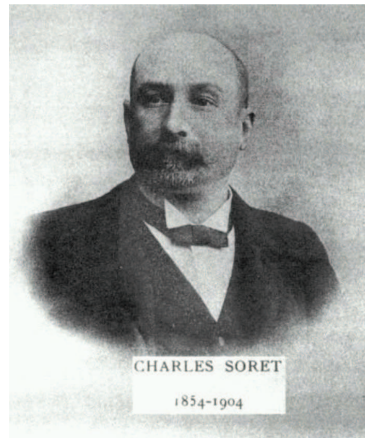
Figure 2.1.: *Charles Soret (23th Sept 1854 - 4th Apr 1904) [159].*

hydrated water molecules lower the local solvent quality around the polymer and S_T becomes negative. A Soret sign change due to a change in the solvent quality has also been observed for PEO in a mixed solvent of water and ethanol [31,32,46,47,62] from a positive to a negative Soret coefficient for increasing water concentration. The sign change occurs at a solvent composition where large structural changes take place.

2.1.6. Experimental Setups to study Thermal Diffusion

Several experimental methods have been used to study the thermal diffusion behavior of liquid mixtures. The methods differ in the way how a thermal gradient is applied and the separation effect is detected. Some of the methods are convection-free, others not. In the last two decades different optical methods have been developed which work only analytically and cannot be used to separate different components. In the following, an overview of the methods is given.

Charles Soret (Fig.2.1) was the first scientist who performed systematic measurements of the mass separation in a thermal gradient. He used different kind of tubes which are cooled from the bottom and heated from the top. The hot side was 78 °C and the lower temperature was between 18 °C and 15 °C [2]. The tube length was 0.3 m, so that the temperature gradient was in the order of 200 K/m. The separation effect of ionic components was analyzed after a measuring time of up to 56 days [4]. He obtained a separation ratio of 1.1 % and the ionic component got enriched at the cold end.

A vertical thermogravitational column as sketched in reference [160] was introduced by Clusius and Dickel [77] in 1939 to measure mass separation in a vertical narrow gap with

a height-to-width ratio of larger than 100. The gap is heated or cooled from the side walls and the Soret effect causes a mass transport to the warmer or colder wall. Convection implies, that an additional mass transport parallel to the walls occurs, such that due to the density change at the warmer wall, the convection directs to the top and at the cold wall to the bottom. This induces a vertical concentration gradient if the denser component diffuses to the cold. This setup is a so-called 2-point measurement setup and the concentration ratio of the top or bottom is measured. Nowadays multi-point setups are used [145]. The thermogravitational column allows only the determination of the thermal diffusion coefficient. The diffusion or Soret coefficient cannot be obtained. Thus, it is more applicable for quantitative mass separation analysis, like isotope [12] or gas separation [161–165], and competes with HPLC techniques. Main disadvantages are the build-up of a sufficient strong thermal gradient of 1000 K/m [160], the long equilibration time of more than 90 hours in the case of organic low molar weight mixtures and the fairly large sample volume in the order of 3-27 ml [13, 166].

Recently, the thermogravitational column was used to investigate ternary systems [167–169]. Following the approach by Larre *et al.* [170], the behavior of a ternary system can be estimated by considering the corresponding binary systems of the three containing components. A comparison of the experimental results by Königer *et al.* [171] and Blanco *et al.* [169] revealed pronounced differences in the determined thermal diffusion coefficients of the ternary system.

One of the weaknesses of the thermogravitational columns is, that it only measures the thermal diffusion coefficient and not the mass diffusion coefficient which is required to calculate the Soret coefficient. The mass diffusion coefficient can be obtained by coupling the thermogravitational column with Laser Doppler velocimetry (LDV) which measures the vertical flow velocity amplitude [145]. Light of crossed laser beams is scattered at flowing particles. Due to the Doppler effect, the scattered frequencies are shifted to the reference beam frequencies which results in a beat frequency at the detector. The flow velocity is calculated with a high accuracy from the crossing angle, the wavelength of the lasers beams and the frequency shift. This allows the determination of D.

In the thermal lens setup [18] a laser with a Gaussian intensity profile is used to write a temperature profile in a sample. An absorption in the order of 1-2 cm^{-1} of the sample at the laser wavelength is sufficient. The temperature profile induces a refractive index profile in the sample, such that the refractive index is low in the center of the beam, so that the sample acts like a diverging lens. The additional mass transport in a two com-

ponent mixture induces additionally a concentration lens (Soret lens), which amplifies or diminishes the refractive index profile [48] induced by the thermal effect. The transmitted intensity, in some cases of an additional read-out laser [172, 173], is measured versus time. A steady state is attained within some seconds for low-molecular weight solutions but also high molar weight solutions of proteins or polypeptide solutions can be measured. The investigation of large colloids with a radius of 100 nm and more is not possible, because then convection influences the experiment. If the natural absorption of the solvent is insufficient, a photostable dye is added which has to be inert and should not alter the chemical or physical properties of the sample under investigation [174, 175]. A very strong absorption should be avoided due to nonlinear effects and a low excitation power reduces convection effects. The thermal lens technique is applicable to probe mixtures with a high optical contrast [175].

Giglio and Vendramini [16, 17] described a laser beam deflection technique which probes the build-up of a concentration gradient in a Soret-cell with a laser beam. A similar setup is still used by Piazza *et al.* [37, 146] and the group of Köhler *et al.* [144, 171]. The sample cell with an optical length of a few centimeters is confined between two horizontal metal plates with a gap width between 0.5 mm and 1 mm. Between these plates a temperature gradient is built up. This temperature gradient (≈ 14 K/cm [157]) induces a concentration gradient due to the effect of thermodiffusion. Both gradients cause a refractive index gradient at which a horizontally aligned laser beam is deflected. The position of the laser beam is monitored with time by a position-sensitive detector with a resolution of a few μm. A steady state is reached within less than one hour for a dodecane/isobutylbenzene/1,2,3,4-tetrahydronaphthalene (nC$_{12}$-IBB-THN) system [144]. Putnam and Cahill [176, 177] recently developed a new micron scale beam deflection setup where an oscillating temperature gradient is induced. The beam deflection technique is applicable for molecular and polymer solutions as well. Also the measuring volume is reduced to approximately 1/10 ml. Recently, the normal beam deflection method was extended by a second read-out laser at a different wavelength to measure ternary systems [171] following the approach of Haugen *et al.* [178] that a system of *n* components requires deflections from $(n-1)$ beams of different wavelengths.

The thermal flow field fractionation (*ThFFF*) was employed in 1975 by Giddings [19, 20] for polymer separation. Modifications of this technique are still used [93, 179–182] to analyze or separate biomolecules or to characterize the molecular weight and composition of polymer components [183]. This technique is sensitive to surface effects [89, 184] and thus allows colloidal surface analysis. In ThFFF, a temperature gradient of up to $4 \cdot 10^5$ K/m

for polymer solutions ($M_w \approx 10^5$ g/mol) is vertically applied to a thin channel of 0.1 mm in width [185] and a volume of approximately 1 ml [186]. In a parabolic-like velocity profile the test sample is transported through a channel. In a perpendicular thermal gradient one component accumulates at the cold wall of the channel into regions of a slower flow velocity. Thus, this component enriches in slower flow regimes and elute last from the channel while other components which do not enrich in the cold region elute first. The overall measuring time is in the range of minutes to hours [45]. The ThFFF technique can be used to determine the thermal diffusion coefficient of different polymer solutions and colloidal suspensions which show a large distribution of molecular weights [185] from 10^3 to 10^7 g/mol [90–92]. Only small amounts of sample material of some nano-gram to micro-gram are required. The thermal diffusion coefficient of a retained solute is obtained from the retention time ratio to an unretained solute and the temperature difference between the channel walls [97].

Braun and Libchaber [21] employed in 2002 a fluorescence method to investigate the separation of DNA strains ($M_w \approx 1.6 \cdot 10^7$ g/mol) in an aqueous buffer solution. In this method an IR-laser at 1480 nm heats an aqueous sample so that a temperature gradient of approximately 1-2 K is induced in a thin chamber of 10-25 μm. Thus, temperature gradients of $1 \cdot 10^6$ K/m can be realized [49]. The chamber volume is 2 μl. In this setup, two measurements need to be performed to measure the temperature and the concentration profile. In a first measurement the temperature gradient applied to the solvent is determined. Therefore, a temperature sensitive fluorescent dye is added to the solvent. Differences in the temperature profile are monitored by differences in the fluorescence intensity. The addition of a fluorescent dye can lead to deviations of the measured temperature profile as the fluorescent dye also obeys thermodiffusion principles and is not homogeneously distributed in the sample if a temperature profile is applied. In a second measurement, dye-labeled solutes accumulates in the temperature gradient at the cold or at the warm. The time dependent fluorescence intensity is monitored with a camera. A steady state is attained within 300 s (for DNA strains). Convection inside the chamber is opposed to the thermophoretic repulsion and increases with the chamber thickness. Above a certain convection strength particles get trapped. Both diffusion coefficients can be evaluated from the time dependence of the fluorescence intensity signals in the cold region. The probed solute size is in the nano- to micrometer range [65, 125].

In the thermal diffusion forced Rayleigh scattering ($TDFRS$) technique [22] a holographic interference grating [187] is written in the sample. Due to absorption which is achieved by the addition of an inert dye, the intensity grating is converted into a sinusoidal temperature

gradient. The fringe spacing of the temperature grating is approximately 20 μm and a temperature difference of 20-100 μK can be achieved [24, 25]. Due to thermodiffusion a sinusoidal concentration grating builds up. These sinusoidal changes of temperature and concentration are accompanied by a refractive index modulation which is read out by a HeNe-laser which is not absorbed by the sample and does not alter the temperature. This technique was recently modified for aqueous samples [39, 40], such that the wavelength of the writing laser is chosen at a weak absorption band of water at 980 nm [75]. Thus, in the IR-TDFRS setup the addition of dye is not required in aqueous mixtures. Depending on the used sample cells, sample volumes of less than 0.5 ml are possible. The thin cell geometry avoids convection effects and short measurement times are achieved for low-molecular systems due to a narrow fringe spacing. The measurable size ranges from low-molecular systems up to polymer solutions of 10^7 g/mol [188, 189]. The main disadvantage is the restriction to binary systems. Ternary mixtures could be studied, if another read-out laser with a different wavelength is used, and if the components show a sufficient dispersion in their refractive index increments.

2.2. Binary Micellar systems

Amphiphilic molecules can form micelles in solution in order to minimize the free energy of the system. Micellization occurs as function of concentration or temperature where above a certain concentration or below a certain temperature, micelles will form and coexist with surfactant monomers in the bulk phase. This specific concentration or temperature is called critical micelle concentration (cmc) or critical micelle temperature (cmt), respectively. Accordingly, micellar systems can be tuned slightly in size or shape by varying the concentration or temperature.

So far the thermal diffusion behavior of sugar surfactants has not been studied although the properties this class of surfactants are defined by amphiphilic properties of the surfactant, which will be discussed in Sec.2.2.1. Micelles in water are formed in that way, that the hydrophilic part of the surfactant molecule aligns in the micelle-solvent interface and the hydrophobic forms the core of the micelle. The micellization in aqueous sugar surfactant systems starts at a fairly high concentration compared to other surfactants. This allows a precise investigation of the thermal diffusion properties close to the cmc, which are ruled my monomers below the cmc and by micelles above the cmc, respectively. Results will be shown in chapters 4 and 5.

2.2.1. Nonionic Sugar Surfactants

Nonionic sugar surfactants show an amphiphilic behavior due to a hydrophilic sugar head group and a hydrophobic carbon chain. Compared to other surfactant classes, i.e. nonionic alkyl polyglycolether (C_iE_j) surfactants [190], they are completely biodegradable and can be produced from renewable resources [191, 192]. In the following, the general expression C_iG_j is frequently used, where C_i denotes the number of CH_x-units in the hydrophobic chain and the head group units are denoted as G_j with j being the number of sugar units in the hydrophilic head.

Over the years sugar surfactant systems have been investigated experimentally and theoretically [193–195]. These biocompatible surfactants have frequently been used to study the dissolution and formation of biological membranes and the stabilization of proteins [196–200]. In a clinical context, these surfactants cause marginal skin irritation [201]. Alkyl-monoglucoside surfactants have been used in the formulation of microemulsions for the emulsification of mineral oils [202] and it turned out, that these surfactants are effective amphiphiles [203].

For a systematic study of the amphiphilic properties of the sugar surfactants, the number of head group units j and alkyl groups i can be varied. We will concentrate on three sugar surfactants: n–Octyl β–D–glucopyranoside (C_8G_1), n–Heptyl β–D–glucopyranoside (C_7G_1) and n–Octyl β–D–maltopyranoside (C_8G_2). All surfactants are studied in water.

Many groups investigated the micellar structure of sugar surfactants using different methods. Most studies were performed on water/n–Octyl β–D–glucopyranoside systems. The concentration dependence of the micellar size and shape of C_8G_1 was studied theoretically [54] and experimentally [204–213]. A compact and spherical shape of micelles with a radius of 2.29 nm to 2.35 nm was found which is almost independent from surfactant concentration above to the cmc. The measured radii are confirmed by a theoretical approach which compares the maximum micelle radius with the maximum length of the surfactant molecule [207]. The theoretical approach calculates the radius to 2.16 nm [214] including a hydration layer of water molecules. At higher concentrations ($w \approx 2 \cdot cmc$), the shape turns to rod-like and more heterodisperse micelles due to a maximum accessible micellar diameter which is defined by the length of the surfactant monomers. The micelles grow in length, because both hemispherical ends of the rod are energetically unfavored constellations [205]. Thus, larger rod-like micelles are preferred instead of an increase of spherical micellar number density. At low concentrations slightly above the cmc, attractive interaction forces govern the micellar behavior while at higher concentrations,

repulsive steric interactions between the micelles are dominant (for $w \approx 30 \cdot cmc$) [206]. Contrarily, D'Aprano *et al.* [208] found that the C_8G_1-micelles are already at the *cmc* of rod-like shape and do not change their structure at higher concentrations. These findings for C_8G_1 have also been confirmed for other glucoside micelles (C_iG_1, $i = 7 .. 10$) by Zhang *et al.* [205].

For the C_8G_2-micelles a spherical shape has been determined [215, 216] which is independent of temperature or concentration. Hydrophilic forces between the head groups play an important role in the micellar shape [215] while the hydrophobic alkyl chain favors the formation of micelles to reduce the free energy [217]. This effect becomes stronger for longer carbon chain length (by 0.825 kcal/mol per CH_2-group [214] assuming a constant number of head group units). Due to the strong influence of the hydrophilic forces on the micellar structure, polyglucosides like C_8G_2 prefer spherical micelles to increase the volume per head group in the micellar layer, while monoglucosides like C_8G_1 tend to form rod-like structures to reduce unfavorable hemispherical end caps where water is in contact with the carbon chains.

Another aspect in this work will be the determination of the temperature dependence of the *cmc*. Generally, the *cmc* decreases with increasing temperature [212, 218, 219] for nonionic surfactants, while for ionic surfactants the *cmc* increases with increasing temperature. On the other side, experiments on nonionic polyoxyethylenated and sugar surfactant systems [220–222] indicated a decrease of the *cmc* for increasing temperature which turns into an increase at higher temperatures. A minimum *cmc* has been determined between 40 °C and 50 °C. First theoretical predictions were made by Israelachvili [213], stating that the temperature dependence of *cmc* is more pronounced with increasing carbon chain length. Accordingly, for the short chained C_8G_1, the spherical micelles does not show any remarkable temperature dependence of their size [223]. The solubility of the nonionic surfactant molecule decreases with increasing temperature and the surfactant becomes less hydrophilic due to an increase of hydrophobic forces [215, 224]. Hence, the growth of micelles which is favored by the hydrophobic carbon chains becomes minor, and the micellar size reaches a maximum size at a certain temperature. Aoudia *et al.* and Kameyama *et al.* determined the aggregation number of C_8G_1 in water for several temperatures and found a maximum aggregation number at $T = 35$ °C [220] or $T = 36$ °C [212], respectively. The temperature agrees nearly with the temperature of the minimum *cmc* value. Sugar surfactants exhibit a comparable high aggregation number due to the strong hydrophilicity of the head group units [194, 202, 212]. Literature results vary between 70 and 87 for C_8G_1. The first number was determined in sedimentation equilibrium studies at 20 °C by
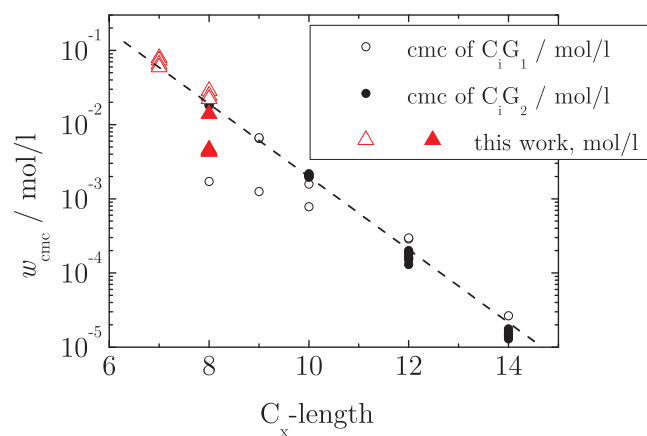
Figure 2.2.: *The measured critical micelle concentrations in this work (red symbols) and from literature (black symbols) versus the carbon chain length are compared. Literature data are taken from references given in Tab.2.1. The dashed line is a linear fit with respect to the logarithmic scaling of the concentration axis. Aqueous mixtures of maltosides (solid symbols) and of glucosides (open symbols) are shown. The lower filled red triangle represents the* cmc *of a* C_8G_2 *batch, which was contaminated. This batch was not used for further measurements.*

Roxby and Mills [211], and the latter one was measured at 22 °**C** by Kameyama *et al.* [212] using light scattering methods.

A general overview on recent *cmc* measurements for glucosides and for maltosides at room temperature is given in Fig.2.2. The plotted data refer to Tab.2.1 for glucosides, and to Tab.2.2 for the maltosides, respectively. In a log-linear plot of the *cmc* versus the alkyl chain length of the surfactant a linear dependence is found (dashed line in Fig.2.2).

2.2.2. Consequences for ongoing Measurements

For the three surfactants under investigation it is expected, that (i) the increase in the alkyl chain causes approximately a three higher *cmc* of C_7G_1 compared to C_8G_1 and C_8G_2 in water which show approximately the same *cmc*. The determined *cmc* in a temperature range between 15 °**C** and 40 °**C** should decrease with increasing temperature for all investigated surfactant systems. (ii) In the low concentration regime close to the *cmc*, we expect the maltoside micelles to be spherical in shape due to strong repulsive forces of the head group units. (iii) Glucoside micelles are also assumed to be spherical if the concentration is slightly above the *cmc*, while at higher concentrations, ellipsoidal glucoside micelles are expected. (iv) In the investigated concentration range the surfactant

surfactant	cmc mol/l	Temperature °C	reference
C_7G_1	0.07	–	Anatrace, USA
C_7G_1	0.079	–	Cammack [225]
C_8G_1	$0.018 - 0.026$	22	Lorber [226]
C_8G_1	0.0232 ± 0.5	25	De Grip [227]
C_8G_1	0.022	25	Giordano [206]
C_8G_1	0.025	25	Shinoda [228, 229]
C_8G_1	0.018	25	Nickel [195]
C_8G_1	0.0204	25	Kakehashi [230]
C_8G_1	0.0254	25	Kameyama [231]
C_8G_1	0.022	22	Kjellin [232]
C_8G_1	0.00172	22	El-Sukkary [233, 234]
C_9G_1	0.006	40	Ericsson [235]
C_9G_1	0.0065	–	De Grip [227]
C_9G_1	0.00126	25	El-Sukkary [233, 234]
$C_{10}G_1$	$7.812 \cdot 10^{-4}$	25	El-Sukkary [233, 234]
$C_{10}G_1$	0.00185	25	Kakehashi [230]
$C_{10}G_1$	0.00195	22	Rosen [236]
$C_{10}G_1$	0.0022	25	Shinoda [229]
$C_{10}G_1$	0.002	25	Aveyard [237]
$C_{10}G_1$	0.00219	25	Mukerjee [238]
$C_{12}G_1$	$2.873 \cdot 10^{-4}$	25	El-Sukkary [234]
$C_{12}G_1$	$2.973 \cdot 10^{-4}$	25	El-Sukkary [233]
$C_{12}G_1$	$1.9 \cdot 10^{-4}$	25	Shinoda [194, 229]
$C_{12}G_1$	$1.92 \cdot 10^{-4}$	25	Mukerjee [238]
$C_{14}G_1$	$1.67 \cdot 10^{-5}$	–	Mukerjee [238]
$C_{14}G_1$	$2.65 \cdot 10^{-5}$	50	El-Sukkary [234]
$C_{14}G_1$	$1.7 \cdot 10^{-4}$	25	Nickel [195]
$C_{16}G_1$	$1.45 \cdot 10^{-6}$	–	Mukerjee [238]

Table 2.1.: *Summary of measured critical micelle concentrations of sugar glucoside surfactants in water from literature.*

surfactant	cmc mol/l	Temperature °C	reference
C_8G_2	$19.1 \cdot 10^{-3}$	25	Boyd [239]
$C_{10}G_2$	$1.99 \cdot 10^{-3}$	25	Boyd [239]
$C_{10}G_2$	$2.11 \cdot 10^{-3}$	40	Majhi [240]
$C_{12}G_2$	$0.13 \cdot 10^{-3}$	25	Boyd [239]
$C_{12}G_2$	$0.18 \cdot 10^{-3}$	25	Zhang [241]
$C_{12}G_2$	$0.16 \cdot 10^{-3}$	-	de Grip [227]
$C_{12}G_2$	$0.15 \cdot 10^{-3}$	25	Drummond [242]
$C_{12}G_2$	$0.20 \cdot 10^{-3}$	25	Dupuy [243]
$C_{14}G_2$	$1.299 \cdot 10^{-5}$	10	Ericsson [244]
$C_{14}G_2$	$1.392 \cdot 10^{-5}$	20	Ericsson [244]
$C_{14}G_2$	$1.392 \cdot 10^{-5}$	20	Ericsson [244] in D_2O
$C_{14}G_2$	$1.764 \cdot 10^{-5}$	40	Ericsson [244]

Table 2.2.: *Summary of measured critical micelle concentrations of sugar maltoside surfactants in water from literature.*

micelles grow with increasing surfactant concentration while at constant concentration, a variation in temperature should leave the micellar size unaffected.

2.3. Microemulsion Systems

Schulman *et al.* [245] firstly introduced the definition of a microemulsion to describe dispersions consisting of uniform spherical droplets of oil or water in a continuous phase which are stabilized by an amphiphilic component. Microemulsions are thermodynamic stable and nanoscopic structured systems of at least three components. These components are polar (A), non-polar (B) and amphiphilic (C).

The interplay of the three components results in a complicated phase behavior [76, 246–249], wherein several states occur (see Sec.2.3.1). In some phases, microemulsion droplets are formed. Two types of droplets are known: o/w and w/o droplets. These droplets are similar to micellar aggregates but the additional component is enclosed in the droplet. For o/w droplets, oil is embedded, while for w/o ones, it is water. Microemulsions are thermodynamically stable systems. In a dynamic equilibrium, the exchange of molecules with the environment is possible which is in the order of microseconds but the stability of droplets is found in timescales of several seconds for typical low molecular weight sur-

factants. In good approximation the interactions between the droplets can be described with a hard sphere potential. Contrarily to synthesized colloids, the interfacial properties of these droplets are reproducible and well defined. The size and shape can be systematically varied by changing the composition, temperature or concentration. For systems containing long chained surfactants, in the 1ϕ region the microemulsion forms spherical droplets at the *efb*. On the water-rich side of the respective phase diagram, the droplets turn to ellipsoidal aggregates and finally to network-like structures at the *ncb* with increasing temperature. At the *efb*, the droplets grow with increasing oil concentration, while an increase in the surfactant-to-water ratio increases the droplet density. Therefore, microemulsions can be regarded as easily adjustable model systems.

2.3.1. Phase Behavior

A variation in temperature, pressure and concentration yields several states of the ternary system whereas the pressure dependence is not considered in this work. The interested reader is referred to a review article by Schneider [250]. A phase prism [251] shows the different phases (see Fig.2.3). The corners of the phase prism represent the three components A, B and C, and the height is the temperature axis. White areas indicate 1ϕ regions, 2ϕ regions are indicated by tie lines and grey areas represent the 3ϕ region. The purple colored area characterizes a 1ϕ region wherein equal amounts of water and oil are solubilized [248].

The phase behavior of the ternary system is mainly determined by the three individual binary systems [252] which are represented by the side planes of the prism.

The oil-water system shows nearly for all mixing ratios a 2ϕ region and only in the high concentration regimes on the water- or on the oil-rich side, the low solubility of water in oil and vice versa allows small 1ϕ regions. The solubilities are slightly enhanced at higher temperatures but this is less important for the overall phase behavior of the ternary system.

An upper miscibility gap is found in the water-surfactant system with a lower critical point (cp_β) at the temperatue T_β [253]. Below this critical point, a 1ϕ region is observed due to the high miscibility of water and surfactant at low temperatures. The upper miscibility gap can be explained by a break of the hydrogen bonds. This upper loop shrinks with increasing hydrophilicity of the surfactant. A further lower miscibility gap of the binary

water-surfactant system is not considered in this work since it lies below the melting point [76].

In the binary oil-surfactant system, the miscibility of surfactant and oil is poor at low temperatures. A lower miscibility gap is found with an upper critical point (cp_α) at the temperature T_α. At higher temperatures above T_α a 1ϕ region exists due to the increasing hydrophobicity of the surfactant. T_α is usually below zero for ternary H_2O/oil/nonionic amphiphile systems [76].

In the ternary system, the critical points cp_α and cp_β are start points of the critical lines cl_α and cl_β in the phase prism (see Fig.2.3). The line cl_β starting from the water-surfactant plane decreases in temperature and ends at the lower temperature T_l at the critical endpoint cep_β. At T_l the surfactant-rich water phase separates into two phases, which are a microemulsion water phase and an oil excess phase. The cl_α-line starting at the oil-surfactant plane develops towards higher temperatures and ends at an upper critical end point (cep_α) at T_u where the surfactant oil-rich phase separates into two phases: a microemulsion oil phase and a water excess phase. Thus, between T_l and T_u a 3ϕ region is formed which has the shape of a triangle (see grey colored area in Fig.2.3). Due to the increased hydrophobicity of the surfactant at higher temperatures at isothermal conditions, the surfactant is mainly dissolved in the oil phase at high temperatures. At lower temperatures, the surfactant becomes more hydrophilic and is mainly dissolved in the water phase. The shape of the 3ϕ triangle is then defined by the temperature dependence of the surfactant: At temperatures slightly above T_l, the composition of the middle microemulsion phase is shifted towards the water side and turns over to the oil side at higher temperatures. At T_l and T_u the 3ϕ triangle ends up in two critical tielines and merges into a $\underline{2}$ and $\overline{2}$ phase, respectively.

The individual concentrations are generally given in mass ratios, where

$$\gamma_a = \frac{m_C}{m_C + m_A} \tag{2.23}$$

gives the mass fraction of component C (mass the of amphiphile, m_C) in component A (mass of water, m_A) and C. The mass fraction of component B (oil) is then given as ratio to the total mass of the system

$$w_B = \frac{m_B}{m_A + m_B + m_C} \tag{2.24}$$

with the mass of the oil, m_B. In this work, we use n-alkanes as oil component and $C_{12}E_5$
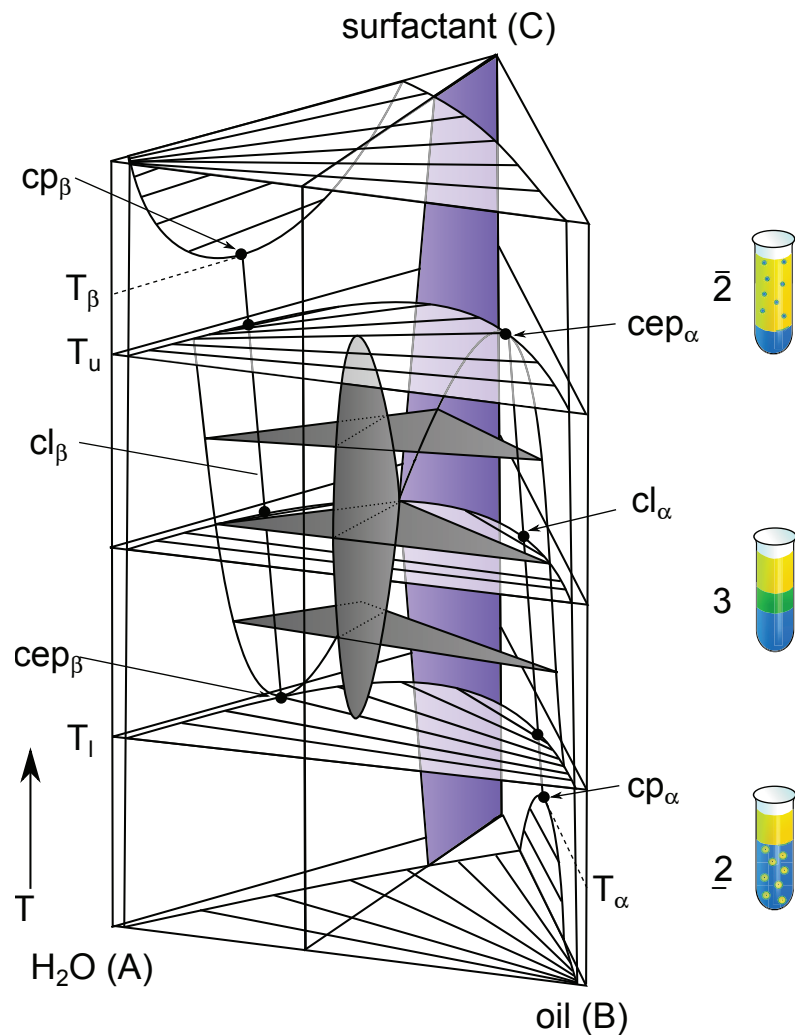
Figure 2.3.: *Typical phase prism of a microemulsion system consisting of water (A), oil (B) and surfactant (C). The temperature dependence is presented by the vertical of the prism. On the right side, different states are sketched: The lower $\underline{2}\phi$ region at low temperatures where the surfactant is dissolved in water with an coexisting oil excess phase, the middle 3ϕ region (grey) and the upper $\bar{2}\phi$ region where the surfactant is dissolved in the oil phase. The 1ϕ regime is colored in purple. The figure was redrawn from Strey [251].*

as the amphiphile. At low surfactant concentrations and at certain temperatures, we find all three components dissolved in one phase (1ϕ). This 1ϕ equilibrium is classified as Winsor IV [254] and exists on the water-rich side and on the oil-rich side in the phase diagram [248] for low concentrations of oil and water, respectively. In this work we focus mainly on the investigation of the water-rich side of the phase prism (see Fig.2.4). Because the surfactant assembles at the water-oil interface, the surfactant film is curved around
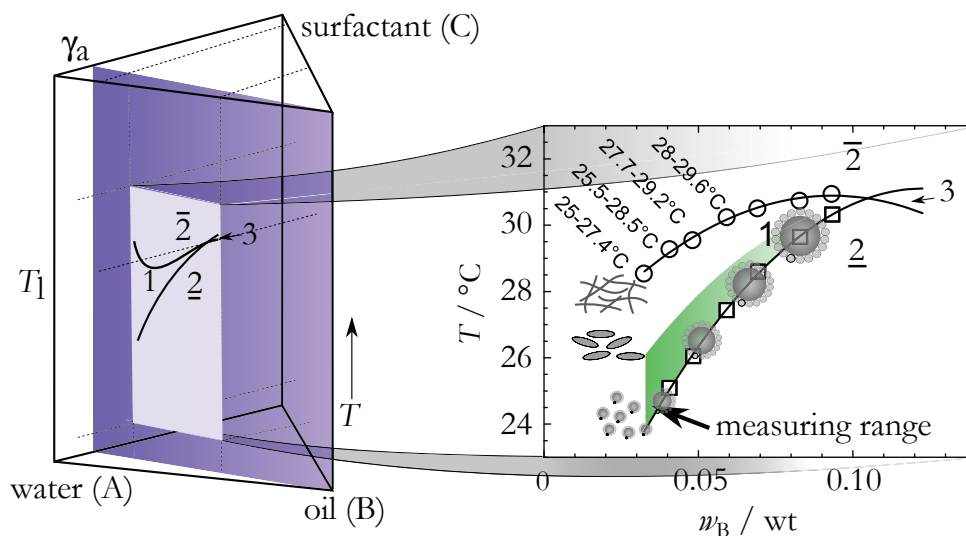
Figure 2.4.: Left: *Cut through the phase diagram of a ternary microemulsion system. Regions of constant γ_a are colored purple. Therein, temperature range and oil fraction span an area (light purple) in which we find a 1ϕ region, surrounded by an upper $\overline{2}\phi$ and a lower $\underline{2}\phi$ region. At higher oil concentrations, a 3ϕ region is observed.* ***Right:*** *On the water-rich side of a water/n-octane/$C_{12}E_5$, this 1ϕ region is observed close to room temperature. In the green area spherical microemulsion droplets are expected.*

the oil and the system forms oil-swollen aggregates at low temperatures which are in the following referred to as oil-in-water (o/w) microemulsion droplets.

This region of o/w-droplets can be characterized by a cut through the phase prism in that way, that a temperature-oil mass fraction ($T(w_B)$) dependence at constant γ_a is achieved (see Fig.2.4). The right part of Fig.2.4 sketches a 1ϕ region of the $H_2O/C_8/C_{12}E_5$ system at constant $\gamma_a = 0.022$ wt. The 1ϕ funnel is confined by two boundaries. The phase boundary at low temperatures is called emulsification failure boundary (*efb*), and at high temperatures the near critical boundary (*ncb*), respectively. The microemulsion aggregates form spherical droplets close to the *efb* [251, 255] while with increasing temperature their shape changes to elongated aggregates and at the *ncb*, the aggregates form network-like structures [256–258] in the case of systems which contain long chain surfactants. The size of the microemulsion droplets at the *efb* increases with increasing oil concentration.

The goal of this work is the investigation of the thermal diffusion behavior of spherical microemulsion droplets of different sizes to determine the radial dependence of the Soret coefficient. Thus, the measurements are restricted to a temperature range close to the *efb* where these droplets remain spherical. Changes in the droplet shape with increasing

temperature limit the temperature range which is marked by the green colored area in Fig.2.4.

THREE

EXPERIMENTAL SETUPS

This chapter describes the experimental setups which are used for the investigation of the binary sugar surfactant solutions and microemulsions and is structured as follows: The TDFRS technique is introduced and the setup is described by means of the IR-TDFRS setup in Sec.3.1.2. Recent improvements are discussed. In Sec.3.3, a report on the determination of the refractive index increment with concentration or temperature is given. For the latter one, a new setup was designed due to experimental difficulties caused by the high turbidity and strong scattering of the microemulsions. The advantages of this setup are outlined and a comparison to the ordinary $(\partial n/\partial T)_{p,w}$ setup is given in Sec.3.3.4. Finally, the dynamic light scattering and the neutron scattering setup are introduced in Sec.3.2 and Sec.3.5, respectively. The latter setups are not in focus of this work but provide necessary information which complete findings obtained by TDFRS setups.

3.1. Thermal Diffusion Forced Rayleigh Scattering

The Thermal Diffusion Forced Rayleigh Scattering (TDFRS) setup is a technique in which a small temperature gradient is created by an interference of two laser beams. The temperature difference is approximately 20-100 μK and the fringe spacing is approximately 20 μm which results in a thermal gradient of 1-5 K/m. This very small fringe spacing leads to measuring times in the range of milliseconds for low-molecular weight solutions [133] up to a few seconds for polymeric systems or macromolecules [259, 260].

Two setups are available: one setup, called classical TDFRS setup, uses a writing laser at 488 nm (Ar-laser, Innova 300C, Coherent, USA), and a second setup is working with an infrared laser at 980 nm (TA 100, Toptica Photonics AG, Germany), which is called IR-TDFRS setup. The latter setup is predestinated for aqueous systems while the classical TDFRS setup requires the addition of dye which leads to a sufficient absorption at the wavelength of the writing laser beams. The selected dye needs to be inert, so that it does not contribute to the signal or alters the system properties. This is in general easy to fulfill for organic systems, but in polar systems the dye changes its absorption properties with pH and can also change the phase behavior of complex systems [38].

In the following, the TDFRS technique will be explained on the basis of the IR-TDFRS setup. The signal detection will be described in Sec.3.1.4. In the last two sections 3.1.5 and 3.1.6, the signal interpretation and analysis are discussed.

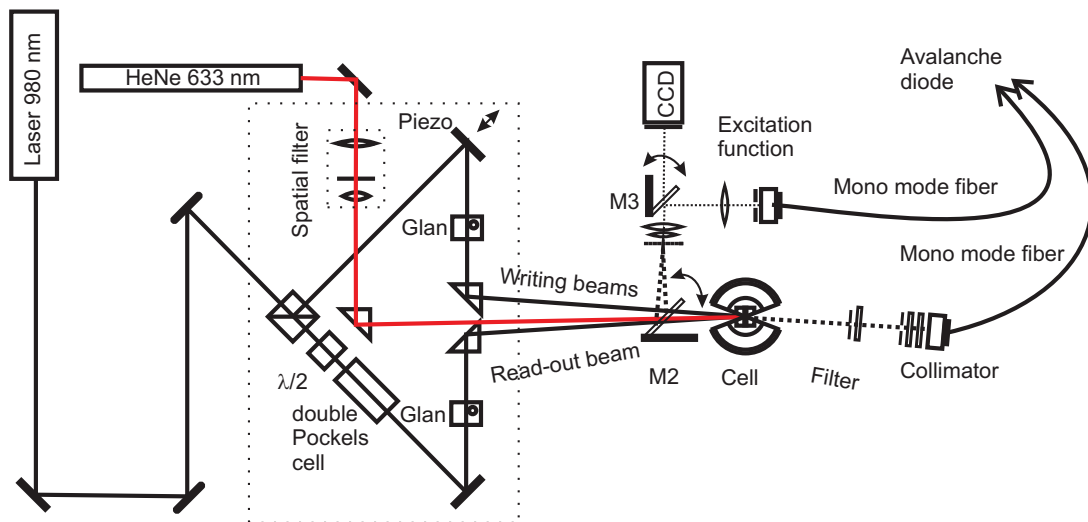## 3.1.1. Absorption of Light in the IR-TDFRS Setup

In this work we used mainly the IR-TDFRS setup to determine the thermal diffusion behavior of aqueous samples. The absorption of water at the writing laser wavelength is sufficiently high in the IR-TDFRS setup that the addition of dye is not needed. The wavelength dependent absorption of water was already determined by Hale and Querry [261], Palmer and Williams [262], Kou *et al.* [263] and Pope [264]. All groups determined an absorption between 0.43 and 0.52 cm^{-1} at 980 nm. We perform absorption measurements using a Cary 50 spectrometer and find an absorption at this wavelength of 0.18 cm^{-1}. Fig.3.1 shows the comparison of absorption spectra results and literature values. Independent from the differences in absorption values, the IR-laser provides sufficiently high power to write a thermal grating into aqueous samples.

3.1.2. Experimental Setup

The IR-TDFRS setup is sketched schematically in Fig.3.2. A vertically polarized laser beam at 980 nm is split into two beams of equal intensity by a beam splitter. One beam, in Fig.3.2 the lower one, passes a $\lambda/2$-plate which rotates the beam polarization from vertical to horizontal. A double Pockels cell is used to rotate the light polarization from horizontal to positive or negative vertical polarization by $+90°$ or $-90°$, respectively. The Pockels cell is controlled by a high voltage amplifier (Leysop, England). The switching
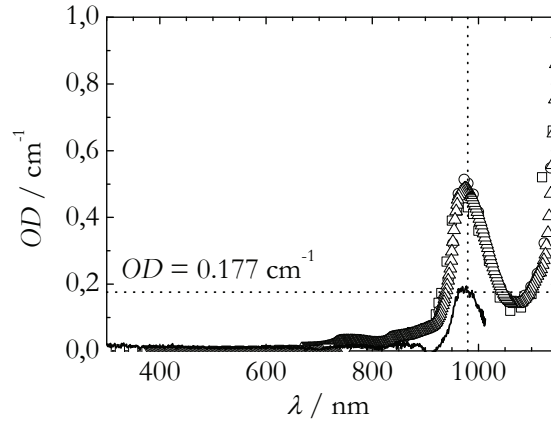
Figure 3.1.: *The absorption of water in the wavelength range of visible light and near infrared. Absorption curves by Hale and Querry [261] (squares), Palmer and Williams [262] (circles), Kou et al. [263] (triangles up) and Pope [264] (triangles down) are compared with measurements performed for this thesis (solid line). The dotted lines are guides to the eyes and mark the absorption at 980 nm which is used in the IR-TDFRS to convert the intensity grating of the writing beams into a thermal grating.*

Figure 3.2.: *The IR-TDFRS setup is working at a wavelength of 980 nm (writing laser). A thermal grating is created by the absorption of the interfering IR-laser beams in the aqueous sample. The analysis of the time dependence of the diffracted red laser beam intensity yields the thermal diffusion parameters.*

time is about 10 μs and thus by a factor of ten faster than the fastest time process to be measured in this setup.
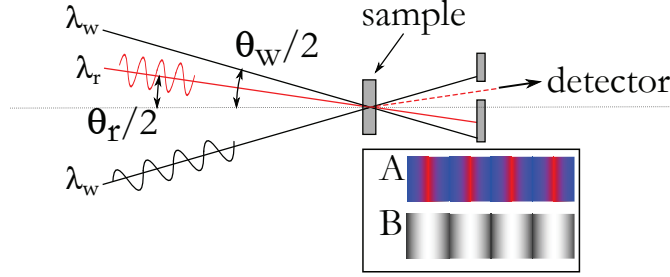
Figure 3.3.: *The laser path ways in the IR-TDFRS setup. The dotted horizontal line is the symmetry axis, the solid lines are the IR-laser (black) and the HeNe-laser (red). The dashed line is the diffracted read-out beam. Inset: sinusoidal temperature (A) and refractive index (B) grating in the sample. In the warm regions (red), the refractive index is lower (white).*

The upper beam in Fig.3.2, is reflected by a mirror which is mounted on a piezo crystal. By applying a voltage to the piezo, the position of the mirror can be changed. Thus, the path length of the beam is controlled and the phase difference to the first beam can be adjusted. Due to the limited coherence length of the laser, the optical path lengths of both writing beams are chosen to be equal. Glan-Thompson polarizers improve the quality of vertical polarization of both beams which interfere afterwards in the sample cell. The light intensity of the interference pattern is converted by absorption into a thermal grating. Due to the temperature dependence of the refractive index of liquids, the thermal grating induces a refractive index grating. Since the derivative of refractive index with temperature is always negative for liquids, the refractive index is higher in the colder regions of the temperature pattern, and lower in the warmer regions, respectively. A third read-out HeNe-laser beam at 632.8 nm (IR-TDFRS: Linos, Germany, Model HeNe 633-30P, 31 mW; class. TDFRS: Research Electro-Optics, Inc., USA, Model-No. 32413, 35 mW) is spatially filtered. The HeNe-laser probes the grating under the *Bragg* angle. The relative alignment to the writing laser beams satisfies the Bragg condition:

$$\frac{4\pi}{\lambda_r} \sin \frac{\theta_r}{2} \quad = \quad q_r \tag{3.1}$$

$$= \quad q_w = \frac{4\pi}{\lambda_w} \sin \frac{\theta_w}{2} \tag{3.2}$$

where the indices r and w mark the read-out and writing beams with the wavelengths λ_r and λ_w, respectively. q is the scattering vector and $\theta_r/2$ and $\theta_w/2$ are the angles to the symmetry axis (see Fig.3.3).

Behind the sample an IR-filter blocks the IR-laser beams, while the intensity of the

diffracted HeNe-laser is detected by an avalanche diode (Model SPCM-AQRH-13-FC, PerkinElmer, Canada). The laser intensity, is adjusted by grey filters to match the optimal count rate range of the diode which is between 1 to 3 MHz. A typical normalized intensity signal in the IR-TDFRS setup versus time is shown in Fig.3.4. A detailed explanation of the signal curve is given in section 3.1.5.

The brass cell holder is temperature controlled by a water bath (E300, Lauda) with a stability of 0.1 K. The typical temperature range in the experiment is between 15 °C and 60 °C. A Pt100 sensor is mounted in the cell holder underneath the sample cell to measure the actual temperature. Apart from the front and back holes for the incoming and outgoing laser beams, the cell holder is completely closed to minimize heat loss to the environment. Flow cells by Hellma are used as sample cells with an optical path length of 0.2 mm. The front and back windows are made of quartz glass and are transparent for all laser beams.

Before the light beams pass the cell holder, a semitransparent mirror reflects approximately 1–2 % of the IR-laser beams through a microscope objective onto a camera to determine the fringe spacing of the interference pattern and therefore the q-vector. Between the semitransparent mirror and the camera a grey filter with an optical density of 2.0 cm^{-1} is mounted to reflect 1–2 % of the intensity onto a second avalanche diode. The grey filter is used to minimize ghost images due to internal reflections. The avalanche diode records the time dependence of the interference pattern (excitation function, see Sec.3.1.3).

The advantage of this setup, working with semitransparent mirrors to split the beam intensity onto both diodes and the camera, is the simultaneous determination of the excitation function and the diffracted signal from the sample. This feature was included into the setup recently. Beforehand the excitation function had to be measured separately which caused a longer overall measurement time. As the excitation functions had been measured at an earlier or later time, the experimental conditions changed slightly in the mean time.

3.1.3. Excitation Function

The mathematical derivation of the working equation (see Eq.3.8) assumes a step function as excitation function. In reality the build up of the high voltage is not infinitely steep but has a finite rising time of 10 μs. In order to compensate for the delay and to account

for a slow change of the grating at long times, the build up of the pure intensity grating is recorded and its function is used to correct the measurement signal following a procedure by Wittko and Köhler [265]. A typical time dependence of the excitation function is shown in Fig.3.4 (dashed line), which is already normalized to the plateau value. The intensity signal starts at zero intensity and increases steeply within microseconds towards a plateau value which is reached after $10\,\mu$s. This is a direct measure of the ability of the Pockels cell to shift the relative phase of the writing beams by $180°$. The excitation function reaches the plateau when the phase shift is completed. For longer times, the intensity ideally remains constant in the plateau if voltage and phase are stable. Otherwise a decrease in the detected intensity is observed which is the case for long measuring times of slow diffusing systems ($\tau_c \geq 5$ s) mainly due to temperature fluctuations along the separated optical paths of the two writing beams.

3.1.4. Heterodyne Signal Detection

Due to the interference of the writing laser beams a sinusoidal intensity grating is written in the sample, which is converted into a thermal grating by absorption. This grating causes a concentration grating due to thermodiffusion. Thermal and concentration grating induce a refractive index grating which is probed by a third read-out laser beam which does not alter the thermal grating. The intensity, which is detected by the avalanche diode (IR-TDFRS) or photomultiplier (classical TDFRS), can be described by the electrical field vectors of the diffracted beam, E_d, the coherent, E_c, and incoherent beam, E_{inc}, as [188]

$$I = |E_c + E_d e^{i\phi}|^2 + E_{inc}^2 = E_d^2 + 2E_c E_d \cos\phi + E_c^2 + E_{inc}^2 \tag{3.3}$$

whereas the homodyne intensity is $I_{homo} = E_d^2$ and the heterodyne intensity is $I_{het} = 2E_d E_c \cos\phi$. The background intensity is $I_b = E_c^2 + E_{inc}^2$ and ϕ is the phase shift between the diffracted beam and the coherent background. Dust particles or scratches on the window of the sample cell generate the coherent background signal. Under standard conditions, we cannot distinguish between the heterodyne and homodyne signal contributions which is essential for the signal interpretation. One way to differentiate between both contributions is a phase modulation by π. Therefore, the Pockels cell shifts the phase of one of the writing beams by π. Thus, we obtain two intensities at the detector, $I_{\phi+\pi}$

and I_ϕ, for the π-shifted and the non-shifted beam, respectively,

$$I_{\phi+\pi} = |E_d e^{i(\phi+\pi)} + E_c|^2 + E_{inc}^2 \tag{3.4}$$

$$I_\phi = |E_d e^{i\phi} + E_c|^2 + E_{inc}^2 . \tag{3.5}$$

The homodyne part of the intensity signal can be written as

$$\zeta_{homo} = \frac{1}{2}\left(I_\phi + I_{\phi+\pi}\right) - I_b \tag{3.6}$$

and the heterodyne part as

$$\zeta_{het} = \frac{1}{2}\left(I_\phi - I_{\phi+\pi}\right) . \tag{3.7}$$

We measure the heterodyne intensity signal, because it is more robust than the homodyne signal [24]. Thereby, a maximization of the heterodyne signal contribution is achieved if the phase shift between coherent background and diffracted beam is zero. As we cannot control the phase of the coherent background, we control and stabilize the phase of the diffracted beam with the piezo mirror. A typical timing diagram is shown in reference [24]. For systems with equilibration times below 10 s the phase control with the piezo mirror is sufficient, but for slow diffusing systems, long term effects occur due to thermal fluctuations and diminish the contrast of the refractive index grating with time. Hence, the phase needs to be adjusted during the measurement. For this real-time phase tracking we analyze the interference grating with the camera, and vary the voltage applied to the piezo to achieve maximum contrast of the grating.

To improve the signal-to-noise ratio, I_ϕ and $I_{\phi+\pi}$ are averaged over time using several repetitions of the measurement (later referred to as runs). The phase is controlled every two or three minutes which is sufficient.

3.1.5. Signal Interpretation

Fig.3.4 sketches the time dependent normalized heterodyne signal which is measured through the sample (open symbols) and the corresponding signal of the excitation function (dashed line). All curves are normalized to the thermal plateau (horizontal dotted line). The excitation function reaches the plateau after 10 μs and usually stays constant if no external disturbance declines the intensity grating and the voltage of the amplifier is stable. The intensity signal from the sample approaches the thermal plateau after approximately 80 μs (vertical dotted line in Fig.3.4). During this time, the light inten-
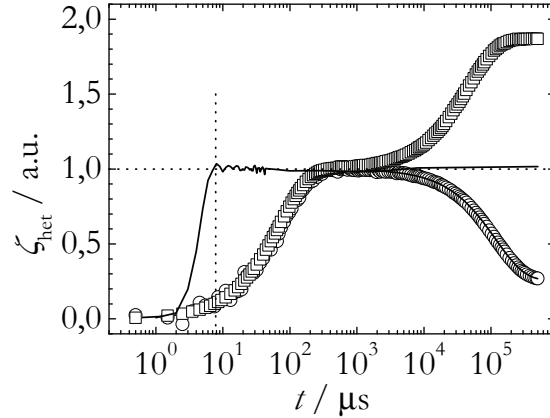
Figure 3.4.: *The normalized heterodyne intensity signal in the IR-TDFRS setup versus time. The sample is C_7G_1/H_2O with $w = 0.069$ wt at $20\,°C$ (circles) and $60\,°C$ (squares). The horizontal dotted line is a guide to the eyes and marks the normalized thermal plateau. The excitation function (solid line) reaches the plateau after $8\,\mu s$ (vertical dotted line).*

sity grating is converted into a thermal grating by light absorption of the sample. The thermal grating causes a refractive index grating. For liquids in general, the refractive index decreases with increasing temperature. This dependence is described by the partial derivative $(\partial n/\partial T)_{p,w}$ at constant concentration and pressure. Thus, the refractive index shows a minimum at warmer regions and a maximum at colder regions, respectively. The read-out laser probes this grating. The detector measures the intensity of this diffraction peak.

Once, the thermal grating is established, it leads to a mass flux due to thermal diffusion. This second process is one or two orders of magnitudes slower than the first thermal process. This makes it possible to separate both processes. The mass flux causes an additional local change in refractive index. One has to distinguish between two cases: In one case, the component with the higher refractive index moves to the cold regions of the thermal profile. This amplifies the refractive index profile in the sample and the detected intensity increases with time. Otherwise, the component with the higher refractive moves to the warm regions and the amplitude of the refractive index profile is lowered. Hence, the detected intensity decreases with time and the concentration plateau is found at lower intensities compared to the thermal plateau. Fig.3.4 shows both situations where the amplitude of the refractive index profile is amplified (squares) or diminished (circles) during the concentration process.

3.1.6. Signal Analysis

The time dependent heterodyne intensity signal, $\zeta_{\text{het}}(t)$, of the diffracted beam is described by an exponential fit function expressing the fast thermal process and the slow concentration process with the thermal time τ_{th} and the equilibration time τ_{c}, respectively, as

$$\zeta_{\text{het}}(t) = B\left\{\left(1 - e^{-\frac{t}{\tau_{\text{th}}}}\right) - \frac{A}{\tau_{\text{c}} - \tau_{\text{th}}} \cdot \left[\tau_{\text{c}}\left(1 - e^{-\frac{t}{\tau_{\text{c}}}}\right) - \tau_{\text{th}}\left(1 - e^{-\frac{t}{\tau_{\text{th}}}}\right)\right]\right\} \qquad (3.8)$$

with the scaling factor, B, and the amplitude of the second plateau, A, which relates to the Soret coefficient as

$$A = \left(\frac{\partial n}{\partial w}\right)_{p,T}\left(\frac{\partial n}{\partial T}\right)_{p,w}^{-1} w(1-w)S_{\text{T}} \qquad (3.9)$$

with the concentration of the referring component of the mixture in equilibrium, w, the Soret coefficient, S_{T}, and the refractive index increment with temperature at constant pressure and concentration, $(\partial n/\partial T)_{p,w}$, or with concentration at constant pressure and temperature, $(\partial n/\partial w)_{p,T}$, respectively. The derivatives of the refractive index have to be determined in separate experiments (see Secs.3.3.1, 3.3.3 and 3.3.4). The refractive index increments are a measure to which extend the refractive index varies with temperature or concentration. These values are known as contrast factors.

We obtain the mass diffusion coefficient

$$D = \left(\tau_{\text{c}}q^2\right)^{-1} \qquad (3.10)$$

from the equilibration time of the concentration process, τ_{c}, and the scattering vector, q. The thermal diffusion coefficient is calculated by Eq.2.22. Traditionally D_{T} can also be determined from the initial slope of the concentration part of the heterodyne intensity signal. We derive D_{T} by expressing Eq.3.8 as a Taylor expansion (see Appendix A). Hereby, the thermal diffusion coefficient is found as a linear factor in the first order term. Higher terms do not improve the expansion accuracy and are neglected.

3.2. Dynamic Light Scattering

Dynamic light scattering (DLS) is a well established method to determine the collective diffusion in a liquid mixture, solution or dispersion [266–271]. DLS is suitable to investi-
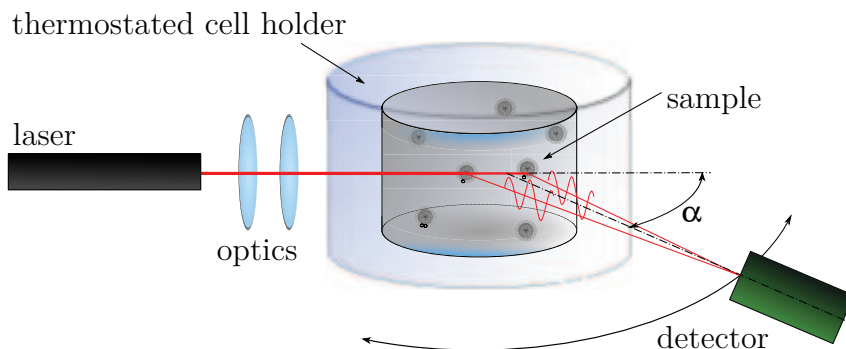
Figure 3.5.: *Sketch of the dynamic light scattering setup. Incident light from a coherent laser is focused on the scattering volume. The inner sample (grey) is in thermal equilibrium with the surrounding toluene bath (blue) which is temperature controlled. The scattered light intensity is recorded by a detector which can be moved to measure at different angles. Due to Brownian motion, the scattered light intensity varies with time.*

gate monodisperse particles or to determine the size distribution of polydisperse samples. The detectable particle size is in the range of some nanometers up to a micron in diameter. The lower range is limited due to the operating speed of the correlator and detectors. For larger particles the DLS technique is not feasible due to the sedimentation of the particles unless they are density matched.

One of the main disadvantages of the DLS method is the determination of the hydrodynamic radius which is the equivalent of a sphere with the same radius. This is not always directly related to the shape or rigidity of the measured solute particles, but also influenced by interactions with the solvent and between the particles. Later investigations of microemulsion droplets (chapter 6) requires the knowledge of the radius of gyration, which is a better measure of the shape of the solute particles. For that purpose, we additionally employ neutron scattering experiments as briefly described in Sec. 3.5.

In the following, the experimental setup is explained and the data analysis is described under the assumption of monodisperse samples. Later, we will also discuss the polydispersity of systems, which have been investigated in this work.

3.2.1. Principle

A cylindric sample cell is mounted in a thermostated toluene bath. On the one hand, the toluene bath provides a precise temperature control with a stability of 0.1 K (Lauda E300 thermostat) and on the other hand it reduces scattering from the sample cell surfaces.

The time dependent intensity of scattered light from a monochromatic and coherent light source (HeNe-laser at 632.8 nm) of the dissolved particles in the scattering volume is detected. The scattering intensity depends on the size of the particles and the scattering angle. The latter one is varied in a range from 30°, which is close to forward scattering, to 150° close to backscattering. The incident light is scattered by particles or concentration fluctuations. Destructive and constructive interference leads to a fluctuating intensity. The time-intensity-correlation function, $g_2(\tau)$, is a measure for the similarity of two scattering states at different times and is described as the averaged sum of the products of the intensities $I(t)$ and $I(t+\tau)$ at times t and $t+\tau$, respectively, at different delay times τ,

$$g_2(\tau) = \langle I(t) \cdot I(t+\tau) \rangle = \frac{1}{t_{total}} \int_0^{t_{total}} I(t) \cdot I(t+\tau) dt \,. \tag{3.11}$$

$g_2(t)$ can be expressed with the normalized field-time correlation function, $g_1(\tau)$, (see Fig.3.6) by the Siegert-relation

$$g_2(\tau) = B_1 + \beta \left(g_1(\tau) \right)^2 \,, \tag{3.12}$$

where B_1 and β are dimensionless instrument factors. $g_1(\tau)$ can be expressed with to

$$g_1(\tau) = e^{-\Gamma \tau} = e^{-q^2 D \tau} \tag{3.13}$$

with the decay rate, Γ, and the translational diffusion coefficient, D. The decay rate is calculated from the correlation function which is in turn fitted by a single exponential function for monodisperse suspensions. Another fit function is a stretched exponential function, the so called Kohlrausch-Williams-Watts (KWW):

$$\varphi_{\text{KWW}}(\tau) = e^{-(\tau \Gamma)_{KWW}^{\beta}} \tag{3.14}$$

with the fit parameter β_{KWW}. A fit of Eq.3.14 on one of the correlation functions, which was measured at a scattering angle of 30°, is drawn as a dashed line in Fig.3.6. This general writing of the KWW function is used in a wide scientific range working with relaxation dynamics or exponential stress decay processes [272, 273]. The translational diffusion coefficient is the linear slope of the $\Gamma(q^2)$-plot. A typical dependence of the decay rate on the squared scattering angle is shown in Fig.3.7 for an aqueous surfactant solution containing 0.021 wt C_8G_1 at 20 °C and 30 °C and scattering angles between 30° and 150°.
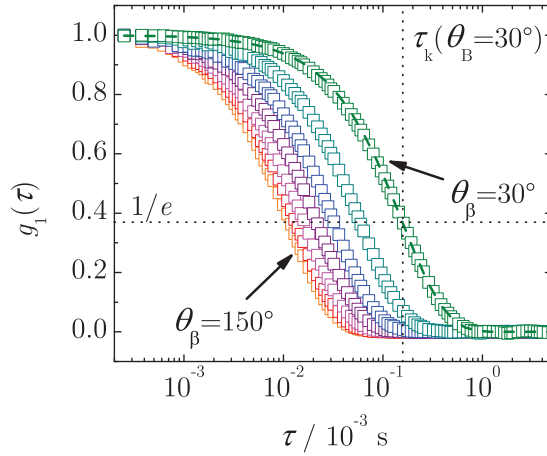
Figure 3.6.: *Correlation signal of a 0.021 wt C_8G_1/H_2O mixture at $T = 20\,°C$. A single exponential KWW-function (dashed line) was fitted to the data points (open circles). The vertical dotted line marks the correlation time obtained by KWW-fit.*

The Stokes-Einstein-Equation is used to calculate the hydrodynamic radius r_H,

$$r_H = \frac{k_B T}{6\pi\eta D} \tag{3.15}$$

with the Boltzmann constant, k_B, the temperature, T, and η is the viscosity of the solvent which is approximately equal to the viscosity of the pure solvent at the respective temperature and concentration. Eq.3.15 can only be used, if the mixture is sufficiently high diluted and far away from critical points ($r_H \cdot \theta << 1$). At higher concentrations the collective diffusion coefficient is measured and not the self-diffusion coefficient and the Brownian theory cannot be applied for the calculation of the hydrodynamic radius [274].

Hence, the hydrodynamic radii of the exemplary investigated surfactant micelles in Figs.3.6 and 3.7, are calculated to $r_H = (3.19 \pm 0.33)$ nm at $20\,°C$ and to $r_H = (3.35 \pm 0.15)$ nm at $30\,°C$. A more detailed discussion of the concentration and temperature dependence of the micellar systems is given in Sec.2.2.1. Due to the small size of the micelles, it is not possible to obtain further details about the shape. This would require SANS measurements.

Up to this point, the latter discussion was based on the assumption of monodisperse samples. However, for polydisperse particles, Eq.3.13 is not usable, as multiple decay times occur in the correlation function. In that case, $g_1(\tau)$ is expressed as a sum of several weighted decay terms, or as a continuous distribution function which is often determined with the (*CONTIN*) program [275, 276]. For microemulsions close to the emulsification
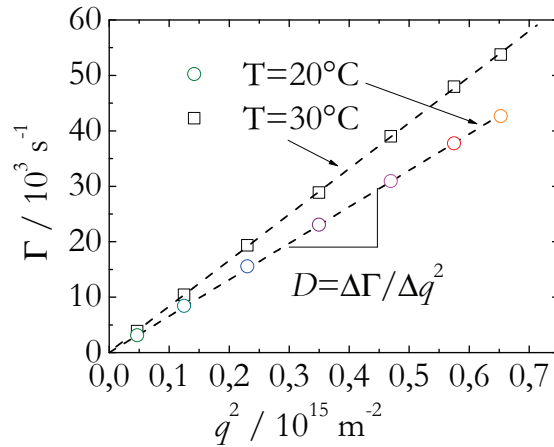
Figure 3.7.: *The decay rate versus the squared wave vector for different scattering angles at* 20 °C *(circles) and* 30 °C *(squares). The diffusion coefficient is given as the linear slope (dashed line). The sample is* C_8G_1/H_2O *with a weight fraction of 0.021 wt.*

failure boundary, CONTIN yields a narrow size distribution while at higher temperatures, CONTIN predicts a wider size distribution [277]. In this case, the most probable size is taken for further calculations.

3.3. Refractive Index

As discussed in Eqs.3.9 the determination of the thermal diffusion coefficient and the Soret coefficient requires the measurement of the refractive index increments. In the following, the experimental setups are introduced which determine the absolute refractive index by critical angle determination in Sec.3.3.1 or the increment of the refractive index with temperature using the change of optical path length in a medium due to temperature changes in Sec.3.3.3 and Sec.3.3.4.

3.3.1. Refractometer

We use a refractometer from Anton Paar (Abbemat RXA 156), working with a synthetical sapphire prism at a wavelength of 589.1 nm (Na-D line) as it is shown in Fig.3.8. In this machine, a 2048 pixel array is used to measure the intensity of refracted light. The critical angle, where the intensity curve shows a pronounced bend, is determined automatically
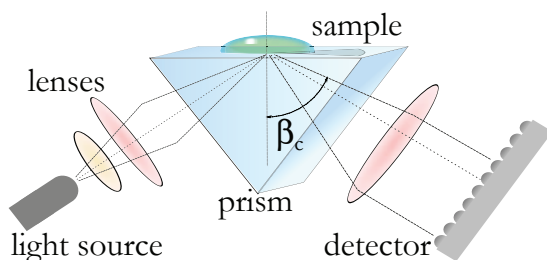
Figure 3.8.: *Sketch of the Abbe refractometer: At the interface between the solution (green) and the prism (blue) light from a diode (dark grey) is refracted. Beforehand, the emitted light is filtered (yellow) and focused (red lens). A pixel array (light grey) detects the angle-dependent light intensity. β_c is the angle of refraction at the critical point where total internal reflection occurs.*

by the instrument. The prism is temperature controlled by a Peltier thermostat with a temperature stability of 0.03 K in a range between 10 °C and 70 °C. A high-power LED is used as light source and the Na-D line is selected by an interference filter yielding a wavelength error of 0.1 nm. The error of the refractive index value is $2 \cdot 10^{-5}$.

3.3.2. $(\partial n/\partial w)_{p,T}$-Determination at Phase Transition Boundaries

The determination of the refractive index derivative with concentration is in general a fast and precise method. We use the refractometer from Anton Paar (see Sec.3.3.1) and measure the refractive index at constant temperature for different concentrations which are slightly lower or higher than the actual concentration ($\pm$ 10%). By that, we determine the slope of the refractive index with respect to concentration for constant pressure and temperature at the desired concentration. The measurement of the refractive index requires homogeneous samples. Therefore, special care needs to be taken if microemulsions are investigated, because due to evaporation the concentration can change, which might lead to a phase separation. Also a change in temperature might bring the system from the 1ϕ region into a 2ϕ region as it is sketched in Fig.3.9. The main problem in 2ϕ is that the composition of the microemulsion changes locally if a second phase occurs (see Sec.2.3.1). This leads also to an inhomogeneous refractive index, which makes a measurement of the refractive index increment unreliable. The refractive indices of the lower concentrations can be directly measured, because they lie in the 1ϕ region (solid stars in Fig.3.9). In order to obtain the refractive index increments of a specific concentration, the refractive indices at higher concentrations need to be extrapolated from the 1ϕ region (pentagons in
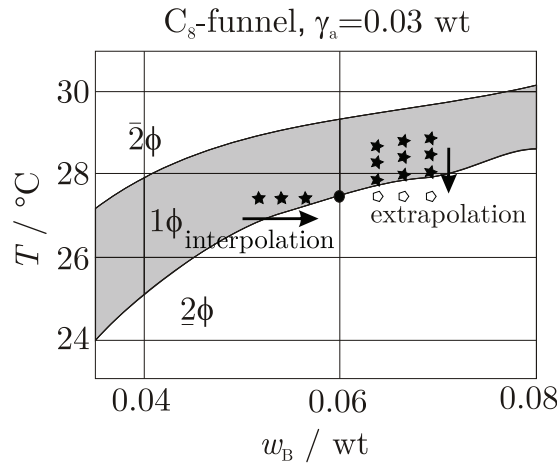
Figure 3.9.: Determination of the refractive index derivative with concentration for microemulsion systems in the 1ϕ phase (grey area). The solid circle marks the desired concentration at which the refractive index increment with concentration is determined. Therefore, the directly measurable concentrations (filled stars) and the extrapolated data points (white pentagons) are used. The pentagons are determined by extrapolating from higher temperatures in 1ϕ.

Fig.3.9). The directly measured and extrapolated refractive indices are used to determine the $(\partial n/\partial w)_{p,T}$-value at the desired concentration (circle in Fig.3.9).

The extrapolation to the data points in 2ϕ region needs a sufficient large temperature range in 1ϕ region. At least three different temperatures are measured. Generally temperatures in the lower third of the 1ϕ funnel close to the *efb* are taken, because network-like structures are formed above. The phase diagrams of nonionic microemulsions show that the funnel shrinks in temperature with increasing oil concentration (Sec.2.3.1). If the temperature range becomes too narrow to perform reliable refractive index measurements in the 1ϕ region, we do not measure at higher concentrations and only take refractive index values from lower concentrations into consideration to determine the slope.

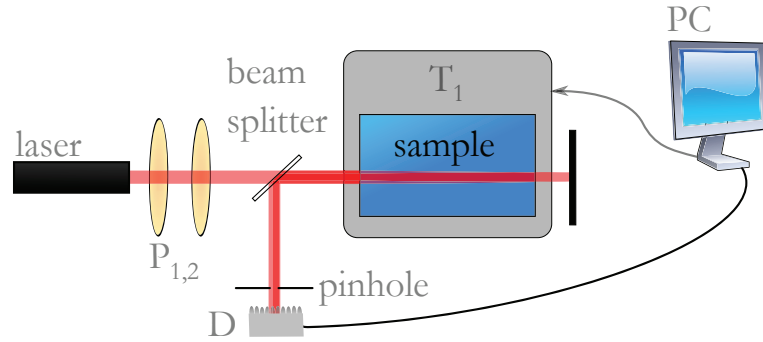### 3.3.3. Michelson Interferometer

In this section, the main principle of the $(\partial n/\partial T)_{p,w}$ determination is discussed. For this purpose we use a Michelson interferometer [265] as shown in Fig.3.10. Later, an improved interferometric setup will be introduced in section 3.3.4.

A HeNe-laser (5 mW at 632.8 nm, Type 25-LHP-151-230, Melles Griot, USA) beam, which intensity is controlled by two polarizers ($P_{1,2}$), passes a beam splitter and is partially

reflected at the surfaces of the sample cell (Hellma, Germany, optical path length: 10 mm). The sample cell is in thermal equilibrium with a brass cell holder (T_1) which is thermally insulated from the environment and temperature controlled by a thermal bath (Lauda E300) with a temperature stability of 0.1 K. The thermal fluctuations inside the sample holder are sufficient low and the temperature is determined by a Pt100 sensor which is connected with a computer. The computer sets the bath temperature and records data during the measurement.

There are four reflections when the laser beam passes the sample cell at the air-glass interfaces and the glass-sample interfaces at the front and at the back side of the cell. The major part of the beam intensity is reflected at the interfaces of higher refractive index difference, which are the air-glass interfaces. Hence, mainly those two reflected beams interfere at the detector, because the front and the back windows are never perfectly parallel. In front of the detector a pinhole of less than 1 mm in diameter detects only a small area of the interference pattern. As the reflected beam from the back window passes the sample twice its intensity will be for a turbid sample much lower than the intensity of the beam reflected at the front window. The optical path length through the sample depends on the refractive index which changes due to a temperature change. A variation in temperature causes a phase modulation of the beam which passes through the sample. Meanwhile the phase remains nearly constant for the primarily reflected beam. The relative phase shift between both beams in turn causes a shift of the interference pattern. By changing the temperature continuously, the interference pattern *moves* which induces a sinusoidal intensity at the photo diode. With an applied temperature gradient of 0.5 K/s, the detected intensity versus time or temperature, respectively, is shown as a black line in Fig.3.11.

We start the measurement at a temperature T_{start} and wait for one hour for thermal equilibration of the sample. Special attention has to be paid to the microemulsion samples, for which the cell, the cell holder, and the microemulsion have to be thermostated before filling to ensure that the sample is in the 1ϕ region and stays there during the measurement. Afterwards, we vary the temperature continuously with time until we reach the end temperature T_{stop}. The applied temperature gradient is in the range of 0.5 mK/s to 1 mK/s and small enough to have the system all time thermally equilibrated. During the measurement, the refractive index is decreasing ($T_{stop} > T_{start}$) or increasing ($T_{stop} < T_{start}$) as the derivative of refractive index with temperature is negative for liquids. Fig.3.11 shows the time dependence of the recorded intensity. The results have been obtained for a microemulsion of H_2O/C_{10}/$C_{12}E_5$, ($\gamma_a = 0.03$ wt, $w_B = 0.029$ wt).

Figure 3.10.: *Sketch of the Michelson interferometer. $P_{1,2}$ are polarizers, T_1 is the thermostated brass cell holder. The computer records data from the photo diode (D) and controls the temperature of the cell holder.*
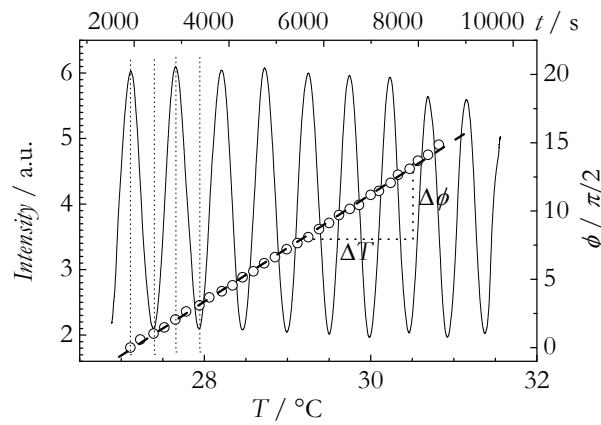
Figure 3.11.: *The detected intensity in the Michelson interferometer versus temperature. The temperature gradient is 0.5 K/s. A microemulsion is used ($H_2O/C_{10}/C_{12}E_5$, $\gamma_a = 0.03$ wt, $w_B = 0.029$ wt). The periodicity in terms of $\pi/2$ versus temperature (open circles) is fitted linearly (dashed line) and the vertically dotted lines are guides to the eyes and mark the π-steps of the intensity function. The slope $\partial\phi/\partial T$ (dashed line) is required in Eq.3.16.*

The refractive index increment can be calculated with [265]

$$\left(\frac{\partial n}{\partial T}\right)_{p,w} = \frac{\lambda}{4\pi l}\left(\frac{\partial \phi}{\partial T}\right)_{p,w} \quad \underbrace{-2\frac{n_w}{l}\left(\frac{\partial l_w}{\partial T}\right)_{p,w}}_{\approx -1.86\cdot10^{-7}} \quad \underbrace{-2\frac{l_w}{l}\left(\frac{\partial n_w}{\partial T}\right)_{p,w}}_{=-2.45\cdot10^{-6}} \quad \underbrace{-\frac{n}{l}\left(\frac{\partial l}{\partial T}\right)_{p,w}}_{\approx 1.13\cdot10^{-6}}.$$
(3.16)

The first term accounts to the phase change with temperature in the sample cell, the second term accounts for the thermal expansion of the cell windows, the third term is

deduced from the changes of the refractive index of the cell windows due to temperature changes and term four relates to the length expansion of the sample cell with temperature. Parameters are the refractive index of the window, $n_w = 1.457$, the thermal expansion coefficient of the front and back windows, $\alpha_w = 5.1 \cdot 10^{-7}$, the thermal expansion coefficient of the cell surfaces parallel to the beam, $\alpha_s = 7.5 \cdot 10^{-7}$, the wavelength of the HeNe-laser, λ, the optical length of the absorption cell, l, the optical window thickness, l_w, and the periodicity of the intensity function, ϕ. Typical values for the characteristic terms of the material properties are given below the equation.
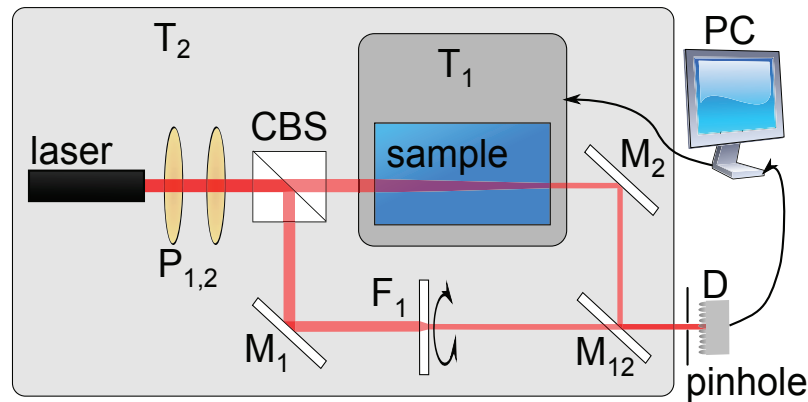
3.3.4. Improvements of the Michelson Interferometer

The advantages of the previously described Michelson interferometer are clear. The setup is compact and thermal fluctuations of the phases are small. One beam passes the absorption cell twice which doubles the investigated optical path length through the sample volume, but this leads to problems for turbid samples.

Technical difficulties arises from the geometry of the cell. The angle of the front and back windows to the laser beam have to be within a tolerance to permit interference. In the standard setup also the number of interfaces for both beams is different. The reflected beam from the back window has to pass seven interfaces while the reflected beam from the front window only passes one interface. The intensity of the laser beam which passes the sample twice, can be reduced by an order of magnitude and more, if the turbidity of the sample is high. This leads to a very weak intensity modulation which can not be analyzed.

We constructed a new Michelson interferometer for the measurement of strong scattering and turbid samples. Additionally, the new setup does not suffer from of the sample cell geometry. At the same time, the main advantages of the previous setup are kept. A sketch is shown in Fig.3.12. The whole setup is aligned on an optical breadboard to avoid mechanical vibrations. The laser beam (HeNe-laser, Polytec, Type PL-750P, 5 mW at 632.8 nm) is split by a beamsplitter cube in two beams of equal intensity. The reference beam is directed through a continuous grey filter wheel (F_1) onto a photodiode (D), while the measuring beam passes the temperature controlled sample cell and is superimposed to the reference beam by a semi-transparent mirror (M_{12}) with a transmission of 50 %. The sample cell and the cell holder are identical to the standard interferometric setup.

The main problem of the construction is that the total path length of the separate beams is

Figure 3.12.: *Sketch of the improved Michelson interferometer, optimized for strong scattering or turbid samples. $P_{1,2}$ are polarizers, D is the photo diode and CBS is the beamsplitter cube, T_1 is the temperature controlled brass cell holder and T_2 is the thermally insulating box surrounding the interferometer. The mirrors are M_1, M_2 (no transparency) and M_{12} (50% transparency). F_1 is the continuous grey filter wheel to match the intensities of both beams. D is the photo diode. The computer records the data from the diode and controls the temperature of the cell holder.*

about 40 cm. Perturbing effects such as temperature fluctuaions have to be minimized as they disturb the optical path length measurement. Therefore, the cell holder is thermally insulated in a box T_1 and the entire setup is surrounded by a box T_2, whereas the laboratory is air conditioned and the room temperature is kept constant with a stability of ± 1 K. The mechanical effects due to vibrations of the building are sufficiently blocked by the optical breadboard. It should be mentioned, that the path length difference of both beams is less than 1 cm and smaller than the coherence length of the HeNe-laser so that we satisfy the conditions for interference.

The interference pattern is optimized by adjusting the intensity of the reference beam to the same intensity level as the measuring beam (which passes the sample cell) with the continuous grey filter. Additionally, both intensities are reduced by the polarizers to a level that the photodiode responses linearly. A power meter (fieldmaster, Coherent, USA, discrepancy of 2% at 632.8 nm) is used to adjust the beam intensities. Finally, the semitransparent mirror M_{12} and the mirror M_1 are used to align both beams onto the photodiode.

Thermal as well as mechanical fluctuations can never be suppressed completely. To determine the strength of present fluctuations, we perform test measurements with pure water in a temperature range between 37 °C and 43 °C to determine the contrast of the
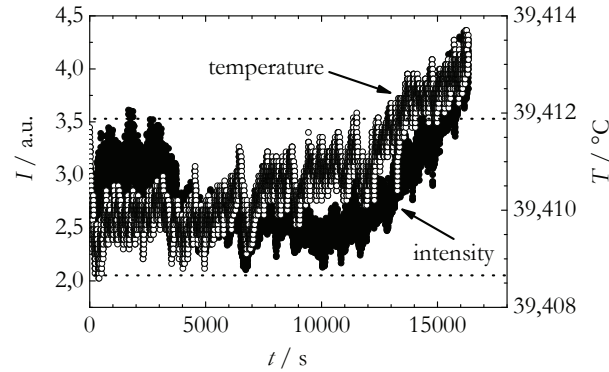
Figure 3.13.: *Intensity (filled symbols) and temperature (open symbols) versus time of water. The dotted lines mark the range used for the error calculation.*

measurement. The inset of Fig.3.14 shows the recorded sinusoidal intensity versus temperature. The full amplitude of the signal is 6.57 in arbitrary units. Then in a second measurement, the temperature was kept constant at $40.00\,°C$ in the water bath. Due to a loss of heat in the water cycle, the real temperature was approximately $39.41\,°C$. After an equilibration time of 60 minutes, the intensity and temperature were recorded for four hours (Fig.3.13). Assuming a perfect measurement, no change in temperature should occur, but an increase in the detected intensity indicates that the temperature was not constant. It is assumed that the room temperature changed.

The distribution of data points versus intensity is fitted by a Gaussian distribution using

$$y(I) = y_0 + \frac{\sigma}{\sigma\sqrt{2\pi}} e^{-\frac{1}{2}\left(\frac{I-\mu}{\sigma}\right)^2} \qquad (3.17)$$

with the standard deviation, σ, the expectation, μ, and the offset, y_0. It is assumed, that $y_0 = 0$. The Gaussian fit is plotted as a dashed line in Fig.3.14. Deviations occur at higher intensities ($I > 2.9$) due to the influence of the room temperature. The Gauss distribution shows a main peak at 2.57 (vertical dotted line) and the full width at half maximum is calculated to $\Delta I = 0.20$ (horizontal dotted line) or 3.0 % regarding the previously determined intensity range of 6.57. This value is taken as a statistic error of the setup.
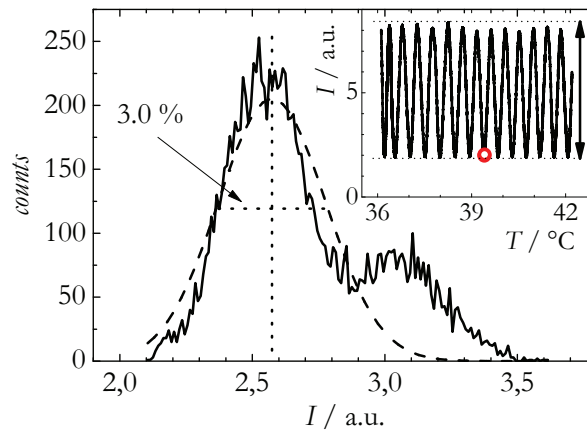
Figure 3.14.: *The intensity distribution (solid line) is fitted with a Gaussian function (dashed line). The full width at half maximum is given as a dotted line. The systematic error is approximately 3.0%. Inset: $(\partial n/\partial T)_{p,w}$-measurement of pure water in temperature variation from 37 °C to 43 °C to determine the achievable minimum and maximum intensities (horizontal dotted lines). The circle marks the temperature at which data from Fig.3.13 were recorded.*

3.4. Surface Tension Measurements

One goal of this work was the determination of the thermal diffusion behavior of aqueous surfactant solutions close to the *cmc*. For the determination of the *cmc*, surface tension measurements have been performed in Köln. Concentration series at different temperatures have been measured for each surfactant. Then, the *cmc* is determined as the concentration, where the surface tension turns from a concentration dependence to an independent behavior.

In general, surface tension is a property of a fluid surface to resist against external forces. It is caused by molecular attraction forces between molecules in the interface to a fluid or gas phase. In the liquid phase, intermolecular cohesion forces are homogeneously distributed and each molecule attracts neighbor molecules. Hence, the total force on a molecule in the liquid phase is zero. Contrarily, in the interface the attraction forces between the molecules are spatial inhomogeneously distributed since there are no more neighbor molecules in the gas phase and the total force points perpendicular to the surface into the bulk (Fig.3.15). Thus, the driving forces push surface molecules into the liquid phase to minimize binding energy. On the other hand, energy is needed to bring a molecule
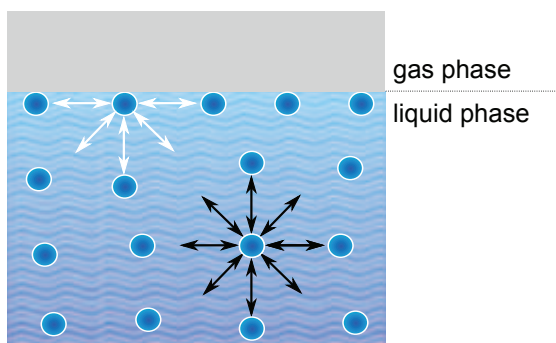
Figure 3.15.: *Intermolecular attraction forces are sketched in the fluid phase (blue) and in the surface layer to the gas phase (grey). The circles sketch water molecules. The total force is zero for molecules in the liquid phase (black arrows), while it is directed perpendicular to the surface area for molecules in the surface layer.*

into the interface as bonds to surrounding molecules have to be broken. Accordingly, a reduction of surface area comes along with a gain in energy.

Then, the surface tension, σ, is given as the ratio of required energy (or work), ΔW, which is needed to enlarge the surface area by ΔA:

$$\sigma = \frac{\Delta W}{\Delta A}\,. \tag{3.18}$$

This work is equal to the change of the Gibbs free energy and the surface tension is defined by

$$\sigma = \left(\frac{\partial G}{\partial A}\right)_{T,p} \tag{3.19}$$

with the Gibbs free energy, G, the area, A, and $\partial/\partial A$ is the partial derivative with the area at constant temperature and pressure.

The surface tension can be decreased by increasing the temperature or by adding a surface active component. We used nonionic sugar surfactants. The surfactants have a hydrophobic carbon chain of different length and one or several hydrophilic sugar rings as head group. These amphiphilic molecules prefer to go into the air-liquid interface. The surface tension decreases with increasing surfactant concentration. At a certain concentration, the surface is saturated with surfactant molecules. This concentration is called the critical micelle concentration (*cmc*). Above this concentration, the surfactant molecules will aggregate in the liquid. It is energetically favorable to screen the carbon chains from water: micelles are formed, wherein the hydrophobic chain is found in the inner micellar core and the hydrophilic surfactant head group is in contact with the aqueous solvent

in the micellar shell. Also single surfactant molecules are dissolved in the solvent and molecular exchange occurs between the micelles and the free surfactant molecules in the liquid or in the surface layer, respectively. The micellar shape and structure depend on the hydrophilicity of the surfactant head group whereas the *cmc* strongly depends on the hydrophobicity of the surfactant carbon chain which generally initiates the formation of micelles (see Sec. 2.2.1).

In the following, the concentration dependence of the surface tension is used to determine the *cmc* (see Sec.3.4.1). As a variation in temperature can also induce the formation of micelles, the respective temperature is called critical micelle temperature (*cmt*). In the following, the experimental method is briefly discussed and the working equations to determine the critical micelle concentration are introduced.

3.4.1. Setup

Several methods are known to measure the surface tension of a liquid-gas [278] or liquid-solid interface [279–281]. We perform the measurements in Köln with a Krüss digital tensiometer K10T using the Du-Noüy ring method [282–284]. A ring, dipped in the liquid phase, is pulled out of the phase. The surface tension causes the liquid film to stick to the ring. By pulling the ring out of the liquid phase, this film is stretched. The maximum force, which is required to stretch the film before the ring looses contact, is measured.

The temperature in the tensiometer is kept constant with a stability of ± 0.1 K within the measuring range between 15 °C and 40 °C. We perform concentration series starting at highest concentration and dilute the mixture stepwise. Before each measurement, we wait until the mixture is in equilibrium and the surface tension is constant for 90 minutes. This equilibration time was also used by Inoue *et al.* [285] for aqueous solutions of polyoxyethylene oleyl and polyoxyethylene stearyl. The concentration series is measured at constant temperature. The surface tension of pure water is taken as the lowest concentration value.

3.4.2. Theory

The experimentally determined surface tension σ^{exp} has to be corrected for finite wall effects [286] by

$$\sigma = 1.07\sigma^{exp}F \tag{3.20}$$
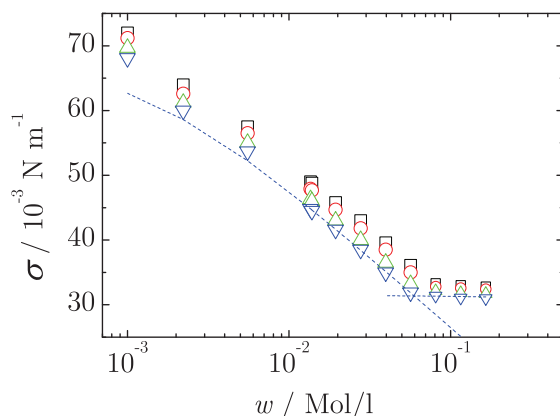
Figure 3.16.: *The surface tension of* C_7G_1/H_2O *at temperatures:* 15 °C *(squares),* 20 °C *(circles),* 30 °C *(triangles up), and* 40 °C *(triangles down). For* $T = 40$ °C *(triangles down), the dashed lines represent the fits: Eq.3.22 is applied in the low concentration regime while a linear fit was used to fit higher concentrations.*

where F is the correction factor [287]

$$F = 0.725 + \sqrt{0.4036 \cdot 10^{-3} \frac{\sigma^{exp}}{\rho^0_{mix} - \rho^0_{air}} + 0.0128} \tag{3.21}$$

with the macroscopic densities ρ^0_{air} and ρ^0_{mix} of air and the mixture, respectively. The corrected surface tension values from Eq.3.20 versus concentration are fitted using a linear regression for $w > cmc$, and the Langmuir-Szyszkowski equation [288] for $w < cmc$:

$$\sigma = \sigma_0 - a\ln(bw + 1) \tag{3.22}$$

with the surfactant concentration, w, and the fit parameters a and b. At the lowest concentration, the Langmuir-Szyszkowski equation deviates but close to the intersection point, Eq.3.22 describes the data at 40 °C accurately and the intersection of both fits provides the cmc. Fig.3.16 shows the surface tension versus the logarithmic concentration for the aqueous C_7G_1 system at several temperatures. The surface tension decreases with increasing temperature.

It was already discussed in Sec. 2.2.1 that the hydrophobic chain of the surfactant plays an important role for micelle formation: By increasing the chain length, the cmc decreases. This behavior is depicted in Fig.2.2 which shows the surface tension versus the concentration for a few C_iG_1/H_2O systems. The cmc of C_8G_1 is a factor of three smaller than

the *cmc* of C_7G_1. The determined critical micelle concentrations of C_7G_1 and C_8G_1 are in good agreement with data given in Tab.2.1, while the *cmc* of C_8G_2 is four times lower than comparable data in Tab.2.2. In Appendix E it is suggested that impurities decrease the *cmc*. Detailed information on the surface tension measurements of all investigated sugar surfactants are given in reference [277]. In this work, we use the determined *cmc* values to estimate the concentration range for the thermal diffusion measurements.

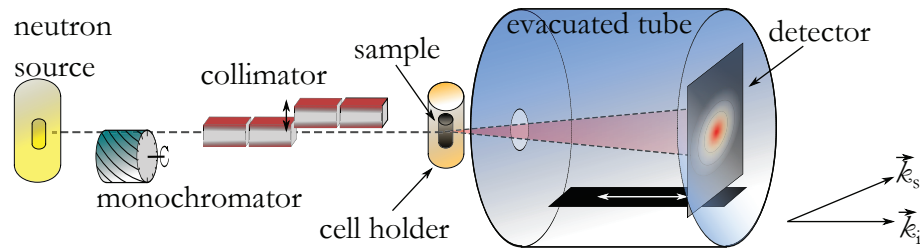# 3.5. Small Angle Neutron Scattering (SANS)

3.5.1. Introduction

Small angle neutron scattering (SANS) is a method to determine the size and shape of nanostructured matter by analyzing the time averaged intensity distribution of scattered neutrons as function of the scattering vector q. An advantage of SANS, and hence of neutrons, is the use of uncharged scattered particles. Contrarily to electrons, which are used as scattered particles in small angle x-ray scattering (SAXS) [289–291] or electron diffraction techniques, neutrons are not influenced by the electric field contribution of the scattering particle. Thus, neutrons are able to penetrate deeply into the atomic structure. As neutrons are scattered at the atomic structure and not at the electron cloud in the shell, SANS is sensitive to isotope effects [292]. Due to a nuclear magnetic moment [293], neutrons are greatly used to investigate magnetic materials [294, 295] as neutrons interact with unpaired spins and orbital moments of the particles. The main disadvantage of neutron sources is the low flux density compared to other scattering techniques.

We perform SANS measurements to determine the size and shape of microemulsion droplets at the *efb*. In the following, the SANS technique is briefly introduced.

3.5.2. Experimental Setup

We performed SANS experiments using the KWS-1 instrument at FRM2 (Garching, Germany) [296] which is sketched in Fig.3.17. The available neutron flux at the reactor is approximately 10^{14} s^{-1} (only thermal neutrons) [297, 298]. At the sample position, the flux is reduced to 10^6 s^{-1} to 10^8 s^{-1} and depends on the apperture settings and the collimation length. For SANS, thermal neutrons are used with a kinetic energy of less than 100 meV which corresponds to typical wavelengths of $3 - 30$ Å. The neutron guide *collects* the reactor neutrons not directly at the source but in a distance of a few centimeters, where the neutrons are slowed down by collisions with the moderator in the reactor containment (D_2O) to thermal energies at 300 K. The enormous energy distribution of neutrons is preselected by a Dornier velocity selector and a chopper. Behind the monochromators, the wavelength distribution is approximately $\Delta\lambda/\lambda \approx 0.2$ [299]. With the *de Broglie* relation the wavelength, λ, is given by the velocity, v, and mass of a neutron, m:

$$\lambda = \frac{h}{mv} \tag{3.23}$$

Figure 3.17.: *Sketch of the setup for small angle neutron scattering. Neutrons from the reactor are filtered by the monochromator and are focused through the collimator on the sample in the thermostated cell holder. The distribution of scattered neutrons is measured at the detector in an evacuated tube. The detector can be moved to vary the sample-detector distance.*

with the Planck constant, h. For our experiments we used wavelengths of 7 Å and 12 Å.

The neutron beam is focused on the sample position by a collimator. In the KWS-1 instrument, the collimator consists of several apertures with a distance to the sample between 2 m and 20 m. Due to the improved brilliance of the collimated neutron beam, the neutron flux is reduced by several orders of magnitude.

Scattered neutrons are detected on a panel matrix of 128 x 128 channels of ^{6}Li glass (max pulse rate of 1 MHz and a detection probability of 95 % for 7 Å neutrons) which is mounted on an area of 60 x 60 cm^2. Unscattered neutrons of the primary beam are blocked. The detector is mounted in the evacuated tube on a slide to tune the distance to the sample between 1.35 m (large scattering angles) and 18 m (small scattering angles).

3.5.3. Contrast Factor

Similar to other neutron scattering methods, i.e. neutron reflectivity (NR), SANS takes advantage from different scattering length densities of nulcei of different elements. Hereby, the scattering length density is a measure of the interaction strength of a neutron and a nucleus. Another important advantage of SANS is, that the scattering length density of hydrogen and deuterium have opposite signs [300]. Thus, a variation of scattering length densities can help to achieve a good contrast easily.

The contrast is generally tuned by the exchange of protonated with deuterated solute or solvent molecules [301–304]. The scattering length density of hydrogen is negative, which means that a neutron scattered at a hydrogen nucleus is 180° out of phase relative to those neutrons scattered by the other elements' nuclei. On the other hand, the scattering

length density is positive and in absolute values two times higher for deuterium [291,305]. For the investigation of the shell contrast of the microemulsion droplets, we deuterated the *n*-alkane. Therefore, the scattering length density of the alkane is matched to the scattering length density of the surrounding bulk phase by mixing deuterated and protonated alkanes. The determined particle radius by SANS then refers approximately to the point between the surfactant head group and the chain. The *effective* radius of a droplet is obtained by adding 6 Å which is approximately the half length of the surfactant molecule in the interface. The composition of the deuterated mixtures was chosen to achieve the same volume fraction as the protonated mixtures which leads to slightly different mass fractions. The deuteration of the solvent also leads to lower temperatures of the phase boundaries [306,307].

3.5.4. Data Analysis

The fundamental variable in SANS measurements is the $\vec{q}$-vector, which is defined by the incident wave vector, $\vec{k}_i$, and the scattered wave vector, $\vec{k}_s$:

$$|\vec{q}| = |\vec{k}_s| - |\vec{k}_i|\,. \tag{3.24}$$

Its magnitude is given as a function of the scattering angle, θ:

$$q = |\vec{q}| = \frac{4\pi n}{\lambda}\sin\frac{\theta}{2} \tag{3.25}$$

with the neutron wavelength, λ, and the refractive index, n.

In SANS measurements, the scattered intensity distribution is recorded at the detector plane. Edge effects of the detector and distracting pixels are removed with a software and the intensity distribution is radially averaged, denoted as I_{sample}. I_{sample} needs to be corrected due to the background intensity and contributions from the cell. Then, the measured intensity is calibrated to a standard to obtain the absolute intensity. Plexiglas of 1.5 mm optical path length was used as the calibration standard for which the absolute incoherent scattering intensity is known. It can be used as a reference to determine the detector sensitivity. The absolute intensity of the sample is then calculated by

$$I(q) = \frac{I_{\text{sample}} - I_{\text{bg}} - \frac{T_{\text{sample}}}{T_{\text{ec}}}(I_{\text{ec}} - I_{\text{bg}})}{I_{\text{plexi}} - I_{\text{bg}} - \frac{T_{\text{plexi}}}{T_{\text{ec}}}(I_{\text{ec}} - I_{\text{bg}})} \cdot \frac{T_{\text{plexi}}d_{\text{plexi}}}{T_{\text{sample}}d_{\text{sample}}} \cdot \frac{d\Sigma}{d\Omega}\bigg|_{\text{plexi}} \tag{3.26}$$

with the transmission of the sample, T_{sample}, the background intensity at the detector, I_{bg}, the scattered intensity and transmission of the empty cell, I_{ec} and T_{ec}, respectively, and the intensity and transmission of the calibration standard, I_{plexi} and T_{plexi}, respectively. d is the optical length of the cell and $d\Sigma/d\Omega\big|_{\text{plexi}}$ is the absolute cross section of the standard.

The absolute intensity as a function of q (Eq.3.26) is proportional to the form factor, $P(q)$, and the structure factor, $S(q)$. By the assumption of monodisperse and spherically symmetric particles it can be written as [308]

$$I(q) = N\,(\Delta\rho)^2 V^2 S(q) P(q)\,, \tag{3.27}$$

with the number density of particles, n, the difference in the scattering length density between the particles and the solvent, $\Delta\rho$, and the volume of the particles, V. The form factor provides information about the structure of the particles while the structure factor provides information about the particle interaction. In the case of highly diluted systems where particle-particle interactions vanish, the structure factor is equal to one and the absolute intensity only depends on the form factor [309].

Several scattering models have been developed to describe the particle geometries and interaction effects. The form factor for spherical micelles of a homogeneous sphere [310] with an extension for diffuse interface has been proposed by Strey *et al.* [307]. For microemulsion droplets, the scattering contribution of the droplet core was taken into account by Foster *et al.* [311] using a model for a polydisperse spherical Gaussian shells with a diffuse interface [312]. Most simple the structure factor can be analytically derived with the Percus-Yevick approximation [313]. A model for the structure factor was introduced by Baxter [314]. A sticky hard-sphere potential is assumed which describes the particles as hard spheres with an attractive delta function potential at the surface. An overview about the various mathematical expressions regarding the form factor and the structure factor which are used in this work can be found in the thesis of Sascha Datta [277].

FOUR

SORET EFFECT OF $\mathbf{C_8G_1}$ IN WATER AROUND THE *CMC*

We studied the thermal diffusion behavior of the nonionic surfactant $\mathbf{C_8G_1}$ (n–Octyl β–D–glucopyranoside) in water for different concentrations between w=0.25 wt% and 2.0 wt% in a temperature range from 15 °C to 60 °C using the classical and infrared thermal diffusion forced Rayleigh scattering (TDFRS) setup.

The purpose of this chapter is the investigation of the thermal diffusion behavior of surfactant systems around the critical micelle concentration (*cmc*), which is independently determined by surface tension measurements.

4.1. Introduction

Several experimental techniques have been used to study the thermal diffusion behavior of surfactant systems. Piazza *et al.* investigated an ionic surfactant, sodium dodecyl sulphate (SDS), in water using a beam deflection and a thermal lens setup [37, 48]. They found that S_{T} increases with increasing salt concentration due to the strong influence of intermicellar interactions. They investigated also the nonionic surfactant β-dodecyl maltoside ($\mathbf{C_{12}G_2}$), which has the same hydrophobic tail as SDS and two glucose rings as head group. $\mathbf{C_{12}G_2}$-micelles showed a strong tendency to move to the cold region ($S_{\mathrm{T}} > 0$), which might be caused by the interaction of the surface of micelles with the solvent via hydrogen bonds. Ning *et al.* studied a series of nonionic surfactants in water
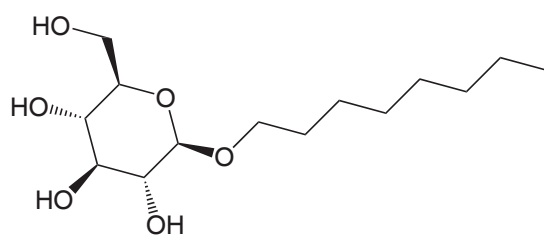
Figure 4.1.: *Molecular structure of β–C_8G_1.*

in a wide temperature and concentration range using the thermal diffusion forced Rayleigh scattering (TDFRS) technique [39,40]. For their measurements a small amount of an ionic dye (Basantol® Yellow) is added in order to create a sufficient temperature gradient. The measurements show that the addition of the dye influences the thermal diffusion behavior considerably. Therefore the IR-TDFRS setup has been developed to avoid the addition of dye for aqueous systems [75].

Santos *et al.* investigated the Soret coefficient of potassium laurate in water and found an abrupt change of the matter lens signal at the *cmc* [34]. Unfortunately, an evaluation of S_T was not possible due to the presence of the dye which complicated the analysis. Therefore, it remained unclear to which extend the *cmc* is also visible in the thermal diffusion, diffusion and Soret coefficient. To clarify these observations the thermal diffusion behavior of micellar systems with a high *cmc* needs to be investigated without the addition of dye.

Among the wide range of surfactants we found nonionic sugar surfactants with a fairly high *cmc*, such as *n*–Octyl β–*D*–glucopyranoside, in the following referred to as C_8G_1 [315]. The β–form has a linear molecular structure which is shown in Fig.4.1. Additionally, an α–*L*–form exists, which differs in the linkage between the hydrophilic head and the hydrophobic chain of the alkyl glucoside [207,316], but this less common α-form will not be considered here.

Many properties such as the phase and structural behavior, the influence of salt, but also the solute-solvent interactions have been studied for aqueous solutions of C_8G_1 [207,223,317]. From previous studies on aqueous systems [62,140] we know that the solute-solvent interaction and the capability to form hydrogen bonds often influence the thermal diffusion behavior. Pastor *et al.* [317] determined the number of water molecules (*hydration number*), surrounding the C_8G_1 molecules. They found a hydration number of 16 for monomers below the *cmc*, which is decaying exponentially above the *cmc* to 8 for concentrations around 1.5 wt%, while at the same time the aggregation number increases
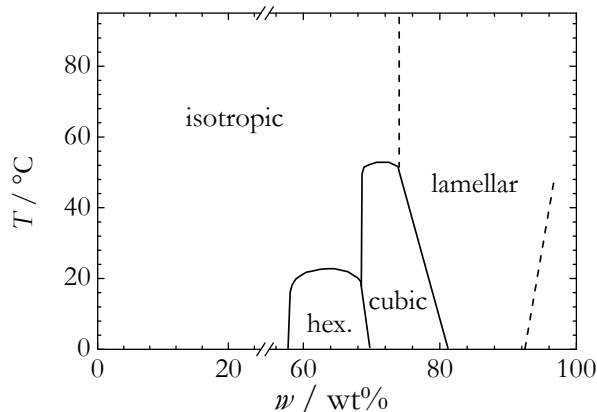
Figure 4.2.: *Phase diagram of* C_8G_1*, redrawn from Nilsson* et al. *[207].*

from 54±5 to 104±5 when increasing the concentration from 0.85 to 1.5 wt%. They also observed a slight shift of the *cmc* to lower concentrations when adding salt.

In the following, we determine the *cmc* of C_8G_1 in water in a temperature range between 15 °C and 40 °C by surface tension measurements and study the thermal diffusion behavior of the system using both, the classical TDFRS as well as the IR-TDFRS. The classical TDFRS has been used to study the system in the presence of dye as it was also done in the work by Santos *et al.* [34]. Therefore, we had also to investigate to which extend the *cmc* is shifted in the presence of the trivalent dye Basantol[®] Yellow. In order to gain a better understanding of the influence of the dye on the transport properties we performed experiments with the IR-TDFRS without and also in the presence of dye.

4.2. Experiment and Data Analysis

4.2.1. Sample Preparation and Characterization

n–Octyl *β*–D–glucopyranoside was purchased from Glycon Biochemicals (Germany) with a purity of 99.5 %. The molecular structure is depicted in Fig.4.1. A phase diagram of the aqueous surfactant system C_8G_1/H_2O (without dye) was recorded by Nilsson *et al.* [207] and is shown in Fig.4.2.

All samples were prepared by weighting with the accuracy of the balance (±0.0001 g). Deionized Milli-Q water was used as solvent. In the classical TDFRS setup we used

for all measurements a tiny amount of 1.5×10^{-4} M of the ionic dye Basantol$^{\circledR}$ Yellow (BASF) [40]. The optical density was adjusted to 2 cm^{-1} at a wavelength of $\lambda = 488$ nm using a Carry 50 spectrometer. For the absorption measurements we use cells with a thickness of 1 mm. For the IR-TDFRS and classical TDFRS measurements, the surfactant solutions were directly filtered into the sample cell by a PTFE (Roth) filter with a mesh size of 5 μm. The Hellma flow cells, used for both TDFRS experiments, have an optical thickness of 0.2 mm.

For all experiments, the sample cell in the TDFRS setups was thermostated in a brass or copper holder for at least half an hour. The selected material of the sample holder has a high thermal conductivity and thus allows a fast equilibration and homogeneous profile of the temperature in the sample holder. The temperature of the holder was controlled by a circulating water bath (Lauda E300 thermostat) with a stability of $\pm$ 0.02 K. The classical TDFRS and IR-TDFRS measurements were performed in a concentration range between 0.25–2.0 wt% and in a temperature between 15 °C and 40 °C, and for chosen samples in a temperature range up to 60 °C.

4.2.2. Determination of the Critical Micelle Concentration

The critical micelle concentration was determined by surface tension measurements, which were performed with a Krüss digital tensiometer K10T. Concentration series of the C_8G_1/water mixture at 15 °C, 20 °C, 30 °C and 40 °C were measured. The dye-containing mixtures were studied at 23 °C and 30 °C, respectively. The temperature was controlled with an accuracy of ± 0.1 K.

The trend of the surface tension versus the logarithm of the concentration was analyzed using the Langmuir-Szyszkowski-equation [288] in eq. 3.22 below the *cmc* (see Fig.4.3). Above the *cmc*, the surface tension is almost constant, thus this range was fitted linearly. The intersection of both curves marks the *cmc*. Detailed information on the measuring method are given in section 3.4.

4.2.3. Influence of the Dye on the cmc

The classical TDFRS setup suffers from the addition of dye to convert the intensity grating of the Ar-laser into a thermal grating. Especially for aqueous mixtures, it has turned out that it is difficult to find an inert dye, which does not influence the experiment.
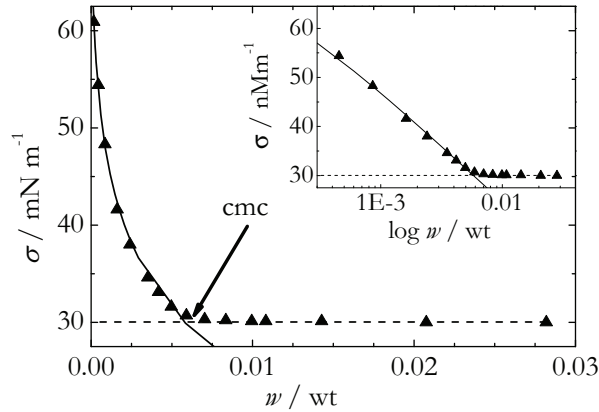
Figure 4.3.: *The surface tension as function of the concentration of the binary system* C_8G_1/H_2O *at 30 °C. The continuous line marks the fit with the Langmuir-Szyszkowski-equation (see Eq. 3.22) at low concentrations, the linear fit (dashed line) was obtained from fitting for the seven highest measured concentrations. The intersection point marks the* cmc. *Inset: The same data plotted in a logarithmic scale of the concentration.*
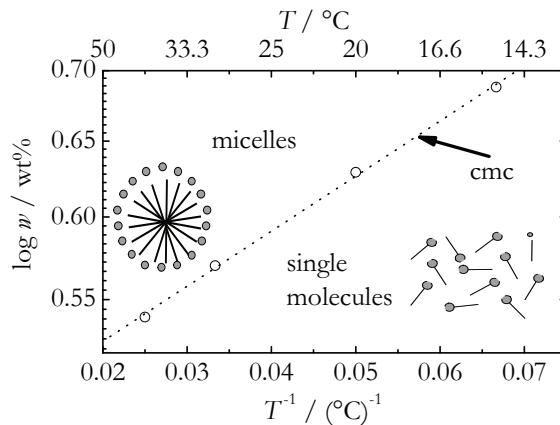
Figure 4.4.: *Temperature dependence of the* cmt *for the* C_8G_1/H_2O *system. The* cmt *scales linearly with the inverse temperature.*

Water soluble dyes often change their absorption behavior with *pH* or temperature [318, 319]. In complex systems the addition of dye can also influence the phase behavior and microstructure of the micellar system and also its thermal diffusion behavior [38].

To investigate the influence of the ionic dye on the *cmc* we performed measurements with the same dye concentrations (full circles and full rectangles in 4.6), corresponding
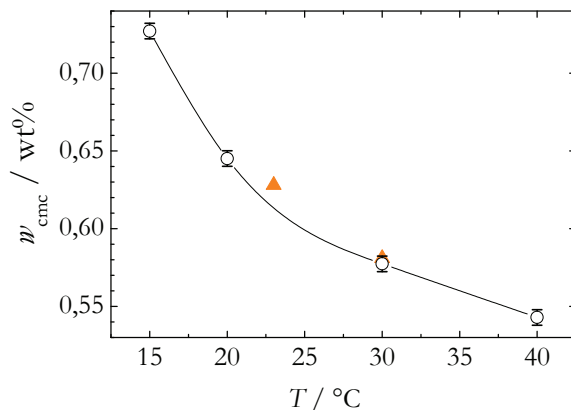
Figure 4.5.: *The critical micelle concentrations at several temperatures for the C_8G_1/H_2O system. The* cmc *of the dye-infected system (triangles up) is compared with the dye-free surfactant system (circles). The effect of the dye on the* cmc *is negligible.*

to the dye-concentration in the TDFRS experiments. Two critical micelle concentrations of C_8G_1/H_2O with dye at 23 °C and 30 °C were determined and compared with dye-free mixtures. The results are shown in Fig.4.5. At this rather low concentration we did not see a significant influence of the dye and the dye infected mixture showed nearly the same *cmc* values as the surfactant mixture which was measured in the absence of dye. Deviations only occurred in the order of the error bars. Pastor *et al.* found a change of the *cmc* of C_8G_1 in water of 10-15 % adding 0.05 M $CaCl_2$ or $ZnCl_2$ [317]. Since the dye concentration in our experiments was about two orders of magnitude smaller we would expect only a change of the *cmc* in the sub-percent range, which is in agreement with our results.

4.2.4. Data Analysis

The normalized diffraction signal, ζ_{het}, is described and analyzed by Eq.3.8. The increment of the refractive index with concentration, $(\partial n/\partial w)_{p,T}$, at constant pressure and temperature was measured with a refractometer (Anton Paar). Five measurements were performed for each concentration to reduce the error.

For the determination of $(\partial n/\partial T)_{p,w}$ at constant pressure and surfactant concentration an Michelson interferometer was used. In general, the $(\partial n/\partial T)_{p,w}$ measurements of C_8G_1 so-

lutions as function of the surfactant weight fraction were done between 15 °C and 40 °C. For a few weight fractions we performed measurements up to 60 °C.

According to Rosen [320] and Preston [321] it should also be possible to determine the critical micelle concentration from the variation of the refractive index with concentration. However, by measuring the refractive index as function of concentration we found an almost perfect linear concentration dependence, which makes it impossible to determine the cmc. To our knowledge, the refractive index measurements are not favored for the cmc determination of C_8G_1 in H_2O. Instead, Strop and Brunger [322] used refractive index measurements for the determination of the surfactant concentration in solution for aqueous systems with low cmc values, namely nonaethylene glycol monododecyl ether ($C_{12}E_9$, $cmc = 100\mu M$ [323]) and n–dodecyl–β–D–maltopyranoside ($C_{12}G_2$, $cmc = 230\mu M$ [324]). They found a linear relationship between the change of the refractive index and the surfactant concentration in the investigated low concentration range. They expect that this relationship can be used for methods to determine the surfactant concentration my measuring the refractive index also for high cmc systems, if lower-sensitivity detectors are used.

4.3. Results and Discussion

4.3.1. Surface Tension Measurements

As already described we determined the critical micelle concentration by surface tension measurements. The temperature dependence of the cmc is shown in Fig.4.6. We studied two different batches of C_8G_1: an old batch (rectangles) (Glycon, 2005) and a new one (circles) (Glycon, 2008). We found systematically larger cmc values for the new batch, however this difference could be explained with a changed workup method in the production process (notice by manufacturer). Anyway, the temperature dependence of the cmc is qualitatively the same for both batches. To avoid misunderstanding, we performed all TDFRS measurements with the new C_8G_1 batch.

The cmc was determined at several temperatures in a range from 15 °C to 40 °C. The cmc decreases with increasing temperature and describes a parabolic shape in a temperature dependence (not shown in Fig.4.5). The polynomial 2nd order fit of this curve shows a minimum point at 42 °C. This is a typical behavior of nonionic systems as the hydrogen bonds break at higher temperatures which is discussed in Sec.2.2.1. It is shown in Fig.4.4,
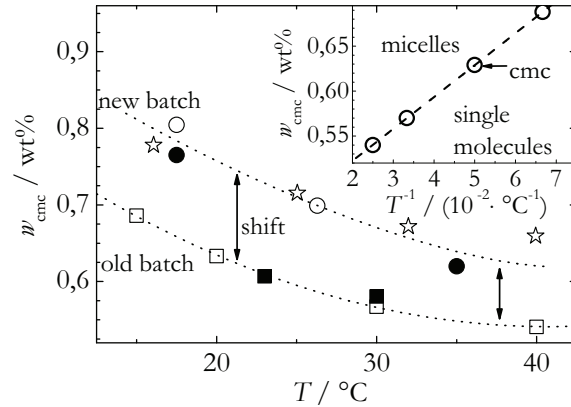
Figure 4.6.: *The* cmc *for* **C_8G_1**/H_2O *was determined by surface tension measurements without ($\bigcirc$, $\square$) and with dye ($\bullet$, $\blacksquare$) for the old ($\square$, $\blacksquare$) and the new surfactant batch ($\bigcirc$, $\bullet$), and compared with literature values by Aoudia and Zana [220] ($\star$). The error bars are in the order of the symbol size. Inset: The* cmc *as function of the inverse temperature in Celsius. The dashed line is a linear fit to the data points.*

that plotting the logarithmic *cmc* versus the inverse temperature gives a linear dependence (dotted line). Below this line the surfactant monomers are dissolved in water, while above a dynamic equilibrium of monomers and micelles exists.

For both batches we observed a decay of the *cmc* with increasing temperature. This can be explained with a decreasing hydrophilicity of the surfactant molecules with increasing temperature due to the decreasing ability to form hydrogen bonds. Typically the *cmc* of nonionic surfactants passes through a minimum and increases at higher temperatures again [220, 221]. In the investigated temperature range up to 40 °C we did not observe the minimum and the final increase, but Aoudia and Zana [220] observed a shallow minimum around 42 °C for the same surfactant system. A polynomial 2nd order fit of our data (dashed line in 4.6) shows, that we can expect a similar minimum temperature at 42 °C for the minimum *cmc*. The position of the minimum is determined by the size of the head group, which is fairly large in the case of the sugar surfactant. Also for different polyoxyethylene glycol monododecyl ethers **$C_{12}E_j$** with oxyethlyene chain units of *j* = 4, 6 and 8 a shift of the minimum from 40 °C to 50 °C has been observed [221].

4.3.2. Thermal Diffusion Behavior around the cmc

Below the *cmc*, the surfactant molecules in solution are in equilibrium with those adsorbed at the water-air interface. Above the *cmc* also micelles are formed in the solution. Therefore, we will observe the thermal diffusion behavior of the individual surfactant molecules below the *cmc*, while above the *cmc* we have additionally a thermophoretic motion of the micelles. This might also lead to a pronounced change of the thermal diffusion or Soret coefficient.

For the surfactant system under study the determined Soret coefficients correspond to an averaged value. We can not differentiate between the contribution stemming from the C_8G_1 molecules and micelles, as it can be done for a polymer in a solvent mixture [62]. In the latter case the diffusion process of the solvent mixture and the polymer can be differentiated, because the time constants of the two processes differ by more than one order of magnitude. For the micellar solution the time constants of the single molecules and the micelles are so close that we can not separate the two processes in the experimental signal. Therefore, we observed only an averaged value, which describes the thermal diffusion motion of C_8G_1 in water. Depending on the location in the phase diagram the signal can be a superposition of different contributions. A detailed analysis of the different contributions in a phenomenological approach suggested by Santos *et al.* is not possible [34].

In the following we compare the results of both TDFRS setups in order to determine the influence of the dye. In Fig.4.7 we show the temperature dependence of the Soret coefficient, the thermal diffusion coefficient and diffusion coefficient for a sample with a surfactant concentration of w=0.6 wt% where we found the *cmc* at 23 °C. In the plot we display data obtained by IR-TDFRS and classical TDFRS. In the latter case the samples contained Basantol® Yellow as dye. Additionally, we performed measurements with the IR-TDFRS in the presence of dye.

The diffusion coefficient, D, and the thermal diffusion coefficient, D_T, increased continuously with temperature. None of the diffusion coefficients showed a noticeable change at the *cmc*. The difference of D obtained with the different setups is almost negligible although D obtained with the classical setup was systematically larger, which might indicate smaller micelles or attractive interactions. In our case the addition of the dye led to charged micelles, which repelled each other and which should have led to slower dynamics [325,326]. Surprisingly, in our case the diffusion became faster, when the micelles were charged (middle chart in Fig.4.7). This might be explained by an inhomogeneous heating of the dye-containing micelles, which leads to a faster movement.
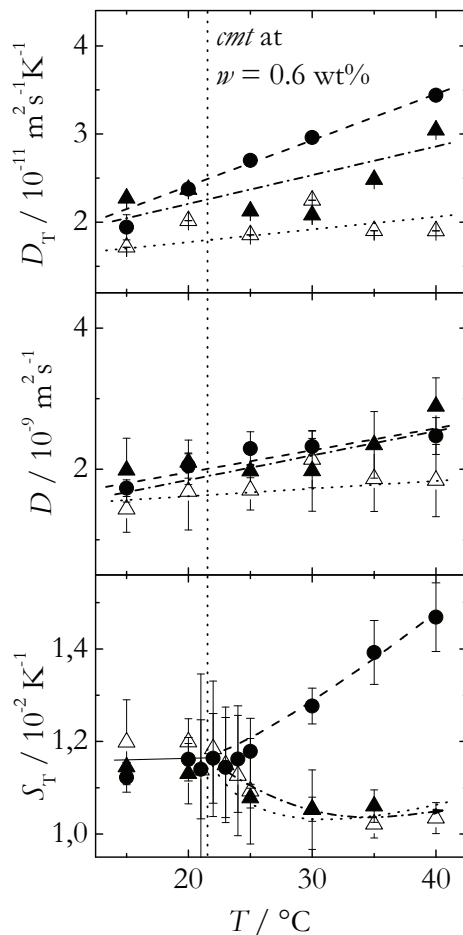
Figure 4.7.: *Comparison of S_T, D_T and D as function of the temperature for w=0.6 wt% in IR-TDFRS ($\triangle$ (without dye), $\blacktriangle$ (with dye)) and classical TDFRS ($\bullet$). Bottom: Above the cmt we observe larger S_T-values in classical TDFRS than in IR-TDFRS. Independent of the method or the presence of the dye we find the same Soret coefficients below the cmt at 23 °C within the error bars of approximately 10 %.*

The temperature dependent slope of D_T measured with the classical TDFRS is larger than the one measured without dye in the IR-TDFRS. We assume that the dye was incorporated into the micelles and the interfacial energy of the micelles changes. This assumption is supported by the fact that the molar fraction of the dye molecules and micelles is in the same order of 1.5×10^{-4} mol/l, if we take into account the aggregation numbers determined by Pastor *et al.* [317]. The incorporation of the dye into the micelles influences also the diffusion coefficient. The reason could be either that the interaction
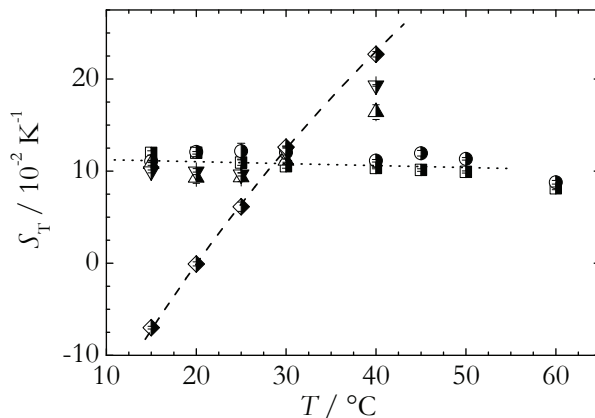
Figure 4.8.: *The Soret coefficient S_T as function of temperature determined with the IR-TDFRS without dye. Concentrations: 0.6 wt% (squares), 0.65 wt% (circles), 0.7 wt% (triangles up), 0.75 wt% (triangles down) and 1.0 wt% (diamonds).*

energy changes due to a modified interfacial energy or that the shape is modified. The latter we will have to confirm by neutron scattering experiments.

Below the *cmc* all Soret coefficients agree within their error bars and S_T is temperature independent (cf. Fig.4.7). For temperatures above the *cmc* we observed, that the Soret coefficient for the classical setup was larger compared to the IR setup. In the classical TDFRS the incorporation of the dye in the micelles probably induced a stronger local heating, which modified the thermal diffusion behavior strongly. This was probably also the reason leading to the abrupt change of the thermal lens signal of the aqueous potassium laurate solution with Congo red [34]. We suspect that it is really necessary to create the thermal grating with the absorbing wavelength, because recent experiments on a nonionic surfactant with Basantol[®] Yellow as dye [38] showed that homogeneous illumination with a blue laser in the IR-TDFRS does not have the same effect.

In Fig.4.8 the temperature dependence of the Soret coefficient is plotted for different concentrations above and below the *cmc*. Those concentrations above 0.65 wt% indicated an increase of S_T with temperature, others below 0.65 wt% not. As we already found, the Soret coefficient is independent from temperature in the molecular regime and only the contribution of micelles cause a change of S_T. Thus, it is expected that the *cmc* is determined in this plot approximately at 0.65 wt%.

We were also able to determine the *cmc* by plotting the Soret coefficient as a function of the sugar surfactant concentration as shown in Fig.4.9. For both temperatures the slope
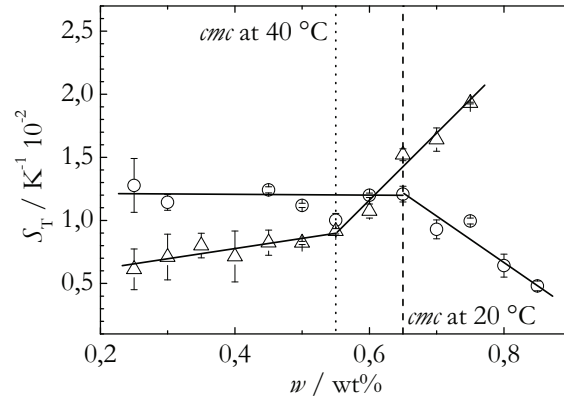
Figure 4.9.: *The Soret coefficient versus the surfactant concentration at constant tem-*
peratures of 20 °C ($\bigcirc$) and 40 °C ($\triangle$) using IR-TDFRS without dye. The vertical lines
mark the cmc at 20 °C (dashed) and 40 °C (dotted). The solid lines are guides to the eye.

of the Soret coefficient changed clearly at the *cmc*. While the slope at 20 °C changed from
zero to negative, the positive slope at 40 °C (dotted vertical line) became more pronounced
above the *cmc*. For both temperatures below the *cmc* the concentration dependence of
S_T was less pronounced. The measurements with the classical TDFRS setup did not give
a better indication of the *cmc*. For clarity the data are not displayed. The obtained *cmc*
values are in good agreement with the results from the surface tension measurements.

4.3.3. Results for higher concentrated Solutions

We also investigated the thermal diffusion behavior for higher surfactant concentrations.
Fig.4.10 shows the thermal diffusion D_T, the diffusion D and the Soret coefficient S_T as
function of concentration at different temperatures.

For all temperatures the thermal diffusion coefficient decreased with increasing surfactant
concentration and with decreasing temperature (cf. top of Fig.4.10). For the three lower
temperatures of T = 15 °C, 20 °C and 25 °C a sign change occurred at a concentration
of 0.9 wt%, 1.0 wt% and 1.6 wt%, while D_T stayed positive at higher temperatures. The
decay of D_T became weaker for higher concentrations. As can be seen in the middle part
of Fig.4.10 the diffusion coefficient D decreased for lower concentrations, while above the
*cmc* the diffusion was almost independent of the concentration.

In the bottom part of Fig.4.10 the concentration dependence of the Soret coefficient is
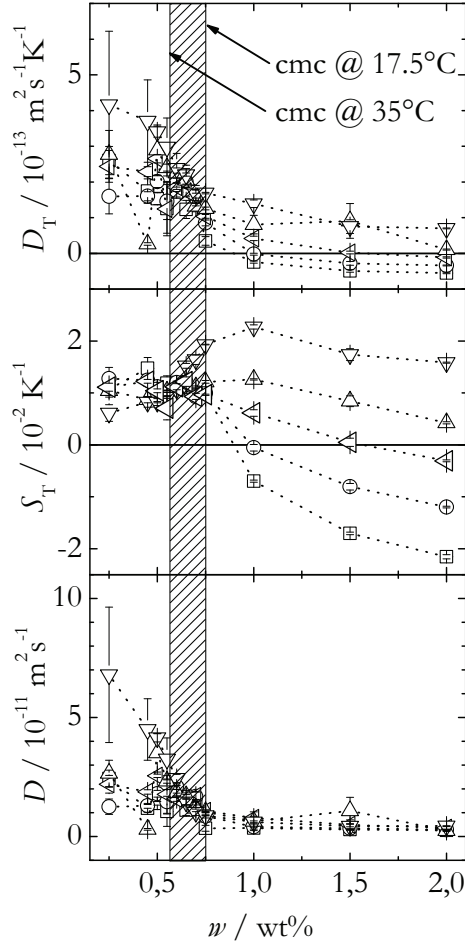
Figure 4.10.: *The thermal diffusion D_{T}, the diffusion D and the Soret coefficient S_{T} versus the concentration at different temperatures:* 15 °C *(□),* 20 °C *(○),* 25 °C *(◁),* 30 °C *(△),* 40 °C *(▽).*

shown for different temperatures. S_{T} passed through a maximum for $T = 20$ °C and 40 °C before it was decaying almost linearly above a concentration of 1.0 wt%. By decreasing the temperature this decay became steeper. For the two highest temperatures at 30 °C and 40 °C we did not observe a sign change in the investigated concentration range, but it is expected that it will occur at higher concentrations.

The decay of the Soret coefficient at high concentrations seems to be a typical phenomena and has also been found for polymer solutions [327] and colloidal dispersions [42]. In the semidilute concentration range the Soret coefficient of the polymeric system showed an asymptotic scaling law with concentration $S_{\mathrm{T}} = C_0 \cdot C^{-0.65}$, whereas the exponent changed
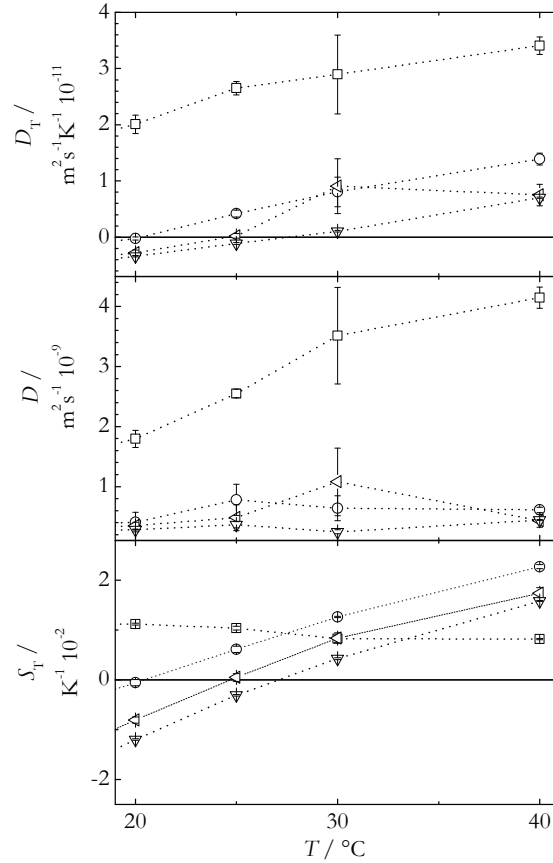
Figure 4.11.: D_T, D and S_T versus temperature in the IR-TDFRS. Concentrations: 0.5 wt% ($\square$), 1.0 wt% ($\bigcirc$), 1.5 wt% ($\triangleleft$) and 2.0 wt%($\triangledown$).

from -0.65 to -1 approaching the concentrated regime. For the colloidal system an asymptotic power law for the Soret coefficient in dependence of the volume fraction ϕ of the form $S_T = \phi_0 \cdot \phi^{-0.0095}$ has been found. For the investigated sugar surfactant system the exponent is not temperature independent but decreases from -0.42 to -1.44 with decreasing temperature.

Fig.4.11 shows the temperature dependence of D_T, D and S_T up to a concentration of 2.0 wt%. The temperature dependence of S_T was negligible small for concentrations below the *cmc*, for instance 0.5 wt%, and became more pronounced for higher concentrations (2.0 wt%). For sufficiently high concentrations we observed a sign change of S_T from negative to positive with increasing temperature. The sign change temperature as well as the slope of the temperature dependence of S_T increased with increasing concentration.

The sign change from negative to positive S_{T}-values is a typical behavior of aqueous polymer and colloidal systems [48,328]. Sugaya *et al.* [328] found for aqueous dextran solutions that the temperature dependence was concentration independent. They were able to shift the sign change temperature towards lower temperatures by adding urea, which functioned as a hydrogen bond breaker so the system becomes more "thermophobic" and dextran moves to the cold side. We observe the same trend with increasing temperature when the hydrogen bond formation is weakened. An increase of the sugar surfactant concentration leads to more surface groups interacting via hydrogen bonds and results in a more "thermophilic behavior".

4.4. Conclusion

We measured the diffusion coefficients and the Soret coefficient of the nonionic sugar surfactant C_8G_1 for different concentrations and temperatures. Special attention has been payed to the region around the critical micelle concentration, which has been determined independently by surface tension measurements.

As expected we find a slower diffusion for the micelles compared to the single sugar surfactant molecules. Although the surface tension measurements indicate that the *cmc* is not influenced by the presence of the dye, we find a pronounced influence of the dye in the thermal diffusion measurements. Below the *cmc* the results for all methods give identical results indicating that the dye diffuses as the sugar surfactant molecules freely in the water. Above the *cmc* we find a much larger value of the Soret coefficient with the classical TDFRS setup compared to the IR-TDFRS. This effect might be explained by local heating of the dye infected micelles. A similar mechanism might also have led to an abrupt change of the matter lens signal in the work by Santos *et al.* [34]. Nevertheless, we find also a change in the slope of the concentration dependence of the Soret coefficient determined with the IR-TDFRS without the dye below and above the critical micelle concentration (cf. Fig.4.9). One hypothesis in understanding the change of the thermodiffusion behavior near the *cmc* is that the thermal diffusion motion arises from unbalanced stresses localized in a thin layer close to the molecule-particle surface, which is primarily determined by the nature and strength of particle-solvent interactions. Following this concept, it seems to be natural to expect a change in the Soret coefficient once micelles are formed, because part of the surfactant molecules are hidden in the inside of the micelles, so that the direct interaction with the solvent is screened.

At higher surfactant concentrations above 1.0 wt% a sign change has been observed. With increasing temperatures the sign change shifts towards higher concentrations and with increasing concentration the sign change occurs at higher temperatures. The behavior is in analogy with results for concentrated polymeric and colloidal systems and part of the behavior can be explained by the balance of the hydrogen bond formation. We expect that a similar behavior can also be observed for other surfactant systems.

CHAPTER

FIVE

INVESTIGATION OF SUGAR SURFACTANT MICELLES
USING IR-TDFRS

In chapter 4 aqueous n–Octyl β–D–glucopyranoside solutions were used as a model system to investigate the thermal diffusion behavior in the vicinity of the critical micelle concentration. It was shown that the cmc is detectable in TDFRS measurements. Additionally, a sign inversion of the Soret coefficient was observed at higher concentrations.

In this chapter, we describe the same measurements in the concentration regime close to the cmc for other sugar surfactants to investigate, if the previous findings are general features of this surfactant class. We also wanted to investigate how structural changes such as the number of head groups or the length of the alkyl chain influence the thermal diffusion properties. Therefore, we selected n–Heptyl β–D–glucopyranoside (C_7G_1) and n–Octyl β–D–maltopyranoside (C_8G_2). As it was introduced in Sec.2.2.1, the cmc of C_8G_1 and C_8G_2 is almost equal but the two head group units of the maltoside (see Fig.5.1-c) cause changes in the micellar shape. In contrast, the shorter carbon chain of C_7G_1 (Fig.5.1-a) decreases the hydrophobicity and thus raises the cmc. The cmc of C_7G_1 and C_8G_2 was precisely determined by surface tension measurements for several temperatures. Although a few literature values of the cmc are available (see Tabs.2.1 and 2.2), the temperature dependence of the cmc is rarely investigated. A second point was the investigation of the S_T sign inversion at higher surfactant concentrations. It was suggested that the sign inversion could be related with the cmc, as both effects originate from changes in the solute-solvent interactions. In the last part of this chapter, the obtained

|	C_7G_1	C_8G_1	C_8G_2
formula	$C_{13}H_{26}O_6$	$C_{14}H_{28}O_6$	$C_{20}H_{38}O_{11}$
M [g/Mol]	278.34	292.37	454.51
estimated cmc [mM]	79 [225]	20.4 [230]	19.1 [239]

Table 5.1.: *Characterization of the sugar surfactants under investigation. Refs. [230] and [239] were measured at 25 °C, the temperature of Ref. [225] is unknown.*

data were correlated with literature results, i.e. the hydration number or the second virial coefficient.

5.1. Sample Preparation and Characterization

The sugar surfactants were bought from Glycon (Germany) and a second batch of C_8G_2 was purchased from Sigma-Aldrich (Germany). All products were used without further purification. It is emphasized that each order of surfactants contains only surfactants from one batch. This is pointed out because the *cmc* of different batches for C_8G_1 (see Fig.4.5) differ because Glycon had modified the synthesis.

Tab.5.1 lists the chemical properties of all investigated surfactants. Millipore water was used as solvent. Hellma flow cells with an optical path length of 0.2 mm were used for the measurements in the IR-TDFRS setup. The aqueous surfactant solutions were directly filtered into the sample cell through a PTFE-filter (Roth) with a pore size of 0.2 μm which was two orders of magnitude larger than the estimated size of micelles. The refractive index increments with temperature were determined in a temperature range from 12 °C to 63 °C using Hellma absorption cells with an optical path length of 10 mm.

(a) C_7G_1 (b) C_8G_1 (c) C_8G_2
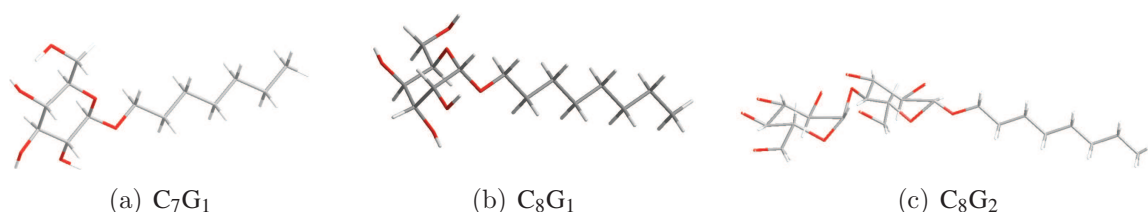
Figure 5.1.: *Molecular structure of the alkyl-polyglucosides under investigation with the sketched hydrogen (white), carbon (grey) and oxygen atoms (red).*
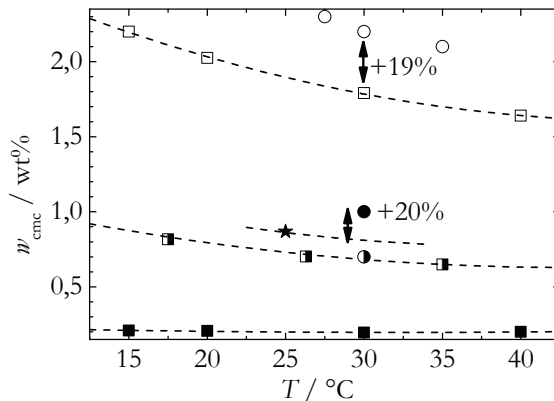
Figure 5.2.: *The* cmc *for* C_iG_j/H_2O *versus temperature. The* cmc *was determined by surface tension measurements (squares) for* C_7G_1 *(open squares),* C_8G_1 *(half-filled squares) and* C_8G_2 *(filled squares). The circles indicate the* cmc *found by IR-TDFRS. The star is a literature value [239]. Dashed lines are quadratic fits.*

5.2. Determination of the cmc

The critical micelle concentration was determined by the group in Köln performing surface tension measurements using the ring-method in a temperature range from 15 °C to 40 °C for C_7G_1 and C_8G_2, and from 17.5 °C to 35 °C for C_8G_1. Fig.5.2 summarizes the *cmc* values. For all surfactants, a continuous decrease of the *cmc* with increasing temperature was observed and a quadratic dependence could be assumed which is typical for nonionic surfactants (see Sec.2.2.1). The highest *cmc* was determined for C_7G_1 (0.02025 wt at 20 °C), followed by C_8G_1 (0.00643 wt at 20 °C) and C_8G_2 had the lowest *cmc* (0.00207 wt at 20 °C). The *cmc* values of C_7G_1 and C_8G_1 were comparable to literature values which are listed in Tab.2.1. In contrast, the determined *cmc* of C_8G_2 was by a factor of four lower than expected. We repeated the determination of the *cmc* for another batch from another manufacturer but found a similar low value. With HPLC-MS we detected some impurities in C_8G_2, which were probably enriched in the interface and led to the much too low *cmc*. A detailed discussion can be found in Appendix E. More details of the surface tension measurements were given by Datta [277]. In this work, the *cmc* values were only used as references to choose the concentration range which had to be investigated in thermal diffusion measurements.

We also calculated the area per surfactant head group in the micelle-solvent interface,

$A_{\min}$, to check whether the number of head group units of the surfactant takes influence on that property. Therefore, we used Eq.5.1 to calculate the maximum surface excess concentration, $\Gamma_{\max}$, at the air-solvent interface

$$\Gamma_{\max} = \frac{1}{2.303nRT} \left(\frac{\partial \gamma}{\partial \log w_{\mathrm{cmc}}} \right)_T \tag{5.1}$$

with the particle density, n, the universal gas constant, R, and $(\partial \gamma / \partial \log w_{\mathrm{cmc}})_T$ is the slope of the surface tension with concentration at constant temperature below the *cmc*. Then, $A_{\min}$ is derived by

$$A_{\min} = (\Gamma_{\max} N_A)^{-1} \tag{5.2}$$

with the Avogadro constant, N_A. We found that $A_{\min}$ increases linearly with increasing temperature. It was indicated that the area per surfactant head group was almost independent from the alkyl chain length for the different glucoside surfactants with slightly larger values for C_7G_1. $A_{\min}$ of the glucoside micelles is in the range between 0.44 nm^2 (15 °C) and 0.48 nm^2 (40 °C). However, we measured much lower values for the maltoside surfactant in the range of 0.35 nm^2 (15 °C) to 0.40 nm^2 (40 °C). The results of the latter surfactant system agree with measurements by Boyd *et al.* [239] who determined an area of 0.42 nm^2 at 25 °C.

Assuming spherical micelles at the *cmc* for all surfactants, we used the determined hydrodynamic radii from IR-TDFRS measurements (they are discussed later) and calculated an aggregation number per micelle of 45 for C_7G_1 ($w = 0.023$ wt, 40 °C), 71 for C_8G_1 ($w = 0.0075$ wt, 40 °C) and 27 for C_8G_2 ($w = 0.01$ wt, 40 °C). The value for C_8G_1 agreed with literature results [211,226,329], those of C_8G_2 agreed with results by Boyd *et al.* [239] and He *et al.* [215].

## 5.2.1. The Soret Coefficient of C_7G_1/H$_2$O Mixtures

All thermal diffusion measurements of the aqueous surfactant solutions were performed in the vicinity of the *cmc* using the IR-TDFRS setup in a temperature range from 15 °C to 60 °C. The concentration range was chosen that it covered the *cmc*, and at least two concentrations above and below in an approximate range between $0.5 \cdot cmc$ and $1.5 \cdot cmc$ were measured.

In Fig.5.3 the temperature dependence of the Soret and diffusion coefficients is shown. In the lower temperature regime the Soret coefficient is below 0.01 K^{-1} and almost the

same for all concentrations within the error bars. A similar behavior was observed for the mass and thermal diffusion coefficient. This indicated that only the surfactant molecules contributed to the thermal diffusion behavior, and all investigated concentrations were below the *cmc* in this temperature regime. At higher temperatures, S_T remained nearly temperature independent for some lower concentrations (0.019 wt and 0.020 wt), while for higher concentrations S_T showed a pronounced change in the slope at 28 °C for 0.023 wt or 36 °C for 0.021 wt. At these temperatures, the Soret coefficient started to increase. This indicated that larger micellar aggregates contributed to the thermal diffusion properties. Because the formation of micelles is a continuous process, it was assumed that the number of micelles increased slowly with temperature above the *cmc* and the influence on the thermal diffusion behavior was continuously strengthened. The existence of micelles at higher temperatures was also observed in the mass diffusion coefficient. Due to a general decrease in viscosity with increasing temperature, D should increase almost linearly with temperature [330,331] as it was indicated by the 0.019 wt sample. In contrast, the samples of higher concentrations showed an almost temperature independent behavior and it was assumed that the increase of D was suppressed by the presence of micelles.

Fig.5.4 shows the concentration dependence of S_T, D_T and D. In this plot, the location of the *cmc* is not so obvious as in Fig.5.3. The Soret coefficient showed a constant and concentration independent behavior for all temperatures below 0.020 wt. Above this concentration, the Soret coefficient, measured at higher temperatures, showed a pronounced increase. For the 60 °C-curve the Soret coefficient increased by a factor of two while below 40 °C the Soret coefficient remained constant at higher concentrations. The mass diffusion coefficient gave only evidence for the *cmc* for the two highest temperatures at 50 °C and 60 °C for which D dramatically decreased between 0.018 wt and 0.02 wt. All other temperature curves indicated equal mass diffusion coefficients which were almost concentration independent. The thermal diffusion coefficient showed no clear concentration dependence behavior.

In Figs.5.5 and 5.6 the hydrodynamic radius is shown in dependence of temperature and concentration, respectively. It should be mentioned that in the vicinity of the *cmc* the determined hydrodynamic radius was not a measure of the size of micelles, but it is an averaged radius of two contributions, which originated from molecules and micelles. At higher concentrations, the micellar contribution prevailed. The determined radii grew with increasing temperature and concentration. Again, for concentrations close to the *cmc* like 0.023 wt, the formation of micelles was indicated by a pronounced increase of the radius at 28 °C from 0.5 nm to 1.3 nm. At higher concentrations above 0.067 wt where the number
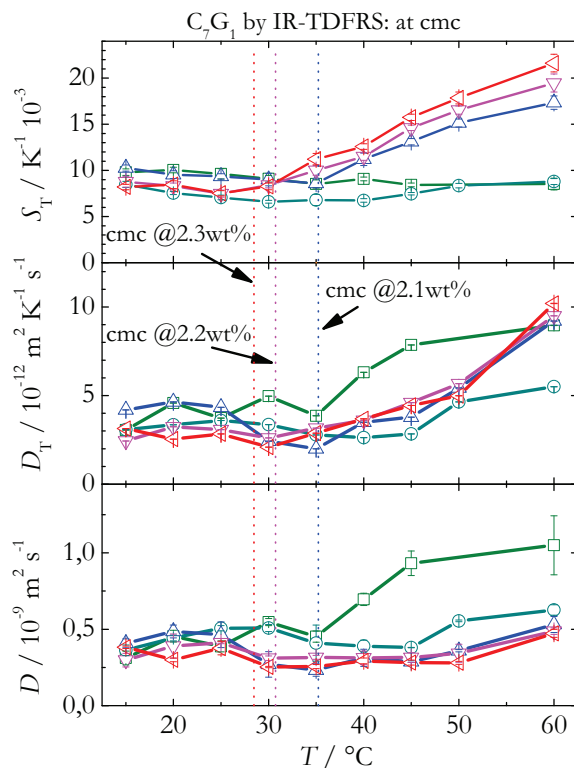
Figure 5.3.: *The Soret, thermal diffusion and mass diffusion coefficients of* C_7G_1/H_2O *versus temperature. The concentrations are close to the* cmc*: 0.019 wt (squares), 0.020 wt (circles), 0.021 wt (triangle up), 0.022 wt (triangles down) and 0.023 wt (triangles left). The determined critical micelle concentrations are marked by vertical dotted lines.*

density of micelles and thus their contribution to the radius was larger, the measured radii of 2.3 nm agreed with the estimated hydrodynamic radius of spherical micelles calculated from the length of a surfactant molecule including a hydrogen layer around the micelle of 0.5 nm. In the higher concentration regime above 0.067 wt, the hydrodynamic radius became almost independent from temperature and concentration. Thus, it was assumed that in the higher concentration regime up to a surfactant mass fraction 12 % an increase in concentration led to an increase in the number density of micelles. Interparticle interaction effects contributing to the thermal diffusion properties [42] were not observed.
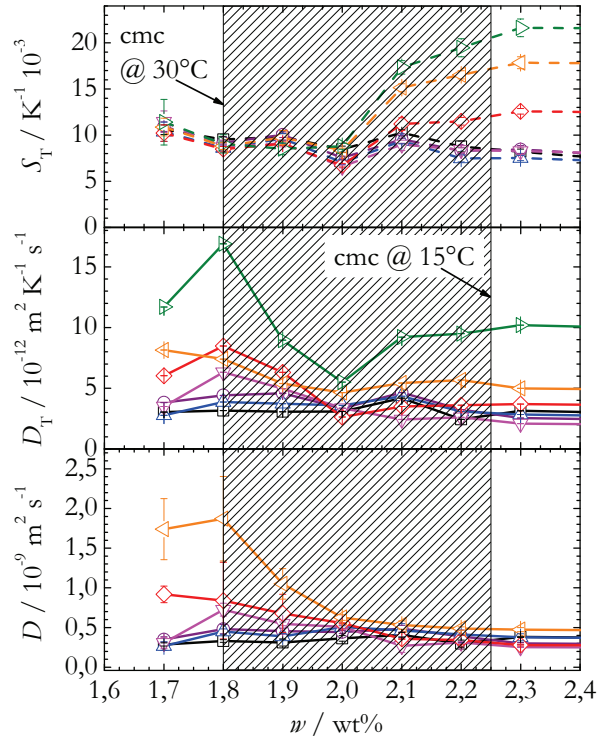
Figure 5.4.: *The Soret, thermal diffusion and mass diffusion coefficients of* C_7G_1/H_2O *versus concentration. The temperatures are 15 °C (squares), 20 °C (circles), 25 °C (triangles up), 30 °C (triangles down), 40 °C (diamonds), 50 °C (triangles left) and 60 °C (triangles right). The shaded area marks the range wherein the* cmc *is found for temperatures between 15 °C and 30 °C.*

5.2.2. Soret Coefficient of C_8G_2/H$_2$O Mixtures

The determination of the *cmc* of the aqueous C_8G_2 system using surface tension methods was problematic, so that we investigated the thermal diffusion properties in a concentration range, which we estimated using literature values. The *cmc* is approximately at 0.0087 wt (25 °C) [239]. We also performed thermal diffusion measurements at concentrations around 0.002 wt, which corresponds to our determined *cmc*.

Fig.5.7 shows the Soret coefficient versus temperature for several concentrations in the vicinity of the *cmc*. For all concentrations, which were expected to lie below the *cmc*, no temperature dependence was observed and the Soret coefficient remained constant at 0.01 K^{-1} which is equal to the values determined for the C_7G_1 and C_8G_1 solutions below the *cmc* in Figs.5.4 and 4.7, respectively. For concentrations above 0.01 wt, S_T showed
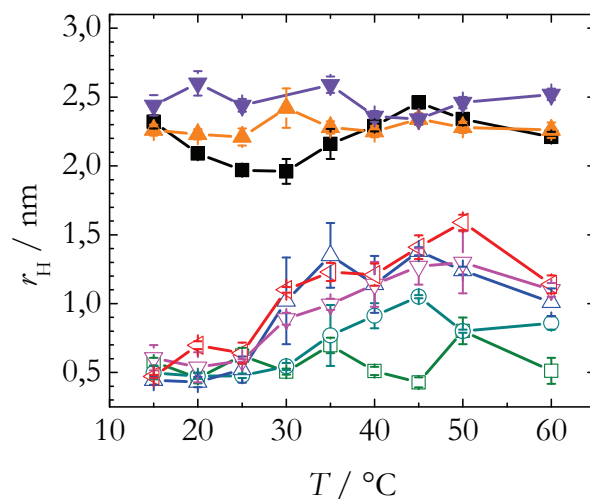
Figure 5.5.: *The hydrodynamic radius versus temperature of* C_7G_1/H_2O. *The concentrations close to the* cmc *are: 0.019 wt (squares), 0.020 wt (circles), 0.021 wt (triangle up), 0.022 wt (triangles down) and 0.023 wt (triangles left). Higher concentration: 0.067 wt (solid squares), 0.069 wt (solid triangles up) and 0.12 wt (solid triangles down).*
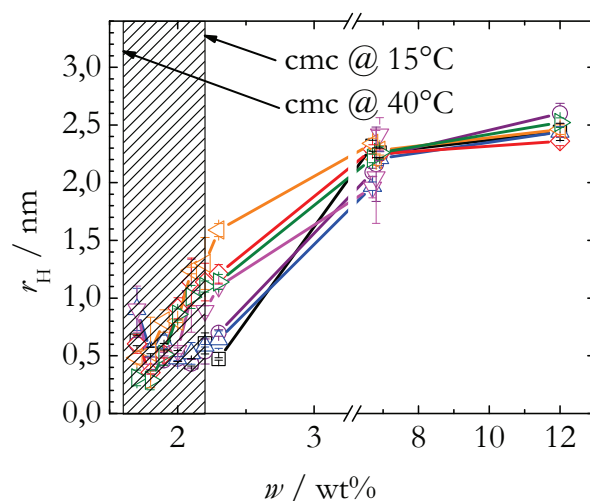
Figure 5.6.: *The hydrodynamic radius versus the surfactant mass fraction of* C_7G_1. *The temperatures are 15 °C (squares), 20 °C (circles), 25 °C (triangles up), 30 °C (triangles down), 40 °C (diamonds), 50 °C (triangles left) and 60 °C (triangles right).*

a pronounced temperature dependence: The Soret coefficient increased with increasing temperature and the slope became steeper with increasing concentration. The two highest
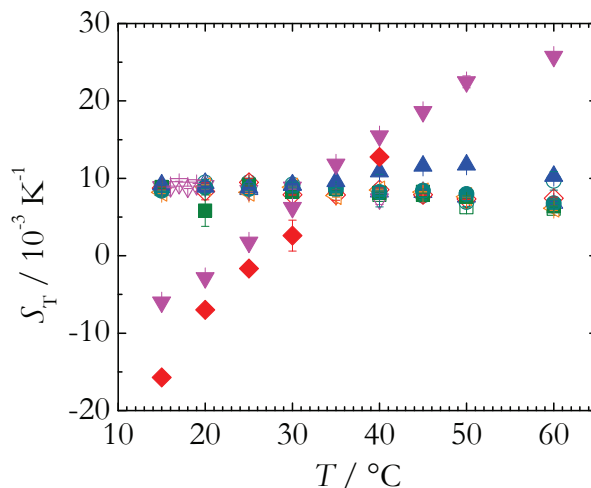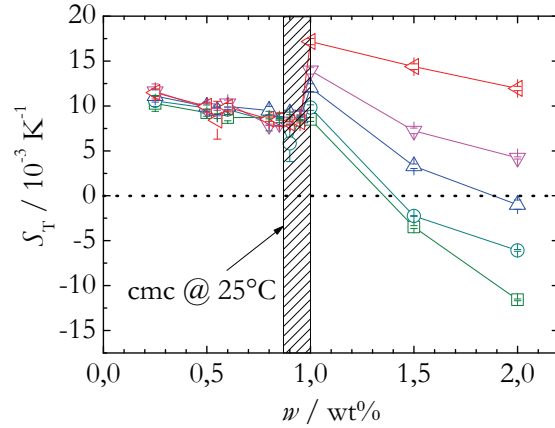
Figure 5.7.: _The Soret coefficient versus temperature of_ C_8G_2/H_2O. _The concentrations are 0.005 wt (open squares), 0.0055 wt (open circles), 0.006 wt (open triangles up), 0.007 wt (open triangles down), 0.008 wt (open diamonds), 0.0085 wt (open triangles left), 0.009 wt (filled squares), 0.0095 wt (filled circles), 0.01 wt (filled triangles up), 0.015 wt (filled triangles down) and 0.02 wt (filled diamonds). Referring to literature values, the filled symbols mark concentrations above the_ cmc _while open symbols represent concentrations below the_ cmc.

concentrations at 0.015 wt and 0.02 wt showed even a sign change of S_T, which will be discussed in Sec.5.3.1.

Fig.5.8 shows the concentration dependence of S_T at different temperatures. Above 0.01 wt, a strong increase of S_T was observed, if the temperature was higher than 25 °C. For lower temperatures, S_T started to decrease. To our best knowledge, this abrupt change of the Soret coefficient indicated the *cmc*. For further increasing concentration, S_T decreased slightly and changed sign from positive to negative for temperatures below 25 °C in this concentration regime (see Sec.5.3.2).

5.3. Sign Inversion Behavior

All sugar surfactants showed a sign inversion of S_T and D_T above the *cmc* at low temperatures. In the following, the temperature and concentration dependence of the sign inversion will be discussed.

Figure 5.8.: *The Soret coefficient versus the surfactant concentration of* C_8G_2/H_2O. *The temperatures are* 15 °C *(squares),* 20 °C *(circles),* 25 °C *(triangles up),* 30 °C *(triangles down),* 40 °C *(triangles left).*

5.3.1. Sign Inversion in a Temperature Dependence

In Fig.5.9 the temperature dependence of the Soret and the diffusion coefficients of C_7G_1 is shown. For all concentrations the sign inversion from negative to positive with increasing temperature occurred. The sign inversion temperature is almost the same for the investigated concentrations and was slightly below 30 °C. The Soret coefficient indicated that it approaches a constant value at infinite temperatures. A similar result was found for C_8G_2 (Fig.5.7) and C_8G_1 (Fig.4.11) but in these systems, the sign inversion temperature spreads over a temperature range of approximately 5 K in the investigated concentration range.

The comparable thermal diffusion behavior of the three investigated sugar surfactants led to the question, if these properties could be described using a general expression. Iacopini *et al.* [33, 64] introduced an empirical function to describe the sign inversion temperature dependence:

$$S_{\mathrm{T}}(T) = S_{\mathrm{T}}^{\infty}(T) \left(1 - exp\left[\frac{T^{\pm} - T}{T_0} \right] \right) \tag{5.3}$$

where S_{T}^{∞} is the Soret coefficient at high temperatures, $T^{\pm}$ is the sign inversion temperature and T_0 is a measure for the strength of temperature effects. Eq.5.3 was not applicable for the sugar surfactant systems because at high temperatures deviations from the estimated master curve occurred such that the data points referring to C_7G_1/H_2O were much
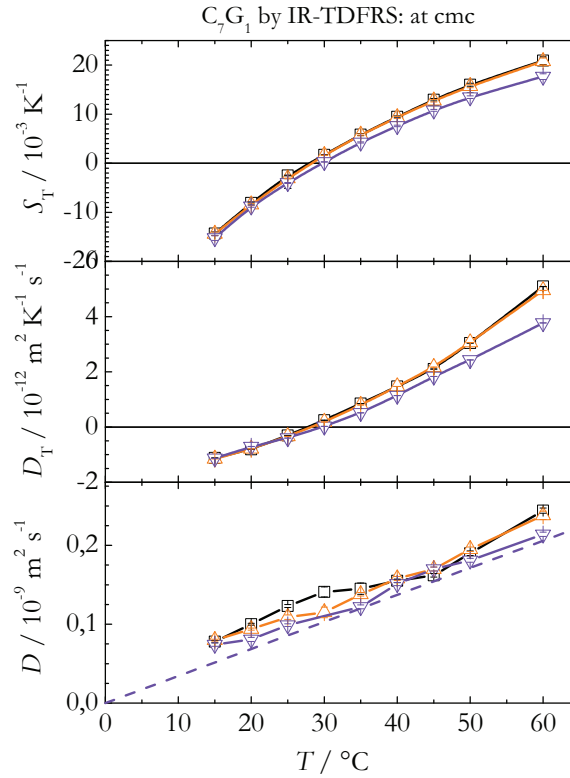
Figure 5.9.: *The Soret coefficient of C_7G_1/H_2O solutions versus temperature. The concentrations are: 0.067 wt (squares), 0.069 wt (triangles up) and 0.12 wt (triangles down). Dashes lines are guides to the eye.*

larger and data points referring to the C_8G_1/H_2O system lay below the master curve (see inset of left Fig.5.10). In contrast, the plot of the (non-normalized) Soret coefficient versus the normalized temperature showed a less pronounced data spreading below 10 % (see left Fig.5.10).

A different approach was introduced, which considers the product of the Soret coefficient and the temperature. The product is the thermal diffusion factor $\alpha_T = TS_T$. In the right plot of Fig.5.10 α_T is plotted versus the normalized temperature, $T/T^{\pm}$, and a good correlation among the investigated surfactant solutions was found within the error bars which are not shown for clarity.
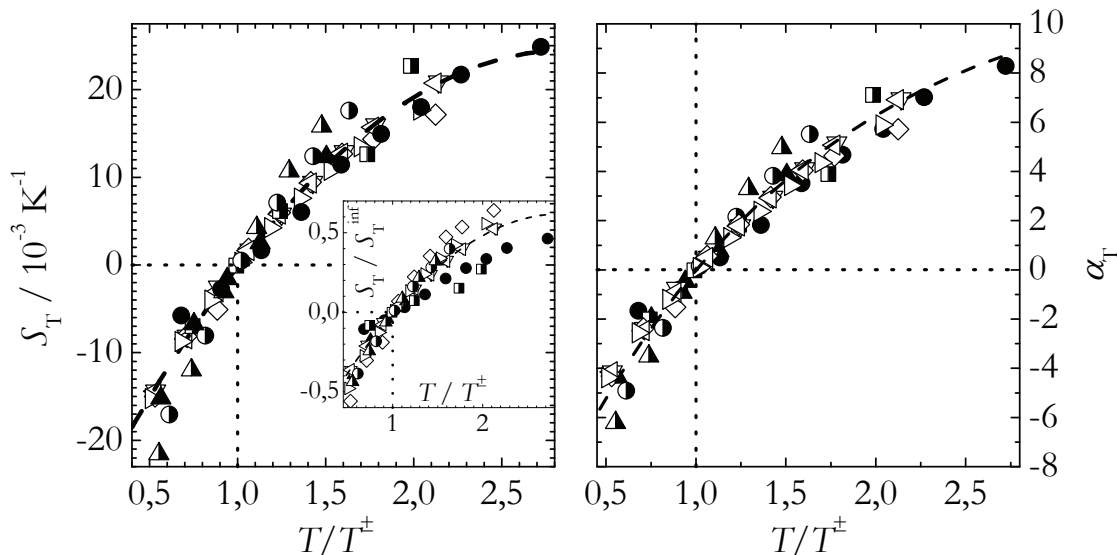
Figure 5.10.: Left: *The Soret coefficient of all investigated sugar surfactant solutions versus the normalized temperature. Inset: normalization using the empirical Eq.5.3 [48].* **Right:** *The thermal diffusion factor versus the normalized temperature. The dashed line marks the averaged master curve. The sign change of α_T occurs at $T/T^{\pm} = 1$.*

5.3.2. Sign Inversion in a Concentration Dependence

As already discussed (c.f. Figs.4.3.3 and 5.8) the Soret coefficient decayes generally with concentration for surfactant mass fractions which were much higher than the *cmc*. The decrease became steeper with decreasing temperature. At a certain concentration, $w_{\pm}$, S_T turned from positive to negative. The sign change concentration shifts to lower concentrations if the temperature is decreased. For instance for the C_7G_1 system, $w_{\pm}$ was shifted from 0.06 wt (25 °C) to 0.04 wt (15 °C).

It was assumed that to a certain extend the sign inversion should correlate with the *cmc* as both effects originate from solute-solvent interactions. Therefore, the Soret coefficient and concentration were scaled by

$$S_T{}^*(T) = S_T(T)/S_T{}^{w,inf}(T) \quad \text{and} \quad w^*(T) = w/w_{cmc}(T) , \qquad (5.4)$$

with the Soret coefficient at infinite concentrations, $S_T{}^{w,inf}$, and the critical micelle concentration, w_{cmc}. Normalized values are superscripted with a star. Eq.5.4 allowed to
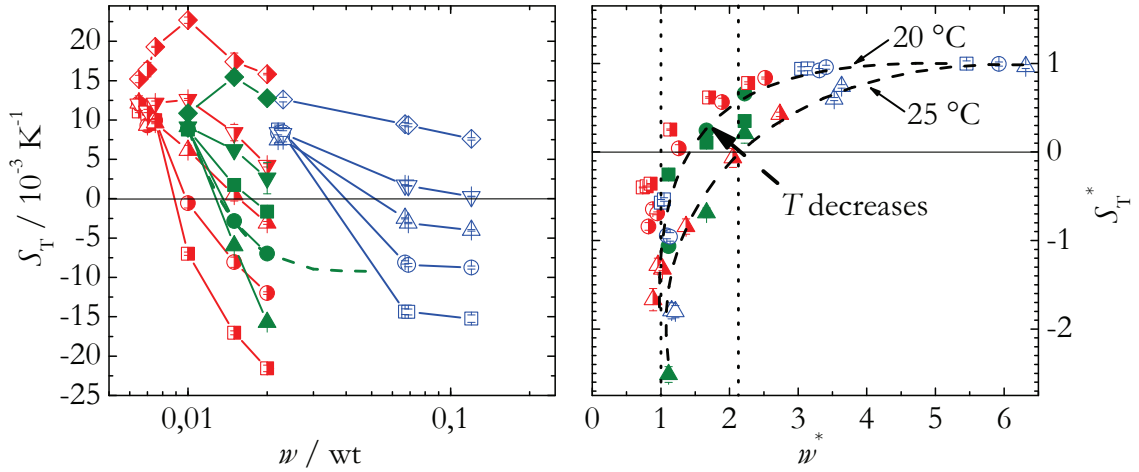
Figure 5.11.: *Left: Comparison of S_T versus the surfactant concentration. The surfactants: C_7G_1 (open, blue), C_8G_1 (open-filled, red), C_8G_2 (filled, green). Temperatures: 15 °C (squares), 20 °C (circles), 25 °C (triangles up). **Right:** The normalized Soret coefficient versus the concentration in scales of the* cmc.

express the concentration as a multiple of the critical micelle concentration, and S_T was normalized with respect to an infinite value at high concentrations. $S_T^{w,inf}$ was obtained by an exponential fit to the $S_T(w)$-curves (dashed line in the left plot of Fig.5.11).

In the left plot of Fig.5.11 the investigated surfactant systems are compared by means of their Soret coefficient which was measured at concentrations above the *cmc*. These data were normalized using Eq.5.4 and are shown in the right plot of Fig.5.11: All measured Soret coefficients of the surfactant systems lay on isotherms. The normalization forced these isotherms to start at $w^* = 1$ at low values of S_T^*, and to end in the high concentration regime at $S_T^* = 1$. Regarding the isotherm at 20 °C or 25 °C, it was observed that the isotherm of the lower temperature converged faster against S_T^*. This confirmed also the previous observation that the sign inversion occurred at lower concentrations if the temperature was lower. For instance by decreasing the temperature by 10 K the sign inversion concentration was almost halved. The normalization of the concentration also indicated that the ratio $w_\pm/w_{cmc}$ is almost equal for the investigated sugar surfactant systems under isothermal conditions.

# 5.4. Dependence on the Ratio of Viscosity and Thermal Expansion Coefficient

For aqueous solutions of monosaccharides and oligosaccharides, the thermal diffusion coefficient depends linearly on the ratio between the thermal expansion and the kinematic viscosity [60, 332, 333]. Also theoretically a linear relation between D_T and α_V is expected [334]. The viscosity, η, and the thermal expansion coefficient, α_V, are parameters which characterize the solvent [335, 336].

The question arose if also the surfactant systems under investigation show a similar behavior in the micellar state above the *cmc*. This might be reasonable, as the surfactant systems are to a certain extend comparable to the sugar systems, because the surfactant micelles interact with the solvent via the glycoside head group units. The viscosity (using a Anton Paar AMVn viscometer), density (using a Anton Paar DMA 4500 densimeter) and thermal expansion coefficient of the C_7G_1/H_2O system were determined for several concentrations from 2.1–12 wt%. The IR-TDFRS measurements indicated that for equimolar concentrations, the hydrodynamic radii of the micelles did not change with temperature (left plot in Fig.5.12) except at the *cmt*. On the other hand, we know that with increasing temperature, the hydrogen bonds break. Hence, the temperature was used as a tool to tune the micelle-solvent interactions.

The right plot in Fig.5.12 shows the thermal diffusion coefficient as a function of the ratio between the thermal expansion coefficient and the viscosity for several concentrations of C_7G_1. A linear dependence of D_T on the ratio of α_V/η was found for the low concentrated systems above the *cmc*. For the highest measured solution at 12 wt%, deviations from the linearity are observed. A similar observation has been made for sugar solutions, so that we assume, that interactions are responsible for the deviations.

5.5. Comparison with Literature Results

The most investigated sugar surfactant is C_8G_1. Other sugar surfactants were rarely investigated. Therefore, this section will emphasize on two interesting studies on C_8G_1/H_2O systems which were assumed to shed some light on the observed sign inversion of the Soret coefficient. Unfortunately, these studies did not investigate the entire temperature and
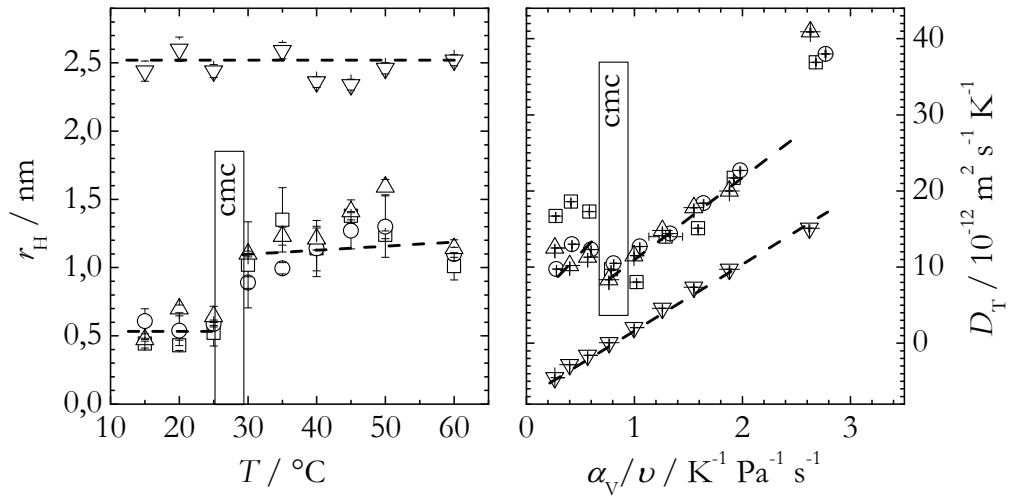
Figure 5.12.: Left: *The hydrodynamic radius versus temperature of* C_7G_1/H_2O *for the concentrations: 2.1 wt% (squares), 2.2 wt% (circles), 2.3 wt% (triangles up) and 12 wt% (triangles down). The white box marks the* cmc *for the three lowest concentrations.* ***Right:*** *The thermal diffusion coefficient versus the ratio* α/ν *of* C_7G_1/H_2O *in a concentration range between 2.1 wt% and 12 wt%.*

concentration range of this work so that the following discussion needs a to be critical scrutinized.

Kameyama and Takagi [212] reported a sign change of the second virial coefficient for C_8G_1 for a concentration slightly above the *cmc* at 1.2 wt% from negative to positive with increasing temperature. The sign change temperature was found at 38 °C. The virial coefficient is directly related to the intermolecular potential [337]. A positive virial coefficient indicates repulsion and a negative attractive interaction potentials [338], respectively. Thus, a change in the virial coefficient indicates changes in the particle-solvent interactions. In the case of the investigated surfactant systems, it was assumed that these are micelle-solvent interactions. To compare our thermodiffusion measurements with the findings by Kameyama and Takagi, we had to separate the micellar contribution of the Soret coefficient, $S_T{}^{mic}$, from the molecular contribution, $S_T{}^{mol}$, like:

$$S_T = S_T{}^{mol} + S_T{}^{mic} . \tag{5.5}$$

Then, $S_T{}^{mic}$ of C_8G_1 was plotted versus the micelle concentration, $w - w_{cmc}$, in Fig.5.13. $S_T{}^{mic}$ changed sign at a micelle concentration of 1.35 wt% and a temperature of 34 °C which agreed with the sign change of the virial coefficient at 1.2 wt% (38 °C) within the error bars.

In a second discussion, we shed some light on the micelle-solvent interface. It was reported that the hydrophilic head group of the sugar surfactants allows high hydration numbers per head group. Pastor *et al.* [317] determined the hydration number, n_h, for C_8G_1 solutions at 25 °C in a concentration regime close to the *cmc*. The bottom plot in Fig.5.14 shows their results: Below the *cmc*, the hydration number per molecule is 16 and independent from concentration. Above the *cmc*, where some surfactant molecules are assimilated into micelles, the hydration number decreases. This is caused by the preferential hydrogen bonding of the bonded surfactant molecule in a micelle with its neighboring surfactant molecules rather than with the water molecules. We compared the hydration number with the Soret coefficient. In the top plot of Fig.5.14, the concentration dependence of the Soret coefficient, also measured at 25 °C, is shown. It was observed that S_T and the hydration number showed almost the same trend in the investigated concentration regime. A sign inversion of S_T was observed at a concentration, where the hydration number had decayed to the half of the initial value at the *cmc*. A parametric plot of n_h and S_T indicated a quadratic dependence (inset in Fig.5.14).

Finally, this comparison confirmed the assumption that the Soret coefficient changes sign
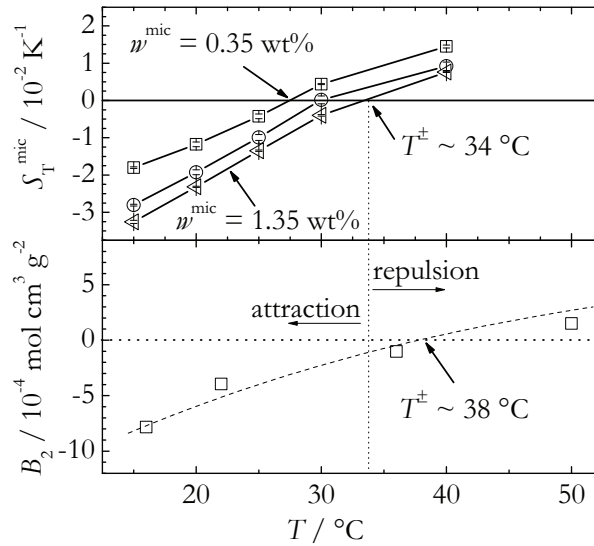
Figure 5.13.: *Top: The micelle-micelle contribution of the Soret coefficient, $S_T - S_T^{mol}$, versus the concentration of micelles, $w - w_{cmc}$. The sign change is approximately at 34 °C which correlates with the sign change of the second virial coefficient determined by Kameyama and Takagi [212] for a 1.2 wt% sample at 38 °C (bottom).*

from negative to positive when the solvent quality becomes bad, because a change in the solvent quality also causes the decrease of hydrated water molecules per surfactant molecule.

5.6. Conclusion

Surface tension measurements were used to determine the *cmc* of three sugar surfactants. The measurements produced reliable results for C_7G_1 and C_8G_1 but failed for C_8G_2. Comparing the *cmc* of C_7G_1 and C_8G_1, it was indicated that the temperature dependence of the *cmc* is more pronounced with decreasing carbon chain length.

Then it was shown that the determined *cmc* is visible in TDFRS measurements by an abrupt change of the Soret coefficient which is caused by the influence of micelles on the thermal diffusion behavior. In the temperature dependence, a pronounced change in the slope of S_T at the *cmc* was observed, while in the concentration dependence S_T showed an abrupt change. Below the *cmc* the Soret coefficient was almost independent from temperature or concentration in the molecular regime. It turned out that the *cmc*,
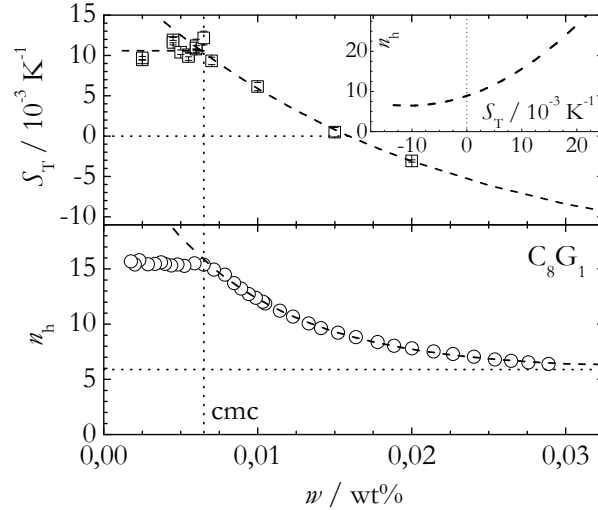
Figure 5.14.: *Top: The Soret coefficient versus the concentration determined by IR-TDFRS. Bottom: The hydration number per surfactant molecule versus the concentration by Pastor [317]. Inset: The hydration number depends quadratically on the Soret coefficient. Dashed lines are fits, dotted lines are guides to the eyes.*

determined by surface tension measurements, was approximately 20 % lower than the *cmc* measured in TDFRS. This was reasonable since in TDFRS we measured in the bulk phase and detected the contribution of the formed micelles, whereas the surface tension measurements determined the wetting of the surface. Although it was not possible to determine the *cmc* of C_8G_2 by surface tension measurements, we observed a pronounced change in the thermal diffusion behavior at 0.01 wt which was approximately 20 % higher than the literature value at $T = 25\,°C$. Regarding the impurities in C_8G_2 (see also App. E), we expected that they were surface-active, rather nonionic than ionic, and did not alter the thermal diffusion properties in the bulk phase. Unfortunately, the TDFRS data did only allow to identify a temperature dependence of the *cmc* for the C_7G_1 solutions.

Above the *cmc*, the concentration dependence of the Soret coefficient was different for the low temperature and the high temperature measurements. The dramatic increase of S_T with increasing concentration was only observed for temperatures above 25 °C, while below this temperature, S_T decreased above the *cmc*. This might be reasonable by a lowered solvent quality at lower temperatures. Also the sign inversion concentration was shifted to lower concentrations if the temperature was lower. The sign change could be attributed to a decrease in the solvent quality, which was also indicated by an decrease of

the hydration number with concentration by Pastor *et al.* [317]. A comparison with the second virial coefficient indicated that at the sign inversion the interaction forces turned from attraction ($S_\mathrm{T} < 0$) to repulsion ($S_\mathrm{T} > 0$).

An empirical approach was found, to describe the temperature dependence of the S_T sign inversion by a master curve using a dimensionless temperature and the thermal diffusion factor, α_T. Previously introduced empirical approaches by Iacopini *et al.* were not successful.

It was also demonstrated that the sign inversion concentration was, to a certain extend, correlated with the *cmc*. By normalizing of the Soret coefficient and expressing the concentration in scales of the *cmc*, isotherms were obtained. They indicated that at constant temperature the ratio between the *cmc* and the sign inversion concentration was almost the same for the investigated sugar surfactant systems.

SIX

MICROEMULSIONS AS MODEL SYSTEMS FOR SPHERES

We use microemulsion droplets as hard-sphere particles to investigate the radial dependence of the Soret coefficient. These droplets can be easily varied in size and shape by concentration and temperature, respectively. Thus, by changing physical parameters, we tune the droplet style while keeping the surface properties untouched. This is the general advantage in comparison to synthesized colloidal particles for which it is not possible to reproduce the same grafting or charge density of the colloidal particle. Therefore, the behavior of the colloidal particles is not solely influenced by a change in radius, but also by the surface properties of the colloid. The radial dependence of S_T of colloidal particles has already been studied by several authors [65–67,99]. Presently it is discussed whether the Soret coefficient depends linearly or quadratically on the particle radius.

A quadratic dependence was observed by Duhr and Braun [65], linear scaling properties are found by Putnam and Cahill [67] for an aqueous solution of carboxyl functionalized polystyrene (PS) spheres and proteins of T4 lysozyme using a microfluidic beam deflection technique. Also Vigolo *et al.* [35] obtained a linear dependence investigating microemulsion droplets with ionic dioctyl sodium sulfosuccinate (AOT) as surfactant, as well as Braibanti *et al.* [66] for polystyrene spheres in 1 mM Tris-HCl buffer. A review was written by Piazza and Parola [99]. Recently, Vigolo *et al.* [33] observed a linear dependence of the thermophoretic mobility, D_T, versus the Debye length for sodium dodecyl sulfate (SDS) solutions. Theoretical approaches are given by Würger [339] predicting a linear radial dependence for solid particles and a quadratic one for soft particles.

type	molecular weight [g/mol]	refractive index	boiling point [°C]	freezing point [°C]
n-octane (C_8)	114.23	1.3974	125.8	-56.8
n-decane (C_{10})	142.28	1.4113	174.1	-29.7
n-dodecane (C_{12})	170.34	1.4212	216	-10
n-tetradecane (C_{14})	198.39	1.428	254	5.5
water	18.02	1.333	100.0	0
$C_{12}E_5$	406.60	$1.452^{\oplus}$	$202\text{-}216^{\oslash}$	–

Table 6.1.: *Characterization of the used chemical products. Values are taken from: ($\oplus$) Binks et al. [342], ($\oslash$) Bergh et al. [343].*

6.1. Experiment and Data Analysis

6.1.1. Sample Characterization

We used ultrapure Milli-Q water (Millipore, USA). The surfactant monododecyl pentaethylene glycol ($C_{12}E_5$) was purchased from Nikkol with a purity $> 98\%$. As hydrophobic component, we chose n-alkanes: n-octane, n-decane, n-dodecane and n-tetradecane. All n-alkanes are products of Sigma-Aldrich with a purity $\geq 98\%$. The n-alkanes and the nonionic surfactant $C_{12}E_5$ were used without further purification. Before the mixtures were prepared, the surfactant was tested for contamination by determining the cloud point. We determined the cloud point of $T_{cp} = (31.40 \pm 0.05)$ °C which agrees with values given by Schubert *et al.* [340] who determined a cloud point temperature of 32.0 °C. This indicates that impurities are negligible.

The refractive indices, boiling and freezing points of the used substances are given in Tab.6.1. The refractive index of the n-alkanes and surfactant is higher than the refractive index of water, which results in a sufficient contrast in the TDFRS experiments if o/w-microemulsions are investigated. The solubility of the n-alkanes in water is negligible: n-octane has the highest solubility of 0.7 mg/l (20 °C [341]). With increasing alkyl chain length the solubility decreases.

Hellma flow cells with an optical path length of 0.2 mm were used in classical TDFRS and IR-TDFRS. The microemulsions were directly filled into the cell. The mixtures were thermostated beforehand in a temperature controlled water bath ($\Delta T = \pm 0.1$ K) for several hours under continuous stirring to ensure that the microemulsions are in the 1ϕ state.

| system $H_2O/C_x/C_{12}E_5$	w_B [wt]	w_0 [wt]	ϕ_0 [vol%]	T_{efb} [°C]	T_{ncb} [°C]
C_8	0.0600	0.0882	10.50	27.54	29.43
$C_{8/10}$ (75/25)	0.0505	0.0789	9.78	27.85	30.32
$C_{8/10}$ (50/50)	0.0444	0.0731	8.98	27.42	30.95
C_{10}	0.0290	0.0581	6.90	27.31	32.24
C_{12}	0.0175	0.0470	5.35	27.85	34.78
C_{14}	0.0131	0.0427	4.76	27.93	35.74

Table 6.2.: *Determination of the* efb *and* ncb *temperatures for each microemulsion system for a given oil concentration, w_B. The droplet concentration, w_0 in mass fraction or ϕ_0 in volume fraction, results from the additional amount of water in the microemulsion.*

The water bath temperature was set to a value which corresponds to a temperature in the 1ϕ funnel on the water-rich side of the phase diagram close to the *efb*. In a controlled temperature environment, the mixture was transferred into the thermal equilibrated flow cells. To ensure that the sample was still in the 1ϕ regime, we measured the scattered light intensity in the IR-TDFRS setup which is by magnitudes higher once the sample has entered the upper or lower 2ϕ region.

6.1.2. Determination of the Phase Transition Boundaries

As already illustrated in Fig.2.4 and Fig.6.1 the phase diagram of microemulsions studied via a $T(w_B)$-section through the phase prism is characterized by a 1ϕ funnel which is confined by the lower *efb* and the upper *ncb*. For temperatures below the *efb* in the $\underline{2}\phi$ region a microemulsion phase coexists with an oil excess phase, while at higher temperatures the *ncb* delimits the 1ϕ region. Above this boundary different phases can be found which are defined here as $\overline{2}\phi$ phase.

In order to determine the temperature-oil concentration dependence $(T(w_B))$ of the *efb* and *ncb* we investigated the phase transition from 2ϕ to 1ϕ as it is described in the following: In the case of the *efb*, we kept the sample at $T < T_{efb}$ in the $\underline{2}\phi$ region in a water bath, whereas the temperature inside the water bath was measured directly at the sample holder. The sample was equilibrated in the water bath at constant temperature and continuous stirring for four minutes (long-chained *n*-alkane solutions: eight minutes) and then we checked visually if the sample was in 1ϕ or 2ϕ. Was the sample still in the $\underline{2}\phi$ region we increased the temperature further until we reached the 1ϕ region. If
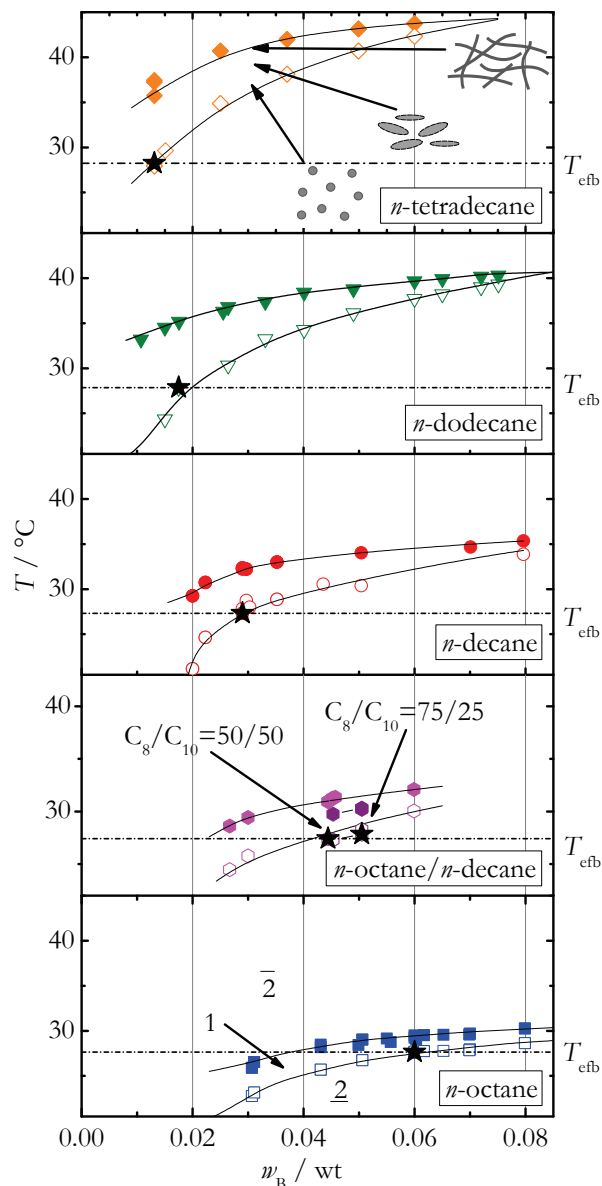
Figure 6.1.: *Determination of the 1ϕ regions of the microemulsions under investigation of the type $H_2O/C_x/C_{12}E_5$ on the water-rich side with $\gamma_a = 0.03$ wt. The temperature is plotted versus the n-alkane concentration, w_B. The points mark measured phase transition temperatures, the lines are guides to the eyes. The stars represent the concentrations at similar efb temperatures which are given in Tab.6.2 and were taken for the IR-TDFRS measurements. From top to bottom: n-tetradecane ($w_B = 0.0131$ wt), n-dodecane ($w_B = 0.0191$ wt), n-decane ($w_B = 0.029$ wt), mixtures of n-octane/n-decane in a 50/50-ratio ($w_B = 0.0444$ wt, lilac) and in a 75/25-ratio ($w_B = 0.0505$ wt, purple), and n-octane ($w_B = 0.060$ wt), respectively. The mixed n-alkane systems had a ratio of 50/50 (lilac) and 75/25 (purple).*
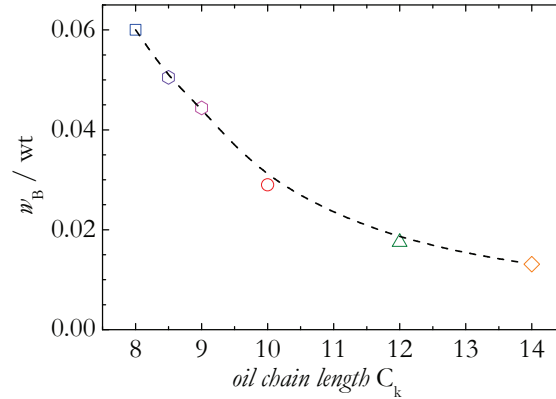
Figure 6.2.: *The* k-*alkane mass fraction* w_B *is plotted versus the carbon chain length of the* k-*alkanes at the determined* efb *temperature (see Tab.6.2). The data points at* $C_k = 9$ *and* $C_k = 8.5$ *are mixed alkane systems with a mass ratio of 50/50 and 75/25 of* n-*octane and* n-*decane. Symbols are used as given in Fig. 6.1.*

the last temperature step was larger than $\Delta T = 0.1$ K, we had to bring the sample back into $\underline{2\phi}$ region and to restart with smaller temperature steps. The sample was quickly cooled down to $T = -17$ °C and then warmed up to a temperature within the $\underline{2\phi}$ region. Sometimes this freezing procedure had to be repeated several times for the long-chained n-alkane systems, until the sample entered the $\underline{2\phi}$ region.

This way, we approached the *efb* temperature iteratively and determined the transition temperature with an accuracy of $\Delta T = \pm 0.15$ K. The *ncb* was determined in a similar way starting in the $\overline{2\phi}$ region and lowering the temperature till the *ncb* was reached.

Fig.6.1 shows the funnels on the water-rich side for four different pure n-alkanes and two n-alkane mixtures. With deceasing chain length of the n-alkane the funnel become narrower and the funnel shifts towards a higher oil content. Hence, the accessible temperature range in the 1ϕ-region shrinks with decreasing chain length of oil component, which complicates the measurements for short n-alkanes. For n-octane the funnel width is only 2 K at $w_B = 0.060$ wt. As can be seen in Fig.6.2 the n-alkane concentration is being reduced by a factor of two, when chain length is increased by two C-atoms under the condition to find the *efb* at the same temperature.

6.1.3. General Considerations about the Characterization of the Microemulsion Droplets

In order to study the radial dependence of the microemulsion droplets we need to be sure to have spherical aggregates. The question is how close do we have to select the temperature to the *efb* in order to measure and work with spherical microemulsion droplets. On the oil-rich side the formation of network like structures leads to a pronounced increase in the conductivity [344]. Comparing with electric conductivity measurements [344] in microemulsions it seems to be reasonable to assume that the transition between spheres and cylindrical networks occurs in the first third of the temperature range between the *efb* and *ncb*.

We define our measurement range in the first third of the temperature range between the *efb* and the *ncb*, in which the spherical microemulsion droplets should dominate the behavior. Therefore, all measurements have been performed between $^1/_3\left(2T_{\mathrm{e}fb}+T_{\mathrm{n}cb}\right)$ and $T_{\mathrm{e}fb}$ which describes the first third of the 1ϕ funnel close to the *efb*. The data at the *efb* are obtained by extrapolation of measurements at different temperatures in the chosen temperature range. Analyzing the dynamic light and static neutron scattering experiments, we will later see, that the range depends on the *n*-alkane or rather on the distance to the tricritical point (c.f. section 6.3.1 and 6.3.3).

6.1.4. Refractive Index Increments

For the determination of the refractive index increments with temperature, $(\partial n/\partial T)_{p,w}$, Hellma absorption cells with an optical path length of 10 mm were used in the improved Michelson interferometer. The change in temperature was approximately 0.5 mK/s such that the microemulsion during the measurement was in thermal equilibrium. We repeated the measurements four times for each sample. During the measurement, the microemulsion was always in the 1ϕ state. A possible phase transition could instantaneously be observed by a decrease of the transmitted intensity.

The refractive index increment with concentration, $(\partial n/\partial w)_{p,T}$, was calculated from refractive index values, which were determined by an Abbe refractometer (Anton Paar, Austria). We determined the refractive index for a given concentration $w_{\mathrm{B},0}$ at several temperatures within the 1ϕ regime. The relevant concentration, w, to determine $(\partial n/\partial w)_{p,T}$, is the mass fraction of the oil component, $w_{\mathrm{B},0}$, because the surfactant concentration is

kept constant. As illustrated in Fig.3.9 a direct measurement of the refractive index values at higher oil mass fractions, $w_{B,0+\delta}$, is not possible, because the system phase separates. The maximal δ is in the order of 0.01 wt, whereas other concentrations are in between $w_{B,0}$ and $w_{B,0+\delta}$. To overcome this problem, measurements of the refractive index values have to be extrapolated from measurements of the refractive index increments in the 1ϕ regime which were measured at higher temperatures at the concentration $w_{B,0+\delta}$. The concentration below $w_{B,0}$ can be measured directly at the desired temperature and do not need to be extrapolated.

We observed that the thermodynamical inhibition of the microemulsion systems had a pronounced influence on the refractive index measurements: The sample took several minutes to equilibrate after changing the temperature in the refractometer. On the other hand, we had to minimize evaporation during the measurements by shortening the waiting time. To satisfy both demands, we worked with a sealed sample container and selected a minimum equilibration time until the refractive index was constant. To examine whether the sample suffers from evaporation during the measurement, we re-measured the first temperature at the end of a run and corrected the obtained refractive index data proportionally by this difference, if necessary. Each series was repeated three times.

To check whether the extrapolation of the refractive indices at higher concentrations $w_{B,0+\delta}$ yields higher error, we compared the calculated $(\partial n/\partial w)_{p,T}$-values with a theoretical approach by Kerker [345], which is a prediction for a simple coated sphere of oil-swollen droplets. This approach is based on the dielectric constant, ε, which is connected to the refractive index by $\varepsilon_i = n_i^2$ where i denotes the components water (A), oil (B) and surfactant (C). Our experimentally determined values agreed with the theoretical values within an averaged error of approximately 3.8 %.

6.2. S_T of the n-octane Microemulsions

We investigated the Soret coefficient of n-octane microemulsion systems at constant surfactant to water ratio $\gamma_a = 0.022$ wt in the 1ϕ region of the phase diagram as it is shown in Fig.6.3. The temperature and the oil mass fraction were varied.

IR-TDFRS measurements have been performed in such way, that the measurement started at a certain temperature where the mircoemulsion is found in the 1ϕ state. In a series of measurements, the temperature was lowered stepwise towards the *efb* temperature. The dependence of the measured Soret coefficient on the temperature is shown in Fig.6.4. At
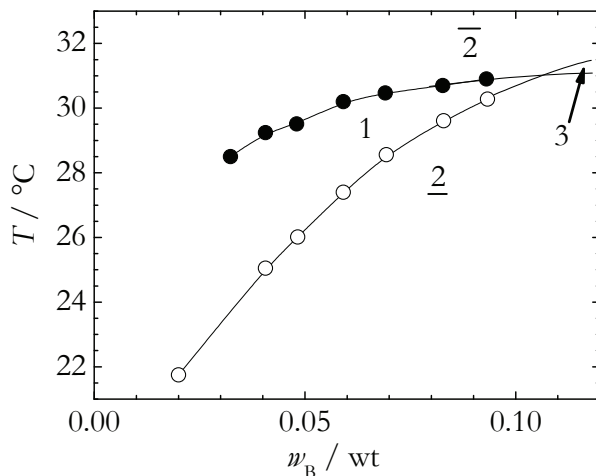
Figure 6.3.: *The 1φ region on the water-rich side of the phase diagram of the* $H_2O/C_8/C_{12}E_5$ *microemulsion with* $\gamma_a = 0.022$ *wt.*

higher temperatures, the Soret coefficient diverged exponentially towards the *ncb* as the formation of network-like structures leads to slower diffusion processes. By decreasing the temperature, the Soret coefficient decreased and approached a plateau value at the *efb*.

In principle it is possible to study the radial dependence of S_T of a microemulsion, if one moves along the *efb* as depicted in Fig.6.3 for the system $H_2O/C_8/C_{12}E_5$ by varying concentration and temperature, respectively. If one moves close to the *efb* the microemulsion droplets are assumed to be spherical [346, 347] and their radius will increase with increasing oil fraction. But apart from the size change, also the temperature will change. Both effects will influence the Soret coefficient and it will be difficult to distinguish between both effects. Fig.6.5 shows the Soret coefficient extrapolated to the *efb* as function of the hydrodynamic radius, which was determined from the diffusion coefficient in the IR-TDFRS experiment using the Stokes-Einstein relation, in doing so interactions between the droplets are negelcted. The description with a linear fit is rather pure taking into account the small investigated radial range from 11.6 nm to 33.9 nm, indicating that the neglect of changes of interactions and interfacial tension might not be justified.

From other studies of aqueous systems [62, 153] we know that specific interactions such as hydrogen-bondings can influence the thermal diffusion properties strongly and even leads to sign changes of S_T. Also C_iE_j in H_2O shows dehydration effects with increasing temperature [348–350], therefore we expect also a temperature effect on S_T, if we study the radial dependence along the *efb*. Therefore, if we want to modify the radius, we need
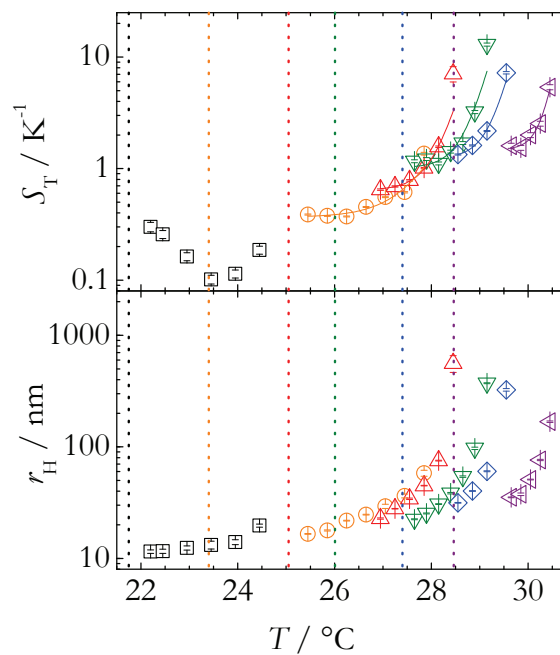
Figure 6.4.: *The Soret coefficient (top) and the hydrodynamic radius (bottom) are plotted versus the temperature for $H_2O/C_8/C_{12}E_5$ microemulsions in the 1ϕ region determined by IR-TDFRS. Concentrations: $w_\mathrm{B} = 0.02$ wt (black squares), $w_\mathrm{B} = 0.03$ wt (orange circles), $w_\mathrm{B} = 0.04$ wt (red triangles top), $w_\mathrm{B} = 0.05$ wt (green triangles down), $w_\mathrm{B} = 0.06$ wt (blue diamonds), and $w_\mathrm{B} = 0.07$ wt (purple triangles left). The* efb *temperatures of the different microemulsions are sketched as vertical dotted lines in the respective colors.*
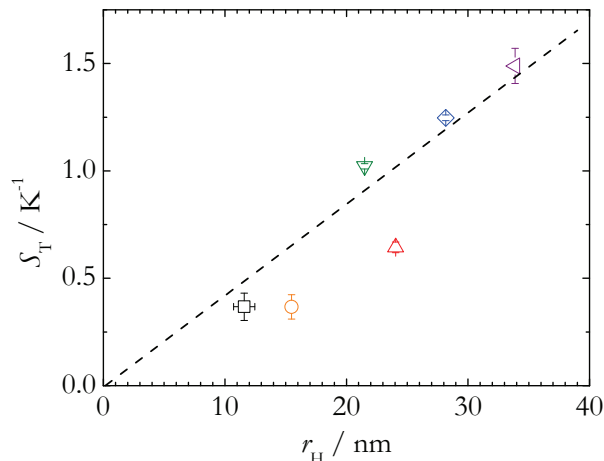
Figure 6.5.: *The Soret coefficient is plotted versus the hydrodynamic radius which was also determined from IR-TDFRS measurements. Symbols are used as given in Fig. 6.1. The dashed line indicates a linear size dependence of S_T.*

to vary the oil component and the concentration of the oil component, so that the *efb* temperature is the same for different systems. To overcome the simultaneous temperature variation, when the radius was changed we used n-tetradecane, n-dodecane, n-decane, n-octane and mixtures of n-decane and n-octane with a mass ratio of 50/50 and 25/75, respectively. The corresponding 1ϕ-funnels for the pure n-alkane mixtures are shown in Fig.6.1.

6.3. S_T of n-alkane Microemulsions

6.3.1. SANS Measurements to check spherical Shape at the efb

We determined the size and shape of the microemulsion aggregates at the *efb* by small angle neutron scattering (SANS) measurements. For that purpose the group in Köln prepared D_2O/n-alkane/$C_{12}E_5$ mixtures. The preparation with D_2O lowers the boundary temperature by approximately 2K [307] compared to the H_2O containing mixtures. Keeping the volume fraction constant, the mass fraction changes from $\gamma_a = 0.03$ wt for the H_2O systems to $\gamma_{a,d} = 0.0272$ wt for the D_2O-systems (see Tab.6.3). The phase boundaries of all samples are given in reference [277].

Before each measurement, the microemulsion and the sample cell were thermostated to a

n-alkane	$\phi_{c,i}$	ϕ_B	ϕ_0	r_{SANS} [nm]	t_{di} [nm]	σ_G [nm]	$\phi_{mon,b}$	d_{eff} [nm]
C$_8$	0.0270	0.0831	0.1115	15.20	0.68	2.80	0.019	31.76
C$_{8/10}$ (50/50)	0.0281	0.0589	0.0880	11.00	0.67	1.90	0.017	23.34
C$_{10}$	0.0291	0.0392	0.0690	8.10	0.65	1.37	0.017	17.50
C$_{12}$	0.0298	0.0252	0.0554	6.00	0.65	0.95	0.017	13.30
C$_{14}$	0.0301	0.0171	0.0475	4.72	0.66	0.76	0.015	10.74

Table 6.3.: *Results obtained from SANS measurements. The listed data are the surfactant volume fraction in the internal interface, ϕ_c, the volume fraction of the n-alkanes, ϕ_B, the droplet volume fraction, ϕ_0, the mean droplet radius, r_{SANS}, the thickness parameter of the diffuse interface, t_{di}, the standard deviation of the Gaussian function describing the radius polydispersity around the mean droplet radius, σ_G, the monomeric dissolved $C_{12}E_5$ in oil, $\phi_{mon,b}$, the effective diameter of the sticky hard spheres, d_{eff}.*

temperature in the 1ϕ regime. The microemulsion was stirred meanwhile and subsequently filled into the sample cell. The distance between the microemulsion containing test tube and the sample cell was as short as possible to avoid temperature effects on the way. Then, the closed sample cell was left for five minutes in the thermostated water bath to equilibrate. We confirmed the state of the phase of the sample visually. The cell holder[1] in the beam line was thermostated to a temperature which is approximately 0.5 K higher than the *efb* temperature of the microemulsion. We measured the temperature precisely in the cell holder with a calibrated thermometer (Greisinger Electronic, High Precision digital Thermometer, GMH3710; with: PT100, GTF401, $\Delta T = 1/10$ DIN between $0 - 100$ °C) with an error of ± 0.044 K in this temperature range. Before transfering the sample cell to the cell holder we checked the microemulsion phase again. Once, the sample was fixed in the cell holder and the holder reached its final position for the measurement, we again checked the state of the phase of the microemulsion. We carefully lowered the temperature of the cell holder to the *efb* temperature to avoid phase separation. Finally, the shutter was opened and each sample was exposed to the neutron beam. The exposure times and collimator settings were chosen to achieve a sufficient signal to noise ratio and not to exceed the detector capacity. After data recording, we checked the phase of microemulsion visually in the cell holder but never found an indication for phase separation during the measurements.

Fig.6.6 shows the experimental scattering intensities $I(q)$ after substraction of the incoher-

---

[1]The cell holder provides space for four cells. Although only one cell is investigated, this holder provides a good thermal stability for the microemulsion sample due to its higher heat storage capacity.

ent background as a function of the scattering vector q for $D_2O/C_x/C_{12}E_5$ microemulsions. The scattering data have been described by a form factor for polydisperse spherical shells with a diffuse interface and core scattering [311]. The assumption for the structure factor $S(q)$ being equal to one, leads to a systematically higher intensities than the experimental data points at low values of q, which indicates that interactions between the microemulsion droplets need to be considered.

These droplet interactions are included in the structure factor using a sticky hard spheres model [313,314]. The interactions were more pronounced for higher droplet concentrations which are found for microemulsion systems with the shorter n-alkanes, like n-octane with a droplet volume fraction of 11.15 vol%. The microemulsion droplets containing n-tetradecane has the smallest droplet volume fraction of 4.75 vol% and showed the smallest interaction effect. The strength of the interaction effects also influences the coencentration dependence of the Soret coefficient, which is weak as long as the concentration is below 10 vol% [42, 327]. We determined a moderate polydispersity of (16.9 ± 0.4) % of the mean droplet radii for all systems and an attractive region (effective sticky hard sphere diameter, $d_{eff} = 2r_{SANS} + t_{di}$) of about 104 % ($C_8$) to 114 % ($C_{14}$) of the mean droplet diameter ($2r_{SANS}$), respectively. The ratio of the hydrodynamic radius determined by IR-TDFRS and the mean droplet radius determined by SANS was for all systems $r_H/r_{SANS} \approx 1.35 \pm 0.06$.

We extrapolated the determined mean droplet radii to zero oil concentration, which corresponds to a L_1-phase of the binary aqueous surfactant system [351], and find a droplet radius of 1.91 nm, which agrees with the value given by Menge *et al.* (see Fig.6.7). The authors investigated the cross sectional radius of gyration of this binary mixture with a mass ratio of $C_{12}E_5$ to water of 7 mg/ml which is approximately four times lower than the ratio γ_a we worked with. Although, systems with different surfactant concentrations are being compared, the extrapolation of the droplet size yields a reliable result as the surfactant content influences the particle density but not the droplet size.

6.3.2. Measurement Procedure and Temperature Correlation

All samples were equilibrated in the lower part of the 1ϕ region and the sample holder in the IR-TDFRS setup was thermostated to the appropriate temperature of each microemulsion system in the 1ϕ region. The measurements started in the 1ϕ regime and ended at the *efb* or slightly below. Due to the fairly large size of the microemulsion
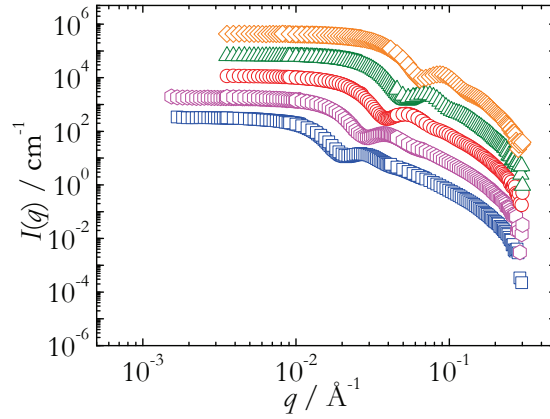
Figure 6.6.: *SANS measurements were performed to determine the shape of the microemulsion aggregates at the* efb *temperature (see Tab.6.2). The scattered intensity is plotted versus the q-vector. The curves for different samples (*C_8*: squares,* $C_{8/10}$ *(1:1): combs,* C_{10}*: circles,* C_{12}*: triangles up,* C_{14}*: diamonds) are shifted by a factor of ten on the logarithmic intensity scale.*
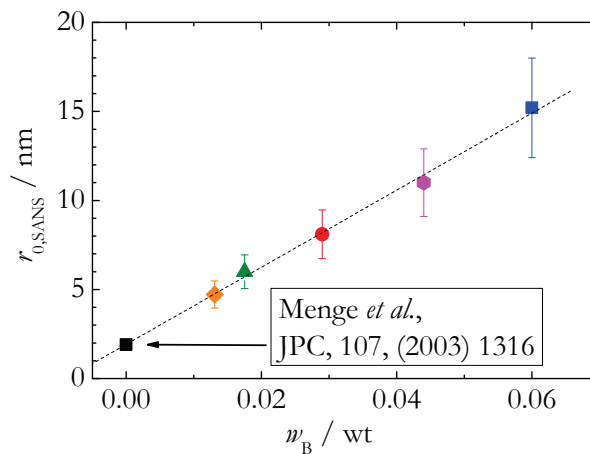
Figure 6.7.: *The mean droplet radius by SANS,* r_{SANS}*, is plotted versus the oil mass fraction. Symbols are used as given in Fig. 6.1. The data have been fitted linearly (dashed line) such that the extrapolation to* $w_B = 0.0$ *wt gives the corresponding mean droplet radius for a water/surfactant solution which exactly fits with literature data by Menge et al. [352] (filled black square).*

droplets in the range of up to $r_H = 20$ nm, the diffusion coefficient was in the order of $20 \cdot 10^{-12}$ m^2/s. Thus, the measurements of each sample at different temperatures took up to five days for the slowest system with n-octane as oil component. During this long measurement time, the water content decreased slightly with time, so that the sample was shifted to a higher n-alkane content, which results in a higher *efb* temperature. To check for evaporation, a sample of $H_2O/C_{8/10}/C_{12}E_5$ ($C_8/C_{10} = 75/25$) was measured twice at 28.45 °C. Between both measurements, the cell was thermostated for almost 48 hours. S_T differs by 0.00557 K^{-1}, which corresponds to an error of 2 %. The typical uncertainty of repeated measurements of S_T is in the order 9 %. Therefore the evaporation effect is neglible.

Additionally, the temperature in the sample was increased due to absorption of the laser light. This effect occurred locally and could not be detected by the temperature sensor in the cell holder. We specified this offset in the IR-TDFRS setup by measuring the intensity of the diffracted read-out laser in the vicinity of the phase transition boundary from 1ϕ to $\overline{2}\phi$. Therefore, we used a well known phase behavior of a H_2O/n-octane/$C_{10}E_4$ microemulsion with a mass ratio of H_2O to C_8 of 50/50 and a concentration of the surfactant in water of $\gamma_a = 0.154$ wt. This system is clear and transparent in the 1ϕ region but turns to be turbid in the $\overline{2}\phi$ region where we measured a strong increase of scattering intensity in the setup (see Appendix C). The determined phase separation temperature by intensity measurements was $\Delta T_{offset} = 0.3$ K lower than the temperature measured with the reference thermometer during the determination of the phase diagram. This systematic temperature shift was taken into account in the following. We assumed the same temperature shift for all microemulsions although the water contents varies slightly between 88.3 vol% (n-octane) and 94.3 vol% (n-tetradecane).

6.3.3. Diffusion Coefficients

The mass diffusion coefficient was directly calculated from the equilibration time, τ_c, and the characteristic scattering vector, q, in the IR-TDFRS setup. Fig.6.8 shows the temperature dependence of the diffusion coefficient for all investigated microemulsion systems close to the *efb*. Starting at the high temperature, the diffusion coefficient first increased with decreasing temperature and finally reached a plateau value below the *efb*.

In the plateau below the *efb* the 1ϕ phase coexists with an oil excess phase. This plateau
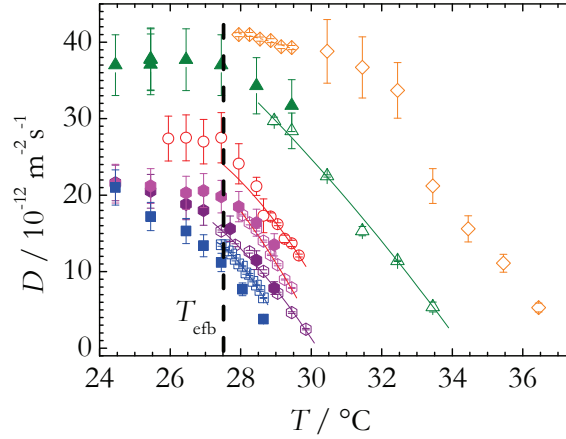
Figure 6.8.: *The mass diffusion coefficient is plotted versus the temperature in the vicinity of the* efb *for several microemulsion systems:* n-*octane (squares),* n-*octane / n-decane (75/25) (hexagon),* n-*octane / n-decane (50/50) (hexagon),* n-*decane (circles),* n-*dodecane (triangles up) and* n-*tetradecane (diamonds). The black dashed line is a guide to the eyes and marks roughly the* efb. *Data from IR-TDFRS (open symbols) and from DLS (solid symbols) are compared.*

was more pronounced for the long-chained *n*-alkane microemulsions, while for the *n*-octane system we could not identify a plateau. The same behavior was reflected in the hydrodynamic radius, which was calculated by the Stokes-Einstein-Equation, assuming a spherical shape of the droplets, using the temperature dependent viscosity of pure water. This simplification was justified, since the solubility of *n*-alkanes in water is negligible. In Fig.6.9 the temperature dependence of the hydrodynamic radius is shown, which decays with decreasing temperature and reaches a plateau at the *efb*.

We obtained the diffusion coefficients and hydrodynamic radii at the *efb* by interpolating the measured data in the 1ϕ region. It turned out that the temperature dependence of the hydrodynamic radius can be described by a single exponential function, which was used to obtain the hydrodynamic radius at the *efb*. We included the data points from the $\underline{2}\phi$ region because the phase transition is continuous and spherical droplets are found on both sides of the boundary as it was observed by Corkill *et al.* [353] with NMR measurements in the $\underline{2}\phi$ region. In the investigated temperature range, the diffusion coefficients and accordingly the hydrodynamic radius were almost temperature independent. For the long-chained *n*-alkane systems, the addition of the $\underline{2}\phi$ data points made the result more
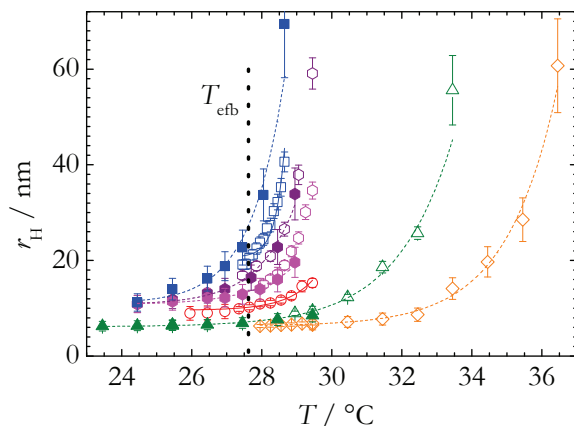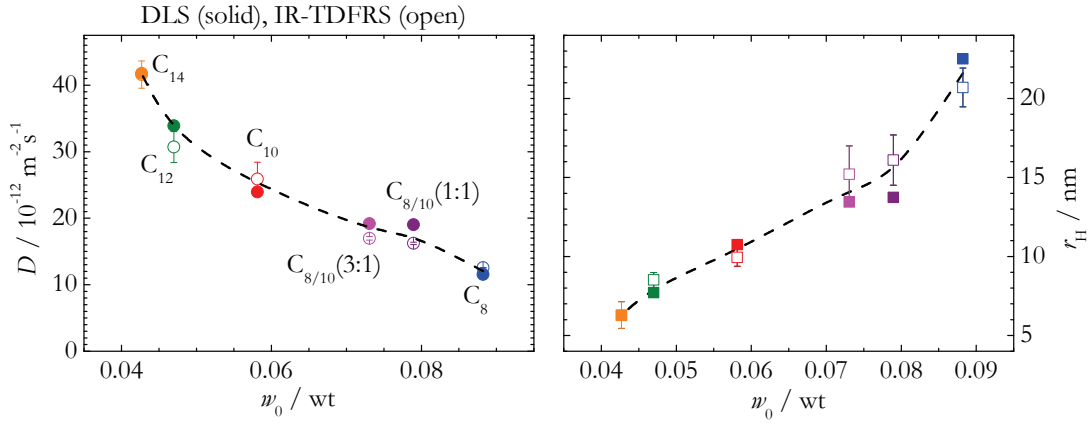
Figure 6.9.: *The hydrodynamic radius is plotted versus the temperature for several mi-croemulsion systems:* n-*octane (squares),* n-*octane /* n-*decane (75/25) (hexagon),* n-*octane /* n-*decane (50/50) (hexagon),* n-*decane (circles),* n-*dodecane (triangles up) and* n-*tetradecane(diamonds). The black dashed line is a guide to the eyes and marks roughly the* efb.

certain, but did not change the value significantly, which we obtained, if we used only values from the 1ϕ region and extrapolated to the *efb*.

6.3.4. Comparison with DLS

Dynamic light scattering (DLS) experiments were performed within the 1ϕ region by the group in Köln. The obtained intensity correlation function $g_2(t)$ was normalized to one for $t = 0$ and was analyzed using the Kohlrausch-Williams-Watts function (Eq.3.14) to determine the diffusion coefficient $D = (\tau q^2)^{-1}$. The time constant of the diffracted intensity signal in the IR-TDFRS experiment, τ_c, is three orders of magnitude smaller than of the DLS setup, because the q-vector is two orders of magnitude smaller. Fig.6.10 compares the extrapolated diffusion coefficients and the hydrodynamic radii at the *efb* obtained by IR-TDFRS and DLS. In the entire concentration range both setups produce equal diffusion coefficients within the error bars. Usually it is expected that different statistical weights in DLS and TDFRS lead to a slower diffusion in DLS compared to TDFRS experiments, but here we observe also the opposite trend, which is not understood yet.

Figure 6.10.: *The extrapolated diffusion coefficient (left plot, circles) and hydrodynamic radius (right plot, squares) of all investigated microemulsion systems ($\gamma_a = 0.03$ wt) are plotted versus the droplet concentration at the* efb. *Two methods were used to measure D: the IR-TDFRS (solid symbols) and the DLS setup (open symbols). Symbol colors are used as given in Fig. 6.1. The dashed lines are guides to the eyes.*

## 6.4. Calculation of S_T and D_T

The Soret coefficient, being the ratio of the thermal diffusion coefficient and the mutual diffusion coefficient, was determined within the characteristic 1ϕ region in the vicinity of the *efb* for each microemulsion system. Fig.6.11 depicts the temperature dependence of S_T which is similar for all microemulsion systems: A plateau value was reached for low temperatures just below or in the vicinity of the *efb*, while approaching against the *ncb*, S_T diverges. In between, a minimum value of S_T is found. Measurements in the vicinity of the *ncb* were not possible because the diffusion coefficient of the microemulsion structures in the upper part of the 1ϕ decays to zero. This characteristic behavior of the Soret coefficient at the *efb* is related to the thermal diffusion coefficient which also shows a plateau at the *efb* (see Fig.6.12). In contrast, near the *ncb* the thermal diffusion coefficient of the microemulsion systems with long-chained *n*-alkanes did not indicate to diverge against the *ncb* as the Soret coefficient did, but relaxed to a rather constant value at $T = 32.5$ °C for C_{12} and $T = 36.5$ °C for C_{14}, respectively. This constant behavior of the thermal diffusion coefficient close to a critical point was also found experimentally by Giglio and Vendramini for a aniline-cyclohexane mixture [16]. A theoretical approach is given by Luettmer-Strathmann [354] who investigated the behavior of D_T close to phase
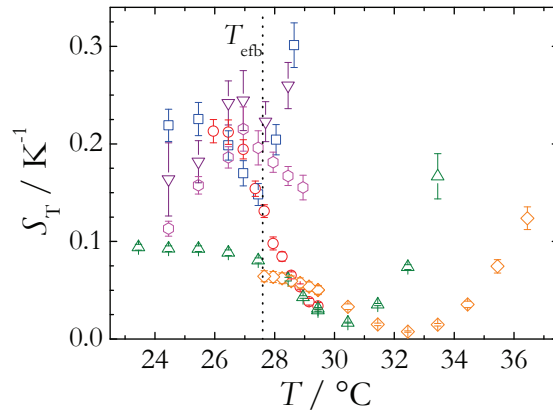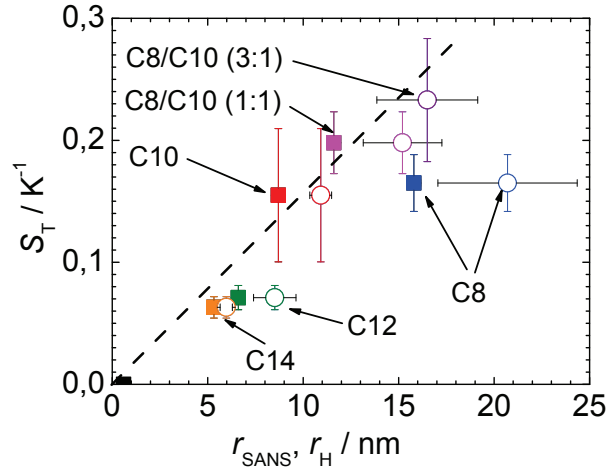
Figure 6.11.: *The Soret coefficient is plotted versus the temperature. A plateau close to the* efb *(dotted line) is reached. The Soret coefficient diverges towards the* ncb. *Symbols are used as given in Fig. 6.1.*

transition boundaries. The typical divergence of S_T near the *ncb* is then caused by a vanishing mutual diffusion coefficient.

The temperature dependence of the Soret and diffusion coefficients was interpolated to the *efb*. While the temperature dependent behavior of the mass diffusion coefficient could
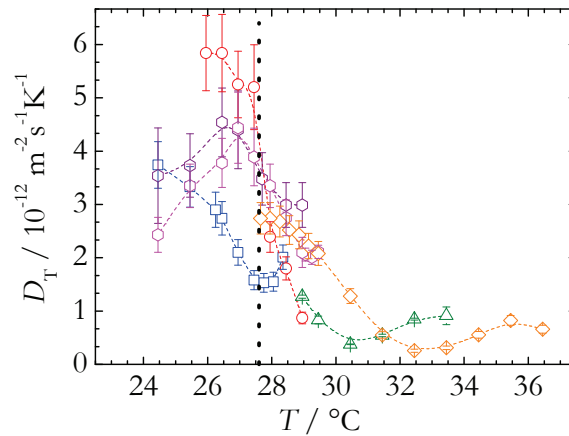
Figure 6.12.: *The thermal diffusion coefficient is plotted versus the temperature. A plateau is observed in the vicinity of the* efb. *The vertical dotted line sketches the* efb *schematically. A divergence in the vicinity of the* ncb, *as it was indicated by the Soret coefficient in Fig.6.11, is not indicated. Symbols are used as given in Fig. 6.1.*
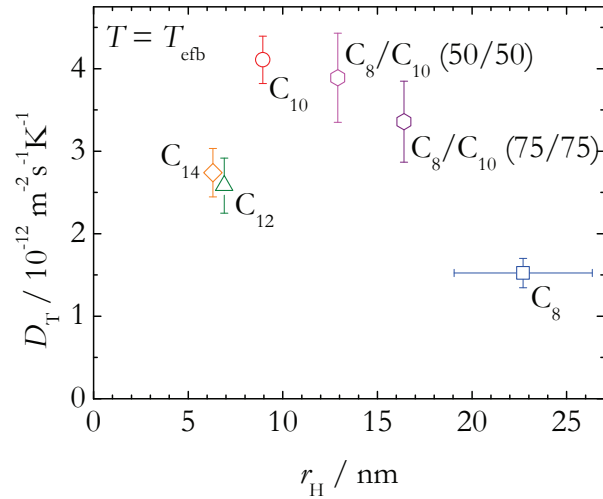
Figure 6.13.: *The Soret coefficient versus the hydrodynamic radius, r_H, (open circles) and versus the mean droplet radius determined by SANS measurements, r_{SANS}, (filled squares) for $T = T_{efb}$. Symbol colors are used as given in Fig. 6.1. The dashed line indicates a linear radial dependencies. S_T and r_H are interpolated values while the mean droplet radius was measured.*

be described by a linear fit above the *efb*, we determined the respective values of the Soret and the thermal diffusion coefficient at the *efb* manually.

In Fig.6.13, the interpolated values of the Soret coefficient are plotted versus the hydrodynamic radius r_H and versus the mean droplet radius, r_{SANS}. The mean droplet radius r_{SANS}, as it was determined by SANS, contains also the width of the surfactant layer, since the measured value of r_{SANS} approximately corresponds to the distance from the center of the particle to the hydrophilic-hydrophobic intersection of the surfactant in the droplet interface. The values of the hydrodynamic radius were calculated from the diffusion coefficients at the *efb*. Neglecting the *n*-octane system S_T shows a linear radial dependence. The *n*-octane system turned out to be the most difficult system to be measured due to the narrow temperature range of the 1ϕ region.

In Fig.6.15 a comparison of the determined radial dependence of the Soret coefficient with literature results is given. It is clearly shown, that the results of this work coincide with the generally obtained linear radial dependence. Performed SANS meausurements showed, that the microemulsion droplets under investigation can be regarded as dynamic solid particles. Thus, the theoretical approach by Würger [339], claiming a linear radial dependence of S_T for solid particles, is also true for the investigated microemulsion systems.

Figure 6.14.: *The thermal diffusion coefficient is plotted versus the hydrodynamic radius. Both values are interpolated to the* efb*. Symbols are used as given in Fig. 6.1.*
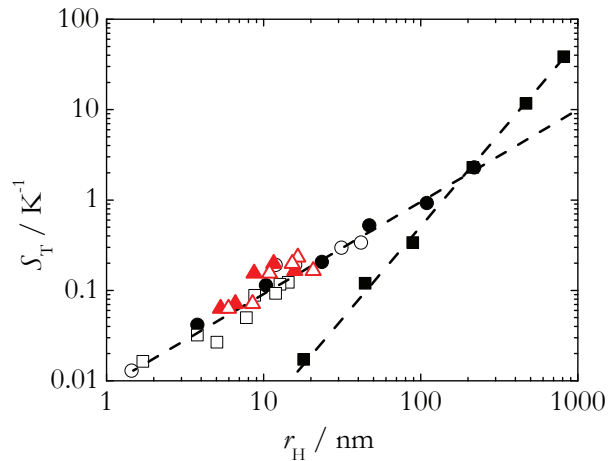
Figure 6.15.: *The determined radial dependence of the Soret coefficient is compared with literature results as summarized in [99]. The black symbols refer to following literature results: [65] (filled squares), [66] (filled circles), [35] (open squares), [67] (open circles). The red symbols refer to measurements of this work: TDFRS (filled triangles) and IR-TDFRS measurements (open triangles). Dashed lines are guides to the eyes.*

As a consequence of the linear radial S_T dependence and Eq.2.22, the thermal diffusion coefficient should be independent of the radius. Fig.6.14 shows the radial dependence of D_T. Both, the radius and the diffusion coefficient, are interpolated to the *efb*. We cannot give a clear radial dependence of D_T due to large data spreading.

6.4.1. Normalization of the Soret Coefficient

Comparing the temperature dependence of the Soret and diffusion coefficients in the 1ϕ regions of the investigated *n*-alkane microemulsions, certain similarities were observed, e.g. the divergence of S_T against the *ncb* or the asymptotical approach towards a plateau close to the *efb* which was found for all systems. For the microemulsion systems under study, this can be explained by the fact that size and structure of the microemulsion droplets in the 1ϕ region are defined by the upper and lower phase boundaries and the point, where *efb* and *ncb* meet. Thus, it might be possible to describe the temperature dependence of the Soret coefficient, measured in the 1ϕ region of different microemulsions, with a master curve. Therefore, temperature and S_T need to be normalized. A normalized temperature was introduced which considers the upper and lower 1ϕ boundaries. The Soret coefficient was normalized to its corresponding value at the *efb*. The multiplication with the hydrodynamic radius considered the size effect of S_T with increasing concentration which was determined to be linear. The normalization was:

$$S_\mathrm{T}{}^* \;\; = \;\; \frac{S_\mathrm{T}}{S_{\mathrm{T},efb} \cdot r_\mathrm{H}} \quad \text{and} \tag{6.1}$$

$$T^* \;\; = \;\; \frac{T - T_{\mathrm{e}fb}}{T_{\mathrm{n}cb} - T_{\mathrm{e}fb}} \; . \tag{6.2}$$

with the temperatures of the *efb* and *ncb*, $T_{\mathrm{e}fb}$ and $T_{\mathrm{n}cb}$, respectively. The normalized values are denoted with a star. At $T = T_{\mathrm{e}fb}$ the reduced temperature is $T^* = 0$, while at $T = T_{\mathrm{n}cb}$ it is $T^* = 1$. Fig.6.16 shows the normalized Soret coefficient plotted versus the normalized temperature: All microemulsion systems showed a minimum at $T^* \approx 0.4$ which is close to the temperature in the 1ϕ region where some microemulsions containing long-chained *n*-alkanes show a slightly pronounced discontinuity in the temperature dependence of the diffusion behavior. Above this temperature, a diverging behavior against the *ncb* was observed, and below this temperature the asymptotic approach against a plateau close to the *efb* is pictured. We found two different plateau values. The lower plateau was
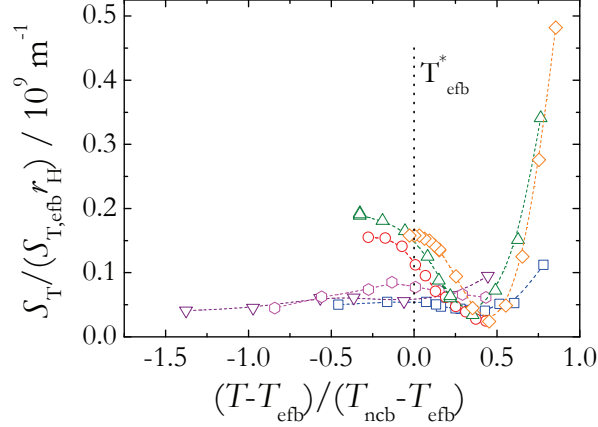
Figure 6.16.: *The normalized Soret coefficient versus the normalized temperature. Deviations from a standardized curve are observed for higher concentrated microemulsions. Symbols are used as given in Fig. 6.1.*

reached for all microemulsion systems containing n-octane, and another higher plateau was found for the systems C_{10}, C_{12} and C_{14}.

6.5. Correlation between S_T and the Interfacial Tension

In microemulsion systems, the interfacial tension between the microemulsion droplets and the solvent varies with composition and temperature. Piazza and Parola *et al.* [99] correlate the Soret coefficient with the interfacial tension of the microemulsion droplets. It is stated that the Soret coefficient can be calculated from the derivative of the interfacial tension with temperature as

$$S_T = \frac{4\pi r}{k_B T} \frac{\partial (l_{fluid} \sigma)}{\partial T} \tag{6.3}$$

with the droplet radius, r, and the length which measures the range of the colloid-solvent interaction, l_{fluid}. Regarding the microemulsion droplets, we assume that $r = r_{SANS} + v_c/a_c^2$ and that $\partial l_{fluid}/\partial T$ is constant. Hence, Eq.6.3 reduces to

$$S_T = \frac{4\pi r_{SANS} l_{fluid}}{k_B T} \frac{\partial \sigma}{\partial T} . \tag{6.4}$$

In order to apply Eq.6.4 to the microemulsion systems, we use the interfacial tension data of the microemulsion droplets at the *efb* determined by Sottmann [355] (Fig.6.17).

He measured the interfacial tension at different temperatures and concentrations using the spinning-drop technique [247, 356, 357] and also determined the mean radius of the investigated microemulsion droplets by SANS measurements. Thus, if we are able to combine the results from the spinning-drop technique with the results from TDFRS, we can investigate, whether Eq.6.4 describes the dependence of the Soret coefficient as function of the interfacial tension qualitatively. Therefore, we have to prove that both systems, the investigated system in this work and that by Sottmann, are comparable to each other. This is the case if the microemulsion structures in both systems have at least the same curvature at a certain temperature and composition. Assuming spherical droplets in the investigated temperature and concentration range, the curvature is the inverse of the droplet radius. In Fig.6.17 the droplet radius is plotted versus the ratio of the volume fractions of surfactant and oil, ϕ_C/ϕ_B. The radius which is given in the work by Sottmann has been determined by SANS, while in this work the radius refers to the hydrodynamic radius determined by IR-TDFRS. As we also determined the radii of some microemulsions by SANS and IR-TDFRS under equal conditions, we use the previously determined factor $r_\mathrm{H}/r_{SANS} = 1.35$ to convert the hydrodynamic radii from IR-TDFRS experiments. Thus, both radii are almost comparable to each other. Fig.6.17 shows that the microemulsion droplets investigated by Sottmann and in this work have equal sizes at equal temperature and ratio of volume fractions.

The surface tension is directly correlated with the principal curvatures (c_1, c_2) of the amphiphilic film [358]. For spherical aggregates, it is $c_1 = c_2 = c$ and hence $\sigma/c^2 \approx kT$.

Hence, we take the measured interfacial tension from the data by Sottmann and calculate the temperature derivative of the interfacial tension at certain radii of the microemulsion droplets at the *efb* which are determined by TDFRS measurements in this work. We additionally consider that the hydrodynamic radii determined by TDFRS experiments are by a factor of 1.35 larger than the mean droplet radii, r_{SANS}, which have to be used instead in Eq. 6.4. For the calculation of l_{fluid} in Eq. 6.4, also the Soret coefficient of the microemulsion droplets at the *efb* (Fig.6.18) is required and is obtained by TDFRS experiments. Consequently, l_{fluid} is determined as a function of the *efb* temperature or mean droplet radius at the *efb*, respectively: With increasing temperature, l_{fluid} increases in absolute values from 0.17 nm at $T = 21.75\,°\mathrm{C}$ to 5.94 nm at $T = 28.46\,°\mathrm{C}$ and is thus in the order of the standard deviation of the Gaussian function describing the radius polydispersity around the mean droplet radius of similar microemulsions (see Sec. 6.3). Tab.6.4 lists important parameters which have been used for Eq.6.4.
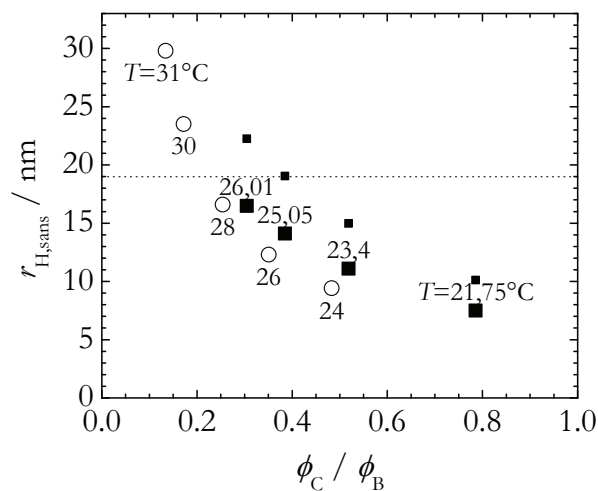
Figure 6.17.: *The radius versus the ratio of the volume fractions of surfactant and oil. The numbers close to the data points give the measurement temperatures. Upper numbers refer to the data by Sottmann [355] (open circles) and the lower numbers refer to the data from this work (solid squares). Small symbols represent the hydrodynamic radius, and large symbols give the calculated mean radius to compare with the radii from Sottmann. The dotted line marks the radius, above which the droplet size does not scale linearly with temperature.*
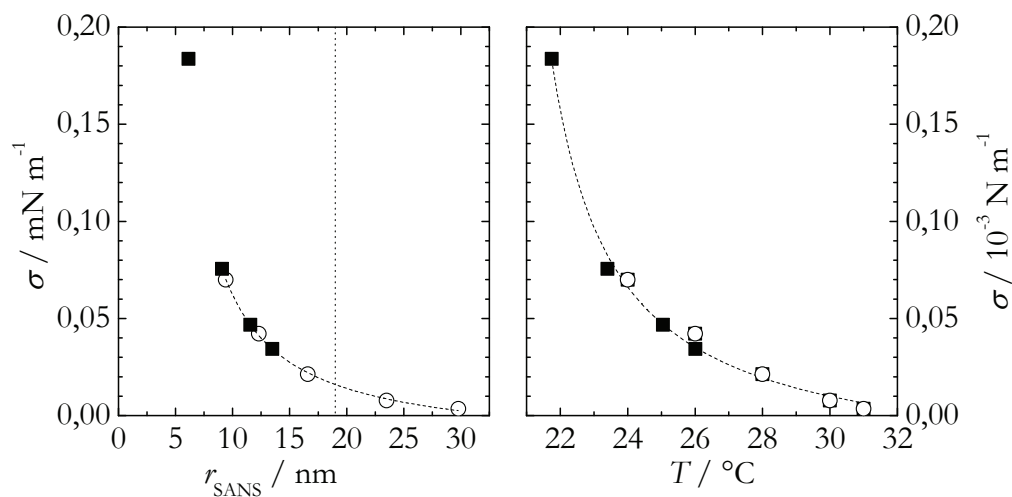
Figure 6.18.: *The interfacial tension versus the mean radius (left) and versus temperature (right). Open symbols are given by Sottmann. A fit (dashed line) on these data allows to interpolate the surface tension values for the systems investigated in this work.*

| w_B wt%	T_{efb} [°C]	r_{SANS} [nm]	σ [10^{-4} N m^{-1}]	$d\sigma/dT$ [10^{-5} N m^{-1}T^{-1}]	S_T [K^{-1}]	l_{fluid} [nm]
0.02	21.75	7.50	1.82	-8.33	0.37	0.19
0.03	23.40	11.09	0.87	-3.77	0.37	0.29
0.04	25.05	14.11	0.44	-1.71	0.64	0.88
0.05	26.01	16.48	0.31	-1.08	1.02	1.89
0.06	27.40	20.87	0.20	-0.55	1.25	3.58
0.07	28.46	25.09	0.16	-0.33	1.49	5.94

Table 6.4.: *The width of the fluid layer, l_{fluid}, is calculated for the H_2O/C_8/$C_{12}E_5$ system ($\gamma_a = 0.022$ wt, w_B-values are given in brackets) at the efb temperature, T_{efb}, using Eq.6.4. The calculated mean radius, $r_{SANS} = r_H/1.35$, and the interpolated interfacial tension, σ, are shown.*

6.6. Preliminary measurements of the w/o-Droplets

In the previous sections, the Soret coefficient of o/w-microemulsion droplets in the 1ϕ region on the water-rich side of the phase diagram has been investigated. For these systems, a linear radial dependence of S_T was found. The main question is, if also the Soret coefficient of w/o-droplets shows a linear radial dependence. These discrete w/o-droplets are formed in a 1ϕ region at the oil-rich side of the phase diagram [359–361] and can be treated as reverse micelles of a monolayer surfactant film which separates water from oil [362]. The inner core is formed by water and the hydrophilic surfactant head group. The hydrophobic surfactant chain is in contact with the surrounding oil phase. One discriminates between a water core, which is impenetrable for the oil, and a flexible penetrable shell. The maximum thickness of the shell is given by the extended length of the surfactant chain and increases with temperature [363]. A sticky hard sphere potential can be assigned to the w/o-droplet for which the flexible layer thickness is regarded as the stickiness parameter of the short-ranged attractive potential [363–365]. A comparison with o/w-droplets shows that attractive interactions between w/o-droplets are less pronounced than attractive interactions between o/w-droplets [366].

We investigated microemulsion droplets in the 1ϕ funnel on the oil-rich side of the $H_2O/C_8/C_{12}E_5$ phase diagram. The oil-to-surfactant ratio was constant at $\gamma_b = 0.04$ wt and the water mass fraction w_A has been varied between 0.02 wt and 0.05 wt. The corresponding 1ϕ-funnel has been measured in Köln and is shown in the left plot of Fig.6.19. The *efb* is the upper phase boundary and the *ncb* is the lower one. All thermal diffusion measurements (here not shown in detail) have been performed in the 1ϕ region. As the measurement directly at the *efb* was not possible, we performed the measurements at different temperatures below the *efb* and extrapolated the Soret coefficient and the hydrodynamic radius to the *efb*. We had to measure carefully because the funnel temperature is approximately 20 °C above room temperature which causes the risk of phase transitions during or even before the measurements. The main problem is, that the microemulsions which have been filled in the thin flow cells in a thermostated environment, cooled down within a few seconds to room temperature while the cells are transferred to the thermostated cell holder of the classical TDFRS setup.

The hydrodynamic radius was determined from classical TDFRS measurements with the assumption of spherical droplets at the *efb*. We also assumed that the viscosity of the solvent is approximately equal to the viscosity of the pure n-octane because the solubility of water in n-octane is low and the surfactant assembles in the oil-water interface. In
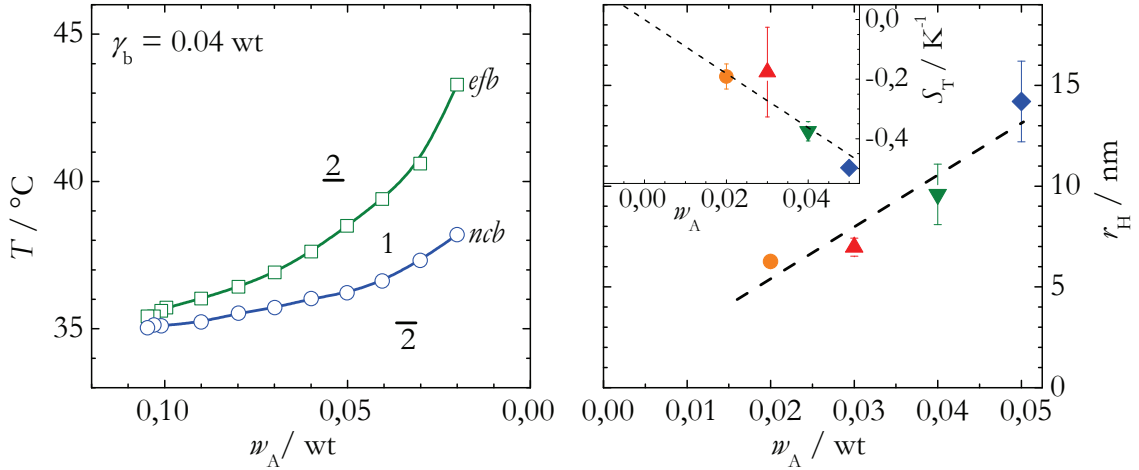
Figure 6.19.: Left: *Phase diagram of the 1φ funnel on the oil-rich side with the* efb *(squares) and the* ncb *(circles).* **Right:** *The hydrodynamic radius versus the water concentration,* w_A. *Mass fractions:* $w_A = 0.02$ *wt (circles),* $w_A = 0.03$ *wt (triangles up),* $w_A = 0.04$ *wt (triangles down) and* $w_A = 0.05$ *wt (diamonds). The dashed line is a linear fit. Inset: The Soret coefficient of* $H_2O/C_8/C_{12}E_5$ *at the* efb *versus the water concentration at constant* $\gamma_b = 0.04$ *wt.*

the inset in the right plot of Fig.6.19 the extrapolated Soret coefficient versus the water concentration is shown. S_T is negative and decreases linearly with increasing water concentration. Nevertheless, the w/o-droplets move to the cold. This unexpected combination of a negative Soret coefficient and the motion to the cold is caused by the negative contrast factor $(\partial n/\partial w)_{p,T}$ as the increase in the water content of the solution will lower the main refractive index.

The plot of the Soret coefficient versus the hydrodynamic radius shows an almost linear radial dependence in the investigated concentration range (see Fig.6.20). The investigation of larger droplets, as they are formed in microemulsions with higher water contents, was not possible because the 1φ funnel becomes narrower in temperature at higher water contents.
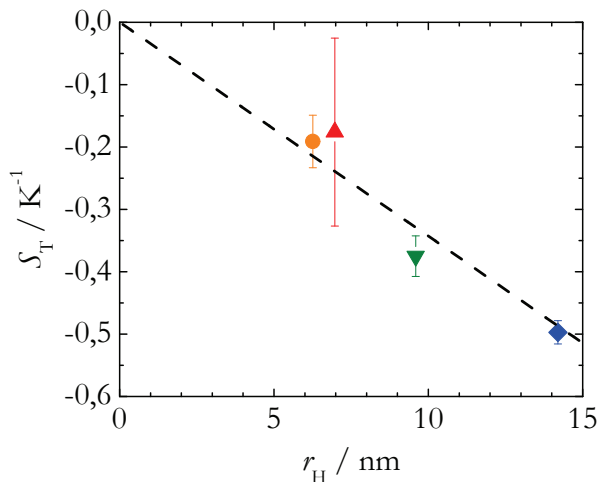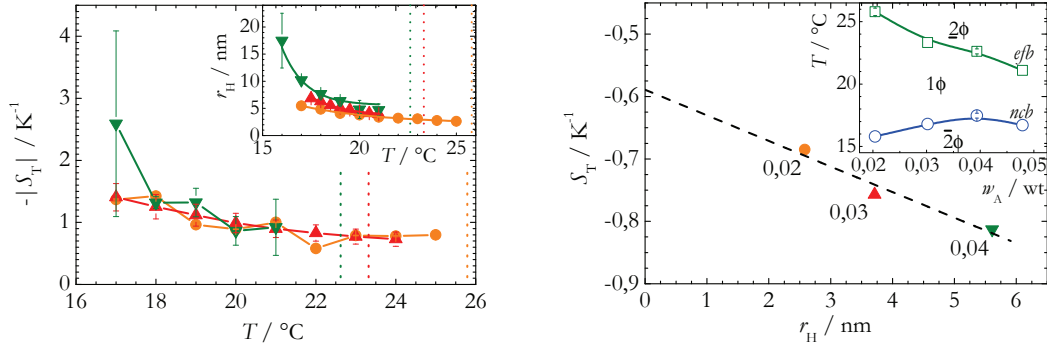
Figure 6.20.: *The Soret coefficient versus the hydrodynamic radius at the* efb *at constant* $\gamma_b = 0.04$ *wt for w/o-droplets of the* $H_2O/C_8/C_{12}E_5$ *microemulsion. Symbols are used as given in Fig. 6.19.*

6.6.1. w/o-Droplets of a quaternary Microemulsion

Most of the problems during the measurements in the 1ϕ region on the oil-rich side of the $H_2O/C_8/C_{12}E_5$ phase diagram stem from the fairly high *efb* temperatures between 38.5 °C ($w_A = 0.05$ wt) and 43.3 °C ($w_A = 0.02$ wt). To overcome these temperature problems, an approach is to add a forth component glycerol, which affects the phase boundaries [367] by lowering the cloud point [368]. Also the main temperature of the 1ϕ region is lowered. The hydrophilic glycerol goes into the water phase and a glycerol-to-water ratio of 0.35 wt/0.65 wt was selected which decreases the temperatures of the *efb* to 21 °C ($w_A = 0.05$ wt) and 26 °C ($w_A = 0.02$ wt). The phase diagram is given in the inset on the right side of Fig.6.21. Thermal diffusion measurements have been performed in the 1ϕ region and the data have been extrapolated to the *efb* using an exponential function. The Soret coefficient and the hydrodynamic radius approach a plateau value close to the *efb* (for both plots see left Fig.6.21).

Finally, the right Fig.6.21 shows a linear size dependence of the Soret coefficient. Differences to the w/o-droplets of the glycerol-free microemulsions are the larger absolute values of the Soret coefficient by a factor of two, and the droplet sizes which are almost halved for each concentration. The different droplet sizes can be explained as follows: Glycerol might cause dehydration of the hydrophilic head groups of the surfactant because it is

Figure 6.21.: Left: *The absolute value of S_T versus temperature. The mass fractions are: $w_A = 0.02$ wt (circles), $w_A = 0.03$ wt (triangles up) and $w_A = 0.04$ wt (triangles down). Vertical lines mark the emulsification failure boundaries. Inset: The corresponding hydrodynamic radius versus temperature.* **Right:** *The Soret coefficient at the* efb *versus the hydrodynamic radius in the H_2O/glycerol/C_8/$C_{12}E_5$ microemulsion at constant $\gamma_b = 0.04$ wt. Symbols are used as given in Fig. 6.19. The dashed line is a linear fit. Inset: The phase diagram.*

a less effective solvent than water. So, glycerol will not preferentially interact with the surfactant head group units but competes with them for water molecules. This causes a dehydration of the hydrophilic surfactant units which in turn causes an increase in the interactions between the surfactant head groups and leads to a contraction of the inner droplet core surface. The micelle shrinks [368, 369].

6.6.2. Conclusion

These preliminary measurements on the oil-rich side of the phase diagram of H_2O/C_8/$C_{12}E_5$ and H_2O/glycerol/C_8/$C_{12}E_5$ have been performed to investigate the thermal diffusion properties of the w/o-droplets. It was shown that the Soret coefficient is negative and approaches a constant value at the *efb*. S_T and the hydrodynamic radius at the *efb* scale almost linearly with the water concentration. A linear radial dependence of the Soret coefficient was found. The addition of glycerol decreased the funnel temperatures which in turn lowered the risk of phase transitions during the measurements. Also for the glycerol system a linear radial dependence of S_T has been observed. But there are still open questions to be answered. To our best knowledge, we assumed spherical droplets at the *efb*, but this has to be investigated, e.g. by SANS measurements. Furthermore, the determined droplet radii do not only include a small layer of *n*-octane molecules.

Additionally, also a layer of dissolved surfactant molecules is included, which spatial distribution is not homogeneous but shows a higher probability for find the surfactants close to the droplet [370].

It is also unclear to which extend the flexible interface of the w/o-droplets influences the thermal diffusion behavior for different droplet sizes. In the case that the interface can be regarded as a soft interface, Würger [68] predicts a quadratic radial dependence of S_T. But this cannot be confirmed by our findings.

Another point is the temperature influence on the thermal diffusion behavior of the w/o-droplets at the *efb*. This influence was pronounced in the water-rich 1ϕ funnel of $H_2O/C_8/C_{12}E_5$, so that the linear radial dependence of S_T turned into a quadratic dependence. For the w/o-droplets, the Soret coefficient depends linearly on the droplet radius even if the variation of the water concentration changed the *efb*-temperature. In future projects, we have to determine the Soret coefficient of different droplet radii without changing the *efb* temperature to identify the temperature influence.

SEVEN

CONCLUSION

The goal of this thesis was twofold: First we studied the thermal diffusion behavior below and above the critical micelle concentration (cmc) of micellar solutions. Second the size dependence of the Soret coefficient by means of microemulsions as model systems has been investigated.

In the first part of this work, the micellar systems were investigated. To our best knowledge, the thermal diffusion behavior of a micellar system around the critical micelle concentration has not been systematically investigated before. This work was motivated by a thermal lens study by Santos *et al.* [34]. They found an abrupt change of the thermal lens signal at the cmc. Unfortunately, they were not able to determine the Soret coefficient due to the presence of dye. In this work, the surfactant n–Octyl β–D–glucopyranoside, which has a fairly high cmc, was used for comprehensive measurements of the thermal diffusion properties in the low concentration regime close to the cmc. We used IR-TDFRS, which uses a weak absorption band of water in the near infrared and works without dye. The cmc was determined by surface tension measurements. It was found that the Soret coefficient is almost temperature- and concentration-independent in the concentration regime below the cmc, while above the cmc, micelles influence the thermal and mass diffusion coefficients. Unfortunately, it was not possible to separate micellar diffusion from molecular diffusion, as the time constants are too close to each other to resolve with IR-TDFRS. To tie in with the work of Santos *et al.*, we performed measurements with classical TD-FRS, which also works with an absorbing dye. Using classical TDFRS we could show that an ionic dye influences the thermal diffusion behavior above the cmc only if the dye

absorbs at the wavelength of the writing laser. A comparison of the different studies with and without dye in both forms of TDFRS showed that the abrupt change in the thermal coefficients also gets enhanced under this conditions.

In the higher concentration regime, corresponding to approximately the twice the *cmc*, where the diffusion is dominated by micelles, the hydrodynamic radius of C_8G_1 micelles determined by TDFRS is equal to the calculated length of the surfactant molecule. It was determined that the Soret coefficient undergoes a sign inversion from positive to negative with increasing concentration. Additionally, a temperature dependence of the sign inversion has been observed.

To check if the concentration and temperature dependencies of the Soret coefficient, determined for the C_8G_1/H_2O system, are general features of this class of sugar surfactants, the measurements were extended to C_7G_1/H_2O and C_8G_2/H_2O. Preliminary measurements of the critical micelle concentrations indicated a *cmc* three times higher of C_7G_1 than that of C_8G_1 due to a reduced hydrophobic chain length. Due to impurities in both batches of C_8G_2 a reliable determination of the *cmc* with the ring method was not possible. In contrast, the TDFRS results showed also for C_8G_2 a pronounced change of S_T at a concentration which is in the same order as the literature value for the *cmc*. This indicates that the micelle formation in the bulk is less influenced by impurities. All investigated systems showed a sign inversion at higher concentrations. Some approaches have been introduced to normalize the Soret coefficient as function of temperature for all investigated solutions.

The second part of this work focused on the investigation of microemulsion systems. Microemulsions were used as model systems of spherical particles to determine the radial dependence of the Soret coefficient, which is controversially discussed in the literature. Whether the Soret coefficient scales linearly or quadratically with the radius, was investigated. In contrast to recently published works using synthesized colloidal particles or ionic microemulsion droplets, the approach of this work employs the same chemical surface composition for all sizes and eliminates surface charge effects. The size of the droplets under investigation is in the range 6.3 nm (*n*-tetradecane) to 19.7 nm (*n*-octane) and is small enough to ensure that sedimentation does not occur.

Microemulsion droplets can be found in the 1ϕ region. A microemulsion of type $H_2O/C_8/C_{12}E_5$ was selected for study because the 1ϕ region is experimentally accessible close to room temperature. The 1ϕ region on the water-rich side of the phase diagram, surrounded by the emulsification failure boundary (*efb*) to the lower $\underline{2\phi}$ region and by the near critical boundary (*ncb*) to the upper $\overline{2\phi}$ region, is called 1ϕ-*funnel*. In this funnel

o/w-droplets are found. These droplets have a spherical shape at the *efb* and grow in size with increasing *n*-octane concentration. An increase in temperature leads to ellipsoidal or network-like structures close to the *ncb*. The phase diagram of the 1ϕ funnel was determined within which thermal diffusion measurements were performed. To calculate the Soret coefficient, the refractive index increment with temperature is required. As some microemulsions are turbid, an optimized Michelson interferometer was constructed.

Because of possible phase transitions at the *efb* from 1ϕ to $\underline{2}\phi$ during the TDFRS measurements, the samples could not be measured at the *efb*. Instead, temperature series were performed in the 1ϕ approaching the *efb*, and the Soret and diffusion coefficients were extrapolated to the *efb*. The temperature dependence of the Soret coefficient, at constant composition, approaches a constant value at the *efb*, while S_T diverges in the vicinity of the *ncb*. A variation of the *n*-octane concentration results in a size variation of the droplets. The determination of the Soret coefficient along the *efb* yields the radial dependence. For $H_2O/C_8/C_{12}E_5$, a linear radial dependence was determined, but the measurements for the different droplet sizes were not performed at the same temperature. It therefore remains unclear whether the result was additionally influenced by temperature changes.

To measure the Soret coefficient of o/w-droplets under isothermal conditions at the *efb*, microemulsion systems, which consisted of different *n*-alkanes, were produced. An increase of the *n*-alkane chain length shifts the 1ϕ region towards higher temperatures and towards lower mass fractions of the *n*-alkane. It is therefore possible that each $H_2O/C_x/C_{12}E_5$ microemulsion shows the *efb* at the same temperature, but with a different droplet size and different *n*-alkane concentrations. The shortest investigated *n*-alkane is *n*-octane, which exhibits a temperature difference of 2 K between the *efb* and the *ncb* at the investigated concentration. The measurement of a shorter *n*-alkane such as *n*-hexane is experimentally difficult, due to an even narrower funnel and a high evaporation rate. The longest *n*-alkane investigated was *n*-tetradecane, due to solubility problems for longer alkane chains. Thus, *n*-alkanes with an even number of carbon units from 8 to 14 were studied. *N*-alkanes with an odd number of carbon units were not considered as they show slightly different physical properties which makes them unsuitable. The investigated samples varied in their droplet volume fraction from 4.75 vol% (*n*-tetradecane) to 11.15 vol% (*n*-octane), and in the droplet hydrodynamic radius from 6.3 nm (*n*-tetradecane) to 19.7 nm (*n*-octane). For all *n*-alkane systems, small angle neutron scattering experiments were performed to confirm the spherical shape at the *efb* and to determine the droplet-droplet interactions. A combination of a sticky hard sphere structure factor and a core-shell form factor was

used to describe the data. As expected, it was found that the interactions are more pronounced at higher droplet volume fractions. Analyzing the Soret coefficient of these different microemulsion systems leads to a linear dependence of the Soret coefficient with droplet size.

An approach by Parola and Piazza [371] gives evidence that the Soret coefficient correlates with the radius of the solute particle, and with the temperature derivative of the product of the particle-solvent interfacial tension and the length which measures the range of the colloid-solvent interaction, $\partial(l_{fluid}\sigma)/\partial T$. It is assumed that S_{T} scales linearly with the particle radius and with $\partial\sigma/\partial T$. The main question was if the width of the fluid layer could be related to the thickness of the diffuse interface of the microemulsion droplets, $t_{\mathrm{d}i}$. The interfacial tension of a $H_2O/C_8/C_{12}E_5$ microemulsion determined by Sottmann was compared with thermal diffusion and SANS measurements. It was found that the thickness parameter of the diffuse interface of the sticky hard sphere potential and the width of the fluid layer are both in the order of a nanometer.

7.1. Outlook

Future projects will be focused on microemulsion systems. In this work, the radial dependence of the Soret coefficient was determined at constant temperature. This system can also be used to investigate the dependence of the droplet density on the Soret coefficient at constant droplet radius and temperature. This allows a systematic study to be made of the thermal diffusion behavior of single-particle and particle-particle interactions, which can be compared with existing theories for colloids. For these measurements, microemulsion systems that have already been characterized, like $H_2O/C_{10}/C_{12}E_5$, can be used. A variation in the droplet density can be achieved by changing the surfactant-to-water ratio, γ_a, and the n-alkane concentration, w_B. Thereby, the *efb*-temperature and the droplet size both are unattached. First measurements of the refractive index increments indicate that the 1ϕ funnel temperatures of these systems are in an experimentally accessible range so that we are able to measure these systems carefully using IR-TDFRS.

On the oil-rich side of the phase diagram of the investigated system $H_2O/C_8/C_{12}E_5$ w/o-droplets are formed. They behave like inverse micelles. The investigation of the thermal diffusion behavior of the w/o-droplet was difficult, due to the high temperatures of the gap between the *efb* and the *ncb* which lays between 35 °C and 43 °C. To lower the temperature regime of the funnel, glycerol can be added. First measurements of this quaternary

system are promising and a Soret coefficient has been determined which depends linearly on the radius. But there are still open questions: An alkane soluble dye, Quinizarin, has been added to convert the intensity grating into a thermal grating. The role of the dye on the thermal diffusion behavior has to be identified. SANS measurements are required to determine how far the dye is incorporated in the microemulsion droplets and to get information about the droplet size and shape, especially if glycerol is added.

Regarding the sample holders in TDFRS, they can be replaced by thermostated toluene baths. Toluene has almost the same refractive index as the quartz glass windows of the sample cells. This reduces perturbing scattering close to the measuring volume. Also the thermal stability of the sample during the measurement will be improved.

TAYLOR EXPANSION OF THE HETERODYNE DIFFRACTION SIGNAL

In general the obtained time dependent intensity function from TDFRS experiments was analyzed using Eq.3.8 to determine the Soret and diffusion coefficients. Sometimes the analysis of the diffraction signal became difficult, for instance if the thermal plateau was less apparent due to a pronounced amplitude of the concentration plateau. This case was often observed for microemulsion systems at temperatures close to the near critical boundary, near which the amplitude of the diffraction signal diverged. Fig.A.1 shows an example for a $H_2O/C_{8/10}$ (75/25)/$C_{12}E_5$ ($\gamma_a = 0.03$ wt, $w_B = 0.0505$ wt, $T = 29.05$ °C), where the thermal plateau was rather small, so that the standard fit procedure failed. Instead, a partial analysis of the measurement signal was used. Here, a Taylor expansion was used to analyze the slope of the concentration process to determine D_T which is the slope of that function.

The concentration process of the normalized heterodyne intensity signal is

$$\zeta_{het}(t) = A \left[1 - w_0 \frac{D_T}{D} \frac{\left(\frac{\partial n}{\partial T}\right)_{p,w}}{\left(\frac{\partial n}{\partial w}\right)_{p,T}} \left(1 - e^{-\frac{t}{\tau_c}}\right) \right] \tag{A.1}$$

with the heterodyne intensity signal, ζ_{het}, the amplitude of the signal, A, the diffusion co-eeifficients, D_T and D, the process time for the concentration mode, τ_c and the derivatives of the refractive index by temperature, $(\partial n/\partial T)_{p,w}$, and by concentration, $(\partial n/\partial w)_{p,T}$,
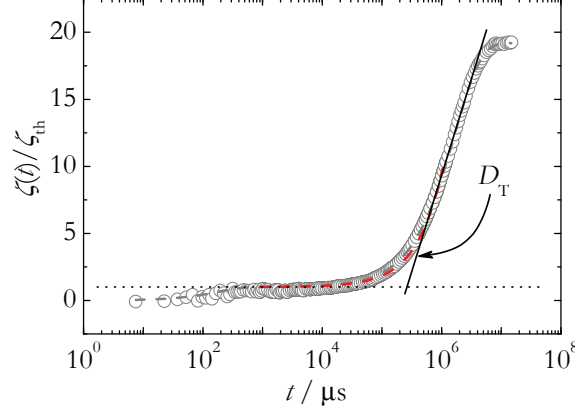
Figure A.1.: *The normalized heterodyne intensity signal versus time (circles). The dashed line represents the Taylor function. Data points which were used to fit Taylor are colored black, others grey. Dotted lines are guides to the eyes. The time scale is logarithmic. The mean square deviation of the fit is less then 1 %. Sample: $H_2O/C_{8/10}$ (75/25)/$C_{12}E_5$, $\gamma_a = 0.03$ wt, $w_B = 0.0505$ wt, $T = 29.05$ °C.*

respectively. w_0 is the mass ratio of the microemulsion droplets to the total mass. We shorten the expression in Eq.A.1 to

$$\zeta_{\text{het}}(t) = C_1 \left[1 - C_2 \left(1 - e^{-\frac{t}{\tau_c}} \right) \right] \tag{A.2}$$

and insert C_1 and C_2 as coefficients for the following comparison with a polynomial Taylor function $P(t)$

$$P(t) = p_0 + p_1 t + p_2 t^2 + p_3 t^3 + ... \tag{A.3}$$

where $p_i t^i$ are the polynomial terms of the ith-order. The approximation of ζ_{het} by Taylor expansion follows the sum of terms of the derivative functions at the single point $a = 0$

$$P_\zeta(t) = \sum_{n=0}^{\infty} \frac{\zeta_{\text{het}}^{(n)}(a)}{n!} (t - a)^n \tag{A.4}$$

which is expanded to the first order and given by

$$P_\zeta(t) = C_1 - C_1 C_2 \frac{t}{\tau_c} \tag{A.5}$$

The process time τ_c will later cancel with a term included in C_2 as $C_2 \sim \tau_c^{-1}$. If terms of higher orders were considered, the process time would remain as an additional parameter.

The Taylor function was also expended to the second order term (not shown here) but it was indicated that the accuracy was not enhanced. Thus, the comparison of the first to terms in Eqs.A.3 and A.5 give the relations

$$p_0 \;=\; C_1 = A \text{ and} \tag{A.6}$$

$$p_1 \;=\; -C_1 C_2 \frac{1}{\tau_c} = -A c_0 \frac{D_T}{D} \frac{\left(\frac{\partial n}{\partial T}\right)_{p,w}}{\left(\frac{\partial n}{\partial w}\right)_{p,T}} \frac{1}{\tau_c} \; . \tag{A.7}$$

with the ratio of both Taylor parameters

$$\frac{p_1}{p_0} = -c_0 q^2 D_T \frac{\left(\frac{\partial n}{\partial T}\right)_{p,w}}{\left(\frac{\partial n}{\partial w}\right)_{p,T}} \tag{A.8}$$

where the relation for the mass diffusion coefficient $D = \left(q^2 \tau_c\right)^{-1}$ with the wave vector q is used. Finally, an expression for D_T was achieved which is independent of the concentration process time, τ_c, and the amplitude, A. The Taylor expression for D_T is

$$D_T = -\frac{p_1}{p_0} \cdot \frac{1}{q^2 c_0} \frac{\left(\frac{\partial n}{\partial T}\right)_{p,w}}{\left(\frac{\partial n}{\partial w}\right)_{p,T}} \; . \tag{A.9}$$

Fig.A.1 shows the heterodyne intensity signal versus time. The dashed black line is the Taylor function from Eq.A.5. The wave vector in the IR-TDFRS setup was determined to $q = 306010$ m^{-1}, and the increment of the refractive index with concentration and temperautre, $(\partial n / \partial w)_{p,T} = 0.13$ wt^{-1} and $(\partial n / \partial T)_{p,w} = 5.24 \cdot 10^{-5}$ T^{-1}, were determined in separate experiments.

INFLUENCE OF DYE ON MICROEMULSION SYSTEMS IN THE TDFRS SETUPS

The effect of ionic dye in a nonionic surfactant solution on the thermal diffusion behavior was discussed in Chapter 4. For a binary micellar solution it was shown that the dye only influenced the micellar concentration regime above the *cmc*. This effect was enhanced if the dye absorbed at the writing laser wavelength. The question emerged if this behavior could also be observed for o/w-microemulsion droplets.

First measurements of o/w-microemulsion droplets were performed for $H_2O/C_8/C_{12}E_5$ systems using the classical- and the IR-TDFRS setup, respectively. Basantol® Yellow was added to the microemulsion system to achieve an optical density of 2.0 cm^{-1} at 488 nm (which is equal to a volume fraction of $1.504 \cdot 10^{-7}$ mol/g Basantol® Yellow). In IR-TDFRS the samples were measured with and without dye.

It is expected that the ionic dye molecules are dissolved in water or attached to the surfactant layer of the droplet [39] where they are known to affect the molecular diffusion due to electrostatic interactions. We investigated the dye influence using a $H_2O/C_{8/10}$ (75/25)/$C_{12}E_5$ microemulsion with $\gamma_a = 0.03$ wt and $w_B = 0.0505$ wt. All measurements were performed in the 1ϕ region which showed the *efb* approximately at $T = 27.40$ °C. The starting temperature was 29.85 °C and after each measurement, the temperature was decreased by 0.40 K until the *efb* temperature was reached.

Fig.B.1 shows the determined Soret and diffusion coefficients and the hydrodynamic radius versus temperature. The top figure presents the hydrodynamic radius. The exponential

decay of the radius with decreasing temperature is indicated for the dye-free microemulsion. Comparing the results obtained by IR-TDFRS, it is assumed that the dye-containing sample consist of smaller droplets which are 2–10 times smaller than the aggregates of the dye-free sample. This difference is constant over a relatively large temperature range close to the *efb* and becomes larger above 29 °C. We assumed, that this is the critical temperature where the dye-free microemulsion changed shape. In contrast, this is hindered by the influence of the dye. The droplet size diverged stronger against the *ncb* in the absence of dye. Thus, it is predicted, that the ionic influence of the dye hindered the formation of aggregates above 20 nm in radius due to electrostatic repulsion. This behavior was also observed for the dye-containing sample in the classical TDFRS setup. In the classical setup, the dye absorbs on the wavelength of the writing laser which influenced the thermal diffusion behavior of the droplets: The thermal diffusion coefficient determined in IR-TDFRS is equal and almost temperature independent for the dye-containing and dye-free sample but in the classical setup, D_T increased linearly with temperature.

Consequently the Soret coefficient behaved as follows: S_T increased with temperature and diverged against the *ncb* for the dye-containing microemulsion in classical TDFRS and the dye-free microemulsion in IR-TDFRS. The increase was less pronounced for the dye-containing sample in IR-TDFRS. In the investigated temperature range, the Soret coefficient was the largest for the microemulsion measured in classical TDFRS, followed by the dye-free sample in IR-TDFRS and S_T was the smallest for the dye-containing sample in IR-TDFRS. At the *efb* the Soret coefficient was equal for all measurements.

The discrepancy in the classical setup is a matter of the laser wavelength. In this setup a second concentration process was induced due to the local heating of the dye-infected microemulsion droplets. A similar behavior was observed for nonionic micelles in water by Ning *et al.* [38, 39]. After the temperature profile was created, the microemulsion aggregates moved to the cold region, which led to a further increase in the heterodyne intensity signal. Then, induced by a local temperature profile around dye-infected droplets, the dye-infected droplets migrated to the warm. Assuming that the warm region is colder than the local temperature around the dye-infected droplets, this motion can be interpreted as a migration to the cold from the point of view of a droplet. This second concentration process caused a loss in the contrast of the refractive index profile and the diffraction signal decreased. After approximately 10 s a steady state was reached (see Fig.B.2). Fig.B.2 also indicates, that the change in the refractive index grating caused by the concentration process was more pronounced in the IR-TDFRS in the absence of dye which directly correlates to the difference in hydrodynamic radius (inset in Fig.B.2).
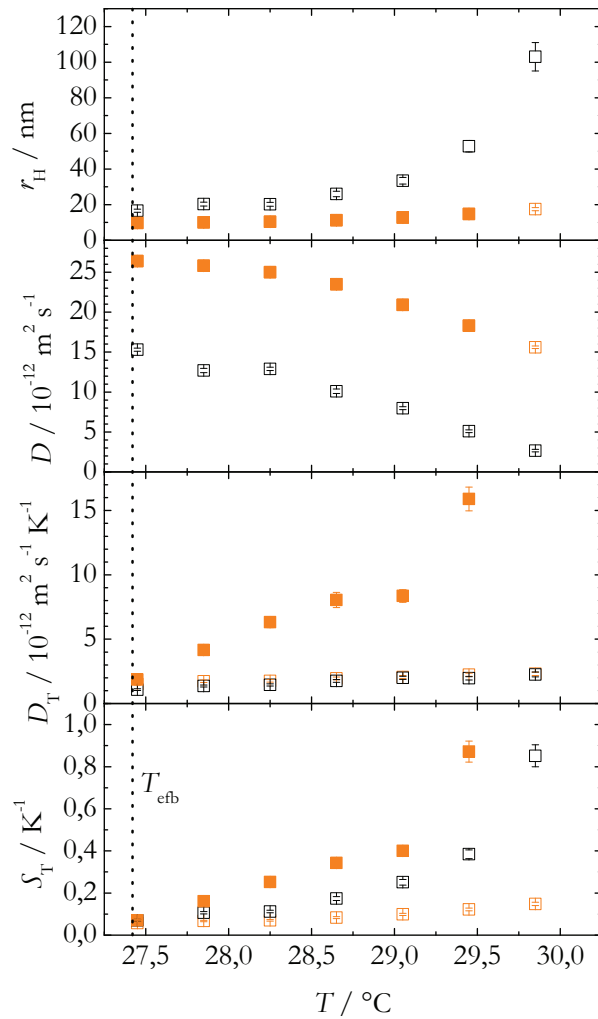
Figure B.1.: *From top to bottom: The temperature dependence of r_H, D, D_T and S_T for the microemulsion system $H_2O/C_{8,10}$ (75/25)/$C_{12}E_5$ with $\gamma_a = 0.03$ wt and $w_B = 0.0505$ wt. The vertical dotted line marks the efb. Symbols are filled (classical TDFRS) or open (IR-TDFRS). Sample with dye (orange) and without dye (black) were investigated.*
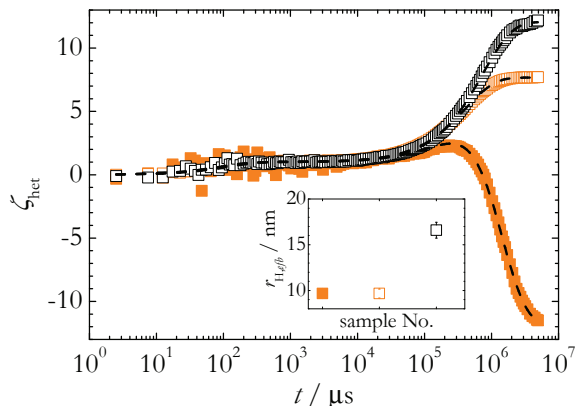
Figure B.2.: *Comparison of TFDRS measurements of the same microemulsion system $H_2O/C_{8,10}/C_{12}E_5$ with $\gamma_a = 0.03$ wt and $w_B = 0.0505$ wt at $T = 27.4$ °C. Symbols are filled (classical TDFRS) or open (IR-TDFRS) and the orange color indicates dye-containing samples while the black symbols represent measurements of dye-free samples. The sample in the classical TDFRS setup shows a second concentration mode while the samples in the IR-TDFRS setup indicate a single concentration plateau. Inset: the hydrodynamic radius at the* efb *of the dye-free sample is nearly twice of the radius of the dye-containing samples.*

The measurements from the classical TDFRS setup indicated a second concentration mode which made the analysis more difficult. To simplify the analysis, the calculated diffusivity, the process time and the amplitude of the single concentration process from IR-TDFRS measurements had been copied as initial values for the triple exponential function, which was used to analyze the classical TDFRS data, which requires two additional parameters: the amplitude and the equilibration time of the second concentration process. The fit procedure was repeated for several times. In each single repetition only an arbitrary pair of the five available parameters was set variable such that after innumerable number of repetitions, the fit function showed a sufficient correlation to the data points.

Contrarily to the o/w-aggregates, the w/o-aggregates were measured in the classical TD-FRS (and only there) by adding Quinizarin. The results (not shown here) did not show a second concentration mode. This indicated that the second mode effect was caused by charged molecules acting like a cosurfactant [38].

DETERMINATION OF THE TEMPERATURE OFFSET IN THE IR-TDFRS SETUP

Two interfering laser beams at 980 nm are used in the IR-TDFRS setup to write a thermal grating into the sample. The low absorption of water is used to convert the intensity grating into a temperature grating. It is suggested that the aqueous samples are locally heated by the laser. This heating cannot be detected by the temperature sensor underneath the sample position in the cell holder. The main problem is that microemulsions depend strongly on temperature and a small temperature variation can cause a phase transition. Thus, we have to ensure to which extend the samples are heated by the IR-laser. First remarks were made by Köhler and Rossmanith [24]. They calculated the additional sample heating based on the thermal conductivity $(1.4 \cdot 10^{-1}\,\mathrm{J\,cm^{-1}\,s^{-1}\,K^{-1}})$ and the thickness of the used cell window (1.25 mm), and the measured specific surface emissivity $(3.5\,\mathrm{mW^{-1}\,cm^{-2}\,K^{-1}})$ to be at 0.2 K.

To determine the temperature offset in the investigated microemulsions, we performed measurements in IR-TDFRS using a microemulsion for which the phase diagram was precisely investigated. The used microemulsion is a composition of water, n-octane and tetraethylene glycol monodecyl ether $(C_{10}E_4)$ with a mass fraction of oil to water of 50/50. The phase diagram was measured in cooperation with the group of Prof. Strey and is shown in Fig.C.1. Measurements in IR-TDFRS were performed with a mass fraction of surfactant to water at $\gamma = 0.154$ wt to determine the upper phase boundary from 1ϕ to $\overline{2}\phi$ as a measure of the intensity of the diffracted read-out beam. The boundary temperature
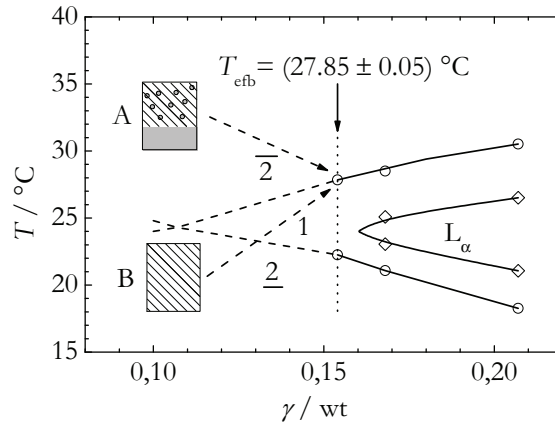
Figure C.1.: *The phase diagram of $H_2O/C_8/C_{10}E_4$. The mass fraction of water to n-octane is 50/50. The temperature is plotted versus the mass fraction of surfactant to water. At $\gamma = 0.154$ wt (dotted vertical line) the* efb *was determined at $T = (27.85 \pm 0.05)$ °C in a water bath. The insets sketch the microemulsion in the upper $\overline{2}\phi$ region with an occurring water excess phase (A) and in the 1ϕ region (B).*

was previously determined at $T = 27.85 \pm 0.05$ °C. It was expected that in the $\overline{2}\phi$ region the light scattering is higher than in 1ϕ because the $\overline{2}\phi$ region is turbid and the 1ϕ region is clear and transparent.

For our measurements in the IR-TDFRS setup the sample cell and the cell holder are thermostated to a temperature corresponding to where we find the $C_{10}E_4$ microemulsion in the 1ϕ region. The microemulsion was equilibrated in the 1ϕ region under stirring and filled into the cell. We started the measurements at a temperature in the 1ϕ region below the upper boundary and increased the temperature stepwise by +0.1 K. After each increase, the system was thermally equilibrated and we measured the intensity of the read-out beam for several minutes. The time average was taken. In the 1ϕ region, we read a count rate of approximately 190 kHz (at $T < 27.50$ °C). Additionally, we measured a high contrast of the heterodyne signal which indicated that the incoherent light scattering was small. At $T > T = 27.60$ °C the intensity was strongly increased by a factor of 25 and reached 4700 kHz. Simultaneously the contrast dropped (see Fig.C.2). The interpretation is that the scattered light gained in intensity and was more pronounced than the intensity of the diffracted light. This indicated that the sample was in the upper $\overline{2}\phi$ region. We determined the phase boundary at an average set temperature of $T = 27.55 \pm 0.05$ °C. This values is 0.3 K below the expected temperature and corresponds to a temperature
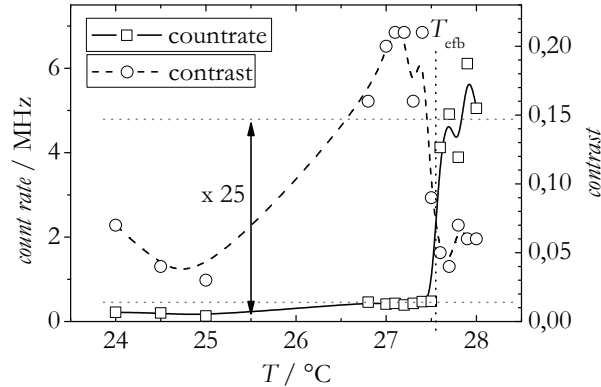
Figure C.2.: *The temperature dependence of the count rate (open squares, left axis) and of the contrast (open circles, right axis) is shown for the heterodyne intensity signal in the IR-TDFRS setup for the investigated $H_2O/C_8/C_{10}E_4$ microemulsion. The determined phase transition from 1ϕ to $\overline{2}\phi$ is found at $T = 27.55\,°C$ (vertical dotted line). The horizontal dotted lines are guides to the eyes and mark the average count rates in 1ϕ and $\overline{2}\phi$.*

offset in the IR-TDFRS setup which needs to be considered, if microemulsion systems are measured in this setup. To our best knowledge, we cannot determine how far the temperature offset changes with the water content in the microemulsion but we assume that the temperature offset can be adopted to all microemulsion samples.

We compared the hydrodynamic radius of a $C_{8/10}$ (50/50)-microemulsion determined by IR-TDFRS and DLS to check if the determined temperature offset allows a reliable data analysis. In Fig.C.3, the grey colored solid symbols present the original data from IR-TDFRS measurements and the black colored points are shifted in temperature by $+0.3$ K. Including this offset, the IR-TDFRS data fits with DLS data in the vicinity of the *efb* (dotted vertical line). To exclude systematic deviations in the hydrodynamic radius, the concentration process in the IR-TDFRS data was additionally analyzed using the Kohlrausch-Williams-Watts (KWW) method, which was used to analyze the DLS data. The difference between both, the standard (squares) and the KWW method (circles), is negligible and in the order of the error bars at low temperatures.
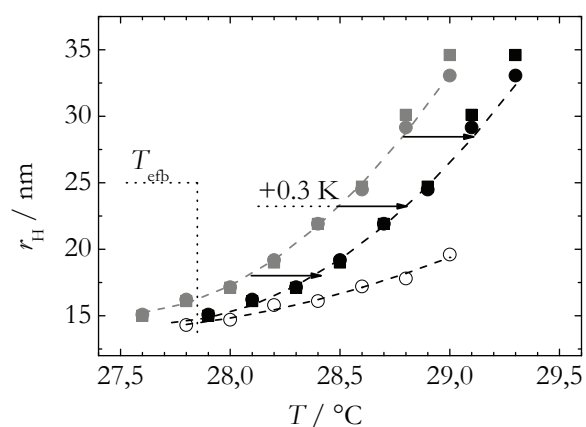
Figure C.3.: *The temperature dependence of the hydrodynamic radius is plotted for a*
$H_2O/C_{8/10}$ *(50/50)/*$C_{12}E_5$ *microemulsion measured by IR-TDFRS (solid symbols) and
DLS (open symbols). The radius without (grey) and with the temperature offset (black).
The vertical dotted line marks the* efb*.*

INFLUENCE OF WRITING LASER POWER IN THE TDFRS SETUP

Both TDFRS setups use interfering laser beams to write an optical grating into the sample. The classical TDFRS setup uses a 488 nm Ar-laser with a light intensity of 300 mW, the IR-TDFRS setup works with a 980 nm laser with an output of 1000 mW. A higher light intensity is required for the aqueous samples in the IR-TDFRS setup due to the lower absorption ($\alpha_{ir} = 0.18$ cm^{-1}) in comparison to the dye-containing samples in the classical setup with $\alpha_{class} = 2.0$ cm^{-1} which is of factor 10 higher. The main question is in how far the Soret coefficient is affected by the laser intensity.

We investigated the dependence of the thermal diffusion behavior on the light intensity in the classical TDFRS setup as the Ar-laser was easily to tune. A mixture of C_8G_1/H_2O with a surfactant mass fraction of 0.02 wt was used to which dye was added such that an optical density of 2.47 cm^{-1} was achieved. We performed measurements at 15 °C and varied the light intensity from $I_w = 237$ mW to 764 mW. The minimum intensity was slightly higher than the lasing threshold, whereas 764 mW was close to the maximum achievable output power of the Ar-laser. In Fig.D.1 the Soret and diffusion coefficients are plotted versus the light intensity. The measurements started at the highest light intensity. After each measurement, the intensity was stepwise decreased until the lowest light intensity was reached. Finally, the highest intensity measurement was repeated to ensure that the sample did not suffer from evaporation meanwhile.

An almost intensity independent behavior was observed for the mass diffusion coefficient,
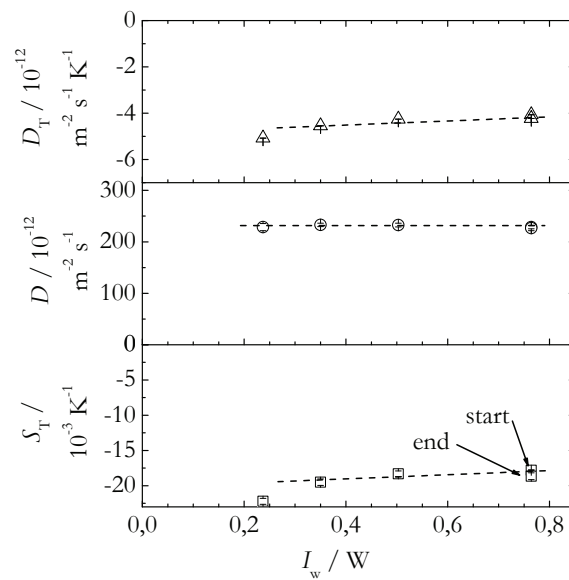
Figure D.1.: *Influence of the light intensity of the writing laser in the classical TDFRS setup on the Soret and diffusion coefficients. The sample is a C_8G_1/H_2O solution with $\gamma_a = 0.02$ wt at 15 °C. The first measurement (labeled as* start*) at 764 mW was repeated to check for evaporation effects (labeled as* end*) after measurements at different laser light powers were performed.*

while the thermal diffusion and Soret coefficient decreased with decreasing intensity below 300 mW. Above this value, they were independent from changes in the light intensity. This confirmed that the experimentally used light intensity, which varied between 300 mW and 600 mW as a consequence of the aging process of the laser, did not influence the thermal diffusion behavior of the investigated samples.

E

PURITY OF C_8G_2

The extremely low *cmc*, which was determined by the group in Köln for C_8G_2, was probably a consequence of impurities because the other determined critical micelle concentrations agreed with literature values, so that we could assume that the setup was reliable. In this chapter we want to discuss, why the surfactant is especially sensitive to impurities.

In the case of the glucosides, traces of *n*-octanol or further amounts of poly-glucosides were expected. The manufacturer pointed out that the amount of *n*-octanol was negligible as the surfactant was lyophilized. Hence, we focused on the determination of traces of poly-glucosides or other impurities by HPLC-MS and an absorption method.

HPLC-MS (high performance liquid chromatography with coupled mass spectroscopy) measurements were performed by Dr. Björn Thiele (ZCH, FZ Jülich), and indicated a low level of impurities. It was shown by Billian [372] that the alkyl-polyglucosides and their monomers, which were assumed to be present in the sample, are separable with this technique. For the preparation of the sample, 10.4 mg of C_8G_2 were dissolved in 10 ml pure water and diluted up to 230 μM before filling in the column. The applied flow rate in the columns was between 250 μl/min (column II) and 700 μl/min (column I). The required mass-to-charge ratio for the mass spectroscopy was accomplished by electrospray ionization and set to m/z=472 which related to the solution [M + NH$_4$] without HPLC. Once the mass spectroscopy parameters were calibrated, MS was connected to the HPLC eluent flow.

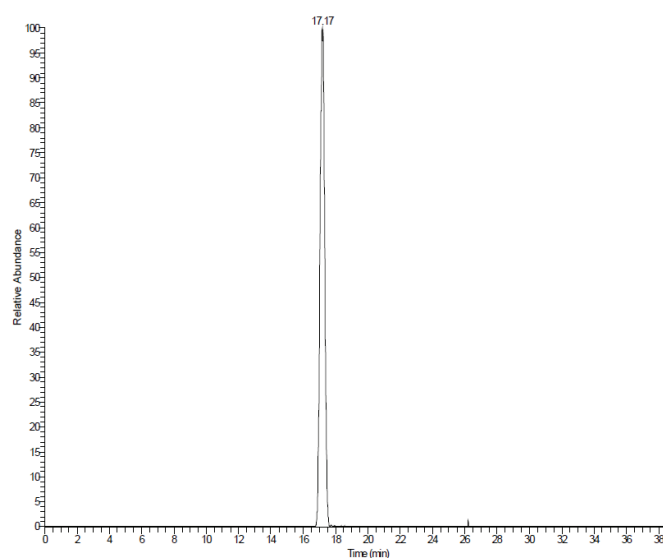|	column I	column II
column type	Nucleodex s-OH, 150 x 3 mm, 5 μm particle size (Macherey-Nagel)	Luna 3μ C18, 150 x 2 mm, 3 μm particle size (Phenomenex)
gradient by	A: 5 mM NH$_4$Ac (pH 4)	A: 5 mM NH$_4$Ac (pH 4)
	B: acetonitrile	B: methanol
MS method	ESI(+) (Electrospray-Ionization), Spray Voltage: 4000 V, Sheath Gas Pressure: 10; Aux Gas Pressure: 5; Capillary Temperature: 270 °C; tube Lens: 110 V.	

Table E.1.: *Specifications Columns of the HPLC method. HPLC-system: Agilent 1100. MS-system: Thermo Electron TSQ Quantum.*

Figs.E.1 and E.2 illustrate the relative abundance versus time measured with different columns. Details about the columns are given in Tab.E.1. The main peak in Fig.E.1 at 13.25 min (Fig.E.2: at 17.17 min) marks the eluting C_8G_2. Another shorter peak at smaller times in Fig.E.1 indicates a relatively lighter component, and the presence of two peaks at later times indicate larger components. The relative intensity of these secondary peaks is less than 2 % and only the most intense peak in Fig.E.1 at 20.9 min is also detected with column II in Fig.E.2 at 26.2 min.

The results promised only a low amount of impurities in the C_8G_2 sample but it could
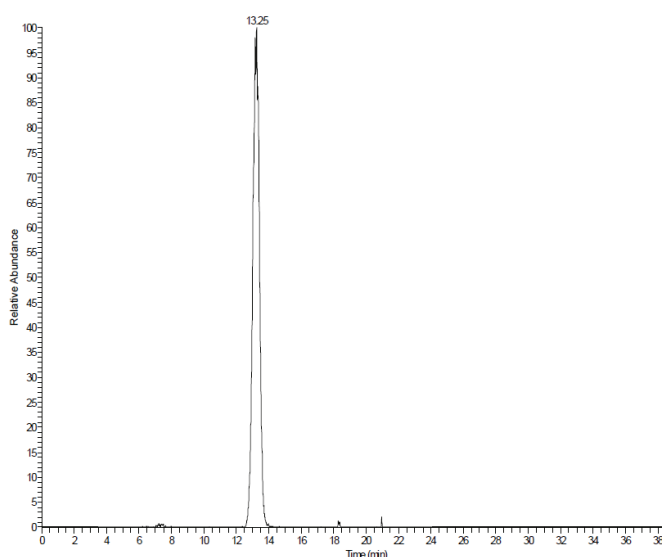
Figure E.1.: *The time resolution of the elute from HPLC-MS method using column I (see Tab.5.1). The main peak at 13.25 min corresponds to n–Octyl β–D–maltopyranoside.*

Figure E.2.: *The time resolution of the elute from HPLC-MS method using column II (see Tab.5.1). The main peak at 17.17 min corresponds to n–Octyl β–D–maltopyranoside.*

be expected that the impurities went to the interface and caused a change of the *cmc*. Depending on the column type, several smaller peaks were observed which could not be identified to a certain component.

LIST OF FIGURES

LIST OF TABLES

BIBLIOGRAPHY

[1] C. Ludwig. Diffusion zwischen ungleich erwärmten orten gleich zusammengesetzter lösungen. *Sitz. Ber. Akad. Wiss. Wien Math.-naturw. Kl*, 20:539, 1856.

[2] C. Soret. Sur l'état d'équilibre que prend au point de vue de sa concentration une dissolution saaline primitivement homogéne dont deux parties sont portées a des températures différentes. *Arch. Geneve*, 3:48–64, 1879.

[3] C. Soret. Influence de la température sur la distribution des sels dans leurs solutions. *C.R. Acad. Sci. Paris*, 91:289–291, 1880.

[4] C. Soret. Sur l'état d'équilibre que prend au point de vue de sa concentration une dissolution saaline primitivement homogéne dont deux parties sont portées a des températures différentes. *Ann. Chim. Phys.*, 22:293–297, 1881.

[5] A. L. Jones and R. W. Foreman. Liquid thermal diffusion of tall oil. *Ind. Eng. Chem.*, 44(9):2249–2253, 1952.

[6] W. J. Roos and W.M. Rutherford. Separation of xenon isotopes in thermal diffusion column. *J. Chem. Phys.*, 52(4):1684–1687, 1970.

[7] R. S. Norris. *Racing for the bomb – General Leslie R. Groves, The Manhattan Projectś Indispensable Man*. Steerforth Press, 1 edition, 2002.

[8] J. G. Hershberg. Racing for the bomb: General leslie r. groves, the manhattan projectś indispensable man. *Bull. At. Sci.*, 58(3):63–65, 2002.

[9] D. R. Caldwell and S. A. Eide. Separation of seawater by soret diffusion. *Deep-Sea Res.*, 32(8):965–982, 1985.

[10] L. Monchick. Thermal-diffusion in ionized-gases and planetary and solar processes. *Johns Hopkins Apl. Technical. Digest.*, 7(1):39–41, 1986.

[11] W. Larcher. *Physiological Plant Ecology*, volume XX of *Ecophysiology and Stress Physiology of Functional Groups*. Springer Verlag, Berlin Heidelberg New York, 4th edition, 2003.

[12] K. Clusius and G. Dickel. Neues verfahren zur gasentmischung und isotopentrennung. *Naturwissenschaften*, 26:546, 1938.

[13] H. Korsching and K. Wirtz. Trennung vonflüssigkeitsgemischen durch thermodiffusion. *Ber. Dtsch. Chem. Ges.*, 73(3):249–269, 1940.

[14] L. Guczi and H. J. V. Tyrrell. A modified type of thermal-diffusion cell and its application to measurement of soret coefficients for solutions of carbon tetrachloride in benzene. *J. Chem. Soc.*, (Nov):6576–6586, 1965.

[15] G. Farsang and H. J. V. Tyrrell. Thermal diffusion factors and heats of transfer in benzene-methanol and benzene-ethanol mixtures at 25 degrees. *J. Chem. Soc. A*, (12):1839–1843, 1969.

[16] M. Giglio and A. Vendramini. Thermal-diffusion measurements near a consolute critical-point. *Phys. Rev. Lett.*, 34(10):561–564, 1975.

[17] M. Giglio and A. Vendramini. Soret-type motion of macromolecules in solution. *Phys. Rev. Lett.*, 38(1):26–30, 1977.

[18] J. P. Gordon, R. C. C. Leite, R. S. Moore, S. P. S. Porto, and J. R. Whinnery. Long-transient effects in lasers with inserted liquid samples. *J. Appl. Phys.*, 36(1):3–8, 1965.

[19] J. C. Giddings, Y. H. Yoon, and M. N. Myers. Evaluation and comparison of gel-permeation chromatography and thermal field-flow fractionation for polymer separations. *Anal. Chem.*, 47(1):126–131, 1975.

[20] J. C. Giddings, K. D. Caldwell, and M. N. Myers. Thermal-diffusion of polystyrene in 8 solvents by an improved thermal field-flow fractionation methodology. *Macromolecules*, 9(1):106–112, 1976.

[21] D. Braun and A. Libchaber. Trapping of dna by thermophoretic depletion and convection. *Phys. Rev. Lett.*, 89(18):188103, 2002.

[22] K. Thyagarajan and P. Lallemand. Determination of thermal-diffusion ratio in a binary mixture by forced rayleigh-scattering. *Opt. Commun.*, 26(1):54–57, 1978.

[23] R. Schäfer, A. Becker, and W. Köhler. Stochastic thermal-diffusion forced rayleigh scattering. *Int. J. Thermophys.*, 20(1):1–18, 1999.

[24] W. Köhler and P. Rossmanith. Aspects of thermal-diffusion forced rayleigh-scattering - heterodyne-detection, active phase tracking, and experimental constraints. *J. Phys. Chem.*, 99(16):5838–5847, 1995.

[25] W. Köhler, C. Rosenauer, and P. Rossmanith. Holographic grating study of mass and thermal-diffusion of polystyrene toluene solutions. *Int. J. Thermophys.*, 16(1):11–21, 1995.

[26] S. Chapman. The kinetic theory of simple and composite monatomic gases viscosity, thermal conduction, and diffusion. *Proc. Roy. Soc. A*, 93(646):1–20, 1916.

[27] D. Enskog. Bemerkung zu einer fundamentalgleichung in der kinetischen gastheorie. *Phys. Z.*, 12(58):533–539, 1911.

[28] A. Würger. Molecular-weight dependent thermal diffusion in dilute polymer solutions. *Phys. Rev. Lett.*, 102(7):078302, 2009.

[29] J. K. G. Dhont and W. J. Briels. Single-particle thermal diffusion of charged colloids: Double-layer theory in a temperature gradient. *Eur. Phys. J. E*, 25(1):61–76, 2008.

[30] A. Würger. Heat capacity-driven inverse soret effect. *Europhys. Lett.*, 74(4):658–664, 2006.

[31] J. Luettmer-Strathmann. Lattice model for thermodiffusion in polymer solutions. *Int. J. Thermophys.*, 26(6):1693–1707, 2005.

[32] J. Luettmer-Strathmann. Two-chamber lattice model for thermodiffusion in polymer solutions. *J. Chem. Phys.*, 119(5):2892–2902, 2003.

[33] D. Vigolo, S. Buzzaccaro, and R. Piazza. Thermophoresis and thermoelectricity in surfactant solutions. *Langmuir*, 26(11):7792–7801, 2010.

[34] M. P. Santos, S. L. Gomez, E. Bringuier, and A. M. F. Neto. Thermodiffusion in a multicomponent lyotropic mixture in the vicinity of the critical micellar concentration by using the z-scan technique. *Phys. Rev. E*, 77(1):011403, 2008.

[35] D. Vigolo, G. Brambilla, and R. Piazza. Thermophoresis of microemulsion droplets: Size dependence of the soret effect. *Phys. Rev. E*, 75(4):040401, 2007.

[36] R. Piazza. Thermal diffusion in ionic micellar solutions. *Phil. Mag.*, 83(17-18):2067–2085, 2003.

[37] R. Piazza and A. Guarino. Soret effect in interacting micellar solutions. *Phys. Rev. Lett.*, 88(20):208302, 2002.

[38] H. Ning, S. Datta, T. Sottmann, and S. Wiegand. Soret effect of nonionic surfactants in water studied by different transient grating setups. *J. Phys. Chem. B*, 112(35):10927–10934, 2008.

[39] H. Ning, R. Kita, H. Kriegs, J. Luettmer-Strathmann, and S. Wiegand. Thermal diffusion behavior of nonionic surfactants in water. *J. Phys. Chem. B*, 110(22):10746–10756, 2006.

[40] H. Ning, R. Kita, and S. Wiegand. Soret effect in a nonionic surfactant. *Prog. Colloid Polym. Sci.*, 133:111–115, 2005.

[41] N. Arnaud and J. Georges. Thermal lens spectrometry in aqueous solutions of brij 35: Investigation of micelle effects on the time-resolved and steady-state signals. *Spectrochim. Acta, Part A: Mol. Biomol. Spectros.*, 57(5):1085–1092, 2001.

[42] H. Ning, J. Buitenhuis, J. K. G. Dhont, and S. Wiegand. Thermal diffusion behavior of hard-sphere suspensions. *J. Chem. Phys.*, 125(20):204911, 2006.

[43] S. A. Putnam and D. G. Cahill. Transport of nanoscale latex spheres in a temperature gradient. *Langmuir*, 21(12):5317–5323, 2005.

[44] S. Alves, G. Demouchy, A. Bee, D. Talbot, A. Bourdon, and A. M. F. Neto. Investigation of the sign of the soret coefficient in different ionic and surfacted magnetic colloids using forced rayleigh scattering and single-beam z-scan techniques. *Phil. Mag.*, 83(17-18):2059–2066, 2003.

[45] M. E. Schimpf and S. N. Semenov. Mechanism of polymer thermophoresis in non-aqueous solvents. *J. Phys. Chem. B*, 104(42):9935–9942, 2000.

[46] B. J. de Gans, R. Kita, S. Wiegand, and J. Luettmer-Strathmann. Unusual thermal diffusion in polymer solutions. *Phys. Rev. Lett.*, 91(24):245501, 2003.

[47] B. J. de Gans, R. Kita, B. Muller, and S. Wiegand. Negative thermodiffusion of polymers and colloids in solvent mixtures. *J. Chem. Phys.*, 118(17):8073–8081, 2003.

[48] S. Iacopini, R. Rusconi, and R. Piazza. The "macromolecular tourist": Universal temperature dependence of thermal diffusion in aqueous colloidal suspensions. *Eur. Phys. J. E*, 19(1):59–67, 2006.

[49] S. Duhr, S. Arduini, and D. Braun. Thermophoresis of dna determined by microfluidic fluorescence. *Eur. Phys. J. E*, 15(3):277–286, 2004.

[50] M. Hartung, J. Rauch, and W. Köhler. Thermal diffusion of dilute polymer solutions: The role of solvent viscosity. *J. Chem. Phys.*, 125(21):214904, 2006.

[51] B. Rousseau, C. Nieto-Draghi, and J. Bonet Avalos. The role of molecular interaction in the change of sign of the soret coefficient. *Europhys. Lett.*, 67(6):976–982, 2004.

[52] V. Cuny, M. Antoni, M. Arbelot, and L. Liggieri. Numerical analysis of nonionic surfactant monolayers at water/air interfaces. *J. Phys. Chem. B*, 108(35):13353–13363, 2004.

[53] S. Bogusz, R. M. Venable, and R. W. Pastor. Molecular dynamics simulations of octyl glucoside micelles: Dynamic properties. *J. Phys. Chem. B*, 105(35):8312–8321, 2001.

[54] S. Bogusz, R. M. Venable, and R. W. Pastor. Molecular dynamics simulations of octyl glucoside micelles: Structural properties. *J. Phys. Chem. B*, 104(23):5462–5470, 2000.

[55] A. Würger. Temperature dependence of the soret motion in colloids. *Langmuir*, 25(12):6696–6701, 2009.

[56] S. N. Rasuli and R. Golestanian. Soret motion of a charged spherical colloid. *Phys. Rev. Lett.*, 101(10):108301 (4pp), 2008.

[57] E. Ruckenstein. Can phoretic motions be treated as interfacial-tension gradient driven phenomena. *J. Colloid Interface Sci.*, 83(1):77–81, 1981.

[58] B. Arlt, S. Datta, T. Sottmann, and S. Wiegand. Soret effect of n-octyl β-d-glucopyranoside (C_8G_1) in water around the critical micelle concentration. *J. Phys. Chem. B*, 114(6):2118–2123, 2010.

[59] P. Polyakov and S. Wiegand. Systematic study of the thermal diffusion in associated mixtures. *J. Chem. Phys.*, 128(3):034505 (7pp), 2008.

[60] P. Blanco, H. Kriegs, B. Arlt, and S. Wiegand. Thermal diffusion of oligosaccharide solutions: The role of chain length and structure. *J. Phys. Chem. B*, 114(33):10740–10747, 2010.

[61] R. Kita, G. Kircher, and S. Wiegand. Thermally induced sign change of soret coefficient for dilute and semidilute solutions of poly. n-isopropylacrylamide in ethanol. *J. Chem. Phys.*, 121(18):9140–9145, 2004.

[62] R. Kita, S. Wiegand, and J. Luettmer-Strathmann. Sign change of the soret coefficient of poly(ethylene oxide) in water/ethanol mixtures observed by tdfrs. *J. Chem. Phys.*, 121(8):3874–3885, 2004.

[63] G. Wittko and W. Köhler. universal isotope effect in thermal diffuison of mixtures containing cyclohexane and cyclohexane-d_{12}. *J. Chem. Phys.*, 123(1):014506 (6pp), 2005.

[64] S. Iacopini and R. Piazza. Thermophoresis in protein solutions. *Europhys. Lett.*, 63(2):247–253, 2003.

[65] S. Duhr and D. Braun. Thermophoretic depletion follows boltzmann distribution. *Phys. Rev. Lett.*, 96(16):168301 (4pp), 2006.

[66] M. Braibanti, D. Vigolo, and R. Piazza. Does thermophoretic mobility depend on particle size? *Phys. Rev. Lett.*, 100(10):108303 (4pp), 2008.

[67] S. A. Putnam, D. G. Cahill, and G. C. L. Wong. Temperature dependence of thermodiffusion in aqueous suspensions of charged nanoparticles. *Langmuir*, 23(18):9221–9228, 2007.

[68] A. Würger. Thermal non-equilibrium transport in colloids. *Rep. Prog. Phys.*, 73(12):126601 (35 pp), 2010.

[69] T. H. Anderson, S. H. Donaldson, H. B. Zeng, and J. N. Israelachvili. Direct measurement of double-layer, van der waals, and polymer depletion attraction forces between supported cationic bilayers. *Langmuir*, 26(18):14458–14465, 2010.

[70] B. F. Qiao and D. L. Zhao. Van der waals condensed behavior of polymer fluids. *Chem. J. Chinese. U*, 27(9):1779–1781, 2006.

[71] J. K. G. Dhont. Thermodiffusion of interacting colloids. i. a statistical thermodynamics approach. *J. Chem. Phys.*, 120(3):1632–1641, 2004.

[72] J. K. G. Dhont. Thermodiffusion of interacting colloids. ii. a microscopic approach. *J. Chem. Phys.*, 120(3):1642–1653, 2004.

[73] Y. Tamai, H. Tanaka, and K. Nakanishi. Molecular dynamics study of polymer-water interaction in hydrogels .1. hydrogen-bond structure. *Macromolecules*, 29(21):6750–6760, 1996.

[74] Y. Tamai, H. Tanaka, and K. Nakanishi. Molecular dynamics study of polymer-water interaction in hydrogels .2. hydrogen-bond dynamics. *Macromolecules*, 29(21):6761–6769, 1996.

[75] S. Wiegand, H. Ning, and H. Kriegs. Thermal diffusion forced rayleigh scattering setup optimized for aqueous mixtures. *J. Phys. Chem. B*, 111(51):14169–14174, 2007.

[76] M. Kahlweit and R. Strey. Phase-behavior of ternary-systems of the type h2o-oil-nonionic amphiphile (microemulsions). *Angew. Chem. Int. Ed.*, 24(8):654–668, 1985.

[77] K. Clusius and G. Dickel. Zur trennung der chlorisotope. *Naturwissenschaften*, 27:148–149, 1939.

[78] L. Waldmann. The theory of the gas separation procedure of clusius and dickel. *Naturwissenschaften*, 27(14):230–231, 1939.

[79] GlobalSecurity.org. Thermal diffusion uranium enrichment, 2005.

[80] F. Settle. Nuclear chemistry uranium enrichment, 2005.

[81] J. P. G. Villaluenga, B. Seoane, V. M. Barragan, and C. Ruiz-Bauza. Thermo-osmosis of mixtures of water and methanol through a nafion membrane. *J. Membr. Sci.*, 274(1-2):116–122, 2006.

[82] M. Tasaka and H. Futamura. The effect of temperature on thermoosmosis. *J. Membr. Sci.*, 28(2):183–190, 1986.

[83] C. Fernández-Pineda and M. I. Vázquez-Gonzalez. Temperature-dependence of thermo-osmosis - a solution model. *J. Chem. Soc., Faraday Trans. 1*, 85(5):1019–1025, 1989.

[84] P. G. Brewer, T. R. S. Wilson, J. W. Murray, R. G. Munns, and C. D. Densmore. Hydrographic observations on red-sea brines indicate a marked increase in temperature. *Nature*, 231(5297):37–38, 1971.

[85] Z. S. A. Rehim and M. A. Ziada. Thermal behavior study of salt-gradient solar pond located in cairo. *Energ Source Part A*, 30(4):349–360, 2008.

[86] C. Nielsen, A. Akbarzadeh, J. Andrews, H.R.L. Becerra, and P. Golding. The history of solar pond science and technology. In *Proceedings of the 2005 Solar World Conference*.

[87] J. Andrews and A. Akbarzadeh. Enhancing the thermal efficiency of solar ponds by extracting heat from the gradient layer. *Solar Energy*, 78(6):704–716, 2005.

[88] J. Srinivasan. Solar pond technology. *Sadhana-Acad. Proc. Eng. Sci.*, 18:39–55, 1993.

[89] P. M. Shiundu and J. C. Giddings. Influence of bulk and surface-composition on the retention of colloidal particles in thermal field-flow fractionation. *J. Chromatogr. A*, 715(1):117–126, 1995.

[90] M. N. Myers, P. Chen, and J. C. Giddings. Polymer separation and molecular-weight distribution by thermal field-flow fractionation. *ACS Sym. Ser.*, 521:47–62, 1993.

[91] M. Martin and R. Reynaud. Polymer analysis by thermal field-flow fractionation. *Anal. Chem.*, 52(14):2293–2298, 1980.

[92] J. C. Giddings, L. K. Smith, and M. N. Myers. Thermal field-flow fractionation - extension to lower molecular-weight separations by increasing liquid temperature-range using a pressurized system. *Anal. Chem.*, 47(14):2389–2394, 1975.

[93] J. Janca. Polarization, steric, and focusing micro-thermal field-flow fractionation principles, theory, instrumentation, and applications in polymers and particles analysis. *Anal. Chim. Acta*, 540(1):187–196, 2005.

[94] G. Stegeman, A. C. Vanasten, J. C. Kraak, H. Poppe, and R. Tijssen. Comparison of resolving power and separation time in thermal field-flow fractionation, hydrodynamic chromatography, and size-exclusion chromatography. *Anal. Chem.*, 66(7):1147–1160, 1994.

[95] J. J. Kirkland and S. W. Rementer. Polymer molecular-weight distributions by thermal field flow fractionation using mark-houwink constants. *Anal. Chem.*, 64(8):904–913, 1992.

[96] J. J. Kirkland, S. W. Rementer, and W. W. Yau. Molecular-weight distributions of polymers by thermal field flow fractionation with exponential temperature programming. *Anal. Chem.*, 60(7):610–616, 1988.

[97] H. Cölfen and M. Antonietti. *Field-flow fractionation techniques for polymer and colloid analysis*, volume 150 of *Adv. Polym. Sci.*, pages 67–187. 2000.

[98] K. I. Morozov. Soret effect in molecular mixtures. *Phys. Rev. E*, 79(3):031204, 2009.

[99] R. Piazza and A. Parola. Thermophoresis in colloidal suspensions. *J. Phys. Condens. Matter*, 20(15):153102–153120, 2008.

[100] E. Bringuier and A. Bourdon. Colloid transport in nonuniform temperature. *Phys. Rev. E*, 67(1):011404 (6pp), 2003.

[101] K.I. Morozov. On the theory of the soret effect in colloids. In W. Köhler and S. Wiegand, editors, *Thermal Nonequilibrium Phenomena in Fluid Mixtures*, volume LNP 584 of *Lect. Notes Phys.*, pages 38–60. Springer, Berlin, 2002.

[102] D. Reith and F. Müller-Plathe. On the nature of thermal diffusion in binary lennard-jones liquids. *J. Chem. Phys.*, 112(5):2436–2443, 2000.

[103] K.I. Morozov. Thermodiffusion in magnetic colloids. *J. Magn. Magn. Mater.*, 201:248–251, 1999.

[104] J. Keizer. *Statistical Thermodynamics of Nonequilibrium Processes*. Springer-Verlag, Berlin, Heidelberg, New York, 1st edition, 1987.

[105] S.R. de Groot and P. Mazur. *Non-equilibrium Thermodynamics*. Dover, New York, 1984.

[106] A. Perronace, C. Leppla, F. Leroy, B. Rousseau, and S. Wiegand. Soret and mass diffusion measurements and molecular dynamics simulations of n-pentane-n-decane mixtures. *J. Chem. Phys.*, 116(9):3718–3729, 2002.

[107] A. Boushehri and A. Abbaspour. Diffusion thermo-effect in gases (the dufour effect). *Bull. Chem. Soc. Jpn.*, 52(7):2097–2098, 1979.

[108] P. Atkins and J. de Paula. *Atkins Physical Chemistry*. Oxford University Press, Oxford, 7th edition, 2002.

[109] A. Firoozabadi, K. Ghorayeb, and K. Shukla. Theoretical model of thermal diffusion factors in multicomponent mixtures. *Aiche J.*, 46(5):892–900, 2000.

[110] S. Chapman and F.W. Dootson. A note on thermal diffusion. *Phil. Mag.*, 33(193-98):248–253, 1917.

[111] H. Vanbeijeren. Equilibrium distribution of hard-sphere systems and revised enskog theory. *Phys. Rev. Lett.*, 51(17):1503–1505, 1983.

[112] K. Wada, A. Suzuki, H. Sato, and R. Kikuchi. Soret effect in solids. *J. Phys. Chem. Solids*, 46(10):1195–1205, 1985.

[113] S. A. Akbar, M. Kaburagi, and H. Sato. Soret effect in solid. 2. *J. Phys. Chem. Solids*, 48(6):579–586, 1987.

[114] V. Y. Rudyak and S. L. Krasnolutskii. On thermal diffusion of nanoparticles in gases. *Tech. Phys.*, 55(8):1124–1127, 2010.

[115] K. Harstad. Modeling the soret effect in dense media mixtures. *Ind. Eng. Chem. Res.*, 48(15):6907–6915, 2009.

[116] M. Zhang and F. Müller-Plathe. The soret effect in dilute polymer solutions: Influence of chain length, chain stiffness, and solvent quality. *J. Chem. Phys.*, 125(12):124903 (6pp), 2006.

[117] C. Nieto-Draghi, J. B. Avalos, and B. Rousseau. Computing the soret coefficient in aqueous mixtures using boundary driven nonequilibrium molecular dynamics. *J. Chem. Phys.*, 122(11):114503 (8 pp), 2005.

[118] B. Hafskjold. Computer Simulations of Thermal Diffusion in Binary Fluid Mixtures. In W. Köhler and S. Wiegand, editors, *Thermal nonequilibrium phenomena in fluid mixtures*, Lecture Notes in Physics, pages 3–23, Heidelberg, 2002. Springer.

[119] J. M. Kincaid and B. Hafskjold. Thermal-diffusion factors for the lennard-jones spline system. *Mol. Phys.*, 82(6):1099–1114, 1994.

[120] G. Galliero, M. Bugel, B. Duguay, and F. Montel. Mass effect on thermodiffusion using molecular dynamics. *J. Non-Equilib. Thermodyn.*, 32(3):251–258, 2007.

[121] V. S. Vikhrenko, G. S. Bokun, D. V. Gapanjuk, and Y. G. Groda. Thermal diffusion of interacting lattice gases. *Solid State Ionics*, 157(1-4):221–226, 2003.

[122] G. Galliero and S. Volz. Thermodiffusion in model nanofluids by molecular dynamics simulations. *J. Chem. Phys.*, 128(6):064505 (8pp), 2008.

[123] J.L. Anderson. Colloid transport by interfacial forces. *Ann. Rev. Fluid Mech.*, 21:61–99, 1989.

[124] B. Derjaguin, N. Churaev, and V. Muller. *Surface Forces*. Kluwer Academic / Plenum, New York, 1st edition, 1987.

[125] S. Duhr and D. Braun. Why molecules move along a temperature gradient. *P. Natl. Acad. Sci.*, 103(52):19678–19682, 2006.

[126] N. Ghofraniha, G. Ruocco, and C. Conti. Collective thermal diffusion of silica colloids studied by nonlinear optics. *Langmuir*, 25(21):12495–12500, 2009.

[127] J. K. G. Dhont, S. Wiegand, S. Duhr, and D. Braun. Thermodiffusion of charged colloids: Single-particle diffusion. *Langmuir*, 23(4):1674–1683, 2007.

[128] S. Fayolle, T. Bickel, and A. Würger. Thermophoresis of charged colloidal particles. *Phys. Rev. E*, 77(4):041404 (12pp), 2008.

[129] S. Fayolle, T. Bickel, S. Le Boiteux, and A. Würger. Thermaldiffusion of charged micelles. *Phys. Rev. Lett.*, 95(20):208301–1–208304–4, 2005.

[130] S. Wiegand. Thermal diffusion in liquid mixtures and polymer solutions. *J. Phys. Condens. Matter*, 16(10):R357–R379, 2004.

[131] S. Wiegand, H. Ning, and R. Kita. Universal concentration dependence of the soret coefficient in aqueous systems. *J. Non-Equilib. Thermodyn.*, 32(3):193–201, 2007.

[132] P. Polyakov, M. Zhang, F. Müller-Plathe, and S. Wiegand. Thermal diffusion measurements and simulations of binary mixtures of spherical molecules. *J. Chem. Phys.*, 127(1):014502, 2007.

[133] P. Polyakov, J. Luettmer-Strathmann, and S. Wiegand. Study of the thermal diffusion behavior of alkane/benzene mixtures by thermal diffusion forced rayleigh scattering experiments and lattice model calculations. *J. Phys. Chem. B*, 110(51):26215–26224, 2006.

[134] A. L. Jones and E. C. Milberger. Separation of organic liquid mixtures by thermal diffusion. *Ind. Eng. Chem.*, 45(12):2689–2696, 1953.

[135] R. D. Trengove, H. L. Robjohns, M. L. Martin, and P. J. Dunlop. The pressure dependences of the thermal-diffusion factors of the systems he-ar, he-co$_2$ and he-sf6 at 300-k. *Physica A*, 108(2-3):502–510, 1981.

[136] W. W. Watson and D. Woernley. Thermal diffusion with ammonia. *Phys. Rev.*, 63(5-6):181–184, 1943.

[137] K. E. Grew. Change of sign of the thermal diffusion factor. *Nature*, 150:320, 1942.

[138] S. Chapman. Dependence of thermal diffusion on the concentration ratio. *Nature*, 146(3700):431, 1940.

[139] S. Chapman. The characteristics of thermal diffusion. *Proc. R. Soc. London, Ser. A*, 177(A968):38–62, 1940.

[140] R. Kita, P. Polyakov, and S. Wiegand. Ludwig-soret effect of poly(n-isopropylacrylamide): Temperature dependence study in monohydric alcohols. *Macromolecules*, 40(5):1638–1642, 2007.

[141] C. Debuschewitz and W. Köhler. Molecular origin of thermal diffusion in benzene plus cyclohexane mixtures. *Phys. Rev. Lett.*, 87(5):055901 (4pp), 2001.

[142] G. Wittko and W. Köhler. Influence of isotopic substitution on the diffusion and thermal diffusion coefficient of binary liquids. *Eur. Phys. J. E*, 21(4):283–291, 2006.

[143] M. Klein and S. Wiegand. The soret effect of mono-, di- and tri-glycols in ethanol. *Phys. Chem. Chem. Phys.*, accepted:DOI: 10.1039/c1cp00022e, 2011.

[144] A. Königer, B. Meier, and W. Köhler. Measurement of the soret, diffusion, and thermal diffusion coefficients of three binary organic benchmark mixtures and of ethanol-water mixtures using a beam deflection technique. *Philos. Mag.*, 89(10):907–923, 2009.

[145] J. F. Dutrieux, J. K. Platten, G. Chavepeyer, and M. M. Bou-Ali. On the measurement of positive soret coefficients. *J. Phys. Chem. B*, 106(23):6104–6114, 2002.

[146] K. J. Zhang, M. E. Briggs, R. W. Gammon, and J. V. Sengers. Optical measurement of the soret coefficient and the diffusion coefficient of liquid mixtures. *J. Chem. Phys.*, 104(17):6881–6892, 1996.

[147] P. Kolodner, H. Williams, and C. Moe. Optical measurement of the soret coefficient of ethanol water solutions. *J. Chem. Phys.*, 88(10):6512–6524, 1988.

[148] P. F. Vanvelden, H. G. P. van der Voort, and C. J. Gorter. Etude sur la diffusion thermique dans des melanges liquides alcool-eau au moyen de la methode thermogravitationnelle de separation. *Physica*, 12(2-3):151–162, 1946.

[149] P. A. Artola and B. Rousseau. Microscopic interpretation of a pure chemical contribution to the soret effect. *Phys. Rev. Lett.*, 98(12):125901 (4pp), 2007.

[150] G. Wittko and W. Köhler. On the temperature dependence of thermal diffusion of liquid mixtures. *Eur. Phys. Lett.*, 78(4):46007–46013, 2007.

[151] I. Prigogine, L. Debrouckere, and R. Amand. Recherches sur la thermodiffusion en phase liquide. 2. *Physica*, 16(11-1):851–860, 1950.

[152] P. A. Artola, B. Rousseau, and G. Galliero. A new model for thermal diffusion: Kinetic approach. *Journal of the American Chemical Society*, 130(33):10963–10969, 2008.

[153] H. Ning and S. Wiegand. Experimental investigation of the soret effect in acetone/water and dimethylsulfoxide/water mixtures. *J. Chem. Phys.*, 125(22):221102, 2006.

[154] R. Piazza, S. Iacopini, and B. Triulzi. Thermophoresis as a probe of particle-solvent interactions: The case of protein solutions. *Phys. Chem. Chem. Phys.*, 6:1616–1622, 2004.

[155] J. Rauch and W. Köhler. On the molar mass dependence of the thermal diffusion coefficient of polymer solutions. *Macromolecules*, 38:3571–3573, 2005.

[156] J. Rauch and W. Köhler. Diffusion and thermal diffusion of semidilute to concentrated solutions of polystyrene in toluene in the vicinity of the glass transition. *Phys. Rev. Let.*, 88(18):185901, 2002.

[157] K. J. Zhang, M. E. Briggs, R. W. Gammon, J. V. Sengers, and J. F. Douglas. Thermal and mass diffusion in a semidilute good solvent-polymer solution. *J. Chem. Phys.*, 111(5):2270–2282, 1999.

[158] G. Rehage, O. Ernst, and J. Fuhrmann. Fickian and non-fickian diffusion in high polymer systems. *Discuss Faraday Soc*, 1-278(49):208–221, 1970.

[159] J. K. Platten and P. Costesèque. Charles soret. a short biography - on the occasion of the hundredth anniversary of his death. *Eur. Phys. J. E*, 15(3):235–239, 2004.

[160] P. Costesèque and J. C. Loubet. Measuring the soret coefficient of binary hydrocarbon mixtures in packed thermogravitational columns (contribution of toulouse university to the benchmark test). *Phil. Mag.*, 83(17-18):2017–2022, 2003.

[161] W. M. Rutherford. Thermal diffusion column transport coefficients for mass 28 and mass 29 carbon monoxide. *J. Chem. Phys.*, 42(3):869–872, 1965.

[162] W.M. Rutherford and K. J. Kaminski. Experimental verification of theory of thermal-diffusion column. *J. Chem. Phys.*, 47(12):5427–5432, 1967.

[163] W.M. Rutherford, F. W. Weyler, and C. F. Eck. Apparatus for thermal diffusion separation of stable gaseous isotopes. *Rev. Sci. Instrum.*, 39(1):94–100, 1968.

[164] W.M. Rutherford. Thermal-diffusion column transport coefficients for isotopically substituted methane. *J. Chem. Phys.*, 46(3):900–905, 1967.

[165] W. M. Rutherford, W. J. Roos, and K. J. Kaminski. Experimental verification of thermal diffusion column theory as applied to separation of isotopically substituted nitrogen and isotopically substituted oxygen. *J. Chem. Phys.*, 50(12):5359–5365, 1969.

[166] H. F. John and H. E. Bent. Separation of organic solutions by thermal diffusion. *J. Phys. Chem.*, 60(11):1524–1528, 1956.

[167] A. Leahy-Dios, M. M. Bou-Ali, J. K. Platten, and A. Firoozabadi. Measurements of molecular and thermal diffusion coefficients in ternary mixtures. *J. Chem. Phys.*, 122(23):234502 (12pp), 2005.

[168] B. A. S. M. Mounir and J. K. Platten. Metrology of the thermodiffusion coefficients in a ternary system. *J. Non-Equilib. Thermodyn.*, 30(4):385–399, 2005.

[169] P. Blanco, M. M. Bou-Ali, J. K. Platten, D. A. de Mezquia, J. A. Madariaga, and C. Santamaria. Thermodiffusion coefficients of binary and ternary hydrocarbon mixtures. *J. Chem. Phys.*, 132(11):114506 (6pp), 2010.

[170] J. P. Larre, J. K. Platten, and G. Chavepeyer. Soret effects in ternary systems heated from below. *Int. J. Heat Fluid Fl.*, 40(3):545–555, 1997.

[171] A. Königer, H. Wunderlich, and W. Köhler. Measurement of diffusion and thermal diffusion in ternary fluid mixtures using a two-color optical beam deflection technique. *J. Chem. Phys.*, 132(17):174506 (8pp), 2010.

[172] H. Cabrera, L. Marti-Lopez, E. Sira, K. Rahn, and M. Garcia-Sucre. Thermal lens measurement of the soret coefficient in acetone/water mixtures. *J. Chem. Phys.*, 131(3):031106 (3pp), 2009.

[173] H. Cabrera, E. Sira, K. Rahn, and M. Garcia-Sucre. A thermal lens model including the soret effect. *Appl. Phys. Lett.*, 94(5):051103 (3pp), 2009.

[174] R. Rusconi, L. Isa, and R. Piazza. Thermal-lensing measurement of particle thermophoresis in aqueous dispersions. *J. Opt. Soc. Am. B*, 21(3):605–616, 2004.

[175] P. Polyakov and S. Wiegand. Investigation of the soret effect in aqueous and non-aqueous mixtures by the thermal lens technique. *Phys. Chem. Chem. Phys.*, 11(5):864–871, 2009.

[176] S. A. Putnam and D. G. Cahill. Micron-scale apparatus for measurements of thermodiffusion in liquids. *Rev. Sci. Instrum.*, 75(7):2368–2372, 2004.

[177] D. G. Cahill, X. Zheng, and J. C. Zhao. Spatially resolved measurements of thermal stresses by picosecond time-domain probe beam deflection. *J. Therm. Stresses*, 33(1):9–14, 2010.

[178] K. B. Haugen and A. Firoozabadi. On measurement of molecular and thermal diffusion coefficients in multicomponent mixtures. *J. Phys. Chem. B*, 110(35):17678–17682, 2006.

[179] J. Janca and I. A. Ananieva. On the concentration effects in micro-thermal field-flow fractionation of polymers. *J. Liq. Chromatogr. Related Technol.*, 31(18):2721–2736, 2008.

[180] L. Pasti, S. Agnolet, and F. Dondi. Thermal field-flow fractionation of charged submicrometer particles in aqueous media. *Anal. Chem.*, 79(14):5284–5296, 2007.

[181] P. M. Shiundu, P. S. Williams, and J. C. Giddings. Magnitude and direction of thermal diffusion of colloidal particles measured by thermal field-flow fractionation. *J. Chromatogr. A*, 715(1):117–126, 1995.

[182] M. E. Schimpf. Polymer analysis by thermal field-flow fractionation. *J. Liq. Chromatogr. Related Technol.*, 25(13-15):2101–2134, 2002.

[183] C. A. Rue and M. E. Schimpf. Thermal-diffusion in liquid-mixtures and its effect on polymer retention in thermal field-flow fractionation. *Anal. Chem.*, 66(22):4054–4062, 1994.

[184] P. M. Shiundu, G. G. Liu, and J. C. Giddings. Separation of particles in nonaqueous suspensions by thermal field-flow fractionation. *Anal. Chem.*, 67(15):2705–2713, 1995.

[185] M. E. Schimpf and J. C. Giddings. Characterization of thermal-diffusion in polymer-solutions by thermal field-flow fractionation - dependence on polymer and solvent parameters. *J. Polym. Sci. Pol. Phys.*, 27(6):1317–1332, 1989.

[186] M. Nguyen, R. Beckett, L. Pille, and D. H. Solomon. Determination of thermal diffusion coefficients for polydisperse polymers and microgels by thfff and sec-malls. *Macromolecules*, 31(20):7003–7009, 1998.

[187] J. P. Lallemand, R. Desailly, and C. Froehly. Determination of velocity-field in a liquid by diffusion of coherent-light. *Acta Astronaut.*, 4(3-4):343–356, 1977.

[188] W. Köhler and R. Schäfer. Polymer analysis by thermal-diffusion forced rayleigh scattering. In M. Schmidt, editor, *New Developments in Polymer Analytics Ii*, volume 151 of *Adv. Polym. Sci.*, pages 1–59. Springer, Berlin, 2000.

[189] P. Rossmanith and W. Köhler. Polymer polydispersity analysis by thermal diffusion forced rayleigh scattering. *Macromolecules*, 29(9):3203–3211, 1996.

[190] O. Lade, K. Beizai, T. Sottmann, and R. Strey. Polymerizable nonionic microemulsions: Phase behavior of h_2o-n-alkyl methacrylate-n-alkyl poly(ethylene glycol) ether (ciej). *Langmuir*, 16(9):4122–4130, 2000.

[191] J. Steber, W. Guhl, N. Stelter, and F. R. Schröder. *Alkyl Polyglycosides – Technology, Properties and Applications*, pages 177–190. VCH, Weinheim, 1997.

[192] W. von Rybinski and K. Hill. Alkyl polyglycosides - properties and applications of a new class of surfactants. *Angew. Chem. Int. Ed.*, 110(10):1394–1412, 1998.

[193] E. Fischer. Über die glucoside der alkohole. *Ber. Dtsch. Chem. Ges.*, 26(3):2400–2412, 1893.

[194] K. Shinoda, T. Yamaguchi, and R. Hori. The surface tension and the critical micelle concentration in aqueous solution of beta-d-alkyl glucosides and their mixtures. *Bull. Chem. Soc. Jpn.*, 34(2):237–241, 1961.

[195] D. Nickel, C. Nitsch, P. Kurzendörfer, and W. von Rybinski. Interfacial properties of surfactant mixtures with alkyl polyglycosides. *Prog. Colloid Polym. Sci.*, 89(1992):249–252, 1992.

[196] M. Kasahara and P.C. Hinkle. Reconstitution of d-glucose transport catalyzed by a protein fraction from human erythrocytes in sonicated liposomes. *Proc. Natl. Acad. Sci. USA*, 73(2):396–400, 1976.

[197] M. Ollivon, O. Eidelman, R. Blumenthal, and A. Walter. Micelle vesicle transition of egg phosphatidylcholine and octyl glucoside. *Biochem.*, 27(5):1695–1703, 1988.

[198] P. K. Vinson, Y. Talmon, and A. Walter. Vesicle-micelle transition of phosphatidyl-choline and octyl glucoside elucidated by cryo-transmission electron microscopy. *Biophys. J.*, 56(4):669–681, 1989.

[199] N. A. Dencher and M. P. Heyn. Formation and properties of bacteriorhodopsin monomers in the non-ionic detergents octyl-β-d-glucoside and triton x-100. *FEBS Letters*, 96(2):322–326, 1978.

[200] H. Michel and D. Oesterhelt. 3-dimensional crystals of membrane-proteins - bacteriorhodopsin. *Proc. Natl. Acad. Sci. USA: Biol. Sci.*, 77(3):1283–1285, 1980.

[201] J. Haller and U. Kaatze. Ultrasonic spectrometry of aqueous solutions of alkyl maltosides: Kinetics of micelle formation and head-group isomerization. *Chem. Phys. Chem.*, 10(15):2703–2710, 2009.

[202] M. Kahlweit, G. Busse, and B. Faulhaber. Preparing microemulsions with alkyl monoglucosides and the role of n-alkanols. *Langmuir*, 11(9):3382–3387, 1995.

[203] A. Weerawardena, B. J. Boyd, C. J. Drummond, and D. N. Furlong. Removal of a solid organic soil from a hard surface by glucose-derived surfactants: effect of surfactant chain length, headgroup polymerisation and anomeric configuration. *Colloids Surf., A*, 169(1-3):317–328, 2000.

[204] J.N. Israelachvili. *Intermolecular and Surface Forces*. Academic Press, London, 3rd edition, 2010.

[205] R. T. Zhang, P. A. Marone, P. Thiyagarajan, and D. M. Tiede. Structure and molecular fluctuations of n-alkyl-beta-d-glucopyranoside micelles determined by x-ray and neutron scattering. *Langmuir*, 15(22):7510–7519, 1999.

[206] R. Giordano, G. Maisano, and J. Teixeira. Sans studies of octyl-β-glucoside and glycine micellar solutions. *J. Appl. Crystallogr.*, 30(5-2):761–764, 1997.

[207] F. Nilsson, O. Söderman, and I. Johansson. Physical-chemical properties of the n-octyl beta-d-glucoside/water system. a phase diagram, self-diffusion nmr, and saxs study. *Langmuir*, 12(4):902–908, 1996.

[208] A. D'Aprano, R. Giordano, M. P. Jannelli, S. Magazu, G. Maisano, and B. Sesta. Qels and sans studies of octyl-β-glucoside micellar solutions. *J. Mol. Struct.*, 383(1-3):177–182, 1996.

[209] P. Thiyagarajan and D. M. Tiede. Detergent micelle structure and micelle-micelle interactions determined by small-angle neutron-scattering under solution conditions used for membrane-protein crystallization. *J. Phys. Chem.*, 98(40):10343–10351, 1994.

[210] C. Mesa, A. Bonincontro, and B. Sesta. Solution properties of octyl β-d glucoside. part 1: Aggregate size. shape and hydration. *Colloid Polym. Sci.*, 271(12):1165–1171, 1993.

[211] R. W. Roxby and B. P. Mills. Micelle size distribution and free monomer con-

centration in aqueous-solutions of octyl glucoside. *J. Phys. Chem.*, 94(1):456–459, 1990.

[212] K. Kameyama and T. Takagi. Micellar properties of octylglucoside in aqueous-solutions. *J. Colloid Interface Sci.*, 137(1):1–10, 1990.

[213] J. N. Israelachvili, D. J. Mitchell, and B. W. Ninham. Theory of self-assembly of hydrocarbon amphiphiles into micelles and bilayers. *J. Chem. Soc., Faraday Trans. II*, 72:1525–1568, 1976.

[214] C. Tanford. *The Hydrophobic Effect: Formation of Micelles and Biological Membranes.* John Wiley & Sons Inc, New York, 2 edition, 1980.

[215] L. Z. He, V. M. Garamus, S. S. Funari, M. Malfois, R. Willumeit, and B. Niemeyer. Comparison of small-angle scattering methods for the structural analysis of octyl-beta-maltopyranoside micelles. *J. Phys. Chem. B*, 106(31):7596–7604, 2002.

[216] J. Lipfert, L. Columbus, V. B. Chu, S. A. Lesley, and S. Doniach. Size and shape of detergent micelles determined by small-angle x-ray scattering. *J. Phys. Chem. B*, 111(43):12427–12438, 2007.

[217] L. Maibaum, A. R. Dinner, and D. Chandler. Micelle formation and the hydrophobic effect. *J. Phys. Chem. B*, 108(21):6778–6781, 2004.

[218] J. M. Corkill, J. F. Goodman, and S. P. Harrold. Thermodynamics of micellization of non-ionic detergents. *Trans. Faraday Soc.*, 60(4931):202–207, 1964.

[219] M. J. Schick. Effect of temperature on critical micelle concentration of nonionic detergents - thermodynamics of micelle formation. *J. Phys. Chem.*, 67(9):1796–1799, 1963.

[220] M. Aoudia and R. Zana. Aggregation behavior of sugar surfactants in aqueous solutions: Effects of temperature and the addition of nonionic polymers. *J. Colloid Interface Sci.*, 206(1):158–167, 1998.

[221] L. J. Chen, S. Y. Lin, C. C. Huang, and E. M. Chen. Temperature dependence of critical micelle concentration of polyoxyethylenated non-ionic surfactants. *Colloids Surf., A*, 135(1-3):175–181, 1998.

[222] E. H. Crook, G. F. Trebbi, and D. B. Fordyce. Thermodynamic properties of solutions of homogeneous p,t-octylphenoxyethoxyethanols (ope$_{1-10}$). *J. Phys. Chem.*, 68(12):3592–3599, 1964.

[223] F. Nilsson, O. Söderman, and I. Johansson. Four different c8g1 alkylglucosides. anomeric effects and the influence of straight vs branched hydrocarbon chains. *J. Colloid Interface Sci.*, 203(1):131–139, 1998.

[224] D. Paschek, TH. Engels, W. von Rybinski, and A. Geiger. *Hydrophobic Aggregation of Nonionic Surfactants in Aqueous Solution: An MD Simulation Study*, pages 126–133. Springer, Berlin, 1999.

[225] R. Cammack and T. Attwood. *Oxford Dictionary of Biochemistry and Molecular Biology.* Oxford University Press, Oxford, 2nd edition, 2006.

[226] B. Lorber, J. B. Bishop, and L. J. Delucas. Purification of octyl beta-d-glucopyranoside and reestimation of its micellar size. *Biochim. Biophys. Acta*, 1023(2):254–265, 1990.

[227] W. J. Degrip and P. H. M. Boveegeurts. Synthesis and properties of alkylglucosides with mild detergent action - improved synthesis and purification of beta-1-octyl-glucose, beta-1-nonyl-glucose and beta-1-decyl-glucose - synthesis of beta-1-undecylglucose and beta-1-dodecylmaltose. *Chem. Phys. Lipids*, 23(4):321–335, 1979.

[228] K. Shinoda, T. Yamanaka, and K. Kinoshita. Surface chemical properties in aqueous solutions of nonionic surfactants - octyl glycol ether, alpha-octyl glyceryl ether and octyl glucoside. *J. Phys. Chem.*, 63(5):648–650, 1959.

[229] K. Shinoda, T. Yamaguchi, and R. Hori. The surface tension and the critical micelle concentration in aqueous solution of β-d-alkyl glucosides and their mixtures. *Bull. Chem. Soc. Jpn.*, 34(2):237–241, 1989.

[230] R. Kakehashi, M. Shizuma, S. Yamamura, and T. Takeda. Mixed micelles containing sodium oleate: the effect of the chain length and the polar head group. *J. Colloid Interface Sci.*, 279(1):253–258, 2004.

[231] K. Kameyama, A. Muroya, and T. Takagi. Properties of a mixed micellar system of sodium dodecyl sulfate and octylglucoside. *J. Colloid Interface Sci.*, 196(1):48–52, 1997.

[232] U. R. M. Kjellin, P. M. Claesson, and E. N. Vulfson. Studies of n-dodecyllactobionamide, maltose 6′o-dodecanoate, and octyl-β-glucoside with surface tension, surface force, and wetting techniques. *Langmuir*, 17(6):1941–1949, 2001.

[233] M. M. A. El-Sukkary, N. A. Syed, I. Aiad, and W. I. M. El-Azab. Synthesis and characterization of some alkyl polyglycosides surfactants. *J. Surf. Det.*, 11(2):129–137, 2008.

[234] M. M. A. El-Sukkary, N. A. Syed, I. Aiad, S. M. Helmy, and W. I. M. El-Azab. Aqueous solution properties, biodegradability, and antimicrobial activity of some alkylpolyglycosides surfactants. *Tenside Surf. Det.*, 46(5):311–316, 2009.

[235] C.A. Ericsson, O. Söderman, V.M. Garamus, M. Bergström, and S. Ulvenlund. Effects of temperature, salt, and deuterium oxide on the self-aggregation of alkylglycosides in dilute solution. 1. n-nonyl-β-d-glucoside. *Langmuir*, 20(4):1401–1408, 2004.

[236] M. J. Rosen and S. B. Sulthana. The interaction of alkylglycosides with other surfactants. *J. Colloid Interface Sci.*, 239(2):528–534, 2001.

[237] R. Aveyard, B. P. Binks, J. Chen, J. Esquena, P. D. I. Fletcher, R. Buscall, and S. Davies. Surface and colloid chemistry of systems containing pure sugar surfactant. *Langmuir*, 14(17):4699–4709, 1998.

[238] P. Mukerjee, K. J. Mysels, and Critical. Critical micelle concentrations of aqueous surfactant systems. *Nat. Stand. Ref. Data Ser., Nat. Bur. Stand. (U.S.)*, 36(Feb):1–227, 1971.

[239] B. J. Boyd, C. J. Drummond, I. Krodkiewska, and F. Grieser. How chain length, headgroup polymerization, and anomeric configuration govern the thermotropic and lyotropic liquid crystalline phase behavior and the air-water interfacial adsorption of glucose-based surfactants. *Langmuir*, 16(19):7359–7367, 2000.

[240] P. R. Majhi and A. Blume. Thermodynamic characterization of temperature-induced micellization and demicellization of detergents studied by differential scanning calorimetry. *Langmuir*, 17(13):3844–3851, 2001.

[241] L. Zhang, P. Somasundaran, and C. Maltesh. Electrolyte effects on the surface tension and micellization of n-dodecyl β-d-maltoside solutions. *Langmuir*, 12(10):2371–2373, 1996.

[242] C. J. Drummond, G. G. Warr, F. Grieser, B. W. Ninham, and D. F. Evans. Surface-properties and micellar interfacial microenvironment of n-dodecyl beta-d-maltoside. *J. Phys. Chem.*, 89(10):2103–2109, 1985.

[243] C. Dupuy, X. Auvray, and C. Petipas. Anomeric effects on the structure of micelles of alkyl maltosides in water. *Langmuir*, 13(15):3965–3967, 1997.

[244] C. A. Ericsson, O. Söderman, V. M. Garamus, M. Bergström, and S. Ulvenlund. Effects of temperature, salt, and deuterium oxide on the self-aggregation of alkylglycosides in dilute solution. 2. n-tetradecyl-beta-d-maltoside. *Langmuir*, 21(4):1507–1515, 2005.

[245] J. H. Schulman, W. Stoeckenius, and L. M. Prince. Mechanism of formation and structure of micro emulsions by electron microscopy. *J. Phys. Chem.*, 63(10):1677–1680, 1959.

[246] T. Sottmann and R. Strey. *Microemulsions*, volume V. Academic Press, 2005.

[247] T. Sottmann and R. Strey. Ultralow interfacial tensions in water-n-alkane-surfactant systems. *J. Chem. Phys.*, 106(20):8606–8615, 1997.

[248] M. Kahlweit, R. Strey, D. Haase, H. Kunieda, T. Schmeling, B. Faulhaber, M. Borkovec, H. F. Eicke, G. Busse, F. Eggers, T. Funck, H. Richmann, L. Magid, O. Söderman, P. Stilbs, J. Winkler, A. Dittrich, and W. Jahn. How to study microemulsions. *J. Colloid Interface Sci.*, 118(2):436–453, 1987.

[249] M. Kahlweit, R. Strey, and D. Haase. Phase-behavior of multicomponent systems water-oil-amphiphile-electrolyte. 3. *J. Phys. Chem.*, 89(1):163, 1985.

[250] G. M. Schneider. Fluid mixtures at high-pressures. *Pure Appl. Chem.*, 55(3):479–492, 1983.

[251] R. Strey. Microemulsion microstructure and interfacial curvature. *Colloid Polym. Sci.*, 272(8):1005–1019, 1994.

[252] M. Kahlweit, R. Strey, and G. Busse. Microemulsions - a qualitative thermodynamic approach. *J. Phys. Chem.*, 94(10):3881–3894, 1990.

[253] R. E. Goldstein and J. S. Walker. Theory of multiple phase separations in binary-mixtures - phase-diagrams, thermodynamic properties, and comparisons with experiments. *J. Chem. Phys.*, 78(3):1492–1512, 1983.

[254] P.A. Winsor. *Solvent properties of amphiphilic compounds.* Butterworths Scientific Publications, London, 1954.

[255] M. S. Leaver, U. Olsson, H. Wennerstrom, and R. Strey. Emulsification failure in a ternary microemulsion. *Journal De Physique Ii*, 4(3):515–531, 1994.

[256] A. Bernheim-Groswasser, T. Tlusty, S. A. Safran, and Y. Talmon. Direct observation of phase separation in microemulsion networks. *Langmuir*, 15(17):5448–5453, 1999.

[257] I. S. Barnes, S. T. Hyde, B. W. Ninham, P. J. Derian, M. Drifford, and T. N. Zemb. Small-angle x-ray-scattering from ternary microemulsions determines microstructure. *J. Phys. Chem.*, 92(8):2286–2293, 1988.

[258] B. W. Ninham, I. S. Barnes, S. T. Hyde, P. J. Derian, and T. N. Zemb. Random connected cylinders - a new structure in 3-component microemulsions. *Europhysics Letters*, 4(5):561–568, 1987.

[259] W. Köhler. Thermodiffusion in polymer-solutions as observed by forced rayleigh-scattering. *J. Chem. Phys.*, 98(1):660–668, 1993.

[260] P. Blanco, H. Kriegs, M. P. Lettinga, P. Holmqvist, and S. Wiegand. Thermal diffusion of a stiff rod-like mutant y21m fd-virus. *Biomacromolecules*, 2011.

[261] G. M. Hale and M. R. Querry. Optical-constants of water in 200 nm to 200 μm wavelength region. *Appl. Optics*, 12(3):555–563, 1973.

[262] K. F. Palmer and D. Williams. Optical-properties of water in near-infrared. *J. Opt. Soc. Am.*, 64(8):1107–1110, 1974.

[263] L. H. Kou, D. Labrie, and P. Chylek. Refractive-indexes of water and ice in the 0.65-2.5 μm spectral range. *Appl. Optics*, 32(19):3531–3540, 1993.

[264] R. M. Pope. Optical absorption of pure water and sea water using the integrating cavity absorption meter. *Dyn. Atmos. Oceans*, 31(1-4):307–320, 1993.

[265] G. Wittko and W. Köhler. Precise determination of the soret, thermal diffusion and mass diffusion coefficients of binary mixtures of dodecane, isobutylbenzene and 1,2,3,4-tetrahydronaphthalene by a holographic grating technique. *Phil. Mag.*, 83(17-18):1973–1987, 2003.

[266] A. J. C. Ladd, H. Gang, J. X. Zhu, and D. A. Weitz. Time-dependent collective diffusion of colloidal particles. *Phys. Rev. Lett.*, 74(2):318–321, 1995.

[267] W. Vanmegen and P. N. Pusey. Dynamic light-scattering study of the glass-transition in a colloidal suspension. *Phys. Rev. A*, 43(10):5429–5441, 1991.

[268] S. Mintova, N. H. Olson, V. Valtchev, and T. Bein. Mechanism of zeolite a nanocrystal growth from colloids at room temperature. *Science*, 283(5404):958–960, 1999.

[269] M. Kroon, G. H. Wegdam, and R. Sprik. Dynamic light scattering studies on the sol-gel transition of a suspension of anisotropic colloidal particles. *Phys. Rev. E*, 54(6):6541–6550, 1996.

[270] P. N. Pusey, A. D. Pirie, and W. C. K. Poon. Dynamics of colloid polymer mixtures. *Physica A*, 201(1-3):322–331, 1993.

[271] A. Brunsting and P. F. Mullaney. Differential light-scattering from spherical mammalian-cells. *Biophys. J.*, 14(6):439–453, 1974.

[272] S. A. Baeurle, A. Hotta, and A. A. Gusev. A new semi-phenomenological approach to predict the stress relaxation behavior of thermoplastic elastomers. *Polymer*, 46(12):4344–4354, 2005.

[273] A. Hotta, S. M. Clarke, and E. M. Terentjev. Stress relaxation in transient networks of symmetric triblock styrene-isoprene-styrene copolymer. *Macromolecules*, 35(1):271–277, 2002.

[274] P.N. Pusey and R.J.A. Tough. *Dynamic Light Scattering.* Plenum Press, New York, London, 1985.

[275] S. W. Provencher. A constrained regularization method for inverting data represented by linear algebraic or integral-equations. *Comput. Phys. Commun.*, 27(3):213–227, 1982.

[276] S. W. Provencher and P. Stepanek. Global analysis of dynamic light scattering autocorrelation functions. *Part. Part. Syst. Char.*, 13(5):291–294, 1996.

[277] S. Datta. *Non-ionic Binary Surfactant Systems and Microemulsions as Model Systems for Thermal Diffusion Studies.* PhD thesis, Universität zu Köln, 2010.

[278] N. Wu, J. L. Dai, and F. J. Micale. Dynamic surface tension measurement with a dynamic wilhelmy plate technique. *J. Colloid Interface Sci.*, 215(2):258–269, 1999.

[279] F. Thomsen and C. Bilke-Krause. Auf den kopf gestellt: Oberflächenenergiemessung von textilien mit der captive-bubble-methode. *Krüss Advancing Surface Science*, 03(12):1 (1p), 2006.

[280] J. P. van den Brink. Thermal expansion coefficient measurements of molten glasses using the sessile drop technique. *J. Non-Cryst. Solids*, 253(1-3):163–169, 1999.

[281] W. Zhang, M. Wahlgren, and B. Sivik. Membrane characterization by the contact-angle technique. 2. characterization of uf-membranes and comparison between the captive bubble and sessile drop as methods to obtain water contact angles. *Desalination*, 72(3):263–273, 1989.

[282] P. L. du Noüy. A new apparatus for measuring surface tension. *J. Gen. Physiol.*, 1(5):521–524, 1919.

[283] L. Du Noüy. Ring method for measuring surface tension. *Nature*, 135:397, 1935.

[284] A. W. Adamson. *The Physical Chemistry of Surfaces*. Wiley, New York, 6 edition, 1976.

[285] T. Inoue, K. Nakashima, and M. Suzuki. Surface tension study on aqueous solution of nonionc surfactant with unsaturated hydrocarbon chain. *J. Oleo Sci.*, 51(12):753–760, 2002.

[286] D. N. Furlong, P. A. Freeman, I. M. Metcalfe, and L. R. White. Wall effects in du noüy ring tensiometry - theory and experiment. *J. Chem. Soc. Farad. Trans. 1*, 79:1701–1719, 1983.

[287] Krüss. Manual, k10t.

[288] B. von Szyszkowski. Experimentelle studien über kapillare eigenschaften der wässrigen lösungen von fettsäuren. *Z. Phys. Chem*, 64:385, 1908.

[289] A. H. Compton. On the mechanism of x-ray scattering. *Proc. Natl. Acad. Sci. USA*, 11(6):303–306, 1925.

[290] S. K. Sinha. Complementary use of neutron and synchrotron x-ray scattering for problems of interest in condensed matter physics. *J. Phys. Chem. Solids*, 68(11):2048–2051, 2007.

[291] W. T. Heller. Small-angle neutron scattering and contrast variation: a powerful combination for studying biological structures. *Acta Crystallogr., Sect. D: Biol. Crystallogr.*, 66(11):1213–1217, 2010.

[292] D. V. Fenby, Z. S. Kooner, and J. R. Khurma. Deuterium-isotope effects in liquid liquid-phase diagrams - a review. *Fluid Phase Equilib.*, 7(3-4):327–338, 1981.

[293] Yu. A. Alexandrov. *Landolt-Börnstein - Group I Elementary Particles, Nuclei and Atoms; Numerical Data and Functional Relationships in Science and Technology*, volume 16A1 of *2 The neutron as an elementary particle*. Springer-Verlag, 2000.

[294] A. Michels and J. Weissmüller. Magnetic-field-dependent small-angle neutron scattering on random anisotropy ferromagnets. *Rep. Prog. Phys.*, 71(6):1–37, 2008.

[295] A. Wiedenmann. Static and dynamic correlations in magnetic nanomaterials studied by small angle neutron scattering techniques. *Collect. SFN*, 11:219–242, 2010.

[296] JCNS. Kws 1 - small angle neutron scattering spectrometer, 2009.

[297] X. L. Lin, R. Henkelmann, A. Turler, H. Gerstenberg, and F. De Corte. Neutron flux parameters at irradiation positions in the new research reactor frm-ii. *Nucl. Instrum. Methods Phys. Res., Sect. A*, 564(2):641–644, 2006.

[298] A. Röhrmoser. Core model of new german neutron source frm ii. *Nucl. Eng. Des.*, 240(6):1417–1432, 2010.

[299] JCNS. Preliminary parameters for kws-1 due to the actual design.

[300] S. Kayillo, R. A. Shalliker, and G. R. Dennis. Thermodynamic differences between deuterated and protonated polystyrenes evaluated using reversed phase liquid chromatography. *Macromol. Chem. Phys.*, 206(20):2013–2017, 2005.

[301] S. J. Perkins. Structural studies of proteins by high-flux x-ray and neutron solution scattering. *Biochem. J.*, 254(2):313–327, 1988.

[302] J. D. Londono, A. H. Narten, G. D. Wignall, K. G. Honnell, E. T. Hsieh, T. W. Johnson, and F. S. Bates. Composition dependence of the interaction parameter in isotopic polymer blends. *Macromolecules*, 27(10):2864–2871, 1994.

[303] V. F. Sears. Fundamental-aspects of neutron optics. *Phys. Rep.*, 82(1):1–29, 1982.

[304] W. Ketter, W. Heil, G. Badurek, M. Baron, R. Loidl, and H. Rauch. Measurement of the coherent neutron scattering length of he-3. *J. Res. Natl. Inst. Stan.*, 110(3):241–244, 2005.

[305] B. Jacrot. Study of biological structures by neutron-scattering from solution. *Rep. Prog. Phys.*, 39(10):911–953, 1976.

[306] B. Hammouda, D. Ho, and S. Kline. Sans from poly(ethylene oxide)/water systems. *Macromolecules*, 35(22):8578–8585, 2002.

[307] R. Strey, J. Winkler, and L. Magid. Small-angle neutron-scattering from diffuse interfaces .1. monolayers and bilayers in the water octane c12e5 system. *J. Phys. Chem.*, 95(19):7502–7507, 1991.

[308] J. S. Pedersen. Analysis of small-angle scattering data from colloids and polymer solutions: modeling and least-squares fitting. *Adv. Colloid Interface Sci.*, 70:171–210, 1997.

[309] M. Kotlarchyk and S. H. Chen. Analysis of small-angle neutron-scattering spectra from polydisperse interacting colloids. *J. Chem. Phys.*, 79(5):2461–2469, 1983.

[310] L. Rayleigh. The incidence of light upon a transparent sphere of dimensions comparable with the wave-length. *Proc. R. Soc. London, Ser. A*, 84(567):25–46, 1910.

[311] T. Foster, T. Sottmann, R. Schweins, and R. Strey. Small-angle neutron scattering from giant water-in-oil microemulsion droplets. i. ternary system. *J. Chem. Phys.*, 128(5):054502, 2008.

[312] M. Gradzielski, D. Langevin, L. Magid, and R. Strey. Small-angle neutron-scattering from diffuse interfaces .2. polydisperse shells in water-n-alkane-c(10)e(4) microemulsions. *J. Phys. Chem.*, 99(35):13232–13238, 1995.

[313] S. V. G. Menon, V. K. Kelkar, and C. Manohar. Application of baxter model to the theory of cloud points of nonionic surfactant solutions. *Phys. Rev. A*, 43(2):1130–1133, 1991.

[314] R. J. Baxter. Percus-yevick equation for hard spheres with surface adhesion. *J. Chem. Phys.*, 49(6):2770–2774, 1968.

[315] E. M. Kutschmann, G. H. Findenegg, D. Nickel, and W. von Rybinski. Interfacial-tension of alkylglucosides in different apg/oil/water systems. *Colloid Polym. Sci.*, 273(6):565–571, 1995.

[316] H. van Koningsveld, J.C. Jansen, and A.J.J. Straathof. The crystal structure of anhydrous octyl β-d-glucopyranoside. a comparison with its hemi- and monohydrate. *Acta Crystallogr. C*, 44(6):1054–1057, 1988.

[317] O. Pastor, E. Junquera, and E. Aicart. Hydration and micellization processes of n-octyl beta-d-glucopyranoside in aqueous solution. a thermodynamic and fluorimetric study in the absence and presence of salts. *Langmuir*, 14(11):2950–2957, 1998.

[318] J. Kriwanek, D. Lotzsch, R. Vetter, and A. Seeboth. Influence of a zwitterionic surfactant on the chromogenic behavior of a dye-containing aqueous pva-polyether gel network. *Polym. Adv. Technol.*, 14(2):79–82, 2003.

[319] Y. Takahashi, A. Maeda, K. Kojima, and K. Uchida. Ph dependence of luminescence in dye-doped sol-gel coating film. *Jpn. J. Appl. Phys., Part 2*, 39(3ab):L218–L220, 2000.

[320] M. J. Rosen. *Surfactants and interfacial Phenomena*. Wiley Interscience publication, 2nd edition, 1989.

[321] W. C. Preston. Some correlating principles of detergent action. *J. Phys. Colloid Chem.*, 52(1):84–97, 1948.

[322] P. Strop and A. T. Brunger. Refractive index-based determination of detergent concentration and its application to the study of membrane proteins. *Protein Sci.*, 14(8):2207–2211, 2005.

[323] H. Lange. Untersuchungen über adsorbierte und gespreitete monomolekulare schichten von dodecylpolyglyköläthern auf wasser. *Colloid. Polym. Sci.*, 201(2):131–136, 1965.

[324] M. K. Matsson, B. Kronberg, and P. M. Claesson. Enhanced adsorption of alkyl glucosides on the silica/water interface by addition of amine oxides. *Langmuir*, 21(7):2766–2772, 2005.

[325] J. Appell, G. Porte, and E. Buhler. Self-diffusion and collective diffusion of charged colloids studied by dynamic light scattering. *J. Phys. Chem. B*, 109(27):13186–13194, 2005.

[326] C. J. Hogberg, A. Maliniak, and A. P. Lyubartsev. Dynamical and structural properties of charged and uncharged lidocaine in a lipid bilayer. *Biophys. Chem.*, 125(2-3):416–424, 2007.

[327] J. Rauch and W. Köhler. Collective and thermal diffusion in dilute, semidilute, and concentrated solutions of polystyrene in toluene. *J. Chem. Phys.*, 119(22):11977–11988, 2003.

[328] R. Sugaya, B. A. Wolf, and R. Kita. Thermal diffusion of dextran in aqueous

solutions in the absence and the presence of urea. *Biomacromolecules*, 7(2):435–440, 2006.

[329] H. R. Lasser and H. G. Elias. Association of soaps .3. association behavior of beta d-octylglucoside in water. *Kolloid-Zeitschrift and Zeitschrift Für Polymere*, 250(1):58–63, 1972.

[330] K. Rah and B. C. Eu. Free volume and density and temperature dependence of diffusion coefficients of liquid mixtures. *Phys. Rev. Lett.*, 88(6):065901 (4pp), 2002.

[331] K. Rah and B. C. Eu. The generic van der waals equation of state and self-diffusion coefficients of liquids. *J. Chem. Phys.*, 115(6):2634–2640, 2001.

[332] P. Blanco, M. M. Bou-Ali, J. K. Platten, P. Urteaga, J. A. Madariaga, and C. Santamaria. Determination of thermal diffusion coefficient in equimolar n-alkane mixtures: Empirical correlations. *J. Chem. Phys.*, 129(17):174504 (6pp), 2008.

[333] P. Blanco and S. Wiegand. Study of the soret effect in monosaccharide solutions. *J. Phys. Chem. B*, 114(8):2807–2813, 2010.

[334] H. Brenner. Elementary kinematical model of thermal diffusion in liquids and gases. *Phys. Rev. E*, 74(3):036306 (20pp), 2006.

[335] M. Eslamian and M. Z. Saghir. Microscopic study and modeling of thermodiffusion in binary associating mixtures. *Phys. Rev. E*, 80(6):061201, 2009.

[336] S. Semenov and M. Schimpf. Thermophoresis of dissolved molecules and polymers: Consideration of the temperature-induced macroscopic pressure gradient. *Phys. Rev. E*, 69(1):011201 (8pp), 2004.

[337] A. Yokozeki, H. Sato, and K. Watanabe. Ideal-gas heat capacities and virial coefficients of hfc refrigerants. *Int. J. Thermophys.*, 19(1):89–127, 1998.

[338] M. L. Kurnaz and J. V. Maher. Measurement of the second virial coefficient for the interaction of dilute colloidal particles in a mixed solvent. *Phys. Rev. E*, 55(1):572–576, 1997.

[339] A. Würger. Thermophoresis in colloidal suspensions driven by marangoni forces. *Phys. Rev. Lett.*, 98(13):138301 (4pp), 2007.

[340] K. V. Schubert, R. Strey, and M. Kahlweit. A new purification technique for alkyl polyglycol-ethers and miscibility gaps for water ciej. *J. Colloid Interface Sci.*, 141(1):21–29, 1991.

[341] Deutsche Gesetzliche Unfallversicherung. Gestis-stoffdatenbank, 2010.

[342] B. P. Binks, P. D. I. Fletcher, V. N. Paunov, and D. Segal. Equilibrium and dynamic adsorption of c12e5 at the air-water surface investigated using ellipsometry and tensiometry. *Langmuir*, 16(23):8926–8931, 2000.

[343] M. Bergh, L. P. Shao, K. Magnusson, E. Gafvert, J. L. G. Nilsson, and A. T. Karlberg. Atmospheric oxidation of poly(oxyethylene) alcohols. identification of

ethoxylated formates as oxidation products and study of their contact allergenic activity. *J. Pharm. Sci.*, 88(4):483–488, 1999.

[344] W. Meier. Poly(oxyethylene) adsorption in water oil microemulsions: A conductivity study. *Langmuir*, 12(5):1188–1192, 1996.

[345] M. Kerker. *The Scattering of Light and Other Electromagnetic Radiation.* Academic Press, New York, 1969.

[346] U. Olsson and P. Schurtenberger. Structure, interactions, and diffusion in a ternary nonionic microemulsion near emulsification failure. *Langmuir*, 9(12):3389–3394, 1993.

[347] M. S. Leaver, U. Olsson, H. Wennerstrom, and R. Strey. Emulsification failure in a ternary microemulsion. *J. Phys. II*, 4(3):515–531, 1994.

[348] S. Schrödle, G. Hefter, W. Kunz, and R. Buchner. Effects of nonionic surfactant c12e5 on the cooperative dynamics of water. *Langmuir*, 22(3):924–932, 2006.

[349] J.M. Corkill and J.F. Goodman. The interaction of non-ionic surface-active agents with water. *Adv. Colloid Interface Sci.*, 2(3):298–330, 1969.

[350] G. Briganti, G. D'Arrigo, L. Falconi, and M. Maccarini. Interfacial properties of nonionic micellar aggregates as a function of temperature and concentration. *Colloids Surf., A*, 164(1):19–25, 2000.

[351] R. Strey, R. Schomacker, D. Roux, F. Nallet, and U. Olsson. Dilute lamellar and l3 phases in the binary water-c12e5 system. *J. Chem. Soc., Faraday Trans.*, 86(12):2253–2261, 1990.

[352] U. Menge, P. Lang, G. H. Findenegg, and P. Strunz. Structural transition of oil-swollen cylindrical micelles of c12e5 in water studied by sans. *J. Phys. Chem. B*, 107(6):1316–1320, 2003.

[353] J. M. Corkill, J. F. Goodman, and J. Wyer. Nuclear magnetic resonance of aqueous solutions of alkylpolyoxyethylene glycol monoethers. *Trans. Faraday Soc.*, 65(553P):9–18, 1969.

[354] J. Luettmer-Strathmann. Thermodiffusion in the critical region. In W. Küler and S. Wiegand, editors, *IMT4*, Thermal nonequilibrium phenomena in fluid mixtures, pages 24–37, Bayreuth, 2000. Springer.

[355] T. Sottmann. *Mikroemulsionen: Eigenschaften von internen Grenzflächen.* PhD thesis, 1997.

[356] M. Burkowsky and C. Marx. Applications for the spinning-drop technique for determining low interfacial tension. *Tenside Deterg.*, 15(5):247–251, 1978.

[357] J. L. Cayias, R. S. Schechter, and W. H. Wade. *The Measurement of Low Interfacial Tension via the Spinning Drop Technique*, volume 8, chapter 17, pages 234–247. ACS Symposium Series, Washington, D.C., 1975.

[358] R. Strey. Phase behavior and interfacial curvature in water-oil-surfactant systems. *Curr. Opin. Colloid In.*, 1:402–410, 1996.

[359] S. P. Moulik and B. K. Paul. Structure, dynamics and transport properties of microemulsions. *Adv. Colloid Interface Sci.*, 78(2):99–195, 1998.

[360] K. V. Schubert, R. Strey, and M. Kahlweit. Similarities of aqueous and nonaqueous microemulsions. In C. Helm, M. Lösche, and H. Möhwald, editors, *Trends in Colloid and Interface Science VI*, volume 89 of *Prog. Colloid Polym. Sci.*, pages 263–267. Deutsche Kolloidgesellschaft, 1992.

[361] K. P. Das, A. Ceglie, B. Lindman, and S. E. Friberg. Fourier-transform nmr self-diffusion studies of a nonaqueous microemulsion system. *J. Colloid Interface Sci.*, 116(2):390–400, 1987.

[362] D. Gazzillo, A. Giacometti, R. Fantoni, and P. Sollich. Multicomponent adhesive hard sphere models and short-ranged attractive interactions in colloidal or micellar solutions. *Phys. Rev. E*, 74(5):051407, 2006.

[363] M. Bouaskarne, S. Amokrane, and C. Regnaut. Effective interaction between reverse micelles: A study from the potential of mean force at infinite dilution. *J. Chem. Phys.*, 114(5):2442–2451, 2001.

[364] S. Amokrane and C. Regnaut. Surface layers overlap and effective adhesion in reverse micelles: A discussion from the adhesive spheres mixture model. *J. Chem. Phys.*, 106(1):376–387, 1997.

[365] B. Lemaire, P. Bothorel, and D. Roux. Micellar interactions in water-in-oil microemulsions .1. calculated interaction potential. *J. Phys. Chem.*, 87(6):1023–1028, 1983.

[366] C. A. T. Laia, P. Lopez-Cornejo, S. M. B. Costa, J. d'Oliveira, and J. M. G. Martinho. Dynamic light scattering study of aot microemulsions with nonaqueous polar additives in an oil continuous phase. *Langmuir*, 14(13):3531–3537, 1998.

[367] N. J. Kale and L. V. Allen. Studies on microemulsions using brij 96 as surfactant and glycerin, ethylene-glycol and propylene-glycol as cosurfactants. *Int. J. Pharm.*, 57(2):87–93, 1989.

[368] K. Aramaki, U. Olsson, Y. Yamaguchi, and H. Kunieda. Effect of water-soluble alcohols on surfactant aggregation in the c12co8 system. *Langmuir*, 15(19):6226–6232, 1999.

[369] G. D'Errico, D. Ciccarelli, and O. Ortona. Effect of glycerol on micelle formation by ionic and nonionic surfactants at 25 degrees c. *J. Colloid Interface Sci.*, 286(2):747–754, 2005.

[370] T. Hellweg, A. Brulet, and T. Sottmann. Dynamics in an oil-continuous droplet microemulsion as seen by quasielastic scattering techniques. *Physical Chemistry Chemical Physics*, 2(22):5168–5174, 2000.

[371] A. Parola and R. Piazza. Particle thermophoresis in liquids. *Eur. Phys. J. E*, 15(3):255–263, 2004.

[372] P. Billian. *Chemische Charakterisierung von Alkylpolyglucosiden.* PhD thesis, 2000.

Glossar

A	amplitude of the heterodyne signal
A	area (only STM)
A^*	normalized amplitude
$A_{\mathrm{e}fb}$	amplitude of the heterodyne signal at the efb
$A_{\mathrm{h}ead}$	area per surfactant head group
$A_{\min}$	area per surfactant head group in a micelle
A_T	temperature grating
a	single point in the Taylor series
a_{c}	area per molecule in the particle-solvent interface
a, b	parameter of surface tension measurements
B_1, β	dimensionless instrument parameters (DLS)
C_1, C_2	parameters of the Taylor series
c_1, c_2, c	principle curvatures of the amphiphilic film
C_{x}	n-alkane of the type $\mathrm{CH_3 - (CH_2)}_{(x-2)} - \mathrm{CH_3}$
cmc	critical micelle concentration
cmt	critical micelle temperature
D	mass diffusion coefficient
D_{T}	thermal diffusion coefficient
d	the fringe spacing
d_{eff}	effective diameter of the sticky hard spheres
d_{sample}	optical length of the sample cell
d_{water}	optical length of the water cell
$d\Sigma/s\Omega$	differential cross section
$E_{ec,inc}$	coherent, incoherent part of the electrical field
F	correction factor for STM
G	Gibbs free energy
g_1	field-time-correlation function
g_2	intensity-time-correlation function
h	Planck constant
I	measured light intensity
$I(q)$	scattered intensity
I_b	background intensity
I_{bg}	scattered background intensity
I_{ec}	scattered intensity from the empty cell
I_{hetero}	heterodyne intensity
I_{homo}	homodyne intensity
I_{sample}	scattered intensity from the sample
I_w	the writing intensity
I_{water}	scattered intensity from the water cell
$I_\phi, I_{\phi+\pi}$	detected intensities in the TDFRS setup
$J_{1,2}$	mass flux

J_Q	heat flux
k_{B}	Boltzmann constant
$\underline{k}_{i,s}$	field vector of incident / scattered beam
k_s	thermal conductivity of the sample
L	phenomenological coefficient
l	length of the absorption cell
l_{fluid}	range of the colloid-solvent interaction
M	molar mass
m	mass
n	refractive index
n_0	refractive index of the solvent
N	number density of particles
$\mathrm{N_A}$	Avogadro constant
n_{C}	alkane-to-surfactant ratio
n_{core}	refractive index of an inner droplet core
n_{droplet}	refractive index of spherical microemulsion droplet
n_{h}	hydration number
n_{shell}	refractive index of outer surfactant shell of a droplet
n_w	refractive index of the window of the absorption cell
OD	optical density
$P(q)$	form factor
$P_\zeta(t)$	Taylor function of ζ_{het}
p	pressure
$p_0,\ p_1$	parameters of the Taylor series
Q	heat
q	wave vector in the TDFRS setups
R	universal gas constant
r_{H}	hydrodynamic radius
r_{SANS}	mean droplet radius (SANS)
S	entropy
$S(q)$	structure factor
S_{T}	Soret coefficient
$S_{\mathrm{T}}{}^{*}$	normalized Soret coefficient
$S_{\mathrm{T}}{}^{\infty}$	S_{T} at infinite high temperature
$S_{\mathrm{T}}{}^{w,inf}$	S_{T} at infinite high concentration
s	optical path length of the flow cells
T	temperature
T_0	fit parameter for temperature
T^{*}	normalized temperature
$T^{\pm}$	sign inversion temperature
T_{cp}	cloud point temperature
T_{ec}	transmission from the empty cell
T_{efb}	temperature of the *efb*

T_{ncb}	temperature of the ncb
T_{sample}	transmission from the sample
T_{water}	transmission from the water cell
t	time
$t_{\text{d}ecay}$	exponential decay constant
$t_{\text{d}i}$	thickness parameter of the diffuse interface
U	internal energy
$V_{\text{d}isp}$	total volume per droplet
V_{x}	volume of component x
v	velocity
v_{c}	particle volume
W	work
w_0, w	concentration in equilibrium
	and in steady state. Assumption: $w_0 \approx w$
w^*	normalized concentration
$w_{\text{B},A}$	mass ratio of the component A or B to the total mass
$w_c mc$	concentration at the cmc
$w_{\pm}$	sign inversion concentration
X_j	thermodynamic force
α	absorption coefficient of the sample
α_s	thermal expansion coeff. of the absorption cell side walls
α_T	thermal diffusion factor, $\alpha_T = T \cdot S_{\text{T}}$
α_w	thermal expansion coeff. of the absorption cell windows
α_V	thermal diffusion coefficient
$\beta_{\text{K}WW}$	fit parameter (DLS)
Γ	decay rate (DLS)
Γ_{max}	maximum surface excess concentration
$\gamma_{\text{b},a}$	mass ratio of surfactant to the oil (b) or to water (a)
ε_{x}	dielectric constant of component x
ζ_{het}	heterodyne signal in TDFRS
ζ_{homo}	homodyne signal in TDFRS
η	viscosity
$\theta_{r,w}$	angle of the read-out, writing beams
λ	wavelength
μ	chemical potential
ρ	density
ρ^0_{air}	density of air
ρ^0_{mix}	density of the mixture
σ	surface tension
σ_0	surface tension of pure water
σ_{exp}	measured surface tension
σ_{G}	standard deviation
τ_{c}	process time of the concentration mode

τ_d	decay time (DLS)
τ_th	thermal diffusivity
ϕ_0	volume fraction of droplets
ϕ_B	volume fraction of the alkanes
ϕ_c	internal interface
$\phi_{\mathrm{m}on,b}$	monomeric dissolved $C_{12}E_5$ in oil
φ_{chain}	angle between surfactant chain unit and interface
$\varphi_{\mathrm{h}ead}$	angle between surfactant head group and interface
φ_KWW	Kohlrausch-Williams-Watts function

Danksagung

Mein aufrichtiger Dank gilt Herrn Prof. Reinhard Strey für die interessante Themenstellung, für die herzliche Aufnahme in seine Arbeitsgruppe und für die vielen Ideen, die diese Arbeit beflügelt haben.

Ganz persönlich danke ich Simone Wiegand für die aufopferungsvolle Unterstützung in den letzten drei Jahren bis zum letzten Satz dieser Arbeit. Sie betreute die Jülicher Experimente, gab Hilfestellungen beim Verfassen von Veröffentlichungen und Verlängerungsanträgen, und war jederzeit zur Diskussion bereit um Verständnisfragen zu erörtern. Ein nicht geringerer Dank gebührt den Kollegen des DFG-Projektes in Köln, Thomas Sottmann und Sascha Datta für die unzähligen Diskussionen in Köln, Jülich, aber auch des Nachts an der Neutronenquelle in Garching.

Ich möchte mich herzlich bei Jan Dhont bedanken, der es mir ermöglichte die Promotion im Forschungszentrums Jülich durchzuführen. Auf technischer Seite gilt meine Hochachtung Hartmut Kriegs. Mit ihm wurden beinahe zu häufig Hochspannungsverstärker, Laser und andere fehleranfällige Bauteile in den experimentellen Aufbauten gewechselt, ersetzt und justiert. Dieter Triefenbach und Hans Jürgen Hoffmann danke ich für die Unterstützung bei technischen Problemen; Sylvia de Waal und Karin Sellinghoff unterstützten mich in meiner Labortätigkeit. Marie Göcking räumte zuverlässig und stressfrei bürokratische Hürden aus dem Weg. Die Neutronenstreumessungen in Garching wurden professionell von Henrich Frielinghaus begleitet.

Für die vielen fachlichen Diskussionen möchte ich mich bei Gerhard Nägele, Johan Buitenhuis, Peter Holmqvist, Peter Lang, Pavlik Lettinga, Gerd Meier, Wiebke Sager, Pablo Blanco und Pavel Polykov bedanken. Ich danke auch Kyongok Kang, Emmanuel Stiakakis, Donald Guu, Macro Heinen, Yunfei Jia, Christoph July, Gopinath Shanmugavadivelu, Karolina Tomczyk, Claudio Contreras-Aburto und Jing Zhang für die durchlebten Stunden innerhalb und außerhalb des Instituts. Zudem haben sich Michael Klein, Simon Rogers und Zilin Wang viel Mühe beim Korrekturlesen gegeben.

Ich blicke immer wieder gerne auf die vielen dienstlichen und vor allem auf die außerdienstlichen Treffen mit der Kölner Arbeitsgruppe zurück. Es stellte sich schnell heraus, dass man in der Uni nicht nur gut DFG-Projekte bearbeiten, sondern vorzüglich Grillen, Sport treiben, oder ein Bierchen trinken kann. Vielen Dank für die vielen gemeinsamen Stunden!

In meiner PhD-Zeit durfte ich meine Ergebnisse in der *International Helmholtz Research School of Biophysics and Soft Matter* präsentieren und an vielen interessanten Veranstaltungen teilnehmen.

Meiner Familie danke ich für die Geduld und die aufmunternden Worte in stressigen Zeiten.

Erklärung

Ich versichere, dass ich die von mir vorgelegte Dissertation selbständig angefertigt, die benutzten Quellen und Hilfsmittel vollständig angegeben und die Stellen der Arbeit - einschließlich Tabellen, Karten und Abbildungen -, die anderen Werken im Wortlaut oder dem Sinn nach entnommen sind, in jedem Einzelfall als Entlehnung kenntlich gemacht habe; dass diese Dissertation noch keiner anderen Fakultät oder Universität zur Prüfung vorgelegen hat; dass sie - abgesehen von angegebenen Teilpublikationen - noch nicht veröffentlicht worden ist sowie, dass ich eine solche Veröffentlichung vor Abschluß des Promotionsverfahrens nicht vornehmen werde. Die Bestimmungen dieser Promotionsordnung sind mir bekannt. Die von mir vorgelegte Dissertation ist von Prof. Dr. R. Strey betreut worden.

_____

Bastian Arlt

Lebenslauf

Zu meiner Person

Name	Bastian Arlt
Geburtsdatum, -ort	06.04.1981, Herdecke
Staatsangehörigkeit	deutsch

Ausbildung

ab 05/2008	**Promotion** "*Thermal Diffusion in binary Surfactant Systems and Microemulsions*" Forschungszentrum Jülich GmbH und Universität zu Köln, Prof. Strey
09/2006 – 09/2007	**Diplomarbeit** "*Consequences of a generalized Maxwell model for nonlinear flow*" Technische Universität Berlin, Prof. Hess
05/2005 – 05/2007	**Wissenschaftliche Studentische Hilfskraft** Technische Universität Berlin, Prof. Hess
10/2001 – 01/2008	**Diplom Physik** Physik-Studium an der Technischen Universität Berlin 04/2004 Vordiplom 09/2007 Hauptdiplom
08/2000 – 05/2001	**Zivildienst** Medicus GmbH, Oranienburg
07/1987 – 06/2000	**Abitur** 1987 – 1988 Grundschule Blecher 1988 – 1991 Grotenburg Grundschule Krefeld 1991 – 1993 Gymnasium Fabritianum Krefeld 1993 – 2000 Marie-Curie-Gymnasium Hohen Neuendorf Leistungskurse: Physik und Mathematik

Wissenschaftliche Veröffentlichungen

bis 2011	Arlt, B., Datta, S., Sottmann, T., and S. Wiegand. Soret effect of n-Octyl β-D-glucopyranoside (C_8G_1) in water around the critical micelle concentration, *J. Phys. Chem. B*, 114(6):2118–2123 (2010)
	Blanco, P., Kriegs, H., Arlt, B., and Wiegand, S., Thermal Diffusion of Oligosaccharide Solutions: The Role of Chain Length and Structure, *J. Phys. Chem. B*, 114(33):10740–10747 (2010)
	Hess, S., Arlt, B., Heidenreich, S., Ilg, P., Goddard, C., and Hess, O., Flow Properties Inferred from Generalized Maxwell Models, *Z. Naturforsch. A*, 64(1-2):81–95 (2009)

IT-Kenntnisse

Betriebssysteme	Windows XP/7, Linux
Sprachen	C#, LaTeX, HTML, CSS, PHP, JavaScript, Pascal
Datenbanken	SQL, MySQL
Anwenderprogramme	MS Office, Mathematica, Origin

Sonstiges

Fremdsprachen	Englisch (fließend), Französisch (Grundkenntnisse)